Citation: Ladele, E. O. (2003). Vector finite element optimisation of compact spot-size converters in photonics integrated circuits. (Unpublished Doctoral thesis, City, University of London)

Vector Finite Element Optimisation Of Compact Spot-size Converters In Photonics Integrated Circuits

By

Emmanuel Olufemi Ladele

A thesis submitted to the City University in fulfilment of
the requirements for the Degree of Doctor of Philosophy

City University

Photonics Research Group
School of Engineering & Mathematical Sciences
Northampton Square, London EC1V 0HB, UK.

December 2006

To my Mother,
My Wife,
And my children:
Tanimola, Ifeloju and Timilehin,
With Love

Table of Contents

List of Tables

List of Figures

Acknowledgements

Foremost, it gives me a great pleasure to be able to show my unreserved gratitude to Professor B. M. A. Rahman, who has been my mentor over the years, for his complete patience, enthusiasm and understanding – always ready to help. Professor Rahman's accessibility (his door is always open); guidance and encouragement are without blemish. Professor Rahman's excellent knowledge and ability to impart the knowledge, has instills in me a great confidence and unqualified qualities to build on. My unconditional gratitude also goes to Professor K. T. V. Grattan for his impeccable support and encouragement to achieve a state of excellence in our studies. Without them this project will not materialize. I therefore, raise my hand in salutation and say a big THANK YOU.

I would like to show my appreciations to my colleagues in the Photonics research group, Ellie, David, Najm, Raj, Moo, Chris, Fethi, Saif, Alam, Arti and Keja for the friendly, helpful, family-like atmosphere generated during the many years I sojourned in the Laboratory. Special thanks go to Salah for his help with relevant discussions and advise. Special thanks also go to Ferdie, Shyqri, Niranthi and Riyadh, for always being there for me. I am also grateful to the staff at the departmental office, Linda Carr and Joan Rivellini, for being very helpful all the time.

Finally, I am forever indebted to my wonderful and loving Mother. She is my source of inspiration and without her, I will not be educated in the first instance to this level. I am also absolutely indebted and grateful to my wife and children especially Tanimola and my niece Anuoluwapo, who both helped did some typing in this manuscript. Their support and understanding is magnanimous. My sincere thanks go to relatives, friends, and well-wishers too numerous to mention who have contributed in one way or the other to the success of this project.

The overall thanks go to the Almighty God for His constant guidance and protection over my family and me during the ups and downs while undertaking this project. “Great is thy faithfulness”.

Declaration

Abstract

It is well known that one of the major problems of integrated optical systems is the efficient coupling of photonic devices such as semiconductor lasers, amplifiers, modulators, or switches to a single mode fiber (SMF) in such a way that little or no power loss occurs. A well confined beam is needed in order to optimize the performance of a wide range of these photonic devices, because up to 90% of the optical power can be lost due to a large mismatch between their small non-circular spot-size and a SMF with a larger and circular spot-size when they are butt-coupled. Over the last 10 years several attempts have been made to close the gap and reduce such a high loss when coupling a photonic integrated circuit (PIC) to SMF. Among these is the use of a microlens or lensed fiber to enhance the coupling efficiency. However, the disadvantage of this approach is that associated sub-micron alignment tolerances lead to very high packaging costs. For a small business network, such a large cost is preventing the rapid extension of fiber-to-the-home (FTTH).

This makes the problem of optical coupling a big challenge to optoelectronics researchers worldwide as huge efforts were made to expand the narrow spot-size within a PIC, such that efficient coupling to a SMF with a large spot-size can be made. Monolithically integrated spot-size converters (SSCs) have been reported recently as being used to enhance optical coupling without deteriorating alignment tolerances and majority of the expanded SSCs do incorporate tapered structures, operating very close to the modal cut-off, to expand their spot-size.

In this thesis, some compact SSC designs have been carried out using the twin rib (TR), multimode interference (MMI) and silicon-on-insulator (SOI) waveguides to improve the coupling efficiency. The TR and SOI do require a tapered section in their mode of operation to expand the spot-size whereas the MMI does not need a tapered section.

Some numerical techniques have been employed in this thesis as tools in the design, analysis and optimization of the above guided-wave photonics devices. The robust, versatile and accurate full-vector finite element method (FVFEM) is the backbone of all the numerical techniques, as it has been used to obtain the modal solutions of the waveguide sections of the photonic devices throughout this thesis.

The FVFEM has been used in conjunction with the Least squares boundary residual (LSBR) method in the novel compact design, analysis and optimisation of 3-Core multimode waveguide as a device for improving power coupling efficiency. The transmission and reflection coefficients of the guided-waves are obtained as well. In a similar manner, the FVFEM is also used in conjunction with the finite element-based full-vector beam propagation method (FVBPM) to study the propagation of the guided-waves along the longitudinal z-direction of tapered devices for the TR and SOI waveguides. In the analysis, the propagating power, the radiation loss and the spot-size are obtained for these PICs. Tapered spot-size converters, with various high-index SOI waveguides, which consists of secondary polymeric cover, are investigated in this work. Mode beating phenomenon was observed and explained. Also the Δn

characterisation SOI was carried in this work because of the high-index contrast of the SOI materials which is a vital information for any design Engineer since the operations depend heavily on the materials as well as the geometry of the device.

The robust PML boundary conditions have been used to stem down unwanted radiations during propagation and the Pade approximation has been employed to take care of the waves propagating at wide angles to the z-axis. The incorporated popular overlap integral (OI) has been used in the determination of the coupling efficiency of the devices, which in the case of TR is 95%, and SOI is 99.25%.

Symbols and Abbreviations

ALD	Atomic Layer Deposition
ARC	Anti-Reflections Coatings
ATM	Asynchronous Transfer Mode
BEM	Boundary Element Method
BESOI	Bond-and-Etchback Silicon-on-insulator
BPM	Beam Propagation Method
CATV	Cable Television
CMOS	Complementary Metal-Oxide-Semiconductor
CVD	Chemical Vapour Deposition
DWDM	Dense Wavelength Division Multiplexing
EDFA	Erbium Doped Fibre Amplifier
EIM	Effective Index Method
ENM	Equivalent Network Method
FDM	Finite Difference Method
FEM	Finite Element Method
FHD	Flame Hydrolysis Deposition
FFT	Fast Fourier Transform
FTTH	Fibre-To-The-Home
FVBPM	Full-Vectorial Beam Propagation Method
FVFEM	Full-Vectorial Finite Element Method
HDTV	High Definition Television
LED	Light Emitting Diode
LPCVD	Low Pressure Chemical Vapour Deposition
LPE	Liquid Vapour Epitaxy
LLD	Lightly Doped Drain
LOCOS	LOCal Oxidation of Silicon
LSBR	Least Squares Boundary Residual
MAM	Multilayer Approximation Method
MBE	Molecular Beam Epitaxy
MM	Marcatili's method
MMI	Multi-Mode Interference

MMM	Mode Matching Method
MOCVD	Metal-Organic Chemical Vapour Deposition
MOSFET	Metal Oxide Semiconductor Field Effect Transistor
MOVPE	Metal-Organic Vapour Phase Epitaxial
OEIC	Optical-Electronic Integrated Circuit
OFDM	Optical Frequency Division Multiplex
OI	Overlap Integral
OIC	Optical Integrated Circuit
PIC	Photonic Integrated Circuit
PML	Perfectly Matched Layer
PMM	Point-Matching Method
RAM	Ray Approximation Method
RIE	Reactive Ion Etching
SAG	Selective Area Growth
SAW	Surface Acoustic Waves
SIMNI	Separation by Implantation of Nitride
SIMOX	Separation by Implantation of Oxygen
SMF	Single Mode Fiber
SMG	Shadow Masked Growth
SOI	Silicon-on-insulator
SONET	Synchronous Optical Network
SOS	Silicon-on-saphire
SSC	Spot-Size Converter
TDFA	Thulium Erbium doped fibre amplifier
TE	Transverse Electric
TM	Transverse Magnetic
TIR	Total Internal Reflection
TR	Twin Rib
VM	Variational Method
VPE	Vapour Phase Epitaxy
WDM	Wavelength Division Multiplexing
ZMR	Zone Melting Recrystalline
β	Propagation constant

c	Velocity of light in vacuum
ε	Permittivity
k	Wave number
n	Refractive index
ω	Angular frequency
μ	Permeability
λ	Wavelength

Chapter 1

Introduction

1.1 Brief History Of Light

The history of light dates back to the beginning of biblical creation in which God said, "Let there be light, and there was light" about 6000 years BC (Dake Bible, 2006). Ever since then scientists have been investigating the existence of light technology. Notable dates in the developments of light technology relevant to this thesis are discussed in brief in this section. Starting with the John Tyndal in 1870, when he demonstrated the passage of light through a pipe using a phenomenon as 'total internal reflection'. In 1873, James Clerk Maxwell discovered that magnetism and electricity were related and he introduced the concept of single unified theory of electromagnetism. In 1880, the scientist Charles Tainter converted the sunlight directly into electrical energy after developing the first selenium cells. They were later referred to as Photocells or Photoelectric cells and are useful in making light meters and other optical devices for measurements for a wide range of applications.

In 1916, Albert Einstein made one of his most important contributions to light when he explained the concept of the spontaneous and stimulated emissions which are basically processes for interaction between photons and electrons in a solid which result in LEDs and the laser. In the mid 1920s, Henry Round of Marconi Labs and Russian Oleg Vladimirovich Losev independently created the first light emitting diode (LED) when they discovered that a semiconductor junction would produce light. In 1928, German physicist Rudolf Walther Ladenburg first observed stimulated emission, although at the time it seemed to have no practical use.

In 1955, the invention of modern fibre optics is credited simultaneously to both Narinder Kapany (British) (Kapany, 1967) and Brian O'Brien Sr. at the American Optical Company in America. Also in 1955, Rubin Braunstein of the Radio Corporation of America reported on infrared emission from gallium arsenide (GaAs) and other semiconductor alloys. In 1958, Physicists Charles Townes and Arthur Schawlow were the first to publish their ideas for an "optical maser" in a seminal paper in the December 15, 1958, issue of *Physical Review* and applied for patent on Laser devices.

In 1960, the laser was perfected by research scientist Theodore Maiman at the Hughes Laboratory in Malibu California (Maiman, 1960). The term 'LASER' stands for Light Amplification by Stimulated Emission of Radiation. Laser light differs from ordinary light in four ways. Briefly it is much more intense, directional, monochromatic and coherent than conventional sources. More advance development was made in 1962 with the semiconductor laser which is considered more superior to other types of lasers already invented (Hall *et al*, Nathan *et al*, Quist *et al*, 1962). In this technology, direct conversion of electrical energy into coherent light is achievable.

1.2 Optical Communications Developments

The innovations of both the laser and fibre optics as mentioned in the last section had renewed the interest of scientists in optical communications in the 1960s. Production of low loss optical fibre has offered solution to the problem of suitable transmission media for modern optoelectronic systems. Present day optical fibres have transmission rates of optical transmission and data processing experiments at bit rates of up to 160 Gb/s and performance figures are improving year by year (http://www.orc.soton.ac.uk/oc.html). Along with the development of low loss optical fibre came the development of the compact single mode semiconductor laser (Hall *et al.*, 1962; Nathan *et al.*, 1962; Quist *et al.*, 1962). By the early 1970s semiconductor lasers were providing continuous wave coherent sources of laser light (Alferov *et al.*, 1970; Hayashi *et al.*, 1970). Improvements from the 1980's made them reliable sources for use in optical communications systems and so they have been widest used in this field since.

Optical signals transmitted using optical fibres will ultimately have to be converted into electronic form for processing. The speed of operation of electronic components is a major determining factor in the bandwidth of a communications system. This limitation has led to major research into a field now known as optoelectronics, replacing electronic devices with optical devices, switches, modulators, filters, transmitters, connectors and receivers. The potential of this new field is enormous. Will the development of an optical switch eventually lead to an optical computer? That is the hope and aspiration of many workers in this field. Advances in recent times in optoelectronics have led to the development of a wide range of optical components and devices such as directional couplers, Y-branches, waveguide crossings, optical filters, modulators, optical amplifiers and many others (Tamir, 1979). These advances in optical technology have resulted in the availability of consumer goods based on optical technology, such as laser copiers, laser printers, barcode readers, CD and DVD players and many others.

The emerging fields of research in optoelectronics can be classified into the following major categories:

- Optical communications systems
- Optical storage technology
- Waveguide devices and optoelectronic packaging technology
- Photonic devices and materials
- Optical sensor technology, including speciality fibres

The use of the laser for the free space optical communication occurs over a limited range: however the invention of the laser has enabled a significant research effort to be developed in the study of optical components needed to achieve reliable information transfer using light as a carrier. In 1966 Kao and Hockham (Kao and Hockham, 1966) proposed an optical communication system using dielectric waveguides or optical fibres fabricated from glass. Later, in the same year 1966, Werts has considered ways to avoid the degradation of the optical signal. Initially the optical fibres that were available exhibited very high attenuation (i.e. 1000 dB km^{-1}) and this were not comparable in performance with the coaxial cables (i.e. showing 5-10 dB km^{-1} loss). Nevertheless, within ten years optical fibre losses were reduced below 5 dB km^{-1} and suitable loss jointing techniques were perfected. Corning, UK achieved a reduction to 20 dB/km recently.

The development of the fibre waveguides has played a significant role in the development of other optical components which would constitute an optical fibre communication system. Based on the optical operating frequency, this new technology of optical component has used extremely small wavelengths typically 1.3 and 1.55 μm. Thus semiconductor optical sources (i.e. injection lasers and light emitting diodes), as well as matched detectors (i.e. photodiodes and transistors) compatible in size with optical fibres were designed and fabricated to enable successful implementation of the optical fibre communication systems proposed. They were originally fabricated in 1977 from alloys of gallium arsenide ($Al_xGa_{1-x}As$) which emitted in the near infrared between 0.8 and 0.9 µm. More recently, suitable semiconductor laser sources such as these in $In_xGa_{1-x}As_yP_{1-y}$ and Ge detectors for the 1.3 µm wavelength have been developed. In 1980 Bell Labs published a commitment to using single mode 1.3 µm technology and for the first time a transatlantic fibre-optic cable, TAT-8 began service in December 1988. This technology has spread into wider telecommunication applications, and remains the standard for the most fibre communications systems. Since 1988 up to date, the optical fibre has been used solely in the major networks where the bandwidth demands are enormous, and it is becoming easier to have the possibility of transmitting high bandwidth to consumers thereby achieving the 'Fibre to the Home' (FTTH) which has been reported being deployed now most notably in the far-East to date (http://www.orc.soton.ac.uk/oc.html). This development has yielded and opened up a host of high technological service opportunities including video-on-demand, HDTV and internet gaming amongst others at our door steps with more still to come.

1.3 Integrated Optics Developments

In 1969 S. E. Miller (Bell Laboratory) introduced the concept of integrated optics when he put together different optical components (Miller et al, 1969). Integrated Optics in its simple form is a combination of a waveguide, a detector, and a source of light in which each of the devices is made of different materials to form a single optical device which is hybrid in nature (Tamir, 1979). The major problem facing scientists in the hybrid approach is the assembly of these different components in such a way that their performance doesn't suffer seriously if the assembly is not meticulously handled. Accurate alignment of the components is required at the interfaces and any mismatch produces a loss mechanism which is difficult to avoid and usually results in poor performance. This great problem leads to a new technology known as Monolithic integration of all the components whereby all the components are fabricated on a single substrate in which any post production assembly of components and also alignment problems can be avoided (Moerman et al, 1997). Early researchers in this field needed a material substrate that will fulfil the criteria for monolithic integration. The most common and suitable semiconductor device material for optoelectronic application which is also susceptible to mass productions of monolithic optical integrated circuits (OEICs) is Silicon. Despite the favourable properties of silicon especially in the acceptable wavelength range of 1.3 -1.55 μm (Richard et al, 1991, Soref, 1993), it is considered to be unsuitable for active applications because of its indirect band gap. The traditional and direct band gap materials commonly used instead of silicon are the group III – V compounds such as Gallium Arsenide (GaAs) and Indium Phosphide (InP). Recent researches have created a renewed interest in Silicon as a viable alternative to group III – V materials because of its active nature when combined with Germanium to form SiGe compound (Schüppert et al, 1996, Naval et al, 1996, Li et al, 1998).

Optical systems in communications provide the inherent advantage of large bandwidth, parallelism, and reconfigurable configuration. However, such systems do not provide input-output isolation, as electronic devices do and it can be very difficult to focus multiple beams in a parallel system. Therefore it is logical to *couple* electronic and photonic devices, resulting in optoelectronic integration.

The aim of integrated optics is to do signal processing as much as possible directly on the optical chip itself. The basic concept of the integration was proposed by Anderson in 1965 (Anderson, 1965) and considerable progress has been made, although not a great deal of integration has been achieved.

An attractive form of well defined integration is the interconnection of the optical devices which can take a form of free space, integrated optical waveguides, or optical fibre. An illustration via a simple schematic block diagram of an optoelectronic phase integration array antenna system is illustrated in the Fig. 1.1. With optical interconnects and transmission, immunity to manual interference and crosstalk and freedom from capacitive loading effects. The large bandwidth of the optical device contributes to system size reduction, reduced system power, and increased fan-out capabilities of the device.

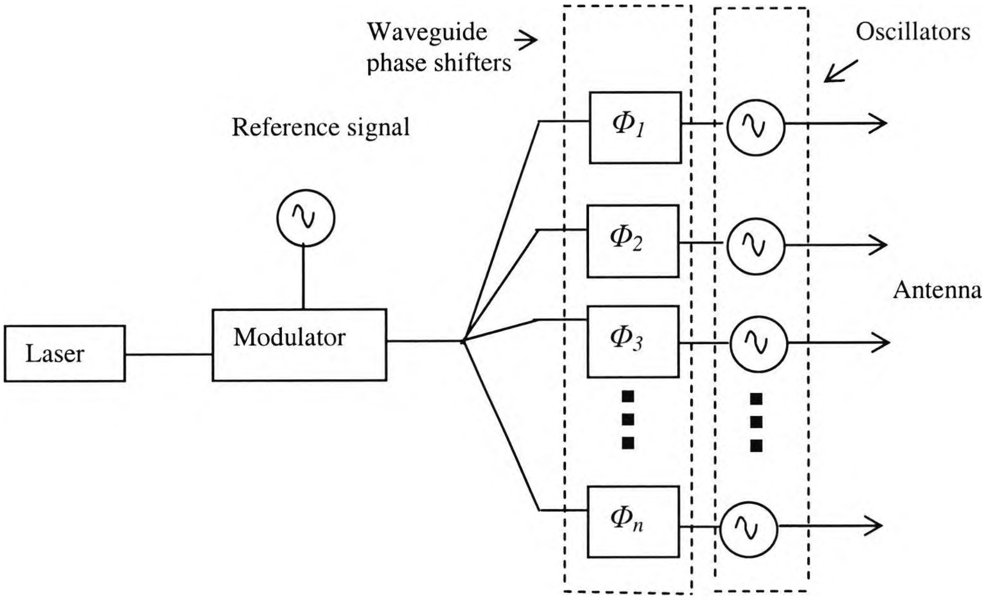

Fig. 1.1 Block diagram of an optoelectronic integrated circuit (OEIC) phase array antenna system.

Optoelectronic integrated circuits (OEIC) involve the integration of electronic and optic components and optical interconnects. The monolithic integration of electronic and optical devices on the same chip will contribute to high-speed, high-sensitivity, compactness, reliability, and low cost. In order to achieve an integration of these devices, first the optical devices, which may have different layer structures must be very high quality and secondly there is a major issue of capability and impedance matching between the devices and, last but not the least, the cost in designing and realisation of OEIC is a relevant factor.

There are two major ways of integration in OEICs, hybrid integration and monolithic. Hybrid integration involves the connection of discrete devices, blocks or chips using electronic (leads) or optic (fibre) interconnects. Alternatively monolithic integration involves the building of all the active and passive components on the same chip, which makes this type of integration a real challenge, because of heterostructures (some components are made of different materials, layers).

Practical integrated optics also can be classified as active and passive. Passive components are used for transmission, splitting, beam splitting, polarization converters, polarization controllers, switches, and wavelength division multiplexer. Active components are usually (electronically controlled) and have both optical and electrical properties, such as lasers, detectors, modulators ($LiNbO_3$), transceivers, and amplifiers. Modulators can be also directly integrated with the laser, like GaAs or as an external modulator, like in $LiNbO_3$.

The two most common semiconductor materials used in optoelectronics are based on the ternary alloy aluminium gallium arsenide ($Al_xGa_{1-x}As$) and the quaternary alloy indium gallium arsenide phosphate $In_xGa_{1-x}As_yP_{1-y}$. The variation of the alloy content between the layers then yields the refractive index difference necessary for a waveguide. Although several types of devices of the kind that will undoubtedly be needed have been successfully demonstrated, they require a wide range of different substrates. These follow some discussion of possible structures for these devices.

1.3.1 Integrated Photonics Elements

The word ‘integrated’ simply means assembly of some basic components, which are common to the integrated optical devices. These components operate in the same way as their traditional counterparts i.e. conventional optical components, but their operating principles may differ. As a result, their designs and fabrications are also different especially with miniature size.

Fig. 1.2 shows some basic integrated photonic devices that have been proposed, modelled, and fabricated. In the optoelectronic industry, many more devices are still being designed and fabricated, but the basic components remain the same. The usual practice is to have a basic components block on which the complex integrated optical devices can be built. The major difference in design of integrated photonic devices and the conventional devices is due to the fact that the operational principle of the conventional devices has its foundation on the properties of light considered as plane waves or rays of light whereas the operational principle of the integrated photonic devices based the modelling and performances on the idea of Maxwell’s equations of the electromagnetic waves. This has to do with the fact that the size of the devices are of the order of nanometers (10^{-9}) whereas that for the conventional devices are of the order of millimeters (10^{-3}).

The building blocks from which the optical components are assembled into systems can be broadly classified into three. These are

1. The Straight waveguide blocks
2. The bend waveguide blocks
3. The Power splitter blocks

These blocks offer the assembly of several basic components, which can easily perform the same optical functions as the conventional devices. The ability to perform a wide range of functions makes the concept of integrated photonic devices elements fantastic.

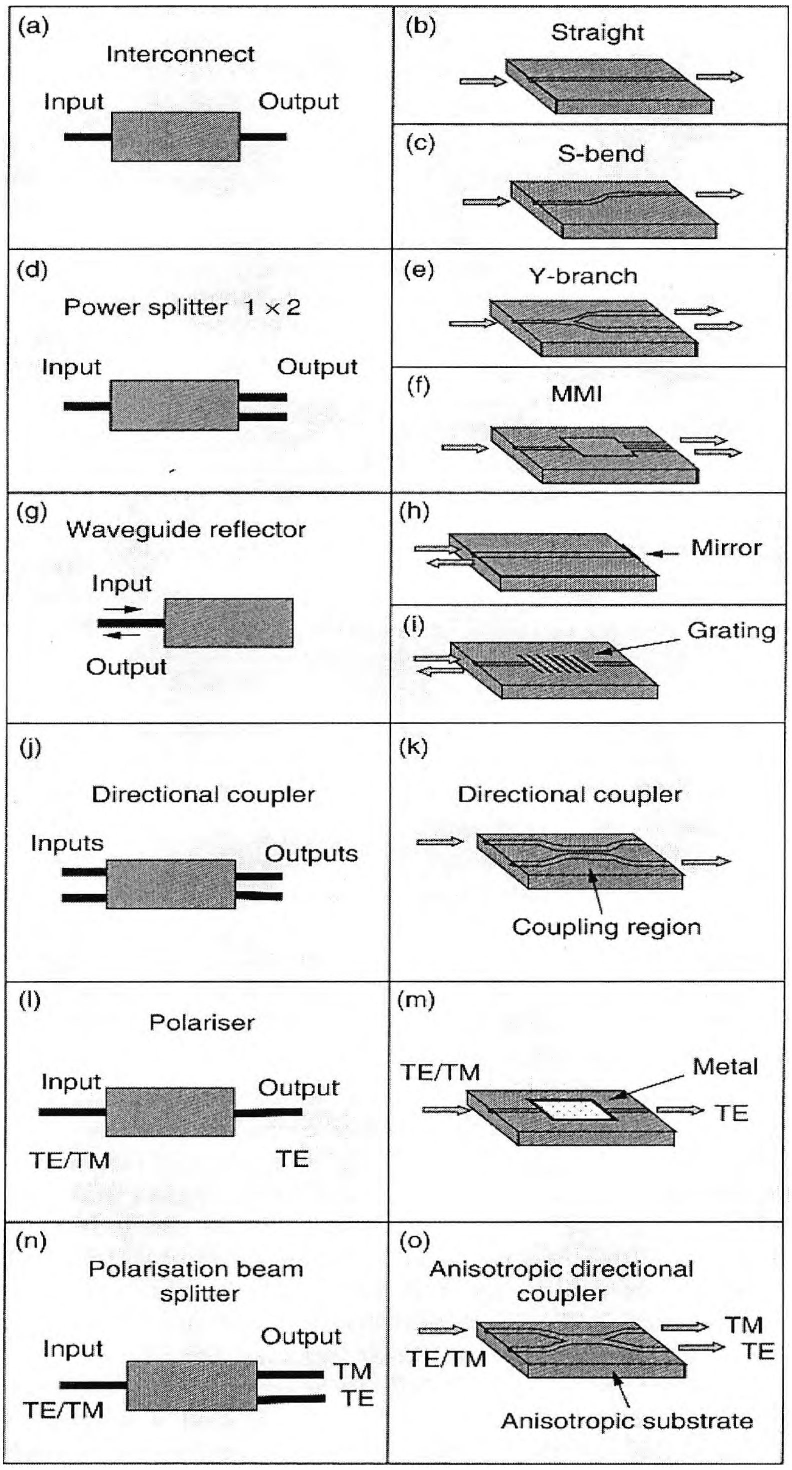

Fig. 1.2 Basic integrated photonics elements (Linfante, 2003)

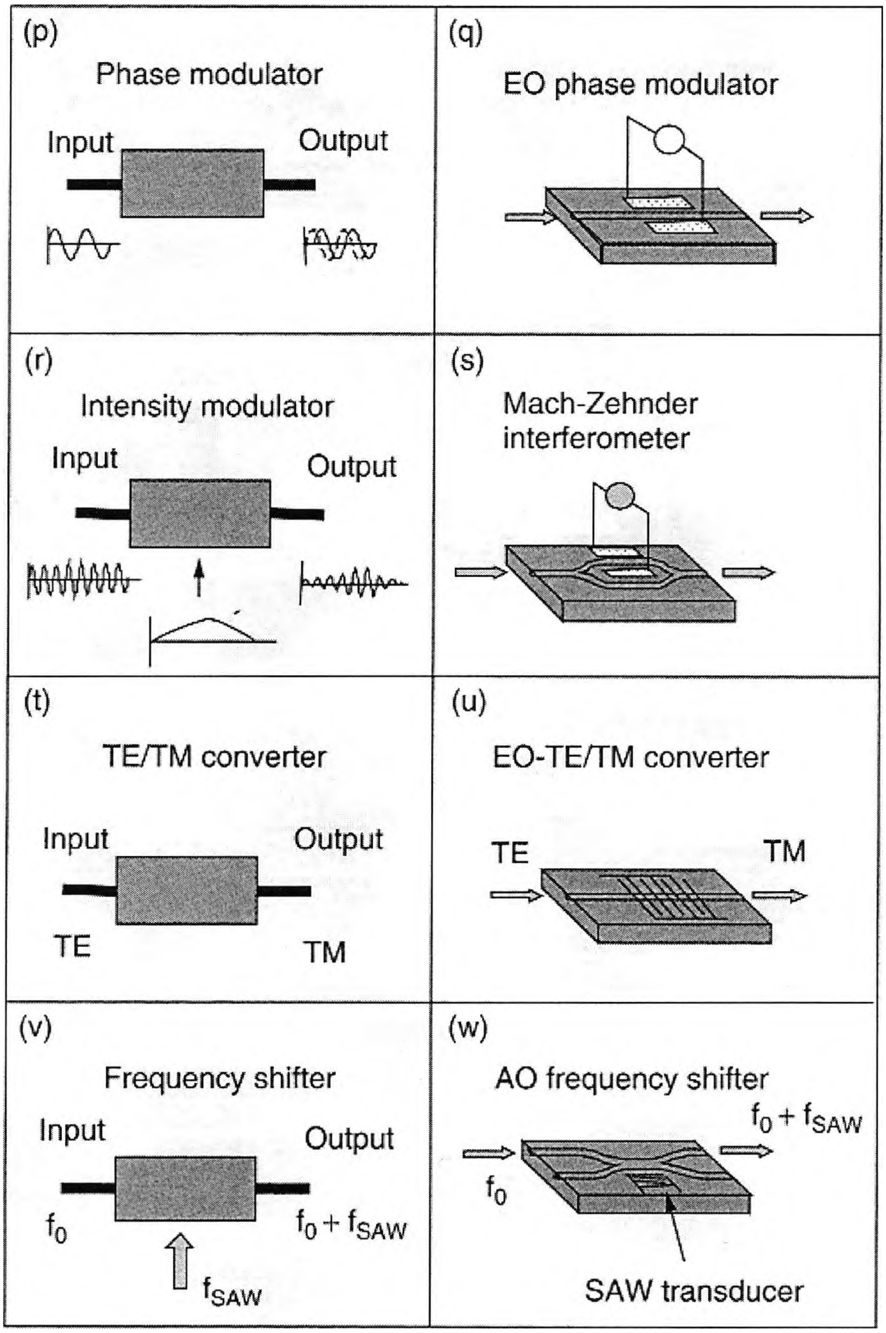

Fig. 1.2 Basic integrated photonics elements continued. (Linfante, 2003)

1.3.2 Brief applications of Integrated Photonics

The applications of integrated photonics can be broadly classify into two groups

1. Performance group: This group has got the characteristic of high bandwidth, low insertion loss and low crosstalk. They represent the communications technology such as telecommunications, data transmission, and optical interconnections which depends explicitly on the performance parameters of photonics components.
2. Enhanced material group: This group due to nature of its materials, has no electromagnetic interference over short distances, no bias problems, no wire tapping, explosion risk protected, low weight and size.

Therefore it can be said that optical communication systems are the technological driver of photonics circuits. Fig. 1.1 shows the general photonic applications where it can said that while the photons are transmitting, the electrons are switching.

As mentioned earlier, the optical fibres can transmit data at many orders of magnitude over the conventional transmission lines. With the increase in demand for new services such as high definition television HDTV distribution, broadband data highways and video telephony, the communications and data traffic require a very high capacity bandwidth and network for optical transmission in the order of 10^{15} Hz. There are three major techniques of accessing the enormous capacity:

- Wavelength Division Multiplex (WDM): In this system the overall data is divided into sets, each having different wavelength. The WDM transmission systems have been developed to “multiplex” optical signals effectively using the existing optical fibre infrastructure more effectively, i.e. sending several optical signals with different wavelengths simultaneously, down the same, single optical fibre. Signals are multiplexed by optical power combiner Optical Frequency Division Multiplex (OFDM) or filter. Signal reception is by direct detection.
- Dense Wavelength Division Multiplex (DWDM): WDM systems have moved further to DWDM systems. This is a technique by which a large number of different wavelengths of light signals are simultaneously transmitted. This has

the effect of increasing the capacity of the fibre to carry information. DWDM system data speeds have risen to 160 Gb/s and beyond. Such a system uses Erbium doped fibre amplifiers (EDFAs) as well as Thulium Erbium doped fibre amplifiers (TDFAs). In such a DWDM optical system, each fibre amplifier provides the gain for more than a hundred signal carriers separated by a frequency difference of 100 GHz or 50 GHz.

- Optical Frequency Division Multiplex (OFDM): Also in this system the overall data is divided into sets each having different wavelength. Signals are multiplexed by optical power combiner or filter. Signals are detected by a laser oscillator.
- Single-Channel Transmission: Single-channel transmission at 40 Gb/s over long terrestrial links, including the wavelengths conversion of a signal has been reported (Matera F. *et al.,* 2002).

Communication networks also provide three types of services:

- Distributive services. This is used in broadcasting of information to all persons involved. Examples are TV, radio services.
- Mailing services. This involves unidirectional transmission of information from one person on a system to another. Examples are e-mail, ftp and fax services.
- Interactive services: This involves bidirectional transmission between two or more persons. Examples are telephony, video conferences services

Other applications include

- Optical interconnections e.g. 1.3 / 1.55 μm multimode waveguide or fibres.
- Sensors and Sensor systems e.g. temperature sensing, vapour sensing etc.
- Consumer photonics e.g. CD players, laser pointers.
- Consumer peripherals e.g. flat panel displays, laser printers, CD-ROMs, DVD discs.
- Industrial environment e.g. sensors, high-power lasers.
- Medical environment e.g. sensors, lasers.

- Military environment e.g. sensors, filters, control and communication systems to avoid wire tapping.

1.4 Motivations for this work

One of the major problems confronting the researchers in optical communications is the efficient coupling of a waveguide to single mode optical fibre because of the mode mismatch of the connecting devices. This leads to the principle of spot-size conversion and optimisation of the device technologies to get the best coupling efficiency and alignment tolerances. Recent advances in optoelectronics have witnessed new technologies, device fabrications and modelling of novel devices. Computer simulation of optical devices has gone a long way to give good insight to modern researcher the ability to visualise solutions to the real problems. The simulations have assisted scientists in optoelectronics research breakthrough and their usefulness cannot be over-emphasised. The use of simulations in modelling of optical devices has helped to shorten the length of designed cycle for existing and emerging optical technologies. It accelerated new developments that may have taken many years to achieve due to high costs.

There are various methods used for the simulations of optical devices but the most important thing is that they must be able to determine the stability of any designs within the range of fabrication and operational tolerances. It is therefore valuable to perform simulations for a range of device parameters to achieve optimum design. There are two major methods used in device modelling which are (1) Analytical approximation methods and (2) Numerical methods. Analytical approximation methods can only handle simple cases in which there are no complexities with regards to the arbitrary device geometry and composite refractive index. It is limited in wide range of parameters of optical devices that can be modelled and cannot accommodate iterative methods which are not only fast but accurate. Numerical methods are more versatile and accurate with the ability to handle the complex device geometry including 3-D. Iterative methods are there to take care of arbitrary refractive index distributions and give the researcher genuine knowledge of the operation of the device. Many numerical methods have been explored in literature such as Finite Difference Method (FDM) (Davies, 1989), Effective Index Method (EIM) (Knox and Toulios, 1970), Spectral Index Method (SIM) (Kendall *et al.*, 1989; Stern *et al.*, 1990), Variational Method (VM) (Rahman and Davies, 1984*a*) to name a few, but the one used in this thesis is the versatile Finite Element Method (FEM) (Rahman and Davies, 1984*a*; Koshiba and Inoue, 1992) together with the famous and robust Beam Propagation Method (BPM) (Feit and Fleck, 1978). They are readily applied to complex device cross-sections with passive or active materials and full 3-D investigation of complex integrated circuits. The philosophy of vectorial finite element method (VFEM) and FVBPM have been applied throughout this thesis to the investigation of coupling some optical devices such as Rib and taper waveguides, submicron SOI waveguides to a SMF, SSC and calculation of associated transmission loss due to mode mismatch and coupling efficiency of the whole system. A lot of work was done to investigate the high index profile of the submicron SOI waveguides and how mode-beating phenomenon can be avoided using polymer material as secondary and connecting waveguide. The VFEM and least squares boundary residual (LSBR) have successfully been applied to MMI couplers, to determine the transmission and reflection coefficients as well as the coupling efficiency of the assembly. Successful designs of suitable SOI waveguides and tapers coupled to a SMF in this thesis will go a long way to assist researchers in manufacturing OEICs devices which will fulfil the desired need for an efficient, reliable and low cost coupling technique. The ultimate mass production of these OEICs will provide increased bit-rates to a single subscriber through the FTTH package.

As a sequel to the aforementioned, the technological achievements in the field of communication in recent years and the role of integrated optics within the broad field of communication in facilitating an efficient dissemination of information form the basis for the work carried out in this thesis. The primary aims and objectives of this research can be summarised as follows:

(1) To review different fabrication technologies and suitable materials in the production of optical waveguides especially the complementary metal oxide semiconductor (CMOS) process for silicon integrated circuits.

(2) To investigate different approaches to the solution of optical waveguide problems and to provide a basis for the effective employment of the finite element method.

(3) To develop and implement the rigorous, accurate and efficient finite element method based on vector **H**-field variational formulation for the analysis of optical waveguides with arbitrary cross sectional shapes.

(4) To implement the LSBR in conjunction with the accurate modal solutions obtained from the finite element method in order to develop accurate coupling properties of MMI coupler waveguides.

(5) To apply full-vectorial finite elements techniques developed and implemented in (3) in the study of designing a spot-size to solve mode-matching problems in optoelectronics.

(6) To develop and implement an efficient and robust beam propagation method which combines the finite element discretization in the transverse domain with the stable z-stepping Crank-Nicholson scheme in the longitudinal direction.

(7) To apply the developed and implemented beam propagation method in the design and optimisation of a novel semiconductor based (AlGaAs-GaAs) spot-size converters by using full vectorial numerical methods implemented in (3) to the characterisation of GaAs and vector **H**-field variational formulation of tapers.

(8) To apply the full vectorial numerical techniques implemented in (3) and (6) in the study of designing and characterising various optical waveguides involved in SOI spot-size converter issues in optoelectronics.

The above research is aimed at providing the optical designer an intuitive grasp of the design and operation of optoelectronic integrated circuit devices and therefore to supply a useful tool to the systems developer to be used in the novel design of optical devices.

1.5 Structure Of The Thesis

The work presented in this thesis is based on the research carried out by the author in the use of the vector **H**-field variational formulation based modal analysis method in the study of various types of taper waveguides together with the versatile and robust full vectorial beam propagation method. Both direct and indirect semiconductors, AlGaAs-GaAs and silicon-wire taper waveguides were investigated Other work was also carried out with LSBR on MMI couplers program on spot-size converters and the following discussion gives the summary of the chapters in this thesis starting with this introduction as the first chapter. The first chapter gives a brief history of light relevant to this thesis, from the beginning to the present day highlighting eminent scholars who have contributed to the development of light technology over the years. This is followed by a brief account of the development of light as a means of communication. The advent of communication systems such as laser copiers, laser printers, barcode readers, CD players to name a few find their way to consumers. The development of fibre optics as a means of transporting light was given. Other problems such as attenuation, storage, device compatibility, packaging etc, which confronted researchers in the world of optical communication technology, are mentioned. The development of integrated optical technology leads to the optoelectronic integrated circuits, the science of combining electronics and optical devices on a chip for optimum performance. A brief account of evolution of photonic devices such as waveguides, lasers, modulators, switches, photodetectors, oscillators, antenna etc. is given.

Chapter 2 treated the background theory which covers the light as an electromagnetic spectrum and discuss the fundamental laws of optics as well as the Clerk Maxwell's equations of electromagnetics on which foundation this theory is based. This section also provides a brief description of some representative and important numerical techniques useful for waveguide and millimetre-wave structures such as analytical and numerical solution techniques for optical waveguides, to achieve. In particular, Chapter 2 presents a discussion of the fabrication methods which involve various epitaxial growth techniques, photolithographic processes, and etching techniques. The CMOS processes for silicon integrated circuits are also discussed.

In chapter 3 the theoretical formulation of the finite element method as a powerful numerical tool in analysing optical waveguides is presented. This is followed by a brief history of the finite element method is presented with its importance in analysing any type of waveguide. The fundamental mathematical relations derived from Maxwell's equations for the application of this approach in the solution of optical waveguides is derived. Also a comparison of several variational formulations is presented with an emphasis on the vector **H**-field finite element formulation. The utilisation of triangular elements, the shape functions, and the infinite elements is undertaken in order to obtain the propagation constants and the field profiles of different modes propagating through a uniform optical waveguide. The problem of spurious modes is investigated and the penalty function method is introduced to avoid the appearance of the spurious modes.

Chapter 4 deals with the theoretical formulation of the versatile beam propagation algorithms based on finite element discretization in the transverse cross-section and finite difference discretization in the z-domain. The robust perfectly matched layer (PML), the Pade wide angle approximation, Crank Nicholson and their applications to the tapers propagation along the longitudinal direction are all taking into considerations and they present an excellent model. The propagating power, the spot-size and transmission loss in direction of propagation (including evanescent radiation loss) can be calculated arbitrarily. Finally the overlap integral (OI) is incorporated into the algorithm to calculate the coupling efficiency between a PIC and a SMF for different Gaussian radii consecutively.

In chapter 5 results of the application of the VFEM and LSBR to design and optimise a novel semiconductor based (AlGaAs-GaAs) 3-core multimode interference (MMI) couplers. The LSBR is utilised in the calculation of the transmission, reflectance and coupling efficiency of the butt-coupled MMI and SMF.

Chapter 6 is devoted to the applications of the VFEM and FVBPM in a rigorous study of a novel semiconductor based (AlGaAs-GaAs) spot-size converters respectively and their results are compared. Lateral, vertical and combined lateral and vertical tapers were investigated and their coupling efficiency between a PIC and a SMF, the propagating power, the spot-size and transmission loss in direction of propagation were calculated and results presented.

Chapter 7 deals with a painstaking study of the applications of VFEM and FVBPM in the design and optimisation of a simple and realistic monolithically integrated silicon-on-insulator based waveguide spot-size converters for efficient and diverse butt-joint coupling to single mode optical fibre. The fabrications of these SOI-based waveguides are easy and can be obtained by mass production through the CMOS. The OI and Gaussian algorithm are used to determine the coupling efficiency. Tapered spot-size converters with various high-index SOI and a connecting secondary polymeric guiding are investigated in this work.

Chapter 8 consists of summary of the major achievements of the work that has been reported in this thesis. Conclusions are drawn on all these aspects. Some ideas and suggestions for future works are made. These suggestions will help in the advancement of the optoelectronics technology in foreseeable future.

The thesis ends with sections devoted to following:-

1. References' list cited throughout the thesis.
2. List of publications relevant to this work by the author.

Chapter 2

Background Theory & Techniques

2.1 Background Theory

Much has been said about light propagation in optical fibre and other optical waveguide devices to the extent that one need to examine the underlying principles guiding the transmission of light in these devices. The field of integrated optics can broadly be classified into optical fibre waveguides and the optical integrated circuits (Hunsperger, 1984). The optical integrated circuit (OIC) can be regarded as the optical equivalent of the conventional electrical circuit, where the fundamental material that interconnects the various devices of an OIC is the optical waveguide. Unlike electrical circuits where the signal is carried by a current, the signal in an optical waveguide travels in distinct optical modes. A mode can be regarded as the spatial distribution of optical energy in one or more dimensions. The mode can also be regarded as a packet of electromagnetic modes with energy quantized to discrete levels separated by the energy of a photon. The energy of a photon in a mode of frequency ν is

$$E = h\nu = \hbar\omega \tag{2.1}$$

Where $h = 6.63 \times 10^{-34}$ J-s is **Planck's constant** and $\hbar \equiv h/2\pi$. Energy may be added to or taken from this mode in units of $h\nu$ (Saleh and Teich, 1991). Therefore light is made up of particles generally called photons which has zero rest mass and carries electromagnetic energy and momentum.

In this section, Maxwell's equations for the propagation of waves in optical waveguides have been presented, and different types of waveguides are then reviewed.

The simplest and the most basic type of optical waveguide is known as the three layer dielectric waveguide or an asymmetric slab waveguide which is shown in Fig. 2.1.

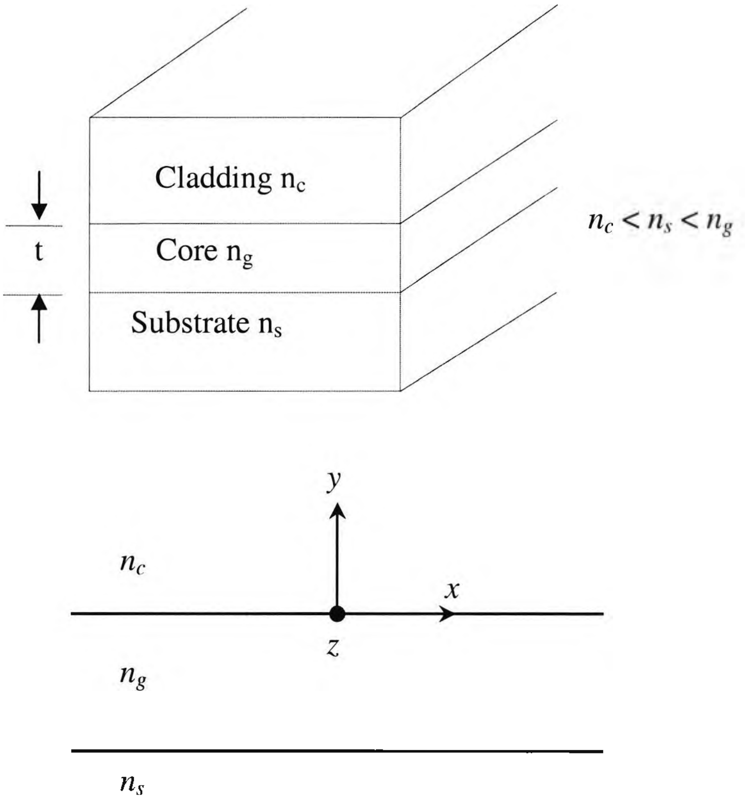

Fig. 2.1. Schematic three-layer dielectric waveguide.

Here n_g, n_s and n_c represent the refractive indices of the guide, substrate and the upper cladding, respectively. By loading a thin film with a higher refractive index than either the substrate or the upper cladding on the substrate surface, the light can be trapped inside this film, which is often called the guide. So the relationship among the refractive indices is $n_c < n_s < n_g$ and t is the guide thickness. However, in most cases, the upper cladding is air, giving $n_c = 1$. When $n_s = n_c$, the waveguide is called a symmetric slab waveguide.

A three-layer dielectric optical waveguide is shown in Fig. 2.1, and it may be assumed that z is the direction of propagation and the waveguide structure is homogeneous in the z-direction. It can be noted from the Fig. 2.2 that a small amount of light is reflected back into the dielectric (internal reflection) and some light is transmitted. In the case when the refraction angle θ_2 is 90^0, the angle of incidence is known as the critical angle θ_c and total internal reflection (TIR) occurs.

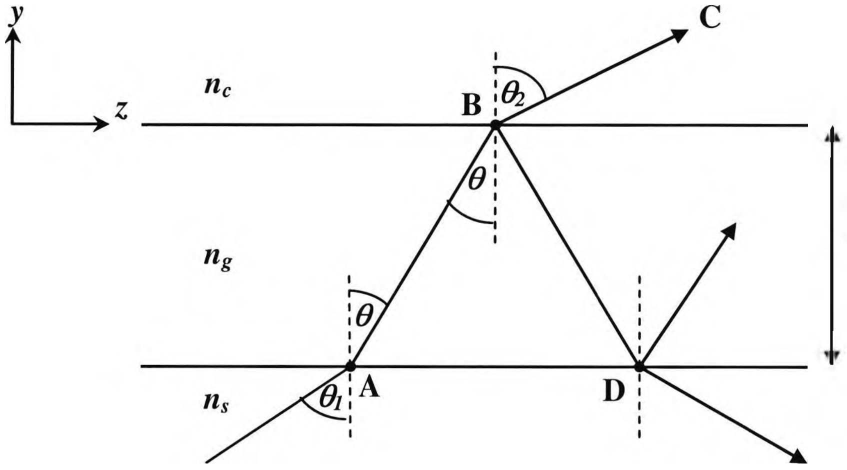

Fig. 2.2 Ray diagram showing refraction and reflection in a slab waveguide.

Consider a coherent light wave incident at an angle θ_l between the wave normal and the normal to the substrate-guide interface, as shown in Fig. 2.2. By using Snell's law the refraction can be expressed as (Kogelnik, 1990),

$$\frac{n_s}{n_g} = \frac{sin\theta}{sin\theta_1} \quad 2.2$$

where θ is the exit angle of the refracted wave AB.

Similarly, for the guide-cladding interface, the Snell's law gives,

$$\frac{n_c}{n_g} = \frac{sin\theta}{sin\theta_2} \quad 2.3$$

where θ_2 is the angle of the refracted ray BC, with the normal to the guide-cladding interface.

The so-called critical angles θ_s and θ_c at the guide-substrate and at the guide-cladding interfaces, respectively, are determined by (Koshiba, 1992),

$$sin\theta_s = \frac{n_s}{n_g} \quad 2.4$$

$$sin\theta_c = \frac{n_c}{n_g} \quad 2.5$$

Here, $\theta_c < \theta_s$, based on the assumption that $n_c < n_s < n_g$. If the angles of incidence to these two interfaces exceed the critical angles, then the total internal reflection phenomenon occurs and the light can be guided inside the material.

Since $n_g > n_c$, the incident ray is refracted into the guide region, following the path AB and when $\theta < \theta_c$, total reflection conditions are not met at the guide-cladding interface, and thereby the ray is refracted to the cladding side. There is essentially no confinement of light and the electromagnetic mode corresponding to this is called a "*radiation mode evanescent waves*".

When the incident angle θ is greater than the critical angle, θ_c, then the total internal reflection occurs and the light ray will follow the path BD. At the guide-substrate interface, if the incident angle $\theta < \theta_s$, then the light ray may refract back in to the substrate through which the light escapes from the structure. These are called "*substrate radiation modes*".

Finally when θ is large enough, i.e. both $\theta_s; \theta_c < \theta$, total internal reflection occurs at both interfaces. Then the light, once it is inside, is trapped and confined in the guide and propagates in a zig-zag path along the +*z* direction. These modes are called the '*guided*' or '*bound*' modes as shown in Fig. 2.3.

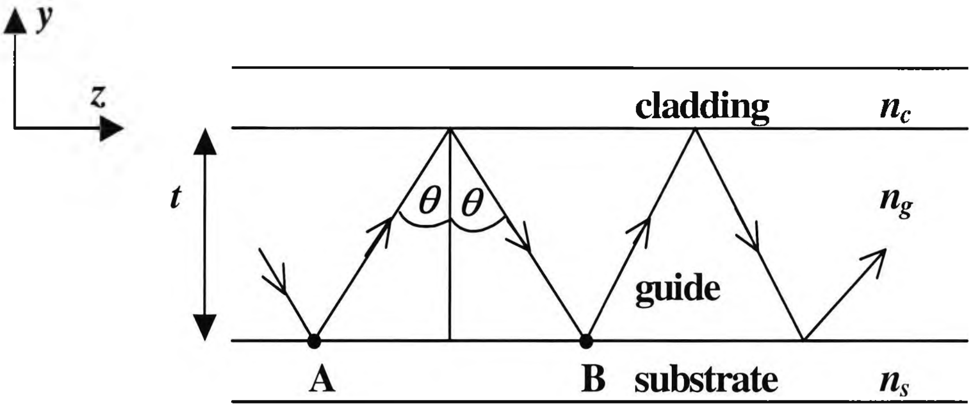

Fig. 2.3. Wave normals of the zig-zag waves corresponding to a guided mode in a slab waveguide.

These modes can be classified as either Transverse Electric (TE) or Transverse Magnetic (TM) modes. In the TE mode, the longitudinal electric field $E_z = 0$ and in TM mode the longitudinal magnetic field $H_z = 0$. These waves travel with a wave vector kn_g in the direction of the wave normal where the absolute value of k is,

$$k = \frac{2\pi}{\lambda} = \frac{\omega}{c} \qquad 2.6$$

k is called the wavenumber and ω, λ and c are the angular frequency, free-space wavelength and the velocity of light in vacuum, respectively.

The propagation constant β in the direction of propagation, and the phase velocity v_p can be defined by (Kogelnik, 1990),

$$\beta = \frac{\omega}{v_p} = kn_g sin\theta \qquad 2.7$$

However not all the values of θ are allowed and only discrete values of θ will yield the "guided mode". The condition for the existence of a guided mode is that the total phase shift in the y-direction during one cycle (from point A to point B in Fig. 2.3) of the plane wave must equal an integral multiple of 2π. The phase change for the plane wave to cross the thickness t of the guide twice (i.e. up and down) is $2kn_gt\ cos\theta$ (Tien, 1971). In addition the wave suffers a phase change of $-2\phi_c$ due to the total internal reflection at the guide-cladding interface, and similarly a phase shift of $-2\phi_s$ on total internal relection at the guide-substrate boundary. Thus, the self-consistency condition can be expressed as follows:

$$2kn_gt\ cos\theta - 2\phi_s - 2\phi_c = 2m\pi \qquad 2.8$$

where m is the order of the mode which is an integer. This expression is also referred to as the eigenvalue or transcendental equation. According to the theory of total reflection and by employing the Fresnel formulas (Kogelnik, 1990), the phase shifts ϕ_s and ϕ_c can be derived in terms of the angle θ, for each polarization;

$$tan\phi_s = \frac{\sqrt{n_g^2 sin^2\theta - n_s^2}}{n_g cos\theta}$$

$$tan\phi_c = \frac{\sqrt{n_g^2 sin^2\theta - n_c^2}}{n_g cos\theta} \qquad 2.9$$

for the TE waves, and,

$$tan\phi_s = \frac{n_g^2\sqrt{n_g^2 sin^2\theta - n_s^2}}{n_s^2 n_g cos\theta}$$

$$tan\phi_c = \frac{n_g^2\sqrt{n_g^2 sin^2\theta - n_c^2}}{n_c^2 n_g cos\theta} \qquad 2.10$$

for the TM waves.

From the above eigenvalue equation (2.8), the propagation constant β of a guided mode at a given angular frequency ω can be calculated. Since the angle of incidence, θ is discrete, only a limited number of discrete values are allowed for β. Therefore the guided mode is sometimes called the discrete mode or discrete spectrum. On the other hand in the radiation mode, the angle of incidence θ and the propagation constant β are continuous quantities. For this reason it is called the continuous mode or the continuous spectrum.

For guided modes, β is bounded by the plane wave propagation constants of substrate and guide (Kogelnik, 1990).

$$kn_s < \beta < kn_g \qquad 2.11$$

From (2.11) it is convenient to define an "*effective refractive index*" (Koshiba, 1992);

$$n_{eff} = \frac{\beta}{k} = n_g \sin\theta \qquad 2.12$$

which is bounded by,

$$n_s < n_{eff} < n_g \qquad 2.13$$

For **TE**-modes $\boldsymbol{E_y} = \boldsymbol{E_z} = \boldsymbol{H_x} = 0$

$$\boldsymbol{E_x} = \begin{cases} A\cos(\kappa t - \phi)e^{-\sigma(y-t)} & (y > t) \\ A\cos(\kappa y - \phi) & (0 \le y \le t) \\ A\cos(\kappa t + \phi)e^{\xi y} & (y < 0) \end{cases} \qquad 2.14$$

For **TM**-modes $\boldsymbol{E_x} = \boldsymbol{H_y} = \boldsymbol{H_z} = 0$

$$\boldsymbol{H}_x = \begin{cases} A\cos(\kappa t - \phi)e^{-\sigma(y-t)} & (y > t) \\ A\cos(\kappa y - \phi) & (0 \le y \le t) \\ A\cos(\kappa t + \phi)e^{\xi y} & (y < 0) \end{cases} \qquad 2.15$$

The electromagnetic field components are continuous at the boundaries of core-cladding interface $(y = t)$, where the wavenumbers in core (n_g) and cladding $(n_c$ and $n_s)$ region are given as:

$$\begin{cases} \kappa = \sqrt{k^2 n_g^2 - \beta^2} \\ \sigma = \sqrt{\beta^2 - k^2 n_c^2} \\ \xi = \sqrt{\beta^2 - k^2 n_s^2} \end{cases} \qquad 2.16$$

$$k = \omega\sqrt{\varepsilon\,\mu} = \frac{\omega}{\lambda} \qquad 2.17$$

After eliminating the constant *A*, the eigenvalue equation for the $\mathbf{TE_m}$ mode is obtained:

$$\tan(u + \phi) = \frac{w}{u} \qquad 2.18$$

$$\tan(u - \phi) = \frac{q}{u} \qquad 2.19$$

where

$$\begin{cases} u = \kappa a \\ w = \xi a \\ q = \sigma a \end{cases} \qquad 2.20$$

The eigenvalue equation can be obtained as:

$$u = \frac{m\pi}{2} + \frac{1}{2}\tan^{-1}\left(\frac{w}{u}\right) + \frac{1}{2}\tan^{-1}\left(\frac{q}{u}\right) \qquad (m = 0,1,2,3,....) \qquad 2.21$$

$$\phi = \frac{m\pi}{2} + \frac{1}{2}\tan^{-1}\left(\frac{w}{u}\right) - \frac{1}{2}\tan^{-1}\left(\frac{q}{u}\right) \qquad 2.22$$

$$v^2 \equiv w^2 + u^2 = k^2 a^2 \left(n_g^2 - n_s^2\right) \qquad 2.23$$

$$\gamma = \frac{n_s^2 - n_c^2}{n_g^2 - n_s^2} \qquad 2.24$$

When the wavelength of the light signal and the geometrical parameters are determined, in other words, the normalized frequency v and the asymmetric parameter γ, then the propagation constant can be easily determined from the above equations. In order for the transverse wave number to be real for the core region, the following condition should be satisfied:

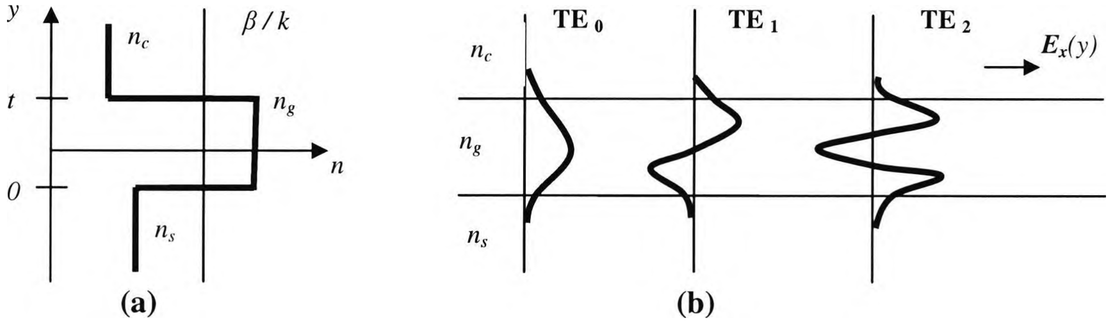

Fig. 2.4. Refractive index profile of the slab waveguide **(a)** and Field distribution for TE_m modes, where $m = 0, 1, 2\ldots$ (First and higher order modes) **(b)**.

$$n_s \le \frac{\beta}{k} \le n_g \qquad 2.25$$

where β / k is the refractive index itself for the plane wave

The effective index may be expressed as:

$$n_{eff} = \frac{\beta}{k} \qquad 2.12$$

When $n_e < n_s$ the electromagnetic field in the cladding region is oscillatory along the transverse direction, this dissipation of the field is called the *radiation mode or evanescent waves* (non-guided mode). The evanescent waves dissipation in the cladding or substrate region is another loss mechanism in waveguides and fibre optics. This critical condition where the field is cut off and becomes a *radiation mode* or *evanescent waves* is called the “cutoff condition” and is expressed by:

$$\beta = kn_s \text{ and } b = 0 \qquad 2.26$$

The condition for the guided mode is

$$0 \le b \le 1 \qquad 2.27$$

where, b is termed the *normalized propagation* constant and it can be expressed as:

$$b = \frac{n_e^2 - n_s^2}{n_g^2 - n_s^2} \qquad 2.28$$

The eigenvalue equation can be rewritten by using the normalized frequency and the normalized propagation constant as:

$$\begin{cases} u = v\sqrt{1-b} \\ w = v\sqrt{b} \\ q = v\sqrt{b+\gamma} \end{cases} \qquad 2.29$$

When the waveguide is symmetric with $n_c = n_s$, $\gamma = 0$ and the dispersion equations (2.21) and (2.22) will be reduced to:

$$u = \frac{m\pi}{2} + \tan^{-1}\left(\frac{w}{u}\right) \tag{2.31}$$

$$\phi = \frac{m\pi}{2} \tag{2.32}$$

or in general form:

$$v\sqrt{1-b} = \frac{m\pi}{2} + \tan^{-1}\sqrt{\frac{b}{1-b}} \tag{2.33}$$

Since the parameters κ and γ are all functions of the propagation constant β, the eigenvalue equation is obviously a function of β as well. However, it is a transcendental equation (which means the solution cannot be written in closed form), so the β-values must be found numerically.

2.2 Optoelectronics Materials

Optoelectronics materials are semiconductors which can be broadly classified into 2 types, direct and indirect bandgap materials. Optical emission and absorption are fundamental processes which are responsible for the conversion of electrical energy into optical energy and vice versa. Therefore optoelectronics is based on the energy conversion processes, for example Light-emitting diodes (LEDs) and Laser diodes convert electrical energy into optical energy. Photodetectors convert optical energy into electrical energy. The bandgap of the semiconductor materials determine their electrical properties as well as their optical properties such as the absorption of photons and the probability of radiative transitions of electrons from the conduction band to the valence band. For the electron transitions to occur between the conduction and valence band and vice versa, two conditions have to be met viz:

- The energy has to be conserved.
- The momentum has to be conserved.

We will consider semiconductor materials generally but emphasis will be placed on the materials used throughout this thesis.

2.2.1Direct Bandgap Materials

Every time an electron recombines with a hole one photon is emitted. This means that the amount of optical energy (power) produced is equal to the number of electrons that recombine multiplied by the energy of the bandgap. Transitions can take place from any energy state in either band to any state in the other band. In this case, the energy and the momentum are easily conserved. The minimum of the conduction band (CB) is directly above the maximum of the valence band (VB) as shown in Fig. 2.5a. When an electron makes a transition from CB to VB, recombination takes place with a hole and a photon with bandgap energy is emitted, i.e. $E = E_g$ as shown in Fig. 2.5a. No phonon is needed for this transition to take place momentum is conserved. Phonons are quantized lattice vibrations present in crystals like semiconductors at room temperature. Typical examples of direct bandgap materials are GaAs, InP, AlAs, $Ga_{1-x}In_xP$, $Al_xGa_{1-x}As$, $In_xGa_{1-x}As$ and $In_xGa_{1-x}As_yP_{1-y}$.

2.2.2 Indirect Bandgap Materials

In indirect bandgap material, energy of the electron is also conserved when transition takes place between the CB and VB as explained in the last section, but the conservation of momentum is a problem. In this case the maximum of the VB is not directly under the minimum of the CB as shown in the Fig. 2.5b below, additional energy is needed for transition to take place and momentum conserved. The magnitude of momentums or the wave vectors ‘k’ of photons are a lot smaller than that of electrons in the semiconductors. To bridge this large difference between the magnitude of a momentum and electron when transition takes place, a phonon has to be emitted or absorbed in order to conserve the momentum. In Fig. 2.5b, E_g is bandgap energy and E_p is the phonon energy. Typical examples of indirect band gap materials are Si, Ge, SiGe and GaP

Advantages

- The probability of radiative transitions in indirect semiconductors is of four to six orders of magnitude lower than that in direct semiconductors. Therefore Silicon devices are usually very poor light emitters.
- Amplification of electromagnetic waves is very much larger for devices fabricated from direct semiconductors than for indirect semiconductors (Dumke, 1962).
- Indirect semiconductors have low quantum efficiencies compared with the direct semiconductors.
- Silicon, GaAs, and InP substrates is of high quality and they have large band gap for high power applications, e.g. radar, radio, and satellite transmissions.

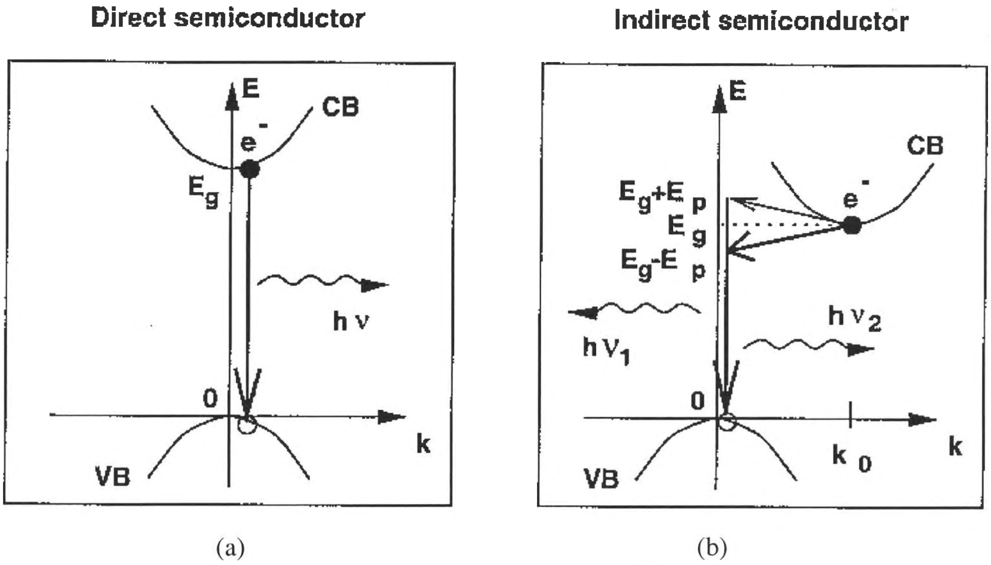

(a) (b)

Fig. 2.5 Electrons transitions in (a) direct and (b) indirect semiconductors for GaAs and Si respectively.

2.3 Types Of Waveguides

It is well known that in most applications in optoelectronics, the optical beams are confined laterally to a finite region in space. Some optical structures are employed to confine and permit the propagation of such optical modes. These structures are generally referred to as Waveguide structures and they are normally used to confine the optical waves in a well defined region and guide their propagation. The waveguides structures can be made from crystalline or non-crystalline in nature. The optical waveguides can be grouped into three major categories viz: (1) Planar waveguides, (2) Channel waveguides and (3) Optical fibres as shown in Fig. 2.6 below.

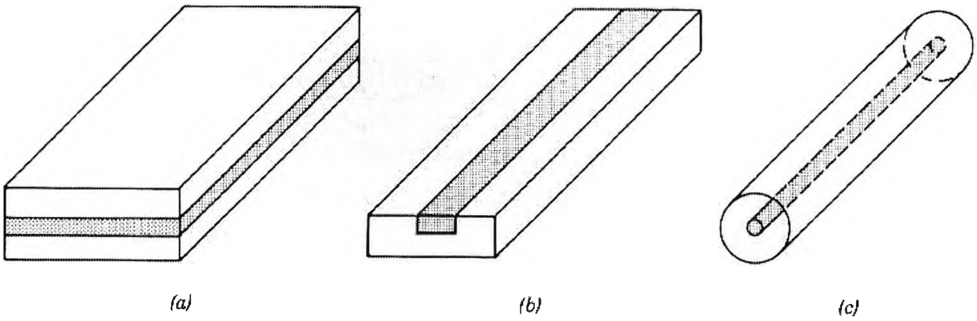

Fig. 2.6. Optical waveguides: (a) slab; (b) channel; (c) fibre.

2.3.1 Planar Waveguides

Planar waveguides are the structures that confine optical beam laterally in a single dimension. These can further be grouped into two categories viz: (1) Step-index and (2) Graded-index.

The step-index planar waveguide is the simplest form for light confinement and it is usually composed of a uniform planar core with a constant refractive index (homogeneous planar, n_g = constant), sandwiched in between two dielectric media of lower refractive indices. The homogeneous upper medium or cladding has a refractive index n_c, and the lower medium with refractive index n_s is known as the substrate. If it is assumed that $n_s = n_c$ then the structure is known as symmetric planar waveguide and if $n_s \neq n_c$ then the structure is asymmetric planar waveguide.

The graded-index planar waveguide is one in which the high index core is not homogeneous and the refractive index depends on the depth of the structure. The refractive index is maximum at the top surface and decreases with depth until it reaches the value corresponding to the refractive index of the substrate.

2.3.2 Channel waveguides

In channel waveguide, the optical beam is confined laterally in a single dimension say y –direction and in addition the beam propagates along the longitudinal direction, z – direction. In this channel waveguide or 2-D waveguide, confinement is achieved by making the refractive index of the core region greater than any of the surrounding media. In terms of classification, symmetric/asymmetric or step-index/graded-index can also be used for channel waveguides, but there are other geometrical shapes in forms of extension to the waveguide structures that needs be mentioned. The popular types of channel waveguides are:

- **Stripe waveguide:** In this type of waveguide, a stripe made of high refractive index material is deposited on top of a lower index structure.
- **Rib waveguide:** In this type of waveguide, a high index layer is deposited on a channel waveguide of lower index structure. The high index top layer is then etched in such a way that the etch is not complete, it forms a stripe and does not reach the substrate. Waveguides with this geometry or similar types are used in most of the investigations in this thesis.
- **Buried waveguide:** In this type of waveguide, a channel waveguide is made by increasing the substrate's refractive index in a well defined region in form of a buried stripe. Diffusion process is usually employed to achieve the local increase of substrate's refractive index.

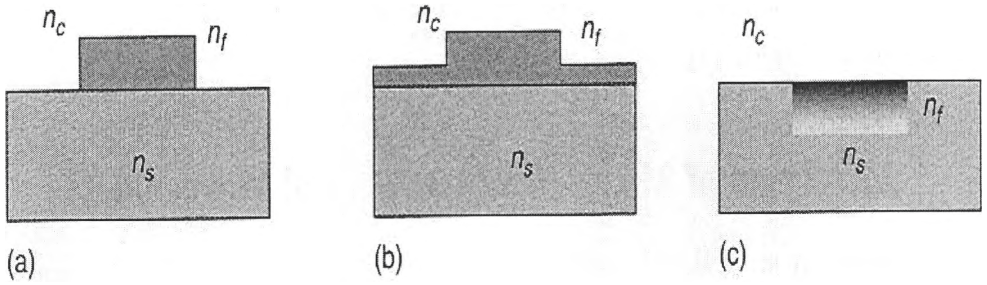

$$n_f > n_c \text{ and } n_f > n_s$$

Fig. 2.7. Three main types of channel waveguides (a) stripe waveguide; (b) rib waveguide; (c) buried waveguide (Linfante, 2003)

2.3.3 Optical Fibre Waveguides

This type of waveguide is completely different in many aspects such as the geometry, material, fabrication methods and applications as well. Optical fibres have cylindrical geometry, and consist of a cylindrical core of radius r, refractive index n_g, surrounded by a cladding with refractive index n_c. Optical fibres can also be grouped into step-index fibres with the homogeneous core in which n_g is constant throughout and graded-index fibres in which the refractive index of the core n_g varies as a function of the radial distance i.e. $n_g = n_g(r)$. This is very useful when high transmission bandwidth is required for long-distance optical communications. Fig. 2.8 show that the light is confined in two dimensions due to the total internal reflection occurring at the core-cover interface.

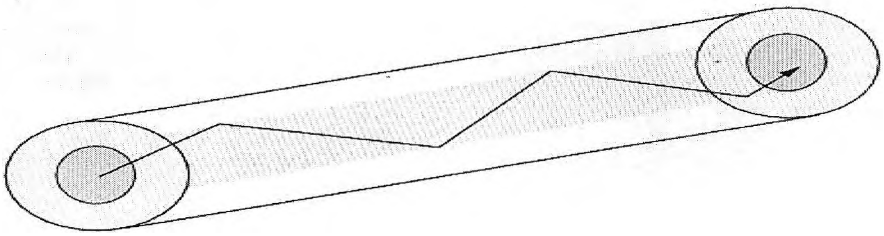

Fig. 2.8. Optical path followed by a ray of light inside an optical fibre. (Linfante, 2003)

2.4 Fabrication Technologies

This section deals with most common fabrication methods and technology normally used in OEICs and device components. These are numerous depending on the substrate material on which the optical device is to be fabricated. Deposition is used mainly for insulation and passivation of discrete devices and integrated circuits. Deposition processes involve the substrate temperature, the deposition rate, film uniformity, the morphology, the electrical and mechanical properties, and the chemical composition of dielectric films. Diffusion and ion implantation are two major processes used to introduce controlled amounts of dopants into semiconductors. They are used to dope selectively the semiconductor substrate to produce either an *n*- or *p*- type region. Both processes have the advantages of precise control of the total amount of dopants, improved reproducibility of impurity profiles, and lower-temperature processing. They can also be used for fabricating discrete devices and integrated circuits. Diffusion is used to form a deep junction like the N-well in CMOS process while ion implantation is used to form a shallow junctionm like a source/drain junction of a MOSFET (Sze, 1985). Deposition techniques are widely used for silica, GaAs, and InP substrate while diffusion techniques are commonly used for lithium niobate. In the case of optical circuits where the lateral dimensions are only a few microns, the fabrication technology needs photolithographic processes. In diffusion techniques, photolithographic masks are used to open the channels through which the diffuse material enters the substrate. One can also deposit a previously mapped out material to be diffused directly onto the substrate. Generally for waveguides fabrication, the material is initially deposited on the substrate surface and geometrical dimensions are defined using etching. The laws governing the diffusion processes are the Fick's laws of diffusion in which the 1st law states that in steady state, the concentration within the diffusion volume does not change with respect to time i.e.

$$\boldsymbol{J} = -\boldsymbol{D}\ \nabla\phi \tag{2.34}$$

The Fick's 2nd law relates to non-steady state when the concentration within the diffusion volume changes with respect to time and can be written as

$$\frac{\partial\phi}{\partial t} = \boldsymbol{D}\ \nabla^2\phi \tag{2.35}$$

Optical integration for optical communication devices can be achieved in two ways, (1) serial integration and (2) parallel integration. Serial integration can be described as one in which different elements are interconnected on optical chip for example laser and driver, modulator and driver electronics, detector and receiver electronics to name a few. Parallel integration is one in which the chip is built by bars of amplifiers, bars of detectors and wavelength multiplexors or demultiplexors. On the other hand optical integration can be broadly classified into two groups namely (1) monolithic integration which is the assembly of all the optical elements including sources, electronics, light controls and detectors on a single substrate and (2) hybrid integration in which there are different modules such as the optical chip, lasers, modulators or detectors, built separately different substrates are directly connected to integrated photonic device by optical fibres. Monolithic integration is widely used in semiconductor materials especially Silicon-on-insulator (SOI), GaAs, and InP (Lifante, 2003).

2.4.1 Epitaxial Growth Techniques

This section deals with various methods of growth techniques (Moerman, 1997), which are discussed below.

2.4.1.1 Liquid Phase Epitaxy (LPE)

In the LPE method, the appropriate compositions of each material are melted into a saturated solution of Ga, Al, and As for $Al_xGa_{1-x}As$, and Ga, In, As, and P for $In_xGa_{1-x}As_yP_{1-y}$. Dopants whether n or p types normally used for concentration are added to the molten solutions as required. The solutions are allowed to cool and crystallized or supercooling takes place at the substrate interface and the growth is allowed to take place under isothermal conditions. In general the composition of epitaxial layer depends on the composition of the molten solutions, the growth temperature, and substrate orientation. For the growth of GaInAsP on InP substrate, the composition must be well chosen so that the epitaxial layer is lattice-matched to the InP and the energy gap E_g is also matched. This is not a problem with AlGaAs because its system is fairly well lattice-matched over its entire range. The thickness of the epitaxial layer depends on the size of the molten composition, cooling rate, growth time, and degree of supercooling if it takes place. In the absence of supercooling, the thickness depends mostly on total temperature change during growth if the cooling rate is very slow.

LPE is extremely useful for laser diode fabrication. It has the advantages of being cheap to set up and can handle Aluminium growth. The disadvantages are that the thickness of epitaxial layers can be difficult to control, especially when growing thick layers in the millimetre range. It has poor uniformity over large areas and can only handle small, thin layers effectively. The optical loss is very high in this method compare to other most common methods like VPE, MBE and MOVCD. Roughness at the interface may be responsible for this loss.

2.4.1.2 Vapour Phase Epitaxy (VPE)

Vapour phase epitaxy (VPE) is very useful in the growth of high-purity GaAs and InP epitaxy layers. It uses chloride transport in a hot-wall reactor and this is not good for Al compounds because of their low melting point. It is therefore good for the growth of GaAs on GaAs and GaInAsP on InP. VPE uses either trichloride or hydride methods to generate the vapours used in the growth process. High-purity H_2 is passed into a reactor chamber which is temperature controlled. There is chemical reaction between $AsCl_3$, Ga, and H_2. The result is a mixture of arsenic vapour and Gallium chloride which is then moved straight into deposition zone where epitaxial growth takes place on the substrate. The trichloride offers the advantage of higher purity while the arsenic hydride offers the advantage of a simpler system for growing the entire range of lattice-matched InP layers.

The advantages of the VPE are that it gives a good epilayer thickness control, good uniformity over large wafers, and good surface interaction. Selective growth can be achieved over submicron dimensions. Low loss can be achieved but not as good as MBE or MOCVD.

2.4.1.3 Metal-organic Chemical Vapour Deposition (MOCVD)

Metal-organic chemical vapour deposition (MOCVD) (Yamazaki *et al.*, 1997; Kasukawa, 1997), is also known as metal-organic vapour phase epitaxial (MOVPE) layer technology (Aoki *et al.*, 1996), but it uses cold-wall reactor and is therefore suitable for Aluminium compounds growth technology. It is good for growing AlGaAs on GaAs. The technology is usually carried out by putting required amounts of constituent elements in the form of metal alkyds into the cold-wall quartz reactor.

The chamber can be operated at room temperature or at low pressure. Dopants can be introduced either in the form of metal-organics like $Zn(C_2H_5)_3$ or in the form of hydrides like SiH_4 or H_2S. The substrate is placed on a heated carbon crucible.

The metal-organics decompose on the hot substrate and growth takes place primarily on this hot surface after some chemical reaction. For example, GaAs grown from trimethyl Gallium and arsine vapour, the chemical reaction at the substrate is

$$Ga(CH_3)_3 + AsH_3 \longrightarrow GaAs + 3CH_4$$

The MOCVD has got so many advantages over previous techniques. It gives a good epilayer thickness control. It exhibits good uniformity, good surface interaction and good control of heterojunction interfaces. Selective growth can be achieved utilizing MOCVD and it has lowest losses for GaAs/AlGaAs waveguides.

2.4.1.4 Molecular Beam Epitaxy (MBE)

The Molecular Beam Epitaxy (MBE) (Colas *et al.*, 1990; Bossi *et al.*, 1991), is an ultra-high-vacuum technique in which all the constituent elements initially heated to vapour are evaporated onto a heated substrate where they become molten enough to form epitaxy layer when condensation takes place. The composition of the epitaxial layer is controlled by controlling the temperature of each oven separately. The growth rate of MBE is very slow, which makes the precise control of layer thickness possible. Therefore long time is needed to grow thick layers. The epitaxial layers are very uniform and have very smooth surfaces.

MBE technology is very good for growth of waveguides and components for quantum wells and superlattices. Losses exhibited by MBE waveguides i.e. waveguides grown by MBE are low and are comparable to those grown by MOCVD. During the growth processing it is possible to use masking above the substrate to limit growth to selected areas of the wafer and method can also be used to produce tapers. This is useful in obtaining direct fabrication of geometrical dimensions for the integrated circuits especially the submicron dimensions

2.4.1.5 Selective Area Growth (SAG)

In this process the substrate is covered by a dielectric mask on which no deposition takes place. The smaller the window of the dielectric mask, i.e. the larger the mask itself, the larger the growth rate because the reactor pressure becomes higher (Brenner and Melchior, 1993), and this can be used to produce a vertical taper by butt-joint coupling. A butt joint is a joinery technique in which two waveguides are simply joined end to end together. Initially the device layers are grown, then the substrate is partially covered by a dielectric mask only leaving the taper region unmasked. The device layers are then removed in the unmasked or taper region. Finally a selective regrowth is performed to form the taper. This technique needs at least one regrowth. A second regrowth can be done for the cladding layers. The main advantage of the butt-joint is its flexibility to separately design the device layers and the taper layers.

2.4.1.6 Shadow Masked Growth (SMG)

This process can be used for a monocrystalline (Moerman *et al.*, 1994; 1995), or silicon (Aoki *et al.*, 1996; 1997), mask that is fixed on a spacer above the substrate. The growth rate during the epitaxial growth through the mask window is influenced by the reactor pressure and the lateral dimensions of the shadow mask. Thickness changes are fully controlled by the lateral dimensions of the shadow mask and the reactor pressure. The disadvantage of this technique is that additional growth of the shadow mask and an additional processing step to remove the shadow mask. This disadvantage can be overcome by using a mechanical mask instead of a monocrystalline mask, e.g. a silicon mask.

2.4.2 CMOS Process – For Silicon Technology

This section deals with the Complementary metal-oxide-semiconductor (CMOS) process which is considered by scientists as economically most important technology for the fabrication of microelectronic circuits especially silicon integrated circuits. Initial technology of CMOS process is a One-well process. Later developments give rise to new process known as Twin-well process shown in Fig. 2.9 (Zimmermann, 2000).

2.4.2.1 One-well Processes

The one-well process makes use of epitaxial silicon wafers in which the substrate is P-type with a required amount of dopant concentration of about 2 x 10^{18} cm^{-3}. A silicon wafer of a certain thickness about 12 μm is used as epitaxial P-layer with a different amount of dopant concentration 2 x 10^{15} cm^{-3} is deposited on the substrate. The N channel MOSFET obtains only low power implant instead of a deep P well and the performance of the well is affected. As a result only N well is formed. The twin-well process was developed to improve the poor performance of the one-well and to optimize the N- and P-channel transistors independently for CMOS circuits.

2.4.2.2 Twin-well Processes

A typical submicrometer CMOS process can be divided into seven major steps:

(1) A P-type silicon substrate with N epitaxial layer doped to about 10^{15} cm^{-3} are initially needed to start the well formations. Twin-well formations are obtained by N- and P-type diffusions and there is independent monitoring of the doping profiles in each well.

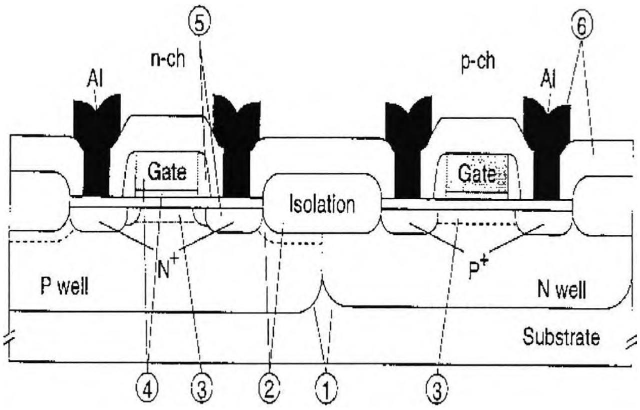

Fig. 2.9. Schematic cross-section of a CMOS chip. A typical CMOS process can be divided broadly into seven major steps. (Zimmermann, 2000)

(2) The next step is the LOCOS, (LOCal Oxidation of Silicon) field isolation in which the channel-stopper regions are formed which isolate the wells from each other electrically. A photoresist mask is used to implant boron selectively through the oxide or nitride layer into the silicon, where the channel-stopper is desired. The P-type channel-stopper is needed to increase the impurity density under the field isolation in P-well regions. Without the channel stopper, there may be diffusion between two neighbouring N-channel metal oxide semiconductor field effect transistor (MOSFET) due to a large amount of positive fixed charge by more LOCOS oxidation.

(3) The ion implantation for the N- and P-MOSFETs are then formed in order to adjust the threshold voltages. The threshold implantation for the N-MOSFET is done in two steps. Firstly a thin oxide is grown prior to the implantation to prevent ion channelling and the doping of the surface channel for the N-MOSFET is done by boron or BF_2 implantation. In the second step, the boron implantation is done to create a buried-channel P-MOSFET simultaneously. The second threshold implantation is done without a mask into all active regions. The resist and all the thin oxides are then removed to obtain a cross-sectional view before gate oxidation is carried out.

(4) The next stage is the gate definition in which the gate oxide is grown thermally in order to obtain a high oxide quality. Then polysilicon which acts as the gate electrode is deposited. The intrinsic polysilicon is then heavily doped to 10^{18} cm^{-3} with phosphorus in a gas of $POCl_3$ at a temperature between 850 and 950 ^{o}C. In a polycide gate process, a silicide layer is then deposited on top of the polysilicon. The N type doped polysilicon layer is defined by lithograph and dry etching. The resist is removed and the gate electrode is exposed to the gate reoxidation or side wall oxidation to prevent gate-oxide integrity near the gate edges from degradation.

(5) Once the gate has been defined, the phosphorus (or lately the arsenic) is implanted as the N type lightly doped drain (LDD) dopant. Once the resist has been removed, oxide is deposited everywhere on the wafer and they are etched to form

sidewall spacers. Arsenic is implanted for N source/drain formation of the N-MOSFET. A resist mask protects the P-MOSFETs from being implanted. This implant is used for the cathode formation of the PIN photodiode. Then boron is implanted selectively into the P-MOSFET source/drain regions using another resist mask.

(6) Two oxide layers are then deposited on the wafer. The first is undoped oxide and the second is boron and/or phosphorus doped which gives a phosphorus-doped silicon dioxide (otherwise known as P-glass) for improving the glass flow property needed for planarization or metallization. This is because P-glass when deposited at low temperatures becomes soft and flows upon heating and subsequently provides a smooth surface which is often used to insulate adjacent metal layers. The process is known as P-glass flow. Contact holes are then defined by lithography and opened by dry etching.

(7) In the semifinal process, the first aluminium layer for contact and interconnect formation is deposited and defined by lithography and dry etching. Other metal alloys dielectric layers and further metal depositions may follow. Finally, passivation takes place i.e. coating (a semiconductor) with inert or passive material to protect it from contamination. In industry, passivating oxide, nitride, or oxynitride layers are deposited by plasma-assisted deposition to protect the chip from impurities and humidity coming from the surroundings. The bonding-pad areas have to be defined and opened.

2.4.3 Photolithograph and Etching Techniques

2.4.3.1 Photolithograph

Photolithography involves a mask usually made from glass which is produced with a pattern. The pattern is then transferred from the mask to the substrate (Syms, 1992). Light-sensitive organic materials popularly known as photoresists are always used in this process. They are grouped into two types, negative and positive optical resists depending on their reactions to radiation. The negative resists are polymerised with a photosensitive compound when exposed to UV light and after exposure, the photosensitive compound absorbs the optical energy and converts it into chemical energy to initiate a chain reaction. Positive resist consists of three components which are 1) a photosensitive compound, 2) a base resin and 3) an organic solvent. Before the exposure, the photosensitive compound is insoluble in the developer solution. After exposure, the photosensitive compound absorbs radiation and becomes soluble in the developer solution. The substrate is covered with a thin film and a photoresist. After aligning the mask with pattern, the substrate is exposed to UV light. The mask is removed and the photoresist is developed. A pattern of resist results on the film layer which can be transferred to the film by etching which is explained in more detail in the following sections.

2.4.3.2 Wet Etching

Generally wet etching techniques suffer from the disadvantage of low reproducibility and the difficulty to define sophisticated taper structures such as parabolic, exponential, and other curved shapes. Those non-linear taper profiles are, however, often used to minimise the taper length. In semiconductors, chemical etchants are used for beating and polishing to give an optically flat and damage-free surface. An etching process is said to be diffusion-limited if the etching rate is limited by the arrival of reactants or removal of reaction products at the solid-liquid interface and the etchant is known as diffusion-limited etchant. In diffusion-limited processes, the rate of etching can be influenced by the agitation and viscosity of the liquid etchant system.

- **Dynamic etch mask technique:** The area of the substrate where the taper is required is covered with a thin material to form the dynamic mask with a higher etch rate than the semiconductor material (Shahar, 1990; Brenner and Melchior, 1993). Then the whole area is covered with a standard mask which is opened near the dynamic mask where the deeply etched end of the taper shall be formed. With chemical etching the dynamic mask is subsequently etched away and thus an increasing area of semiconductor material comes into contact with the etchant.
- **Diffusion limited etch technique:** In this technique, a part of the substrate is covered with a silicon oxide mask and a diffusion limited etchant. Therefore the

amount of etched material can be controlled, by a narrow mask opening results in etch rates. This is used for fabrication of vertical tapers (Brenner and Melchior, 1993).

- **Stepped etching:** In this technique the waveguide core is built from a stack of high refractive index with ultra-thin etch-stop layers sandwiched in between. An optimisation of the layer core thickness is carried out in each section to minimise the loss. For achieving an adiabatic spot-size conversion the number of steps has to be relatively large. This technique offers a better reproduction than other techniques (Koch *et al.*, 1990; Yoshimoto *et al.*, 1992; Mori *et al.*, 1996).
- **Dip-etch process:** This is the simplest technology to realise a vertical taper as presented in (Moerman *et al.*, 1997). By dipping the waveguide in a controlled manner into an etchant the taper can be formed. However with this technique the resulting tapers are relatively long and it is not possible to process a whole wafer.

2.4.3.3 Dry Etching

Dry etching is generally good for producing precise geometry of single taper structures but full wafers cannot be processed with a high density of tapers.

- **Oxide shadow etching:** In this technique, a shadow mask is put over the substrate on top of a spacer. Opposite to this, an oxide layer which has a tapered shape is deposited and then the taper in the substrate is produced by N_2 ion etching (Bossi *et al.*, 1990). The profile of the taper can be controlled by the shape of the shadow mask.
- **Direct shadow etching:** For this method a shadow mask is fixed on top of a spacer above the substrate. The substrate with shadow mask is placed directly in a N_2 ion milling module, with the axis of rotation tilted at oblique incidence with respect to the direction of the ion beam. The substrate is then rotated so that the influence of the shadow mask when changed is dependence on the angle of rotation in order to get the tapered profile (Bossi *et al.*, 1990). In this technique, the taper profile is controlled by the angle with respect to the N_2 beam and the height of the spacer.

- **Shadow masked reactive ion etching (RIE):** A molecular gas is used and the taper length can be controlled by the spacing between the shadow mask and the substrate, i.e. by the thickness of the spacer (Jacobs *et al.*, 1994). This is used for a vertical taper by placing a shadow mask above the substrate in a RIE system. The advantage of the shadow mask RIE is that it can be used to determine the taper length by the spacing of the shadow mask with respect to the substrate during the process.

2.5 Computational Techniques

In the previous sections the underlying principles of the propagation of light in optical fibre and waveguide devices have been investigated and this section is looking into the various ways of finding solutions to problems of the light propagation from source to coupling to the optical fibre. This involves finding the propagation constants and field profiles of the number of modes inside a waveguide at any instant. The wave equation, usually derived from the well-known Maxwell's equations together with the boundary conditions and the geometry of the waveguide are used to determine the propagation characteristics of the field mode profiles. It is well known that precise solution for the wave equation can be obtained for simple structures like planar waveguides, but when it comes to complex structures like planar waveguides with arbitrary refractive index distribution, anisotropic and non-linear optical materials as well as materials with complex refractive index such as semiconductors and metals, the wave solutions are not easy to obtained and in some cases are rather impossible. Researchers have developed various methods of obtaining solutions to the wave equations. There are two major methods of solving the wave equation derived from the Maxwell's equations (1) the analytical approximate methods and (2) the numerical methods. It is easy to obtain exact analytic solution for a 2-D slab waveguide with step refractive index but when the waveguide has got arbitrary or graded refractive index distribution, the exact solutions may not be possible. However various types of analytical approximation solutions have been developed for 2-D stepped optical waveguides which have a gradually changing refractive index distribution in the thickness direction of the waveguide. For example, the ray approximation method

(RAM) (Qiao and Wang, 1992) and the Wentzel, Kramers and Brillouin (WKB) method (Srivastava *et al.*, 1987) are typically known analytical approximation solution techniques for such optical waveguides which is the most familiar example of a semiclassical calculation in quantum mechanics in which the wavefunction is recast as an exponential function, semiclassically expanded, and then either the amplitude or the phase is taken to be slowly changing. This method is named after physicists Wentzel, Kramers, and Brillouin, who all developed the method in 1926. In 1923, mathematician Harold Jeffreys had developed a general method of approximating linear, second-order differential equations, which includes the Schrödinger equation. But since the Schrödinger equation was developed two years later, and Wentzel, Kramers, and Brillouin were apparently unaware of this earlier work, Jeffreys is often neglected credit. Early texts in quantum mechanics contain any number of combinations of their initials, including WBK. The first group includes such approaches as circular harmonic point matching (Goell, 1969), the effective index method (Hocker and Burns, 1977), the spectral index method (Burke, 1990) and the Marcatili method (Marcatili, 1969). Some of the approximate methods provide very good results for the analysis of waveguides far from cutoff but many of these methods are not very suitable for the analysis of a wide range of important practical waveguides. In the case of 3-D optical waveguides for optical integrated circuits, hybrid mode analysis is required in order to satisfy the boundary conditions. However, the analytical approximation solutions developed for these guides do not treat them as hybrid mode and therefore, they are not suitable for accurately analysing the practically used 3-D optical waveguides. Marcatili's method (MM), and the effective index method (EIM) can be treated as the typical analytical approximation solutions for 3-D optical waveguides.

Numerical solutions are the alternative to analytical approximate solutions can be classified into two groups, (1) the domain solution and (2) the boundary solution. The domain solution includes the whole domain of the optical waveguide structure as the operational area, where as the boundary solution includes only the boundaries as the operational area. The former is also called a differential solution, and the latter, an integral solution. Some of the examples of the domain solutions include the finite element method (FEM), finite difference method (FDM), variational method (VM), and multilayer approximation method (MAM). The boundary solutions include the boundary element method (BEM), point-matching method (PMM) and mode-matching method (MMM).

2.5.1 Analytical Approximate Methods

2.5.1.1 Marcatili's Method

The Marcatili's method (Marcatili, 1969), is very useful for determination of modal fields and propagation constants of channel waveguides. It enables us to model waveguides geometry by using analytic approximate solutions to Maxwell's equations derived by Marcatili in his paper since such a waveguide is difficult to analyse exactly. Such a structure shown in Fig. 2.10, will consist of a guide region surrounded on all sides by a confining medium of lesser refractive index. Knowledge of fields in the two slab waveguides, obtained by extending to infinity the width and height of the guide core, are used to approximate the field in the rectangular core.

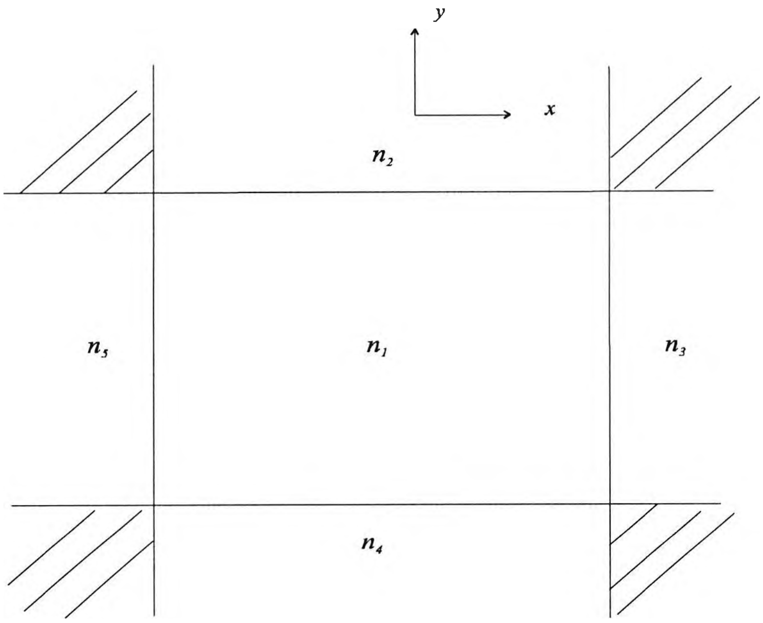

Fig. 2.10. Cross-sectional representation of channel waveguide.

It is assumed that the modes are well guided i.e. far from the cut-off region. Only a small fraction of the mode energy radiates out to the other regions n_2, n_3, n_4, n_5.

Within the guide core, the field is assumed to vary sinusoidally and to decay exponentially within the substrate region. With these assumptions, the problem has been greatly simplified and by matching the boundary conditions along the walls of the core region only, the transcendental equations are derived for each transverse direction (Tamir, 1990).

The propagation constant is obtained from the simultaneous solution of the transcendental equations with the assumption that most of the power is within the guide region. This approach, even though valid for well-confined modes, gives poor results near to cut-off (Chiang, 1994). An exact scalar formulation has been reported by Kumar *et al.* (1983) for a similar rectangular structure used by Marcatili. By using perturbation techniques, more accurate propagation characteristics of practical integrated optical waveguides were obtained.

2.5.1.2 Effective Index Method

This is another analytic approximate solution for determining the propagation constants and modal field of the channel waveguides. The effective index (EI) method was first proposed by Knox and Toulios in 1970 (Knox and Toulios, 1970) with a view of extending Marcatili's method for the fundamental mode of a simple channel waveguide. Soon after, this method became one of the most popular methods for the analysis of optical waveguides. In this approach, the channel waveguide is treated as the superimposition of the two 1-D waveguides such that region 1 confines light in the y-direction while region 2 confines light in the x-direction as shown in Fig. 2.11. The propagating modes that evolved from the x-direction gives rise to the TM modes and the modes that evolved from region 1 in the y-direction gives rise to TE modes. The first step solves the transcendental equation for a vertical slab waveguide by applying the appropriate boundary conditions. The effective index obtained from the solution is used as the refractive index of the horizontal slab waveguide, and by solving the eigenvalue equation gives a good approximation to the effective index of the original waveguide structure. As only the solutions for slab waveguides are required, this method is significantly more efficient than those methods that solve the rectangular structure directly.

The advantage of the EI method is that it can be applied to a wide variety of structures, including channel waveguides, strip waveguides and arrays of such waveguides (Chiang *et al.,* 1996) and also for various types of optical fibres and fibre devices (Chiang, 1986*a*; Van de Velde *et al.*, 1988). The weakness of the method is that it does not give good results when the structure operates near cut-off region. The simplicity and speed of the method have encouraged many engineers to search for different approaches that will improve the accuracy of the EI method. Consequently, many different variants of the EI method have been developed such as the EI method based on linear combinations of solutions (Chiang, 1986*b*; Van Der Tol and Baken, 1988), or the EI method with perturbation correction (Chiang *et al.*, 1996).

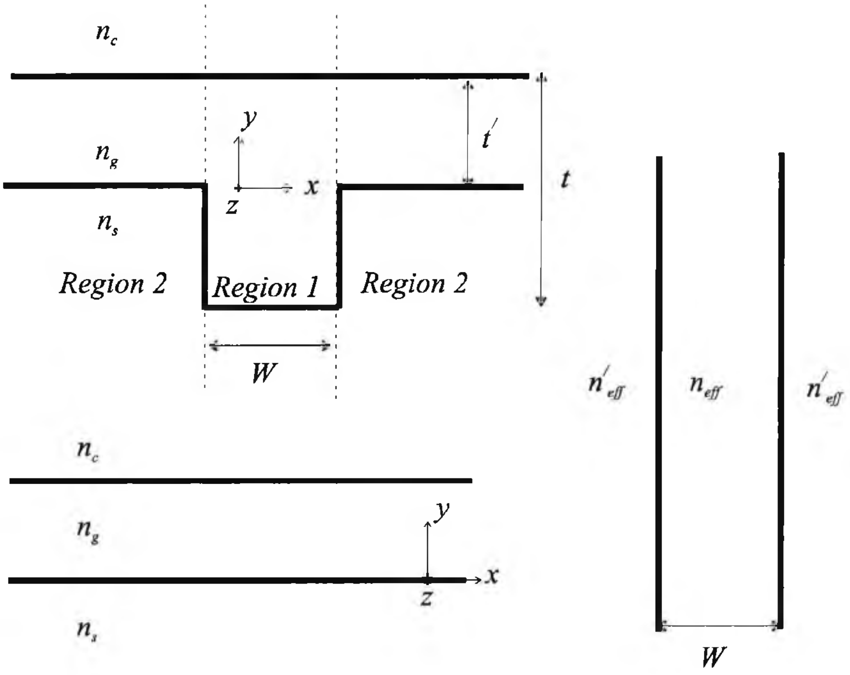

Fig. 2.11. A model for the effective index method

2.5.2 Numerical Methods

The rapid growth in the millimetre-wave, optical fibre, and integrated optics fields has included the use of arbitrarily shaped dielectric waveguides, which in many cases also happened to be arbitrarily inhomogeneous and/or arbitrarily anisotropic. Most of such cases of waveguide arbitrariness do not lend themselves to analytical solutions. Therefore many scientists have given their attention to construct numerical methods to solve such waveguides. Numerical methods may be used to solve Maxwell's equations exactly and the results they provide are accurate enough for the characterisation of most of the devices.

Since the advent of computers with large memories, considerable attention has been paid to methods of obtaining numerical solutions of the boundary and initial value problems. Methods are usually evaluated in terms of their generality, accuracy, efficiency and complexity. It is evident from the review methods (Chiang, 1994; Vassalo, 1997) that every method represents some sort of compromise between these aspects. No method is superior to the other in all aspects. The optimal method should be the one that can solve the problem with acceptable accuracy but requires the minimum effort to implement and run in terms of man-power and computer capacity. The continuing improvement in computer power will make computational efficiency less of an issue in the future.

Some factors with regard to the selection of methods for analysing optical waveguide problems, based on reviews (Davies, 1972; Ng, 1974; Saad, 1985) are given, as follows:

(1) the shape of the cross section of the structure, whether it is curved or polygonal or whether it is convex or non-convex.

(2) whether a method that can be realised as a computer program suitable for the automatic solution of a wide range of structures is needed.

(3) whether a computer program requiring human intervention or some exploratory work with the computer is needed.

(4) the method should be programmable and it has to be written specially for each region of the structure separately.

(5) whether the dominant mode only, or a number of the higher order modes are required.

(6) whether the field distribution, or the cut-off frequency is needed, or the both are needed.

(7) the requirement of accuracy needed for eigenvalues and perhaps eigen functions.

(8) the accuracy of the method in modelling the dielectric boundaries and regions.

(9) the accuracy of the method in specific frequency ranges as an example, near the cut-off frequency.

(10) whether the method has a mechanism of generating spurious numerical solutions and if so whether the method can identify and/or eliminate them.

(11) the computational efficiency of the method, including its computer storage requirements.

In this section, a short overview of these commonly used numerical solution techniques is given.

2.5.2.1 The Boundary Element Method

The boundary element method (BEM) is interpreted as a combination technique of the conventional boundary integral equation method and a discretisation technique, such as the finite element method (Kagami and Fukai, 1984). The BEM is a boundary solution method and therefore the fields are needed only for the nodes which are on the boundaries of the region. The derivation of the integral equations with respect to the unknown fields at boundaries is obtained by using the method of weighted residuals or Green's formula. These integral equations are then discretised to a set of linear equations to be solved for the numerical solutions.

The BEM can be used for the analysis of arbitrarily shaped discontinuities as FEM, but the BEM can be performed using far fewer nodes than by the FEM. Koshiba and

Suzuki have reported (Koshiba and Suzuki, 1986*a*) a numerical approach based on the BEM for analysis of discontinuity problems of TE and TM modes in a dielectric slab waveguide. Moreover, the BEM can handle unbounded field problems easily and therefore has the possibility of modelling domains extending to infinity without an infinite element analysis which is often performed in FEM. However, the BEM can only be applied to homogeneous structures (Hirayama and Koshiba, 1989), and also it has been known that the matrices involved are dense matrices unlike those in FEM which are sparse. Therefore the FE method can be treated as more numerically efficient.

2.5.2.2 The Point Matching Method

The point matching method (PMM) is one of the oldest and simplest 'boundary solution' techniques for the analysis of isotropic homogeneous dielectric waveguides. Its application was first shown by Goell (Goell, 1969) to investigate the propagation characteristics in rectangular cross section dielectric waveguides. Goell's numerical analysis is based on expressing the internal and external fields in terms of circular harmonics. The fields inside the dielectric and outside the dielectric are expressed by a sum of Bessel functions and modified Bessel functions multiplied by trigonometric functions, respectively, and their derivatives. By matching the tangential fields at optimally selected points around the boundary called 'matching points', a system of linear equations is obtained. By applying the condition of nontrivial solution, a characteristic equation including the propagation constant is obtained and solved for the appropriate eigenvalues. The original matrix equation is then solved for each mode eigenfunction by standard matrix techniques.

The PMM is capable of use for analysing dielectric waveguides with arbitrary cross sections and composite structures, and also computing coupling coefficients between two rectangular rods. Improved results for the PMM were reported (Cullen *et al.*, 1971), by rotating the grid of equiangularly spaced matching points in order to place a matching point at the corner of a rectangular dielectric waveguide. However, the PMM is not suitable for the analysis of 3- dimensional waveguide structures with inhomogeneous index distribution, such as graded index fibres.

2.5.2.3 The Mode Matching Method

The mode matching method (MMM), which is also known as the equivalent network method (ENM), is an approximate solution method for the analysis of open dielectric waveguides (Peng and Oliner, 1981). In this approach the structure is artificially bounded, and the waveguide cross section is viewed in terms of constituent parts or building blocks, which are usually portions of uniform dielectric layered structures interfaced by the dielectric step discontinuities. Then each constituent is analysed separately and all the parts are put together to comprise the final structure of interest. A transverse equivalent network for the structure is obtained by representing the uniform dielectric regions as uniform transmission lines and by characterising the step discontinuities as transformers. From this, the dispersion relation can be derived to obtain the waveguide propagation characteristics.

In the earlier analysis of the MMM, due to the artificial bounding of the structure, the continuous spectrum (Peng and Oliner, 1981) and TE to TM coupling at the sides of the waveguide are neglected. Dagli and Fonstad (Dagli and Fonstad, 1986) reported a modified approach, which takes into account the continuous spectra. Rather than artificially bounding the structure to discretise the continuous modal spectrum, here, they are discretised by converting integrals into summations using suitable basis function expansions. Koshiba and Suzuki (Koshiba and Suzuki, 1985; 1986*b*) reported a vectorial wave analysis of rectangular optical waveguides using the ENM, by taking the TE-TM coupling and the discrete-continuous spectrum coupling into account.

2.5.2.4 The Spectral Index

The spectral index (SI) method may be used to find quickly and easily the guided modes and propagation constants of semiconductor rib waveguides (Kendall *et al.*, 1989; Stern *et al.*, 1990). Here the true open structure is replaced by slightly larger, partially closed one, which is simpler to analyse, in order to model the penetration of the optical field into the cladding. The spectral index method can be expressed as the following combination.

(a) In the region below the rib, the Fourier transform is applied in order to reduce the dimensionality of the problem to a one-dimensional structure, and the field is expressed in spectral space using Fourier transform.

(b) In the rib region, the wave equation is exactly expressed using Fourier series in terms of cosine and sine functions.

(c) The two solutions are linked by employing a transfer relationship and consequently, giving a transcendental equation which can be solved for the propagation constant of the original rib structure.

The presence of the strong discontinuities at the dielectric interfaces is dealt with by using an effective rib width and an effective outer slab depth.

The SI method has been extended to include rib coupler problems (Burke, 1989; 1990), cases with loss and gain (Burke, 1994) and also it has been used to analyse multiple rib waveguides (Pola *et al.*, 1996).

2.5.2.5 The Finite Difference Method

The finite difference method (FDM) is the oldest and probably the best known numerical method for the solution of boundary value problems. The importance of the FDM lies with the ease with which many logically complicated operations and functions may be discretised. In this method, the optical waveguide is enclosed in a rectangular box whose cross-section is divided into sub-regions. Operations are then performed not on continuous functions, but rather on values at discrete point sets on the grid. The major advantage of this method is that operations such as differentiation and integration are reduced to simple arithmetic operations, which lend themselves easily to algorithmic solutions. The walls of the rectangular box may either be electric or magnetic. The field at the boundaries of the walls is assumed to be negligible, allowing infinite elements with an associated decay factor to be introduced. A grid with all the dielectric boundaries on it is then used to represent the cross-section. The nodal field of an arbitrary node can be expressed in terms of the neighbouring nodes in the two transverse directions using a five-point formula, (Davies, 1989) of finite differences. The differentiation of the wave equation at the nodes is thus replaced with differences of the fields evaluated at the nodes. This approach leads to a large non-symmetric matrix, which puts constraints on the storage requirements. An iterative procedure using lower order modes is employed to avoid the storage of large matrices by solving directly the matrix eigenvalue equation (Chiang, 1994).

The FDM can also be formulated using the variational principle. The variational expression obtained is arranged into a set of coupled wave equations for each of the transverse directions, H_x and H_y. An eigenvalue matrix equation of the form $Ax - \lambda x = 0$ can be formed which can be solve using sparse matrix techniques.

The accuracy of this method is determined by the size of the computational window. If the computational window is too large, convergence will be slow. A small computational window would, on the other hand, invalidate the assumption of zero field at the boundaries. As the distance between points is made sufficiently small, the method becomes increasingly accurate.

2.5.2.6 The Finite Element Method

The finite element method (FEM) is a well established numerical method for the solution of a wide range of guided wave problems. It can be very easily applied not only to optical waveguides of any shape, but also to optical waveguides with any arbitrary refractive index distributions. This method is based upon dividing the problem region into non-overlapping patchwork of polygons, usually triangular elements. The field over each element is then expressed in terms of polynomials weighted by the field values at the nodes of each element. The total field is found by the linear summation of the fields over each element. By applying the variational principle to the system functional, and thereby differentiating the variational functional with respect to each nodal value, the problem reduces to a standard eigenvalue matrix equation. This is solved using iterative techniques to obtain the propagation constants and the field profiles (Rahman and Davies, 1984*a*; Koshiba and Inoue, 1992).

The accuracy of the FEM can be increased by using finer mesh. Number of formulations have been proposed, however, the full vectorial **H**-field formulation is the most commonly used and versatile method in modelling optical waveguides due to much easier treatment of boundary conditions. This method can accurately solve the open type waveguide problems near the cut-off region and much better results were obtained by introducing infinite elements to extend the region of explicit field representation to infinity (Rahman and Davies, 1984*b*). One drawback associated with this powerful vector formulation is the appearance of spurious or non-physical solutions. Suppression of these spurious solutions can be achieved by introducing a penalty term into the variational expression (Rahman and Davies, 1984*c*). In order to eliminate the spurious solutions completely, another approach is employed using the edge elements (Bossavit and Mayergoyz, 1989; Koshiba and Inoue, 1992).

In modelling more complex structures, the FE method is considered to be more flexible than the FD method, due to the ability of employing irregular mesh. A more detailed study of the FE method is presented in the next chapter.

2.5.2.7 The Beam Propagation Method

The methods considered thus far have been used to obtain the modal properties of an optical waveguide through the solution of a two-dimensional wave equation. Such modal properties of a waveguide can also be obtained through the solution of a three-dimensional wave propagation equation. This method was first proposed for the solution of non-uniform waveguide problems in anisotropic media by Feit and Fleck (Feit and Fleck, 1978).

The beam propagation method is based on different numerical techniques like the Fast Fourier Transform (FFT), the FDM and FEM. In this work, the FEM based BPM have been employed in which the perfectly matched layer (PML) boundary conditions, has been incorporated in order to effectively absorb the unwanted radiations. Also the Pade wide-angle approximation is used to account for accurate guided-wave propagating off-axis in the longitudinal direction. For the analysis of non-uniform waveguides, the beam propagation method is now widely accepted as the most powerful method available. However, for the analysis of uniform structures, this method is not as efficient as those designed specifically for two-dimensional wave equations, because it is required to discretise the structure in both the transverse and the longitudinal planes. To overcome these difficulties, a two-dimensional method such as the FDM or FEM is best employed.

2.6 Summary

In this section, the basic underlying principles such as Snell's law, Fresnel formulas and total internal reflection are used to analyse the propagation of a ray of light in an homogeneous media. The classification of the guidedwave into TE and TM modes with appropriate boundary conditions was discussed. The fabrication technologies are also discussed. Most of the design materials reported in this thesis can be fabricated by using the epitaxial or deposition techniques. The following materials; silica, GaAs, InP substrates fall under the group which undergoes photolithographic processes and etching techniques after deposition because their lateral dimensions are just few microns. These materials are commonly used in practical situations and their material indices are used throughout this thesis. The epitaxial growth techniques are the popular deposition methods for materials like GaAs and InP, while complementary metal- oxide semiconductor (CMOS) is emphasised as the most important technology for the fabrication of microelectronic circuits especially silicon integrated circuits. The technology for Twin-well CMOS process and its usefulness is described. This section also deals with the computational techniques in which various analytical and numerical methods are described briefly. The advantages of numerical method over analytical method is emphasised and the FEM is highlighted as the main tool to be used throughout this thesis.

Chapter 3

The Finite Element Method

3.1 Introduction

In the last six decades the finite element has gain recognition as one of the most versatile, popular and very useful numerical methods and has cut across various research fields of science and engineering such as aeronautics, soil mechanics, fluid mechanics, thermodynamics, electromagnetism, biomedical engineering, etc. Many systems of interest can be either physical or mathematical. The governing equations can be given in differential form or be expressed in terms of integral equations. The method was first introduced in 1943 by Courant (Courant, 1943), who used an assemblage of triangular elements as a way to get approximate numerical solutions for structural problems. A decade later, use of computer made it easy for numerical calculations to be done and their applications were embraced by the industry. It was not until 1956 that Turner, Clough, Martin, and Topp (Turner *et al,* 1956) introduced the finite element concept at the Boeing Aircraft Company and used this method as a useful tool to calculate the stress-strain relations for complex aircraft structures. The finite element method was not applied to electromagnetic problems until 1968

(Ahmed and Daly, 1969; Silvester, 1969).The derivation of these governing equations may not be difficult but their solution by exact analytical methods is very tedious and sometimes impossible (Reddy, 1993). As a result approximate solutions are sought through the use of numerical methods. A numerical method in simple terms, is a technique which converts the infinite degrees of freedom of an unknown analytical solution to a finite set of unknowns which can then be solved computationally. The finite element method (FEM) is one such numerical technique for solving, with a high degree of accuracy, complicated boundary value problems.

The basic idea of the finite element method is to divide the region of interest into a large number of finite elements or sub-regions. These elements may be one, two or three-dimensional. The idea of representing a given domain as a collection of discrete elements is not new, it was reported that ancient mathematicians estimated the value of π by representing the circle as a polygon with a large number of sides. The FEM has been developed on the variational methods such as the Rayleigh-Ritz (Zienkiewicz, 1977) and Galerkin methods or the weighted residual techniques (Zienkiewicz, 1977; Desai, 1979; Silvester and Ferrari, 1990). Both methods have their own disadvantage when it comes to solving problems numerically. Generally the solution starts with the governing differential equation and the assumption of an approximate solution which is substituted into the differential equation. The resulting approximate solution is in turn fed back into the equation and the process is repeated; this is known as iteration. The main disadvantage of these methods is that there is no specific way of choosing the trial functions used in the approximation and, it is difficult to construct the approximate functions for problems with arbitrary domains with changes in material properties. The variational method has some other difficulty since the approximation is applied over the whole domain. As a result, very high degree polynomials have to be used in order to describe the unknown function accurately. This creates a more complicated problem if the domain consists of interfaces which have abrupt material changes. Also for irregular shaped boundaries, it can be really difficult to impose the boundary conditions on the complicated trial functions. The FEM has advantage over the two methods in dealing with the problems mentioned above. The method is endowed with two basic features which account for its superiority over other competing methods. First, a geometrically complex domain of the problem is represented as a collection of geometrically simple sub-domains, called finite elements, avoiding the difficulties associated with the ‘whole domain’ techniques. Second, over each finite element the approximation functions are derived using the basic idea that any continuous function can be represented by a linear combination of algebraic polynomials.

In the past, the FEM has been used to solve complex engineering problems including structural analysis in the aircraft industry, heat transfer, fluid flow, and mass transport. In recent years it has found application in electromagnetic field problems. Most waveguide problems can be described through the use of integral or differential equations. These equations can then be solved using numerical techniques. The finite element method has established itself as one of the most powerful and accurate method for solving problems associated with the sophisticated integrated optical waveguides and microwave devices been developed today. The versatility of the method allows elements of various shapes to be used to represent an arbitrary cross-section. Each element could also be of a different material type, enabling a wide range of practical waveguides to be analysed. The type of waveguide problems considered in this thesis belongs to the class of eigenvalue problems and the emphasis will be on the vector **H** field formulation and the scalar formulation.

3.2 Application of finite element to optical waveguides

The following are the basic principles of finite element method.

- The discretisation of the system or region of interest into elements.
- The interpolating polynomials to describe the variation of the field within each of the elements.

Hence, instead of differential equations for the system under investigation, variational expressions are derived and the piecewise continuous function approximated by a piecewise continuous polynomial within each element. From the equivalent discretised model contribution from each element, an overall system is assembled. This can be regarded as a modified form of the Ritz-Galerkin method in which the trial functions are replaced with polynomial functions. In the classical analytical procedure where the region is not subdivided into regions, only the simplest structures with basic material properties can be considered. The finite difference method is the simplest of all the discretisation procedures and in the traditional version uses a rectangular grid as shown in Fig. 3.1 with nodes at the intersections of the orthogonal straight lines.

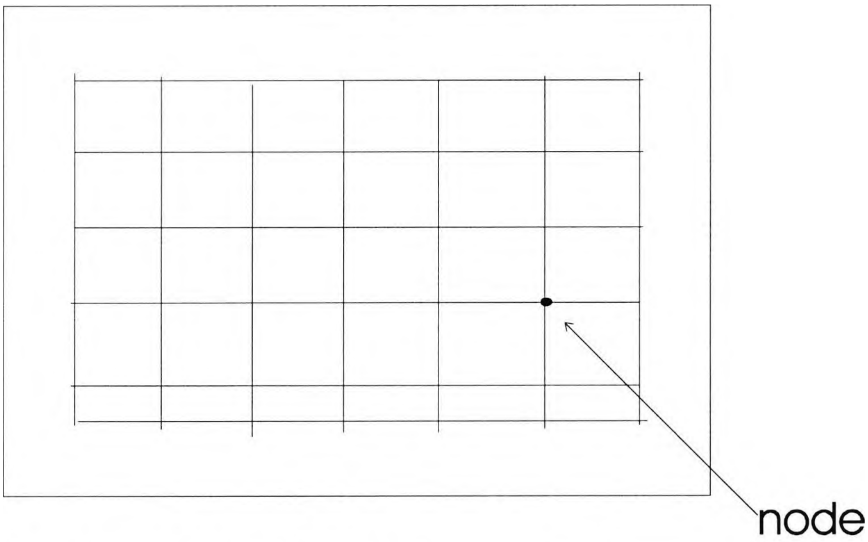

Fig 3.1 Example of domain division using a regular grid.

Such an approach is not particularly suited to irregular geometries with curved boundaries and interfaces since the intersections with the gridlines could be at points other than at the nodes. It is also not well suited to the analysis of problems in which there are steep variations of the field. The finite element method, on the other hand, allows the domain to be subdivided into elements or sub-regions. These elements can be of various shapes such as triangles and rectangles thus enabling the use of irregular grid for a complex waveguide structure as shown in Fig 3.2.

The method can therefore be easily used to analyse problems with steep variations of the field and can be adapted quite readily to anisotropic and inhomogeneous problems. The accuracy of the method could be systematically increased by increasing the number of elements. The method does not rely on the variational method for its establishment; it could be established by the use of the Galerkin method, which is a weighted-residual method. The importance of this last point is that the method could be applied in cases where no variational formulation exists or cannot be found.

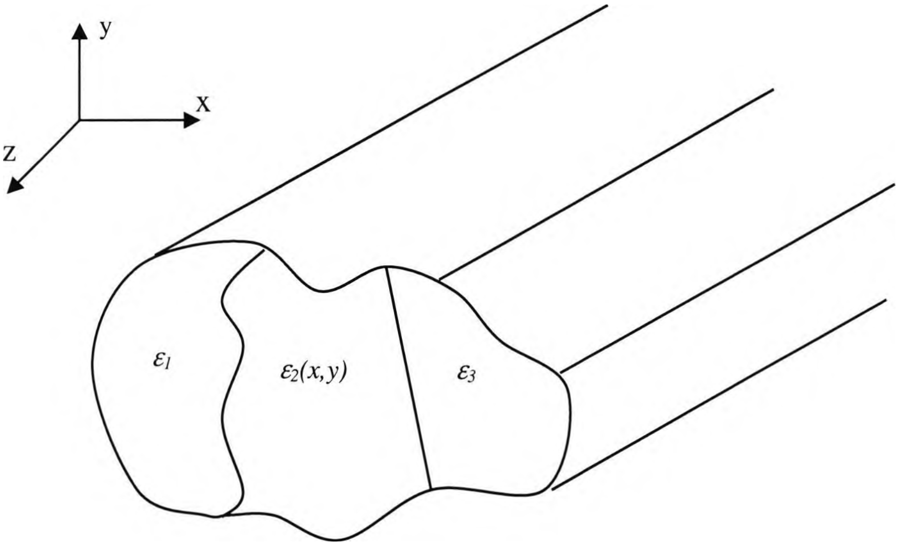

Fig 3.2 Example of an arbitrary shape optical guide with several regions of different material types.

The steps involved in the finite element analysis can be summarised as follows:

- discretize the domain under investigation into sub-domains or elements. The accuracy of the method depends on the level of discretisation. It is recommended to use more elements in areas where the field is thought to have steep variations. It is also not advisable to use elements across physical boundaries or interfaces. For symmetrical domains, the mesh should follow the same type of symmetry.

- the functionals for which the variational principle should be applied for the elements are then derived. In deciding on the interpolation function, certain continuity conditions must be satisfied by the interpolation function across inter-element boundaries. These requirements are normally obvious from physical consideration of the problem. It is however also necessary that the function have to be an admissible member of the Ritz and Galerkin methods. It follows that the polynomial function has to remain unchanged under a linear transformation from one co-ordinate system to the other.

- assemble all the element contributions to form a global matrix.

- solve the system of equations that is obtained, in this case a matrix equation.

Fig 3.3 shows how the discretisation procedure can be applied to a waveguide with different regions, e.g. a cladding, core and substrate. The elements used in this case are triangular since it is much easier to represent an arbitrary cross-section with triangles rather than with rectangles. In 2-D waveguide analysis the triangles can be of any order but the most commonly used triangle orders are the first and second. In Fig. 3.3, the waveguide has been divided into three regions with refractive indices n_c, n_g, *and* n_s for cladding, core and substrate respectively. Each region is sub-divided into triangular meshes numbered 1, 2, 3, 4, 5, 6 ... and so on. This discretisation procedure will be dealt more in detail in subsequent sections in this chapter.

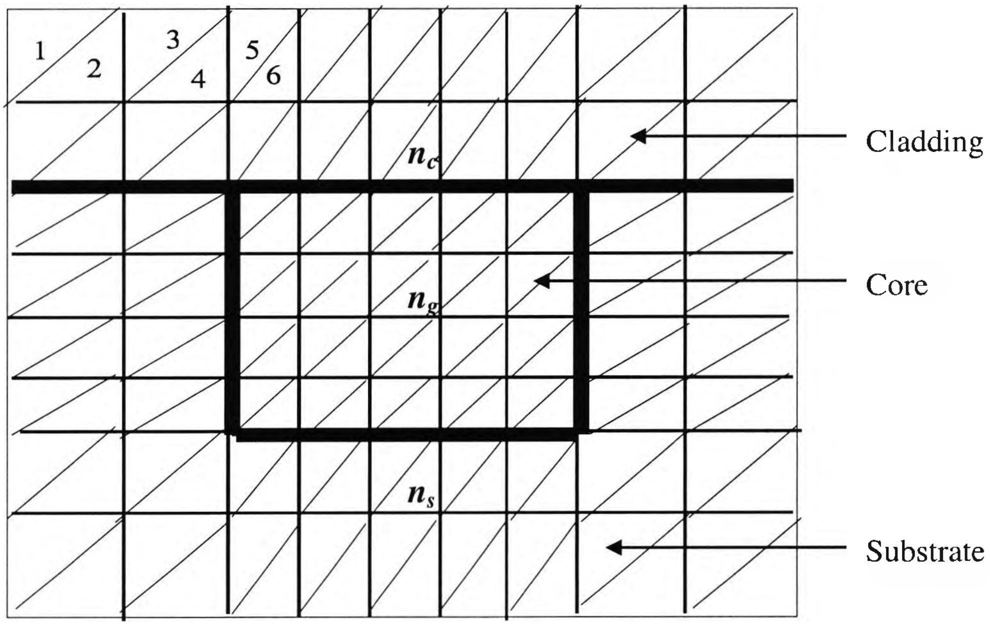

Fig 3.3 Discretisation of an optical waveguide.

3.3 Maxwell's equations

Light is an electromagnetic wave phenomenon. Its field is represented by four electromagnetic field vectors and they can be expressed by Maxwell's equations. The equations can be written in both differential and integral forms. However, in this thesis they are presented only in differential form, as they lead to differential equations to be used by the finite element method.

For general time-varying electromagnetic fields, the differential form of Maxwell's equations:

$$\nabla \times \boldsymbol{E} = \frac{-\partial \boldsymbol{B}}{\partial t} \qquad \text{(Faraday's law)} \qquad 3.1$$

$$\nabla \times \boldsymbol{H} = \frac{\partial \boldsymbol{D}}{\partial t} + \boldsymbol{J} \qquad \text{(Ampere's law)} \qquad 3.2$$

$$\nabla \cdot \boldsymbol{D} = \rho \qquad \text{(Gauss's law)} \qquad 3.3$$

$$\nabla \cdot \boldsymbol{B} = 0 \qquad \text{(Gauss's law for magnetics)} \qquad 3.4$$

E = electric field intensity (volts/metre)
H = magnetic field intensity (amperes/metre)
D = electric flux density (coulombs/metre^2)
B = magnetic flux density (webers/metre^2)
J = electric current density (amperes/metre^2)
ρ = electric charge density (coulombs/metre^3)

The following current continuity equation (or the conservation of charge equation) holds for ***J*** and the charge density, ρ:

$$\nabla \cdot \boldsymbol{J} = \frac{-\partial \rho}{\partial t} \qquad 3.5$$

The associated constitutive relations for the medium can be written as:

$$\boldsymbol{D} = \varepsilon \boldsymbol{E} \qquad 3.6$$

$$\boldsymbol{B} = \mu \boldsymbol{H} \qquad 3.7$$

where ε is the permittivity and μ is the permeability of the medium.

Let the time dependence be assumed to be $\exp(j\omega t)$ for convenience, where j is the imaginary unit, ω is the radian (angular) frequency, and t is the time. Then with this assumption, all the time derivatives may be replaced by $j\omega$ and the factor $\exp(j\omega t)$ will not be included as this factor always occurs as a common factor in all terms. Hence the differential form of Maxwell's equations becomes:

$$\nabla \times \boldsymbol{E} = -j\omega \boldsymbol{B} \qquad 3.8$$

$$\nabla \times \boldsymbol{H} = j\omega \boldsymbol{D} + \boldsymbol{J} \qquad 3.9$$

$$\nabla \cdot \boldsymbol{D} = \rho \qquad 3.10$$

$$\nabla \cdot \boldsymbol{B} = 0 \qquad 3.11$$

and the continuity equation becomes:

$$\nabla \cdot \boldsymbol{J} = -j\omega\rho \qquad 3.12$$

3.4 Boundary Conditions

Boundary conditions are conditions that must be met at the boundary surface where two different media come into contact. It is necessary to subject the Maxwell's equations to boundary conditions at surfaces where abrupt changes of the material constants occur. Fig. 3.4 shows a sketch of such a boundary between two media distinguished by the indices 1 and 2, with the unit normal vector $\boldsymbol{n}$ directed from medium 1 to medium 2.

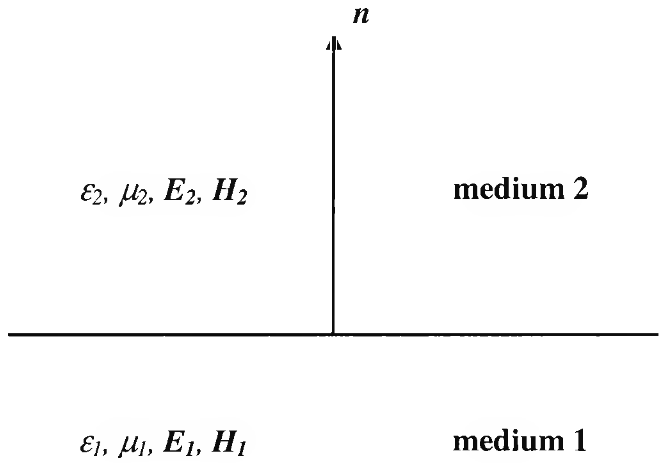

Fig. 3.4 Boundary between two media.

In the absence of surface charges ($\rho = 0$) and surface currents ($\boldsymbol{J} = 0$), the boundary conditions are given as below.

1) The tangential components of the electric field must be continuous.

$$\boldsymbol{n} \times (\boldsymbol{E}_1 - \boldsymbol{E}_2) = 0 \qquad 3.13$$

$$\therefore\ \boldsymbol{E}_{t1} = \boldsymbol{E}_{t2}$$

2) The tangential components of the magnetic field must be continuous.

$$\boldsymbol{n} \times (\boldsymbol{H}_1 - \boldsymbol{H}_2) = 0 \qquad 3.14$$

$$\therefore\ \boldsymbol{H}_{t1} = \boldsymbol{H}_{t2}$$

3) The normal components of the electric flux density must be continuous.

$$n \cdot (D_1 - D_2) = 0 \qquad 3.15a$$

$$\therefore D_{n1} = D_{n2}$$

$$\therefore \varepsilon_1 E_{n1} = \varepsilon_2 E_{n2} \quad \Rightarrow \quad \therefore E_{n1} \neq E_{n2} \qquad 3.15b$$

4) The normal components of the magnetic flux density must be continuous.

$$n \cdot (B_1 = B_2) = 0 \qquad 3.16a$$

$$\therefore B_{n1} = B_{n2}$$

$$\therefore \mu_1 H_{n1} = \mu_2 H_{n2}$$

since, for most of the optical waveguides, $\mu_{r1} = \mu_{r2} = 1$, where μ_{r1} and μ_{r2} are the relative permeabilities in medium 1 and 2, respectively.

$$\therefore H_{n1} = H_{n2} \qquad 3.16b$$

which implies equality of the magnetic field vectors at the boundary.

There is another boundary condition, which is often used in the idealised case of a perfect electric conductor. This can be considered as an 'electric wall' boundary condition:

$$\boldsymbol{n} \times \boldsymbol{E} = 0 \qquad \text{or} \qquad \boldsymbol{n} \cdot \boldsymbol{H} = 0 \qquad 3.17$$

This boundary condition requires that the magnetic field vector, ***H***, must vanish, and ensures the continuity of the electric field vector, ***E***, at the boundary.

When one of the two media becomes a perfect magnetic conductor, a 'magnetic wall' condition is imposed as:

$$\boldsymbol{n} \times \boldsymbol{H} = 0 \qquad \text{or} \qquad \boldsymbol{n} \cdot \boldsymbol{E} = 0 \qquad 3.18$$

This condition will ensure the continuity of the magnetic field component, ***H***, at the boundary and it vanishes the electric field vector, ***E***.

3.5 The Elemental Equations

In order to obtain the element equations it is necessary to perform a co-ordinate transformation. This is because the interpolation function is defined using the local co-ordinates and hence it is necessary to find a means of linking the global derivatives in terms of the local derivatives. Secondly the element volume over which the integration has to be carried out needs to be expressed in terms of local co-ordinates with change of limits as may be appropriate.

Assuming the local co-ordinates ξ_1, ξ_2 and ξ_3 have as a corresponding set, the following global co-ordinates *x*, *y* and *z* as follows:

$$x = x(\xi_1, \xi_2, \xi_3) \qquad 3.19$$

$$y = y(\xi_1, \xi_2, \xi_3) \qquad 3.20$$

$$z = z(\xi_1, \xi_2, \xi_3) \qquad 3.21$$

Using the rules of partial differentiation, the transformation relation for differentiation can be written as

$$\begin{bmatrix} \dfrac{\partial}{\partial \xi_1} \\ \dfrac{\partial}{\partial \xi_2} \\ \dfrac{\partial}{\partial \xi_3} \end{bmatrix} = [J] \begin{bmatrix} \dfrac{\partial}{\partial x} \\ \dfrac{\partial}{\partial y} \\ \dfrac{\partial}{\partial z} \end{bmatrix} \qquad 3.22$$

where the matrix $[J]$ is a Jacobian matrix defined as

$$[J] = \begin{bmatrix} \dfrac{\partial x}{\partial \xi_1} & \dfrac{\partial y}{\partial \xi_1} & \dfrac{\partial z}{\partial \xi_1} \\ \dfrac{\partial x}{\partial \xi_2} & \dfrac{\partial y}{\partial \xi_2} & \dfrac{\partial z}{\partial \xi_2} \\ \dfrac{\partial x}{\partial \xi_3} & \dfrac{\partial y}{\partial \xi_3} & \dfrac{\partial z}{\partial \xi_3} \end{bmatrix} \qquad 3.23$$

The global matrix of the derivatives can then be obtained through an inversion of the Jacobian matrix to give

$$\begin{bmatrix} \frac{\partial}{\partial x} \\ \frac{\partial}{\partial y} \\ \frac{\partial}{\partial z} \end{bmatrix} = [J]^{-1} \begin{bmatrix} \frac{\partial}{\partial \xi_1} \\ \frac{\partial}{\partial \xi_2} \\ \frac{\partial}{\partial \xi_3} \end{bmatrix} \qquad 3.24$$

The following transformation relation for the integration is obtained

$$\iiint f(x,y,z)\,dxdydz = \iiint f(\xi_1,\xi_2,\xi_3)|J(\xi_1,\xi_2,\xi_3)|\,d\xi_1 d\xi_2 d\xi_3 \qquad 3.25$$

3.5.1 Line Elements

As noted, line elements (one-dimensional) are the most fundamental of all the elements used. These elements can be of

a) first order

b) second order or

c) higher order

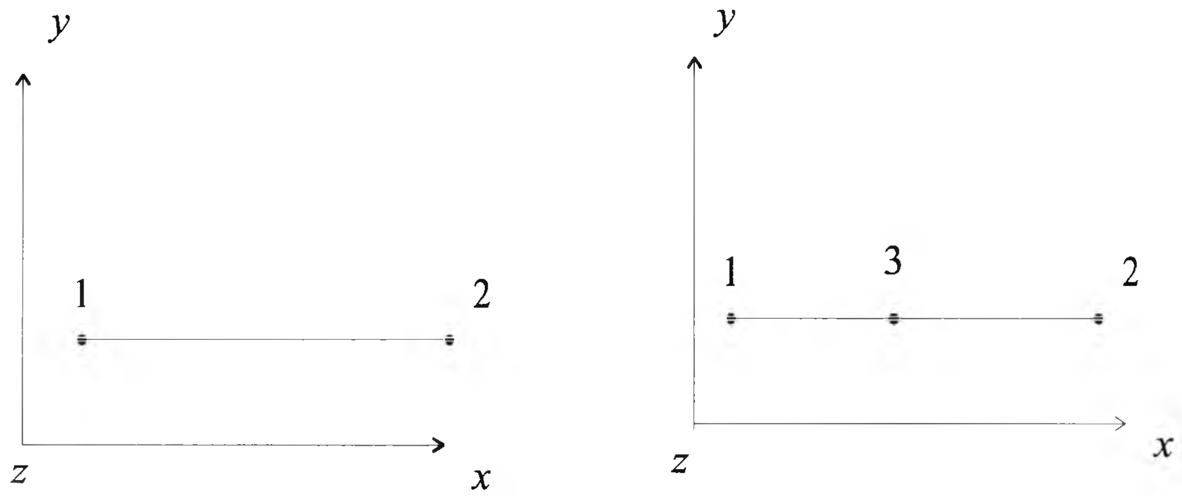

Fig 3.5 Examples of line elements a) Linear element. b) Quadratic element.

Examples of some line elements are shown in Fig 3.5. These are normally used when solving one-dimensional problems. It is necessary to introduce the line co-ordinates L_1 and L_2.

The relation between the line co-ordinates and the Cartesian co-ordinates is given by

$$\begin{bmatrix} L_1 \\ L_2 \end{bmatrix} = \frac{1}{l_e} \begin{bmatrix} x_2 & -1 \\ -x_1 & 1 \end{bmatrix} \begin{bmatrix} 1 \\ x \end{bmatrix} \qquad 3.26$$

where x_1 and x_2 are the Cartesian co-ordinates of the edge of the line and the length of the element is l_e is given by

$$l_e = x_2 - x_1 . \qquad 3.27$$

If the local co-ordinate is now defined as ξ_1 then

$$L_1 = \xi_1 \qquad 3.28a$$

$$L_2 = 1 - L_1 = 1 - \xi_1 \qquad 3.28b$$

The transformation relation for differentiation is then given as

$$\frac{d}{dx} = -\frac{1}{l_e} \frac{d}{d\xi_1} \qquad 3.29$$

For integration, the transformation relation is given by the following

$$\int_e f(x)dx = l_e \int_0^1 f(\xi_1)d\xi_1 \qquad 3.30$$

Using equations (3.29) and (3.30) both the differentiation and integration formulae could be written as

$$\frac{df}{dx}=\frac{1}{l_e}\left(-\frac{\partial f}{\partial L_1}+\frac{\partial f}{\partial L_2}\right) \qquad 3.31$$

$$\int_e L_1^k L_2^l dx = l_e \int_0^1 \xi_1^k (1-\xi_1)^l \, d\xi_1$$

$$= l_e \frac{k!l!}{(k+l+1)!} \qquad 3.32$$

The shape function vector for the linear element and its derivative are given as

$$\{N\}=\begin{bmatrix} L_1 \\ L_2 \end{bmatrix} \qquad 3.33$$

and

$$\{N_{,x}\}=\frac{d\{N\}}{dx}=\frac{1}{l_e}\begin{bmatrix} -1 \\ 1 \end{bmatrix} \qquad 3.34$$

respectively. The nodal co-ordinates (L_1, L_2) of the linear element are given as follows:

node 1: (1,0) node 2: (0,1).

For the quadratic element, the shape function and its derivatives are defined as

$$\{N\}=\begin{bmatrix} L_1(2L_1-1) \\ L_2(2L_2-1) \\ 4L_1L_2 \end{bmatrix} \qquad 3.35$$

and

$$\{N_x\} = \frac{1}{l_e}\begin{bmatrix} 1-4L_1 \\ 4L_2 - 1 \\ 4(L_1 - L_2) \end{bmatrix} \qquad 3.36$$

respectively. The nodal co-ordinates for nodes 1, 2 and 3 are given as (1,0), (0,1) and $(1/2, 1/2)$ respectively.

3.5.2 Triangular Elements

Most practical electromagnetic problems are of the two dimensional type. This makes the use of triangular elements a common practice. These elements can be of either

a) First order
b) Second order or
c) Higher order

Examples of triangular elements of the first and second order are shown in Fig 3.6.

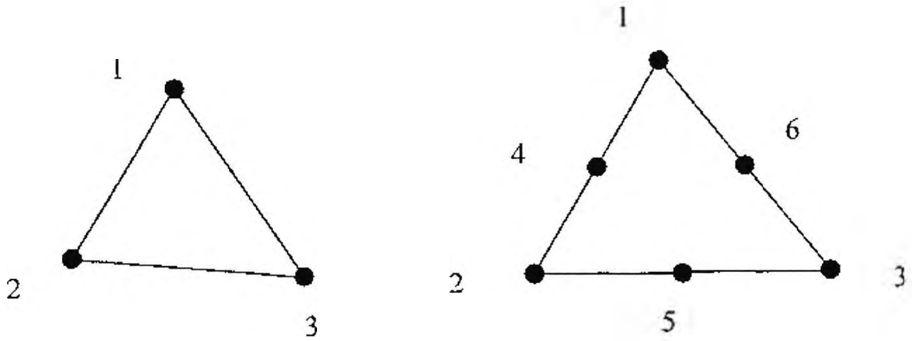

Fig 3.6 Triangular elements a) First order b) second order.

In applying the first order elements it can be seen that nodes occur at the vertices of the triangles while nodes are also defined at the middle of the edges for second order elements. In this work only first order triangular elements are used since the second order elements are costly in terms of the computational time. Since adjacent elements will have common nodes, it is important to adopt a numbering system that will assign to this common nodes the same numbers.

Triangular elements shown in Fig 3.6 are used in two-dimensional problems. For such an element, the area co-ordinates L_1, L_2 and L_3 are introduced. The equation relating the Cartesian co-ordinates to the area co-ordinates is defined as

$$\begin{bmatrix} 1 \\ x \\ y \end{bmatrix} = \begin{bmatrix} 1 & 1 & 1 \\ x_1 & x_2 & x_3 \\ y_1 & y_2 & y_3 \end{bmatrix} \begin{bmatrix} L_1 \\ L_2 \\ L_3 \end{bmatrix} \qquad 3.37$$

or

$$\begin{bmatrix} L_1 \\ L_2 \\ L_3 \end{bmatrix} = \begin{bmatrix} 1 & 1 & 1 \\ x_1 & x_2 & x_3 \\ y_1 & y_2 & y_3 \end{bmatrix}^{-1} \begin{bmatrix} 1 \\ x \\ y \end{bmatrix}$$

$$= \frac{1}{2\Delta_e} \begin{bmatrix} a_1 & b_1 & c_1 \\ a_2 & b_2 & c_2 \\ a_3 & b_3 & c_3 \end{bmatrix} \begin{bmatrix} 1 \\ x \\ y \end{bmatrix} \qquad 3.38$$

where Δ_e is the area of the triangle, (x_1,y_1), (x_2,y_2) and (x_3,y_3) are the Cartesian co-ordinates of the vertex k(k= 1,2 and 3) of the triangle. The coefficients a_k, b_k and c_k are defined as

$$a_k = x_l y_m - x_m y_l \qquad 3.39a$$

$$b_k = y_l - y_m \qquad 3.39b$$

$$c_k = x_m - x_l \qquad 3.39c$$

The subscripts *k, l, m* are cyclical around the three vertices of the triangle. The area Δ_e of the element is given as

$$2\Delta_e = \begin{bmatrix} 1 & 1 & 1 \\ x_1 & x_2 & x_3 \\ y_1 & y_2 & y_3 \end{bmatrix} \qquad 3.40$$

If the local co-ordinates ξ, η are defined as

$$L_1 = \xi \qquad 3.41a$$

$$L_2 = \eta \qquad 3.41b$$

$$L_3 = 1 - L_1 - L_2 = 1 - \xi - \eta \qquad 3.41c$$

then the transformation relation for differentiation will be given by the following

$$\begin{bmatrix} \dfrac{\partial}{\partial \xi} \\ \dfrac{\partial}{\partial \eta} \end{bmatrix} = [J] \begin{bmatrix} \dfrac{\partial}{\partial x} \\ \dfrac{\partial}{\partial y} \end{bmatrix} \qquad 3.42$$

where

$$[J] = \begin{bmatrix} x_1 - x_3 & y_1 - y_3 \\ x_2 - x_3 & y_2 - y_3 \end{bmatrix} \qquad 3.43$$

or

$$\begin{bmatrix} \dfrac{\partial}{\partial x} \\ \dfrac{\partial}{\partial y} \end{bmatrix} = [J]^{-1} \begin{bmatrix} \dfrac{\partial}{\partial \xi} \\ \dfrac{\partial}{\partial \eta} \end{bmatrix} \qquad 3.44$$

with

$$[J]^{-1} = \frac{1}{2\Delta_e}\begin{bmatrix} b_1 & b_2 \\ c_1 & c_2 \end{bmatrix} \qquad 3.45$$

The relation for integration is given as

$$\iint f(x,y)\,dxdy = 2\Delta_e \int_0^1 \int_0^{1-\xi} f(\xi,\eta)\,d\xi d\eta \qquad 3.46$$

Using equations (3.32) through to (3.37), the formulae for both differentiation and integration can be written as

$$\frac{\partial f}{\partial x} = \frac{1}{2\Delta_e}\left(b_1 \frac{\partial f}{\partial L_1} + b_2 \frac{\partial f}{\partial L_2} + b_3 \frac{\partial f}{\partial L_3} \right) \qquad 3.47$$

$$\frac{\partial f}{\partial y} = \frac{1}{2\Delta_e}\left(c_1 \frac{\partial f}{\partial L_1} + c_2 \frac{\partial f}{\partial L_2} + c_3 \frac{\partial f}{\partial L_3} \right) \qquad 3.48$$

$$\iint L_1^k L_2^l L_3^m\,dxdy = 2\Delta_e \int_0^1 \xi^k \left[\int_0^{1-\xi} \eta^l (1-\xi-\eta)^m\,d\eta \right] d\xi$$

$$= 2\Delta_e \frac{k!l!m!}{(k+l+m+2)!} \qquad 3.49.$$

3.5.3 Other Elements

Other type of elements in use include (see Fig. 3.7)

a) rectangular elements – two dimensional elements

b) tetrahedral elements – three dimensional elements

c) ring elements – axisymmetric two dimensional elements

d) triangular ring elements – axisymmetric three dimensional elements

e) special elements – Edge, Isoparametric or boundary elements

All of the above could either be of linear, second or higher order.

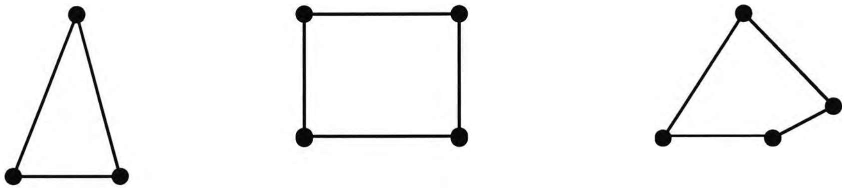

Three-node Triangle *Four-node Rectangle* *Four-node Quadrilatera*

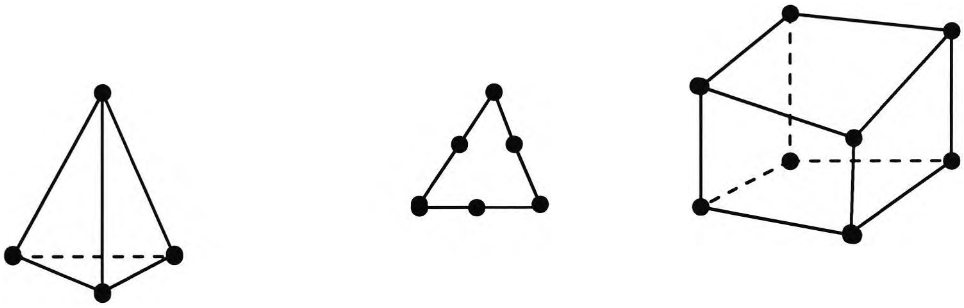

Four-node Tetrahedron *Six-node Triangle* *Eight-node Hexahedron*

Fig. 3.7 The typical elements for two-, and three-dimensional problems.

3.6 The Finite Element Formulations

For the purpose of numerical analysis and characterisation, optical waveguide problems can be classified as either one-dimensional (planar) or two-dimensional. The particular method of analysis used will depend on the waveguide property being investigated. The finite element method is based on either the variational or the weighted residual approach. However the weighted residual approach is more straightforward but however, the variational approach is more advantageous and this is employed to solve most of the electromagnetic field problems. As a result we focus on variational methods which yield a standard eigenvalue problem (Rahman and Davies 1984*a*). There are mainly two types of variational formulations, which can be utilised in finite element method, namely, scalar (Koshiba *et al.*, 1982) and vector formulations (Morishita and Kumagai, 1977; Rahman and Davies, 1984*b*; Koshiba *et al.*, 1985).

3.6.1 The Scalar field formulation

This method is suitable for one dimensional problems for situations where the electric or magnetic field can be expressed approximately in terms of the predominant field component TE and TM modes. It has been applied to the analysis of wave propagation in homogeneous isotropic media (Daly, 1984), open boundary problems (Wu and Chen, 1986) and for the analysis of anisotropic waveguides (Koshiba *et al.*, 1984). For quasi-TE modes in the domain Ω, where the dominant field component is E_x, the formulation can be expressed as (Mabaya *et al.*, 1981):

$$L = \iint_{\Omega} \left[\left(\frac{\partial E_x}{\partial x} \right)^2 + \left(\frac{\partial E_x}{\partial y} \right)^2 - k_o n^2 E_x^2 + \beta^2 E_x^2 \right] d\Omega \qquad 3.50$$

where β is the propagation constant and n is the refractive index k_0 is the free-space wavenumber. A finite element program based on the above mentioned functional yields β^2 as the eigenvalue of the matrix equation for a given k_0.

For quasi-TM modes, with H_x being the dominant field component, the formulation may be given as follows:

$$L = \iint_{\Omega} \left[\frac{1}{n^2} \left(\frac{\partial H_x}{\partial x} \right)^2 + \frac{1}{n^2} \left(\frac{\partial H_x}{\partial y} \right)^2 - k_o H_x^2 + \frac{1}{n^2} \beta^2 H_x^2 \right] d\Omega \qquad 3.51$$

where β, n, and k_0 have their usual meanings defined above. This formulation is not particularly suitable for media where the guided modes are inherently hybrid i.e. highly polarised. A finite element program based on this functional yields k_0^2 as the eigenvalue of the matrix equation for a given propagation constant, β.

In finite element formulations, the physical system or region of interest is divided into mesh elements (commonly known as discretisation) usually triangular in nature (because they are easily adapted to complex shapes) are connected to each other at nodal points on the boundaries of the elements. The unknown field functions at a nodal point are defined by a set of algebraic polynomials over each element, and the field over the guide will be determined by those nodal field values and shape functions. The resulting field components can be continuous over the whole domain by expressing the fields in terms of nodal values.

To obtain the nodal field values, the usual Rayleigh-Ritz procedure is employed for the stationary solution of the functions with respect to each of the nodal variables. This can be written in a matrix eigenvalue equation (Rahman and Davies, 1984a):

$$[\mathbf{A}]\{\boldsymbol{x}\} - \lambda[\mathbf{B}]\{\boldsymbol{x}\} = 0 \qquad 3.52$$

where [**A**] and [**B**] are real symmetric matrices, and [**B**] is also positive definite matrix. The eigenvalue λ may be k_0^2 or β^2 depending on the variational formulation and $\{\boldsymbol{x}\}$ is the eigenvectors representing the unknown nodal field values. It is most desirable for the resulting matrix equation to be of this canonical form, to allow for an efficient and robust solution. This equation (3.52) can be solved by one of various standard subroutines to obtain different eigenvectors and eigenvalues.

One of the most serious problems in using the finite element method for dielectric waveguides is the appearance of the spurious or non physical modes. That means the eigenvectors and eigenvalues of the matrix eigenvalue problem do not represent physical modes or solution of the waveguide but are spurious results introduced by the numerical technique. The reason for the appearance of spurious modes is probably the fact that the functional is not positive definite (Csendes and Silvester, 1970). The appearance of these spurious modes does not affect the calculation of the lowest propagating mode, since the lowest order mode usually corresponds to the first positive eigenvalue of the matrix equation. However, to compute higher order modes, it becomes more difficult and very cumbersome to distinguish between the spurious and the physical modes of the guide.

On the other hand, the scalar approximation does not suffer from this difficulty, since the two scalar functionals are positive definite and therefore all the eigenvalues are positive, each one corresponding to a physical mode of the guide. Consequently, the higher order modes of the guide can be easily computed without any difficulty. Another advantage is that with this method the number of matrix elements to be solved is reduced compared to vector finite element method and therefore a reduction of the computer time can be achieved. The boundary condition, which is automatically satisfied with this variational procedure is another advantage. It is known as the 'natural boundary condition' (nbc). In variational formulations these can be automatically satisfied, if left free. The scalar functional defined in equation (3.50) has the continuity of $\frac{\partial \phi}{\partial \hat{\boldsymbol{n}}}$ as the nbc, and the functional (3.51) has the continuity $\left(\frac{1}{n^2}\right)\left(\frac{\partial \psi}{\partial \hat{\boldsymbol{n}}}\right)$ as the nbc, where $\hat{\boldsymbol{n}}$ is the outward normal unit vector. However, if the physical boundary conditions are not the same as nbc, then physical boundary conditions need to be imposed when solving the equations.

3.6.2 The Vector field formulation

For the accurate characterisation of general waveguides especially for 2-D or 3-D guided modes, a vector formulation with at least two field components is required. They provide better solution convergence for some modal types as compared to corresponding scalar formulations. There are two main types of the full vector formulations namely, the **E**-field and **H**-field. The vector **E**-field approach was first applied by English and Young (English and Young, 1971). This formulation is suitable for generally anisotropic and loss-less problems. The natural boundary condition corresponds to a magnetic wall and as such it is essential to enforce the electric wall as the boundary condition (**n**x**E**=0). Such a condition is quite difficult to impose for an irregular structure. It also requires an additional integral to ensure the continuity of the fields at the dielectric interfaces. The **H**-field formulation, on the other hand, has as its nbc the electric wall and the magnetic field is continuous everywhere. As such it is suitable for dielectric waveguide problems as no boundary conditions need to be imposed.

The followings are various types of finite element methods for vector guided mode analysis:

- Finite element method using longitudinal (axial) electromagnetic (**E** and **H**) field components, $(E_z + H_z)$,
- Finite element method using transverse electromagnetic field components, $(\boldsymbol{E}_t+\boldsymbol{H}_t)$,
- Finite element method using transverse electric field components, $(\boldsymbol{E}_t)$,
- Finite element method using transverse magnetic field components, $(\boldsymbol{H}_t)$,
- Finite element method using the three electric field components, (**E**),
- Finite element method using the three magnetic field components, (**H**),
- Finite element method using the six electromagnetic field components, (**E**+**H**).

Of all the above vector formulations the one of interest, is formulated in terms of all three components of **H** and has the advantage over all other formulations. This vector **H**-field formulation (Rahman and Davies, 1984*b*; Rahman and Davies, 1984*c*; Koshiba *et al.*, 1985) is valid for general anisotropic problems with a non-diagonal permittivity tensor. The natural boundary condition is that of an electric wall ($\boldsymbol{n} \times \mathbf{E} = 0$, $\boldsymbol{n} \cdot \mathbf{H} = 0$), so for the arbitrary conducting guide walls it can be left free. In dielectric waveguides, the permeability is always assumed to be that of free space. Therefore, each component of **H** is continuous in the whole region and thus the variation of the refractive index over the waveguide cross section does not need to impose interface boundary conditions. The total vector **E**+**H** formulation (Svedin, 1989) does not have much advantage over the vector **H** field formulation since all the six components are needed for the formulation giving rise to a complicated problem. The full vector **H**-field formulation is given as (Rahman and Davies, 1984*b*):

$$\omega^2 = \frac{\int (\nabla \times \mathbf{H})^* \cdot \hat{\varepsilon}^{-1} \cdot (\nabla \times \mathbf{H}) d\Omega}{\int \mathbf{H}^* \cdot \mu^{-1} \cdot \mathbf{H} d\Omega} \qquad 3.53$$

where $\hat{\varepsilon}$ and $\hat{\mu}$ are the general anisotropic permittivity and permeability of the loss-free medium, respectively, and the integration is carried out over the waveguide cross section, Ω. The above formulation leads to non-physical or spurious solutions since the divergence condition $\nabla \cdot \mathbf{H} = 0$ is not satisfied. Various methods exist for detecting these spurious modes. A simple way is to examine the field profiles, since these modes are characterised by inconsistency and a random variation of the field they are easy to identify. The mathematical idea underpinning the physical solution is that the condition $\nabla \cdot \mathbf{H} = 0$ is obeyed by the eigenvector. By calculating $\nabla \cdot \mathbf{H}$ for each eigenvector, it is possible to identify the true solutions from the spurious ones. The objective, however, is not simply to detect these modes, but to eliminate them or at least suppress them. The penalty-function method (Rahman and Davies, 1984c) is one the best established methods for eliminating these spurious solutions. The method includes an additional term α, the penalty term, a dimensionless number in the variational formulation, which now is written as:

$$\omega^2 = \frac{\int (\nabla \times \mathbf{H})^* \cdot \hat{\varepsilon}^{-1} \cdot (\nabla \times \mathbf{H}) d\Omega + \left(\frac{\alpha}{\varepsilon_0} \right) \int (\nabla \cdot \mathbf{H})^* (\nabla \cdot \mathbf{H}) d\Omega}{\int \mathbf{H}^* \cdot \mu^{-1} \cdot \mathbf{H} d\Omega} \qquad 3.54$$

The vector **H**-field formulation described above, has the natural boundary condition of an electric wall, i.e. $\boldsymbol{n} \cdot \mathbf{H} = 0$. Therefore there is no need to force any boundary condition on conducting guide walls. At times these natural boundary conditions are not those that are required, as simply they do not correspond to the physical problem under consideration. In some cases if necessary the boundary conditions may be enforced in order to reduce the matrix size, but even in these situations they are automatically satisfied if left free. Sometimes it may be necessary to change unsuitable natural boundary condition by introducing additional surface integral around the desired boundary. In the case where the symmetry of the waveguide exists, then we can easily impose the waveguide symmetry. However, it may be necessary to analyse the structure with complementary symmetry conditions to obtain all the modes, although the exploitation of the symmetry greatly reduces the computational cost.

3.7 The Matrix Equation

It has been stated that the vector formulation leads to a standard eigenvalue problem of the form (Rahman and Davies, 1984a)

$$\mathrm{A}x - \lambda \mathrm{B}x = 0 \qquad 3.55$$

In the above x represents the eigenvector, which holds the nodal field values. If in equation (3.53) the numerator is written as

$$x^T \cdot Ax = \int (\nabla \times \mathbf{H})^* \cdot \varepsilon^{-1} \cdot (\nabla \times \mathbf{H}) d\Omega \qquad 3.56$$

and the denominator as

$$x^T \cdot Bx = \int \mathbf{H}^* \cdot \mu \cdot \mathbf{H} d\Omega \qquad 3.57$$

then the functional

$$J = \int (\nabla \times \mathbf{H})^* \cdot \varepsilon^{-1} \cdot (\nabla \times \mathbf{H}) d\Omega - k_o^2 \int \mathbf{H}^* \cdot \mu \cdot \mathbf{H} d\Omega \qquad 3.58$$

can be written as

$$J = x^T \cdot A \cdot x - \lambda \cdot x^T \cdot B \cdot x \qquad 3.59$$

To find a stationary solution, it is required that

$$\frac{\partial J}{\partial x}=0 \qquad 3.60$$

Applying this minimisation procedure to equation (3.49), the following eigenvalue equation (3.55) is obtained

$$Ax-\lambda Bx=0 \qquad 3.61$$

which can be solved using any standard matrix routine to obtain the field values at the nodes.

3.7.1 Shape Functions

The shape functions are a set of interpolation functions, defined in terms of complete polynomials and which are normalised over each element. If a typical element, as shown in Fig 3.6 is considered, then the shape function is chosen so that it uniquely defines the field within the element under consideration. The unknown field, ***H***, within each element is approximated by means of a suitable choice of the set of polynomials. These functions are called "shape functions" due to the fact that polynomials are relatively easy to manipulate. The choice of the functions should have continuity within each element and across the element boundaries. The actual field over the entire domain should be approximated by trial sets of algebraic functions which can be uniquely defined, differentiated and integrated.

In the simplest case the elements are triangular and first degree polynomials are used. The total number of the terms involved in the polynomial is equal to the number of nodal degrees of freedom of the element. If the highest order term is x^N and y^N, it must also contain all possible terms $x^m y^n$, where $0 < m + n < N$, excluding other terms. The polynomial will be $M=(N+1)(N+2)/2$ terms or as we can see through the Pascal triangle in given in Fig. 3.8. The continuous field $\phi(x,y)$ of the domain may be replaced by a set of discreet values (ϕ_i, $i = 1, 2, 3 \ldots m$) where m is the total number of nodes.

Element with nodes

$1 \longrightarrow$ *(Constant)*

$x \quad y \longrightarrow$ *(linear- 1 terms)*

$x^2 \quad xy \quad y^2 \longrightarrow$ *(quadratic- 2 terms)*

$x^3 \quad x^2y \quad xy^2 \quad y^3 \longrightarrow$ *(cubic- 3 terms)*

$x^4 \quad x^3y \quad x^2y^2 \quad xy^3 \quad y^4 \longrightarrow$ *(quartic- 4 terms)*

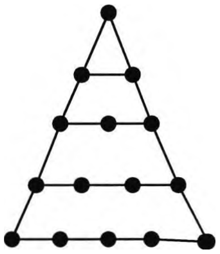

Fig. 3.8 Pattern of nodes on a single element compared with Pascal's triangle.

Our assumption of a linear variation of nodal values, ϕ_i within the triangular elements is the same as assuming that the $\phi_e(x,y)$ is uniform within the element. This continuity can be achieved by introducing the interpolation function, or so called "shape function" $N_i(x, y)$. The field inside the element $\phi_e(x,y)$ can be written as:

$$\phi_e(x,\ y) = \sum_{i}^{3} N_i(x,\ y)\cdot\phi_i \qquad 3.62$$

and in matrix form can be written as follows:

$$\phi_e(x,\ y) = [N_1 \quad N_2 \quad N_3]\cdot\begin{Bmatrix}\phi_1\\ \phi_2\\ \phi_3\end{Bmatrix} = [N]\cdot\{\phi_e\} \qquad 3.63$$

At the nodal points, they take on values equal to the nodal values ϕ_1, ϕ_2 and ϕ_3. It is important therefore that the functions are expressed in terms of their nodal values. Within the triangle, the field value can be adequately modelled by the expression

$$\phi = a + bx + cy \qquad 3.64$$

where *a, b* and *c* are constants. These constants can be represented in terms of the co-ordinates of the nodes. The nodal values of ϕ can then be expressed as

$$\phi_1 = a + bx_1 + cy_1 \tag{3.65a}$$

$$\phi_2 = a + bx_2 + cy_2 \tag{3.65b}$$

$$\phi_3 = a + bx_3 + cy_3 \tag{3.65c}$$

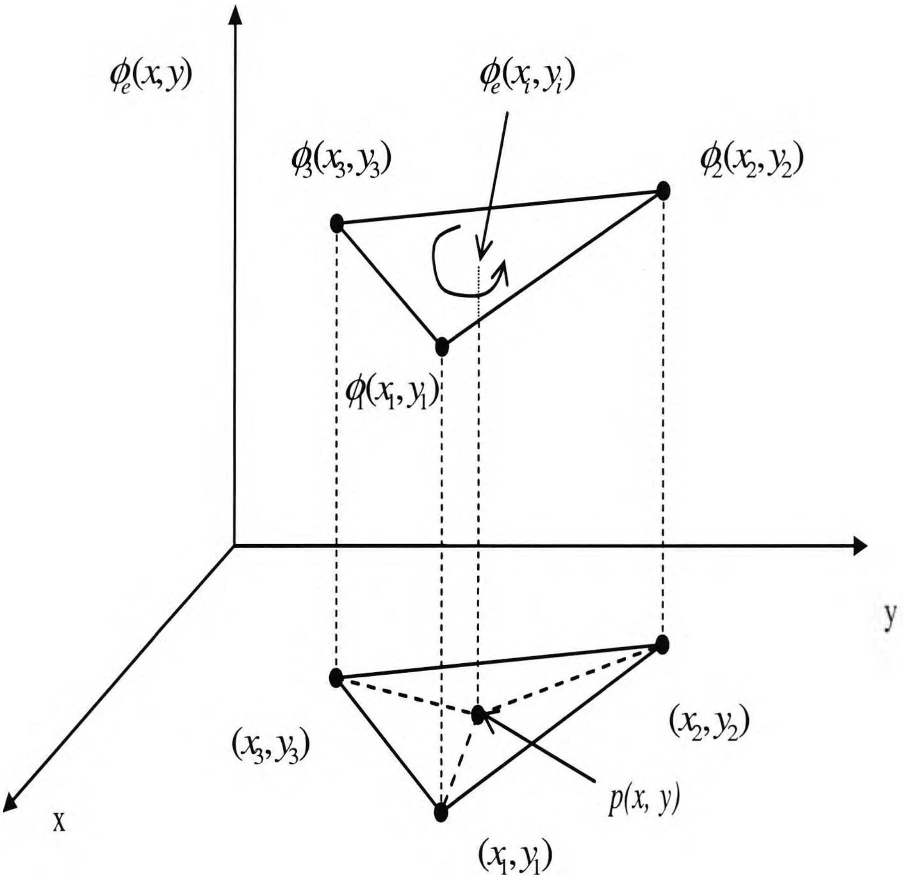

Fig. 3.9 Coordinates and node numbers of a typical first-order triangular elements.

The above system of equations can be solved to determine *a*, *b* and *c* as

$$a = \frac{\phi_1(x_2y_3 - x_3y_2) + \phi_2(x_3y_1 - x_1y_3) + \phi_3(x_1y_2 - x_2y_1)}{2\Delta_e} \tag{3.66a}$$

$$b=\frac{\phi_1(y_2-y_3)+\phi_2(y_3-y_1)+\phi_3(y_1-y_2)}{2\Delta_e} \qquad 3.66b$$

$$c=\frac{\phi_1(x_3-x_2)+\phi_2(x_1-x_3)+\phi_3(x_2-x_1)}{2\Delta_e} \qquad 3.66c$$

Where in the above Δ_e is the area of the triangle. A substitution of these values into equation (3.51) will yield

$$\phi(x,y)=\mathrm{N}_1\phi_1+\mathrm{N}_2\phi_2+\mathrm{N}_3\phi_3 \qquad 3.67$$

or

$$\phi(x,y)=[\mathrm{N}]\{\phi\} \qquad 3.68$$

where

$$\mathrm{N}_1=\frac{1}{2\Delta}[(x_2y_3-x_3y_2)+(y_2-y_3)x+(x_3-x_2)y] \qquad 3.69a$$

$$\mathrm{N}_2=\frac{1}{2\Delta}[(x_3y_1-x_1y_3)+(y_3-y_1)x+(x_1-x_3)y] \qquad 3.69b$$

$$\mathrm{N}_3=\frac{1}{2\Delta}[(x_1y_2-x_2y_1)+(y_1-y_2)x+(x_2-x_1)y] \qquad 3.69c$$

The above can be rewritten as

$$\mathrm{N}_1=\mathrm{a}_1+\mathrm{b}_1\mathrm{x}+\mathrm{c}_1\mathrm{y} \qquad 3.70a$$

$$\mathrm{N}_2=\mathrm{a}_2+\mathrm{b}_2\mathrm{x}+\mathrm{c}_2\mathrm{y} \qquad 3.70b$$

$N_3 = a_3 + b_3 x + c_3 y$ 3.70c

An important property of shape function is that

$N_1+N_2+N_3=1.$ 3.71

The **H**-field components H_x, H_y and H_z can be written as

$H_x(x,y) = N_1 H_{x1} + N_2 H_{x2} + N_3 H_{x3}$ 3.72a

$H_y(x,y) = N_1 H_{y1} + N_2 H_{y2} + N_3 H_{y3}$ 3.72b

$H_z(x,y) = N_1 H_{z1} + N_2 H_{z2} + N_3 H_{z3}$ 3.72c

In matrix form, the above equations can be expressed as

$$\mathbf{H} = \begin{bmatrix} H_x \\ H_y \\ H_z \end{bmatrix} = \begin{bmatrix} N_1 & 0 & 0 & N_2 & 0 & 0 & N_3 & 0 & 0 \\ 0 & N_1 & 0 & 0 & N_2 & 0 & 0 & N_3 & 0 \\ 0 & 0 & N_1 & 0 & 0 & N_2 & 0 & 0 & N_3 \end{bmatrix} \begin{bmatrix} H_{x1} \\ H_{y1} \\ H_{z1} \\ H_{x2} \\ H_{y2} \\ H_{z2} \\ H_{x3} \\ H_{y3} \\ H_{z3} \end{bmatrix} \quad 3.73$$

In a simplified form this is equivalent to $\mathbf{H} = [N]\{\mathbf{H}\}$, where [N] is the 3x9 matrix shown above and $\{\mathbf{H}\}$ is the 9x1 column vector which represents the components of the field.

Similarly, the expression for $\nabla \times \mathbf{H}$ could be written as

$$\nabla \times \mathbf{H} = [\mathrm{Q}] \cdot \mathbf{H} \qquad 3.74$$

where

$$[Q] = \begin{bmatrix} 0 & -\frac{\partial N_1}{\partial z} & \frac{\partial N_1}{\partial y} & 0 & -\frac{\partial N_2}{\partial z} & -\frac{\partial N_2}{\partial y} & 0 & -\frac{\partial N_3}{\partial z} & -\frac{\partial N_3}{\partial y} \\ \frac{\partial N_1}{\partial z} & 0 & -\frac{\partial N_1}{\partial x} & \frac{\partial N_2}{\partial z} & 0 & -\frac{\partial N_2}{\partial x} & \frac{\partial N_3}{\partial z} & 0 & -\frac{\partial N_3}{\partial x} \\ -\frac{\partial N_1}{\partial y} & \frac{\partial N_1}{\partial x} & 0 & -\frac{\partial N_2}{\partial y} & \frac{\partial N_2}{\partial x} & 0 & -\frac{\partial N_3}{\partial y} & \frac{\partial N_3}{\partial x} & 0 \end{bmatrix}$$

3.75

The **Q** matrix, after evaluation i.e. finding the derivative of the shape, with $j\beta z$ being the z-variation, becomes

$$[Q] = \begin{bmatrix} 0 & j\beta N_1 & a_3 & 0 & j\beta N_2 & a_6 & 0 & j\beta N_3 & a_9 \\ -j\beta N_1 & 0 & -a_2 & -j\beta N_2 & 0 & -a_5 & j\beta N_3 & 0 & -a_8 \\ -a_3 & a_2 & 0 & -a_6 & a_5 & 0 & -a_9 & a_8 & 0 \end{bmatrix} \qquad 3.76$$

The **B** matrix can also be calculated in a similar fashion from equation (3.57). Since μ is a scalar quantity, it can be taken outside the integral to give

$$x^T \cdot B \cdot x = \mu \int \mathbf{H}^* \cdot \mathbf{H} \, d\Omega \qquad 3.77$$

since **H**=[N] {**H**}

$$B_e = \int_\Delta [N]^* \cdot [N] \, d\Omega \qquad 3.78$$

The solution of the above expressions yields a 9x9 matrix. The integration is carried out using equation (3.40) and the resulting B_e matrix is as follows:

$$B_e = \begin{bmatrix} \frac{\Delta}{6} & 0 & 0 & \frac{\Delta}{12} & 0 & 0 & \frac{\Delta}{12} & 0 & 0 \\ 0 & \frac{\Delta}{6} & 0 & 0 & \frac{\Delta}{12} & 0 & 0 & \frac{\Delta}{12} & 0 \\ 0 & 0 & \frac{\Delta}{6} & 0 & 0 & \frac{\Delta}{12} & 0 & 0 & \frac{\Delta}{12} \\ \frac{\Delta}{12} & 0 & 0 & \frac{\Delta}{6} & 0 & 0 & \frac{\Delta}{12} & 0 & 0 \\ 0 & \frac{\Delta}{12} & 0 & 0 & \frac{\Delta}{6} & 0 & 0 & \frac{\Delta}{12} & 0 \\ 0 & 0 & \frac{\Delta}{12} & 0 & 0 & \frac{\Delta}{6} & 0 & 0 & \frac{\Delta}{12} \\ \frac{\Delta}{12} & 0 & 0 & \frac{\Delta}{12} & 0 & 0 & \frac{\Delta}{6} & 0 & 0 \\ 0 & \frac{\Delta}{12} & 0 & 0 & \frac{\Delta}{12} & 0 & 0 & \frac{\Delta}{6} & 0 \\ 0 & 0 & \frac{\Delta}{12} & 0 & 0 & \frac{\Delta}{12} & 0 & 0 & \frac{\Delta}{6} \end{bmatrix} \tag{3.79}$$

In the above Δ_e is the area of each element or triangle. The coefficients of the A_e matrix could also be calculated using equation (3.56). Making the following substitutions $\mathbf{H}=[\mathrm{N}]\{\mathbf{H}\}$ and $\nabla \times \mathbf{H} = [\mathrm{Q}] \cdot \{\mathbf{H}\}$, the equation below is obtained:

$$x^T \cdot A_e \cdot x = \int \{\mathbf{H}\}^* \cdot [Q]^* \hat{\varepsilon}^{-1} \cdot [Q] \{\mathbf{H}\} d\Omega \tag{3.80}$$

A simplification of the above will yield an A_e matrix of the form

$$A_e = \int [Q]^* \hat{\varepsilon}^{-1} \cdot [Q] \, d\Omega \tag{3.81}$$

For isotropic media, ε is a scalar quantity and hence can be factored out of the integral sign. For anisotopic media, ε is a tensor defined by a 3x3 matrix

$$\varepsilon = \begin{bmatrix} \varepsilon_{11} & \varepsilon_{12} & \varepsilon_{13} \\ \varepsilon_{21} & \varepsilon_{22} & \varepsilon_{23} \\ \varepsilon_{31} & \varepsilon_{32} & \varepsilon_{33} \end{bmatrix} \tag{3.82}$$

Finding the inverse of ε, $[P]$, equation 3.81 can be written as

$$A_e = \int [Q]^* \cdot [P] \cdot [Q] d\Omega \qquad 3.83$$

Carrying out the necessary algebraic manipulations a 9x9 matrix is obtained. Using the integration formula of equation (3.49) the integrals can be evaluated as

$$\int N_1^2 d\Omega = \frac{A}{6} \qquad 3.84a$$

$$\int N_1 d\Omega = \frac{A}{3} \qquad 3.84b$$

$$\int d\Omega = A \qquad 3.84c$$

As an example the A_{e11} matrix will be given as follows

$$A_{e11} = p_{22}\beta^2 \frac{A}{6} + p_{23}a_3 j\beta \frac{A}{3} + p_{32}a_3 j\beta \frac{A}{3} + p_{33}a_3^2 A \qquad 3.85$$

The other 80 elements of the A_e matrix can be found in a similar fashion.

3.7.2 Element/Global Matrices Assembly

The next stage in the finite element method is the assembly of the element matrices [A$_e$] and [B$_e$] into global matrices [A] and [B] respectively. An appropriate matrix solver is then used to obtain the eigenvalues and eigenvectors of the equation. The assembly of the global matrix is done with respect to the nodes of the domain. Where two or more nodes are common to more than one element then it is advisable to add the contribution of each adjacent element to the global matrix when the calculation for the common node is carried.

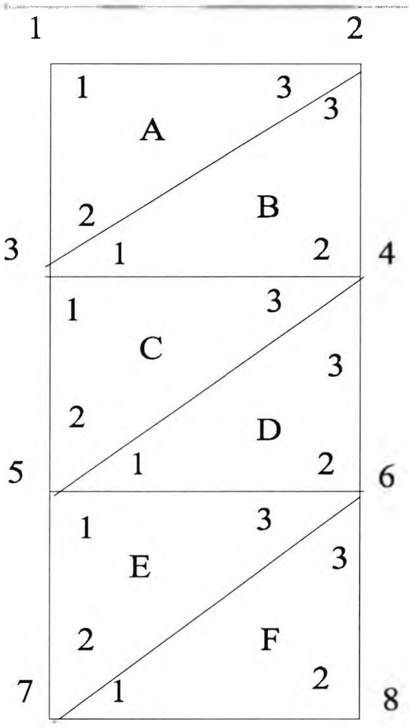

Fig 3.10 Example of domain discretisation using triangular elements.

Fig 3.10 shows a simple diagram of a domain, which has been discretised using 6 first order triangular elements. The node numbers 1-6 are the global node numbers for the domain and are used in the global matrices. The nodal points inside each triangular element are numbered 1-3. For the above structure, the global matrix G, is formed by the addition of the element matrices A, B, C, D, E and F.

As previously noted, for every element in the discretised variational formulation, there is an expression of the form

$$\{H\}[N]\{H\}^T = \{H_1 \cdots H_9\} \begin{bmatrix} N_{11} & \cdot & \cdot & \cdot & N_{19} \\ \cdot & & & & \cdot \\ \cdot & & \cdot & & \cdot \\ \cdot & & & & \cdot \\ N_{91} & \cdot & \cdot & \cdot & N_{99} \end{bmatrix} \begin{bmatrix} H_1 \\ \cdot \\ \cdot \\ \cdot \\ H_9 \end{bmatrix} \qquad 3.86$$

Each term in the matrix N_{ij} relates to two nodal field values where the indices, i and j, correspond to the nodal field values of the vectors {H} and $\{H\}^T$ according to the local numbering of an element. If a scalar formulation is considered, then only one field component need be taken into account H_x for example and the expression can be written as

$$\{H_{x1}\ H_{x2}\ H_{x3}\}\begin{bmatrix} N_{11} & N_{12} & N_{13} \\ N_{21} & N_{22} & N_{23} \\ N_{31} & N_{32} & N_{33} \end{bmatrix}\begin{bmatrix} H_1 \\ H_2 \\ H_3 \end{bmatrix} \qquad 3.87$$

This section explains the derivation of the element and global matrices based on the full vectorial **H**-field variational expression eq. (3.53). Within each triangular element, the three unknown **H**-field components, H_x, H_y and H_z of the magnetic field can be expressed as;

$$H_x(x,y) = [N_1 \quad N_2 \quad N_3]\begin{Bmatrix} H_{x1} \\ H_{x2} \\ H_{x3} \end{Bmatrix} \qquad 3.88a$$

$$H_y(x,y) = [N_1 \quad N_2 \quad N_3]\begin{Bmatrix} H_{y1} \\ H_{y2} \\ H_{y3} \end{Bmatrix} \qquad 3.88b$$

$$H_z(x,y) = [N_1 \quad N_2 \quad N_3]\begin{Bmatrix} H_{z1} \\ H_{z2} \\ H_{z3} \end{Bmatrix} \qquad 3.88c$$

where, H_{xi}, H_{yi} and H_{zi} ; i = 1,2,3, represents the x, y and z components of the nodal magnetic fields. Hence, the element magnetic field vector $[\boldsymbol{H}]_e$ can be expressed by combining equations (3.88a)-(3.88c);

$$[\boldsymbol{H}]_e = \begin{bmatrix} H_x(x,y) \\ H_y(x,y) \\ H_z(x,y) \end{bmatrix} = \begin{bmatrix} N_1 & N_2 & N_3 & 0 & 0 & 0 & 0 & 0 & 0 \\ 0 & 0 & 0 & N_1 & N_2 & N_3 & 0 & 0 & 0 \\ 0 & 0 & 0 & 0 & 0 & 0 & N_1 & N_2 & N_3 \end{bmatrix} \begin{Bmatrix} H_{x1} \\ H_{x2} \\ H_{x3} \\ H_{y1} \\ H_{y2} \\ H_{y3} \\ H_{z1} \\ H_{z2} \\ H_{z3} \end{Bmatrix} \tag{3.89}$$

Equation (3.89) can also be written as;

$$[\boldsymbol{H}]_e = [\mathbf{N}]\ \{\boldsymbol{H}\}_e \tag{3.90}$$

where $\{\boldsymbol{H}\}_e$ is the column vector representing the three components of the nodal field values in the element and **[N]** is the shape function matrix.

Also by substituting (3.90), the $(\nabla \times \boldsymbol{H})_e$ factor within the element can be written as;

$$(\nabla \times \boldsymbol{H})_e = \nabla \times [\mathbf{N}]\{\boldsymbol{H}\}_e = \begin{bmatrix} 0 & \dfrac{-\partial}{\partial z} & \dfrac{\partial}{\partial y} \\ \dfrac{\partial}{\partial z} & 0 & \dfrac{-\partial}{\partial x} \\ \dfrac{-\partial}{\partial y} & \dfrac{\partial}{\partial x} & 0 \end{bmatrix} [\mathbf{N}]\{\boldsymbol{H}\}_e = [Q]\{\boldsymbol{H}\}_e \tag{3.91}$$

where the matrix $[Q]$ can be written as;

$$[Q] = \begin{bmatrix} [0] & \dfrac{-\partial[N]}{\partial z} & \dfrac{\partial[N]}{\partial y} \\ \dfrac{\partial[N]}{\partial z} & [0] & \dfrac{-\partial[N]}{\partial x} \\ \dfrac{-\partial[N]}{\partial y} & \dfrac{\partial[N]}{\partial x} & [0] \end{bmatrix} = \begin{bmatrix} [0] & j\beta[N] & \dfrac{\partial[N]}{\partial y} \\ -j\beta[N] & [0] & \dfrac{-\partial[N]}{\partial x} \\ \dfrac{-\partial[N]}{\partial y} & \dfrac{\partial[N]}{\partial x} & [0] \end{bmatrix} \tag{3.92}$$

where $$[0] = [0 \quad 0 \quad 0] \qquad 3.93$$

$$[N] = [N_1 \quad N_2 \quad N_3] \qquad 3.94$$

and the following arises by using the differentiations of equation (3.70),

$$\frac{\partial [N]}{\partial x} = [b_1 \quad b_2 \quad b_3] \qquad 3.95$$

$$\frac{\partial [N]}{\partial y} = [c_1 \quad c_2 \quad c_3] \qquad 3.96$$

The values of the constants b_1, b_2, b_3, c_1, c_2 and c_3 were given in equations (3.39c) and (3.39c).

By substituting the terms in equations (3.90) and (3.91) into the equation (3.53), the vector **H**-field formulation functional for an element can be obtained as;

$$J_e = \int_{\Delta} \{\boldsymbol{H}\}_e^T [Q]^* \hat{\varepsilon}^{-1} [Q]\{\boldsymbol{H}\}_e \, d\Omega - \omega^2 \int_{\Delta} \{\boldsymbol{H}\}_e^T [\mathbf{N}]^T \hat{\mu} [\mathbf{N}]\{\boldsymbol{H}\}_e \, d\Omega \qquad 3.97$$

Δ represents the integration over the triangular element domain. *T* and * denote the transpose and the complex conjugate transpose, respectively.

If the material is isotropic, then the ε is a scalar value. Here it is assumed that the ε is a scalar quantity. If ε is a tensor, then it should be represented by a 3 × 3 matrix and the inverse of the matrix should be implemented.

The total function, *J*, associated with the whole cross section of the waveguide can be obtained by summing J_e of all the individual elements,

$$J = \sum_{e=1}^{n} J_e \tag{3.98}$$

where n is the number of elements.

The minimisation of the functional given in equation (3.98) is achieved by differentiating with respect to the field nodal values and equating it to zero as below;

$$\frac{\partial J}{\partial \{H\}_e} = 0 \qquad\qquad e = 1,2,\ldots\ldots,n \tag{3.99}$$

This minimisation leads to the following eigenvalue equation;

$$[\mathbf{A}]\{\boldsymbol{H}\} - \omega^2[\mathbf{B}]\{\boldsymbol{H}\} = 0 \tag{3.100}$$

where
$$[\mathbf{A}] = \sum_{e=1}^{n}[\mathrm{A}]_e = \sum_{e=1}^{n}\int_{\Delta} \varepsilon^{-1}[Q]^*[Q]\; d\Omega \tag{3.101}$$

$$[\mathbf{B}] = \sum_{e=1}^{n}[\mathrm{B}]_e = \sum_{e=1}^{n}\int_{\Delta} \mu[\mathrm{N}]^T[\mathrm{N}]\; d\Omega \tag{3.102}$$

Matrix $\{\boldsymbol{H}\}$ contains all the **H**-field nodal values over the whole cross section of the waveguide considered. $[\mathrm{A}]_e$ and $[\mathrm{B}]_e$ represent the element matrices. The assemblage of all the element matrices $[\mathrm{A}]_e$ and $[\mathrm{B}]_e$ over the whole cross section result in the so called global matrices of the eigenvalue equation, given by [**A**] and [**B**], respectively.

For the structure shown in Fig 3.10, the global matrix G_{pq} may be defined as

$$G = \begin{bmatrix} G_{11} & \cdot & \cdot & \cdot & G_{18} \\ \cdot & & & & \cdot \\ \cdot & & \cdot & & \cdot \\ \cdot & & & & \cdot \\ G_{81} & \cdot & \cdot & \cdot & G_{88} \end{bmatrix} \tag{3.103}$$

If P is the total number of nodal points of the structure, the order of the global matrix is PxP, which defines the size of the matrix when only one unknown field component is considered for each node. In our case which is a vector formulation, we have three unknowns per node and size of G matrix for 8 nodes is G = 24 x 24. The terms of the global matrix, G_{pq}, are the field contributions of two nodes, p and q according to the global numbering system. Each term of the global matrix G_{pq} consists of a local contribution from only one element, unless the nodes lie on a shared boundary. The terms of the global matrix, G_{11}, for the first node with respect to itself will be defined as

$$G_{11} = N_{11}^{A} \qquad 3.104$$

where N_{11}^{A} is the term for the element matrix for the element A. The terms of the global matrix for other nodes which do not lie on a shared boundary can be found in a similar manner: $G_{12} = N_{13}^{A}, G_{24} = N_{32}^{B}$ etc. When the nodes are on a shared boundary, then the contributions of each element are added to the node e.g.

$$G_{22} = N_{33}^{A} + N_{33}^{B} \qquad 3.105$$

3.8 Infinite Elements

In electromagnetic terms, the dielectric waveguide is an unbound structure. The electromagnetic field can therefore, in principle, extend over the whole of open space, the area of which is infinite. This may cause problems for waveguides in which the solution exits near the cut-off region. In the finite element method, the discretisation of the waveguide cross-section cannot extend to infinity. Several techniques have therefore been developed for modelling the infinite open space with a finite number of elements.

The most commonly adopted approach is to enclose the core of the waveguide in an artificial conducting boundary, chosen to be sufficiently distant from the core of the waveguide. The finite element method can then be applied to the core region. Although this approach is simple, it is an inefficient method of dealing with the problem as a large number of elements are required in order to give good results. It is still difficult to model cut-off situations accurately with this method.

The use of boundary elements was proposed by Yeh *et al.*, (1979) to model a wide range of optical waveguide structures. In the method, the field in the exterior region was assumed to decay with an exponential factor, an effect incorporated into the finite element matrix. The major disadvantage of the approach is that the decay factor has to be determined heuristically and hence iteratively. In this particular approach, the two co-ordinate systems did not conform and hence the fields used were not continuous.
A method of 'infinite elements' has been proposed and was used by Rahman and Davies (1984*b*) to include explicit field representation in all of the necessary transverse directions by incorporating rectangular strips as shown in Fig 3.10. An infinite element is a finite element that does indeed extend to infinity, extending the domain of the explicit field representation to infinity without increasing the matrix order.

The shape function for such an element should be chosen realistically and must be square integrable over an infinite element area. For such an infinite element extending to infinity in the x-direction, an exponential decay x may be assumed and the shape function can be written as

$$N(x, y) = f(y)\exp(-x/L) \qquad 3.106$$

where L is the decay length and $f(y)$ is the conventional shape function in the y-direction. Exponential decay functions can be assumed in a similar manner for decay in both the x and y directions.

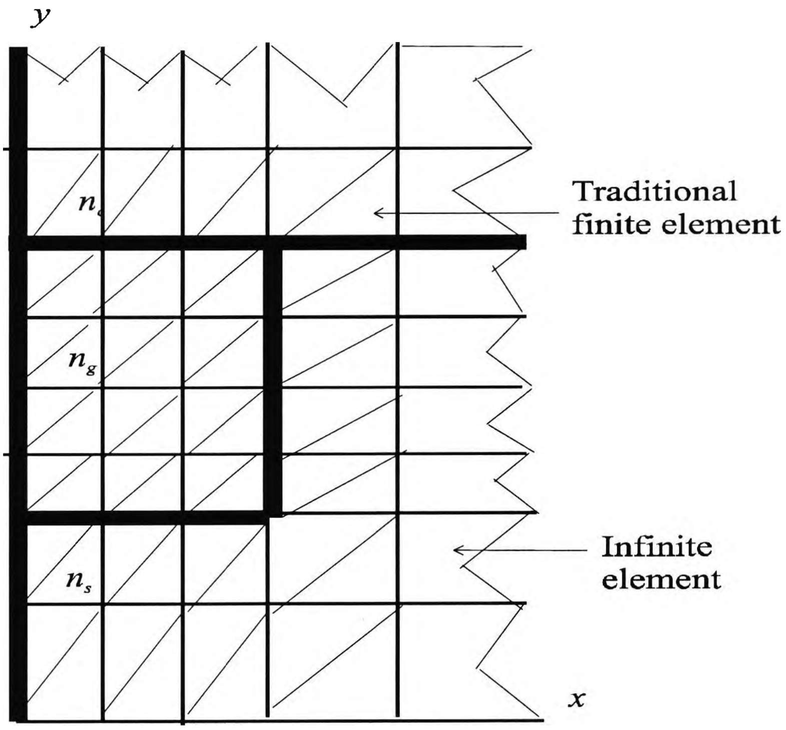

Fig 3.11 Showing the use of infinite elements at the guide boundary.

3.9 Spurious Solutions

The most serious and difficult problem in finite element analysis is the appearance of spurious, or non-physical solutions interspaced with real solutions. Analysis of the optical waveguide is also associated with spurious modes. Many reasons could lie behind the spurious modes, such as the enforcement of the boundary conditions, or due to the nonzero divergence of the trial fields (Rahman and Davies, 1984*a* and 1984*b*). The spurious solution appears also in the finite element analysis using the full vector ***H*** field. Maxwell's equations (3.8) and (3.9) do not satisfy the condition where $\nabla\cdot \boldsymbol{B} \neq 0$ which could be a one of the causes of spurious modes. In order to eliminate these spurious modes Rahman and Davies, (1984*c*) have utilized the penalty function which defines the solution if it is a real or spurious solution, and this can be achieved when the eigenvector of the physical mode satisfies the zero divergence condition $\nabla . \boldsymbol{H} = 0$. After each solution is obtained from the divergence condition, $\nabla . \boldsymbol{H}$ has to be calculated over the waveguide cross section. The value of $\nabla . \boldsymbol{H}$ has to be examined for different solutions, and only solution with a low value of $\nabla.\boldsymbol{H}$ will be considered as a real mode. The value of $\nabla.\boldsymbol{H}$ may be calculated from the discrete nodal field obtained after the solution of the eigenvalue equation, (3.52). Rahman and Davies (1984*c*), have used the penalty function approach, where an integral is added to the functional equation (3.53) in order to satisfy the zero divergence condition, $\nabla.\boldsymbol{H} = 0$. Thus the functional penalty term can be written as in section 3.6.2:

$$\omega^2 = \frac{\int (\nabla \times \boldsymbol{H})^* \cdot \hat{\varepsilon}^{-1} \cdot (\nabla \times \boldsymbol{H}) \; d\Omega + \left(\frac{\alpha}{\varepsilon_0}\right) \int (\nabla \cdot \boldsymbol{H})^* \cdot (\nabla \cdot \boldsymbol{H}) d\Omega}{\int \boldsymbol{H}^* \cdot \mu^{-1} \cdot \boldsymbol{H} \; d\Omega} \qquad 3.54$$

where α is the dimensionless penalty coefficient which can be estimated around $(1/\varepsilon_g)$, where ε_g is the relative permittivity of the waveguide core. It has been confirmed that the higher value of the penalty coefficient leads to a reduction of the spurious modes, but it is possible that propagation constant of the real mode can deteriorate slightly.

Various approaches have been proposed by different research groups in order to reduce the spurious solutions. Mabaya *et al.*, 1981 proposed an scalar finite element formulation, but spurious modes does not appear at all with a scalar formulation. One of the formulations, in terms of the transverse ***H***-field, has been advanced by Hayata *et al.* 1986, and completely eliminates the spurious solution, and the penalty coefficient is not included. The component fields $\boldsymbol{H}_x$ and $\boldsymbol{H}_y$ are represented in the way that the shape functions have been eliminated, but the $\boldsymbol{H}_z$ component involves a stage involving differentials and is more an approximation representation. Davies, 1993, has established a successful new scheme for avoiding the spurious modes. The first method involves a new formulation of the transverse magnetic field with no special new finite elements, while the second method uses equation (3.53) but with a new vector finite element application.

3.10 Matrix solution techniques in finite element method

The choice of the algorithm in solving the eigenvalue matrix equations is very important in computer power and time consumption in the use of the FEM. The global matrices [***A***] and [***B***] given in (3.101) and (3.102) are highly sparse. Both matrices can be complex and asymmetric and this can cause difficulty in solving the problem due to the lack of efficient computer library routines. There is a large number of different methods available to solve the matrix eigenvalue problems involving sparse matrices. In this work the spare matrix eigenvalue problem has been solved by an iteration process applied simultaneously to a subspace of eigenvectors, using the so-called method of subspace iterations (Rahman and Davies, 1984*a*) and (Bathe and Wilson, 1976)

3.11 Summary

In this chapter the finite element method and its application has been presented. The varational principles in the modal solutions for microwave and optical waveguides have been studied. Various aspects of the finite element method have been examined, including, different scalar and vector formulations, boundary conditions, natural boundary conditions, shape functions, global matrices and infinite elements. Finally the use of the penalty term approach to reduce the non-physical solutions or spurious mode has been discussed. This chapter, in conjunction with the least squares boundary residual method presented in Chapter 5, section 5.2 and full-vector beam propagation method in Chapters 6 and 7, represents a solid mathematical basis for the work involved in the analysis of optical waveguide and microwave problems in the subsequent chapters of this thesis.

Chapter 4

The Beam Propagation Method

4.1 Introduction

The previous chapter gives a general analysis of the finite element method as having the capability to design and characterise numerous varieties of optoelectronic devices in their stationary 2-D state or in a situation in which the device is considered to be invariant in the longitudinal direction. In integrated optics, there has been enormous progress in the research and development of OEICs to the extent that it is important to have a design tool that would be able to explore these devices beyond the realms of the 2-D state. Chapter 3 has shown the formulation for the vector **H**-field finite element method as a versatile and powerful tool in the solving the optical waveguide problems. However, there are numerous occasions when it is required to study the propagation of electromagnetic waves in z-variant structures. The vector **H**-field finite element formulation for the modal solutions is not capable of simulating the propagation and interaction of light with media in the longitudinally non-uniform devices such as guided-wave structures like bends, tapers, and junctions. Optoelectronic researchers have developed numerous methods to tackle this problem and one of these is the versatile, robust and efficient Beam Propagation Method

(BPM). This chapter is dedicated to the general analysis of BPM and its usefulness in waveguides. The applications of the BPM as a waveguide explorer is used in chapters 6 and 7 to analyse taper structures. The BPM analysis involves a source of light, usually single moded, launched on one side of a taper as the input and the entire length of the device which is divided into small steps and the output plane which is butt-coupled to a single mode fibre. This work is focused mainly on waveguide taper structures, and the electromagnetic field inside the taper at each step can be calculated if the input field is known and the boundary conditions are well defined. The single moded input field usually obtained from the modal solution of the finite element method is launched into the taper and the evolutionary field calculated at every step to the end of the taper which forms the output.

Feit and Fleck, in 1978, first introduced BPM to study the mode properties of optical fibres. Since then other notable researchers such as Soref, *et al.* (1991), Tsuji, *et al.* (1997) on rib waveguides, Montanari, *et al.* (1998), Lu, *et al.* (1998) on Y-junctions, Anwar, *et al.* (2002), on MZI modulators, Rahman, *et al.* (2005) on semiconductors amplifiers, Obayya, *et al.* (2000), on directional couplers, Park, *et al.* (2001) on mode adapters, to name a few who have thrown more light on the applications and usefulness of the efficient and robust beam propagation method both in the academic circle and industry alike.

4.2 Beam Propagation Algorithms

In order to find solutions to the propagation and interaction of light with inhomogeneous media in the longitudinal direction of optoelectronic devices, researchers embarked on many numerical methods for the analysis and simulations of guided-wave propagation in these devices. The BPM can be based on numerical methods, which can be broadly classified into three types which are:-

- Fast Fourier Transform-based method
- Finite Difference-based method
- Finite Element-based method

4.2.1 Fast Fourier Transform Beam Propagation Method

In this method, the starting point is the Helmholtz equation in which the paraxial form is also known as the Fresnel equation (see section 4.3). This equation is valid for the paraxial propagation in slowly varying optical structures. The solution of this equation normally characterised by the refractive index n, is assumed to be a set of plane waves, which can be represented by a superposition of such plane waves. The algorithm for calculating the field at an arbitrary plane perpendicular to the z axis is given by

$$E(x,y,z) = F^{-1}\{F[E(x,y,0)]\exp(-jk_z z)\}$$

where F^{-1} is the inverse Fourier Transform and F is the Fourier Transform operator. The effect of the index variation n(x,y,z) when the wave travels a distance Δz is a small perturbation of the phase of the distribution of the phase front. The BPM algorithm for the propagation along an arbitrary distance z is achieved through several discrete steps of distance Δz. The implementation of Fast Fourier transformation enables the calculation to be reduced to $N^2\log_2 N$ from N^3 where N is the number of discrete grid mesh points. The advantages are:

(1) It can be applied to structures with arbitrary cross-section.

(2) The guided and radiation waves are taken into consideration in the analysis.

The disadvantages of this method are:

(1) That the input optical field does not correspond exactly to the guided mode profile.

(2) It cannot be applied to structures with large refractive index discontinuities because of the assumption that the refractive index difference is very small so that the phase error term can be expressed by the first term in the Taylor's series.

(3) This method is numerically not very stable.

(4) Noise is produced in the field profile.

(5) The paraxial approximation has been made under the assumption that the beam propagates in the longitudinal direction with a small angle to the axis therefore, wide angle propagation is not valid for this model.

The above problems with FFT-BPM have led researchers to develop more superior methods which will be discussed in the following sections.

4.2.2 Finite Difference Beam Propagation Method

Following the faults attributed to the FFT-BPM, the finite difference schemes have been developed for the beam propagation method. The Finite Difference algorithm are easy to derive and implement starting as usual with the paraxial helmholtz equation. There are three types of finite difference schemes viz:

(1) The Forward-difference scheme which is also known as “explicit scheme”.

(2) The Backward-difference scheme also known as “implicit scheme”.

(3) The Central-difference scheme popularly known as Crank-Nicolson Scheme.

4.2.2.1 The Forward Difference Scheme

The Forward-difference scheme is a scheme which allows the calculation of the optical field $\Phi_j(z + \Delta z)$ after a propagation step Δz from a knowledge of the complete field $\Phi_j(z)$ at the position z. This method based on the direct solution, is accurate to the first order and conditionally stable. The stability condition (Lifante, 2003) is given by:

$$\Delta z \leq \Delta x^2/2\ell = \Delta x^2 n\pi/\lambda \tag{4.1}$$

But Δz will have a small value in order to give assurance of stability and large value of Δz cannot be accommodated from practical point of view. In other words there is lack of stability as step size is increased. There are numerical losses experienced during propagation whenever this scheme is employed.

4.2.2.2 The Backward Difference Scheme

The Backward-difference scheme is a scheme developed to overcome the large Δz unstable problem. It is similar to the forward-difference scheme both in implementation and method of solution but it has the advantage of being unconditionally stable.

4.2.2.3 The Crank-Nicolson Scheme

The Crank-Nicolson Scheme is also known as the Central-difference scheme. It is a linear combination of the forward and backward schemes but this algorithm matches the solution of the entire differential equation at $z + \Delta z/2$. It can be written as:

$$[2K + i\Delta z \alpha H]\Phi(z+\Delta z) = [2K - i\Delta z(1-\alpha)H]\Phi(z) \qquad 4.2$$

where α is a weighting factor and K is the propagation wavevector defined as:

$$K = n_0\omega/c, \qquad 4.3$$

and the operator H is defined as:

$$H\Phi \equiv \frac{\Phi_{j-1} - 2\Phi_j + \Phi_{j+1}}{\Delta x^2} + (n_j^2 - n_0^2)k_0^2\Phi_j \qquad 4.4$$

where n_j is the refractive index in the domain of interest for grid point j = 1,2,3,….N, n_0 is refractive index for the substrate, ω is the angular frequency, k_0 is the wavenumber. The disadvantage of this scheme is that a system of N linear equations has to be solved to obtain the solution of $\Phi(z + \Delta z)$ of the paraxial Helmholtz equation when compared to the Forward-difference algorithm. The computational time increases as N increases although this is better than the FFT-BPM where N increases as $N\log_2 N$ waveguides. However it has the following advantages:

(1) It is unconditionally stable for any propagation step size especially for $\theta > 0.5$, where θ is the angle of propagation of the light with respect to the z-axis.

(2) It provides better approximations to the exact solutions of the problem with a second-order approximation in the propagation step $O(\Delta z^2 + \Delta x^2)$.

(3) It does not produce numerical losses during propagation.

(4) It is able to manage structures with large discontinuities in the refractive index adequately.

(5) It can make use of PML layer for unwanted radiations.

(6) It can also accommodate the wide-angle propagation and full vector algorithms.

4.2.3 The Finite Element Beam Propagation Method

The finite element (FE) algorithm uses the paraxial Helmholtz equation as the Euler-Lagrange equation of a z-transient variational principle and treats the variational principle by a finite element procedure. This is the algorithm used in this thesis where the beam propagation method is employed. There is a window of operation in the xy-plane of the transverse coordinates. The Euler-Lagrange equation can be used to obtain the scalar formulation for the paraxial helmholtz equation for the TE and TM polarisations initially. The FE procedure is applied to the domain of interest and the area is discretized into triangular meshes and planar solutions are obtained inside each mesh. The Garlerkin procedure (Zienkiewicz, 1977; Desai, 1979; Silvester and Ferrari, 1990) is executed with the FE expansion and the optical fields at the nodes depends on the propagation coordinate z. The Crank-Nicolson method is employed to solve the system of differential equations which describe the evolution of the optical field at the nodes in the longitudinal direction. Most of the scalar wave formulations are inadequate when it comes to analysis of polarisation and coupling properties of strongly guiding optical devices based on semiconductor materials. The vectorial FE algorithm used in this work can solve for the three magnetic field components and it incorporates the Pade approximation (Hadley, 1992) for wide angle which replaces the inaccurate paraxial approximation. It can accounts for the light beam propagating off the propagation axis. It also makes use of PML layer for unwanted radiations. The vectorial FE algorithm can do all the FD-BPM algorithm can do and also has the following advantages over the FD approach:

- The FE discretisation of the devices domain is superior to that of the FD scheme when it comes to non-uniform discretisation.
- It enables very good approximation of complex geometrical boundaries.
- It has got flexibility in imposing boundary conditions.

4.3 Paraxial Approximation

The propagation of light in waveguides generally is based on the paraxial form of the Helmholtz equation otherwise known as the Fresnel equation. In cases where the direction of propagation is well defined, then a simple approximation is appropriate and Helmholtz equation could be written as follows for a steady state or time harmonic case

$$\frac{\partial^2\Phi}{\partial x^2}+\frac{\partial^2\Phi}{\partial y^2}+\frac{\partial^2\Phi}{\partial z^2}+\omega^2\mu_o\varepsilon\Phi=0 \qquad 4.5$$

where Φ is for the electromagnetic field, in the case of TE polarisation this will be E_x mode and ω is the angular frequency. From above

$$\omega^2\mu_o\varepsilon\Phi=k_o^2n^2(x,y,z)\Phi \qquad 4.6$$

where $n^2(x,y,z)$ is the refractive index profile in the guide. The electromagnetic field can be written as follows

$$\Phi(x,y,z)=\Phi(x,y,z)e^{-j\beta z} \qquad 4.7$$

where β is the phase constant or the reference value of the wavenumber. If the following two assumptions are now made

1 That the field inside the guide structure can be represented by a field with narrow angular spectrum
2 That the waveguide structure has a definitely marked longitudinal direction (z) and the propagation occurs mainly that direction

then the paraxial or slowly varying amplitude approximation can be made. If the value of β is now chosen such that it forms a central estimate of the value in the spectrum, then the variation of the fields with z will be dictated primarily by the exponential factor in equation (4.7). The term $\Phi(x,y,z)$, will only vary slowly with the axial co-ordinate z. Substituting for the field in the governing differential equation (4.5) and omitting the exponent (as it is a common factor), the following equation is obtained

$$\frac{\partial^2\Phi}{\partial x^2}+\frac{\partial^2\Phi}{\partial y^2}+\frac{\partial^2\Phi}{\partial z^2}-j2\beta\frac{\partial\Phi}{\partial z}-\beta^2\Phi+k_o^2n^2\Phi=0 \qquad 4.8$$

since $\Phi(x,y,z)$ varies slowly in the axial direction, the second order z derivative can be ignored to give the following paraxial equation with $\beta^2=k_o^2n_o^2$

$$\frac{\partial^2\Phi}{\partial x^2}+\frac{\partial^2\Phi}{\partial y^2}-j2k_on_o\frac{\partial\Phi}{\partial z}+k_o^2\left(n^2-n_o^2\right)\Phi=0 \qquad 4.9$$

It will be shown in section 4.6 that waves that propagate with narrow angular spectrum to the propagating axis can have a better approximation by using the Pade approach (Hadley, 1992), which is generally known as Pade wide angle approximation.

4.4 BPM Boundary Conditions

It is well known that the computational domain in BPM is finite therefore the boundary condition for the optical field needs to be specified. This makes the application of the boundary conditions one of the most important features of all the BPM algorithms. This section introduces the absorption and transparent boundary conditions and then give details of the perfectly matched layer which is the BPM boundary condition algorithm used in this work.

4.4.1 Absorption Boundary Condition (ABC)

The boundary condition should be well chosen in such a way that their effects will not have adverse effects on the optical field. These adverse effects can be that the radiation tends to reflect on the limits of the computational window and bounce back to region of interest to cause unnecessary interference when the propagation is done by FD-BPM.

For FFT-BPM the propagation field disappear through a boundary and a new prop-field appear from the opposite boundary of the window. This can be prevented by making the window very wide that when the field gets to the window limits, it is negligible. Boundary reflection can be prevented when using FFT by introducing artificial absorption regions adjacent to the boundaries in question (Feit and Fleck, 1978 and 1980; Lagasse and Baets; 1987). For the method to work well, the dimension of the waveguide, the shape functions and the absorption coefficient must be carefully chosen. This makes the absorption boundary condition geometry dependent which has to be fulfilled for each new problem if the device itself is extended which is a major disadvantage.

4.4.2 Transparent Boundary Condition (TBC)

When using FD-BPM, the optical field at the end points j=0 and j=N+1 are not defined. To have a complete and correct optical field, two extra equations are needed to determine these points. The Newman and Dirichlet boundary conditions can be supplied to solve the problem but none of the boundary conditions give adequate results since their application causes optical field 'reflections' at the window limits because the condition of zero field at the boundaries is not realistic when the propagation sets to the limits of the computational window. The idea of transparent boundary condition (TBC) is to approximate the wave near the boundary of the computational domain as a plane wave.

The algorithm of the transparent boundary condition is introduced to solve the problem of absorption boundary condition (Hadley, 1991 and 1992). In this scheme, the wave is approximated as a plane wave near the boundary of the computational domain which satisfies

$$\frac{\partial \Phi}{\partial x} = -jk\Phi \qquad 4.10$$

where Φ is the field near the boundary, k is the wavevector (computed from field values inside the domain or set as a positive value), and x is the distance in the direction normal to the boundary, i.e. a realistic boundary condition allows the light wave to leave the domain region when it gets to the windows limits and is prevented from bouncing back to the domain. In other words, there is implementation of a virtual boundary from physical point of views where unwanted radiation escapes out of the region and no reflection is experienced. The transparent boundary condition does not depend on the waveguide parameter and therefore problem independent and can be directly applied to arbitrary waveguide structure. Moreover it can be adapted into Crank Nicholson Scheme for both 2- and 3- dimensions. The transparent boundary condition is more accurate and efficient than the absorption boundary condition. The draw back on this scheme is that the plane wave approximation of the outgoing wave near the boundary is not adequate to suppress large radiations, moreover many field values inside the computational domain should be involved in estimating *k*, otherwise some numerical instabilities can be observed (Vassallo and Van de Keur, 1997; Vassallo and Collino, 1996).

4.4.3 The Perfectly Matched Layer (PML)

It was in 1994 that Berenger introduced the concept of the Perfectly Matched Layer (PML) (to replace the absorbing or transparent boundary conditions) with the aim to synthesise an artificial absorbing layer for the Finite Difference Time Domain (FDTD) method. The PML concept has been successfully applied in one-dimensional FD-BPM (Huang *et al.*, 1996) and it has been shown to be more robust than the transparent boundary condition since the latter cannot account for waves propagating with wide angle. But Berenger's original form of PML needs the splitting of the field components into two subcomponents which leads to non-Maxwell's equations which is not the desired form for the application of finite elements. Since then there has been some other BPM algorithms based on finite difference method which are either scalar, semi-vectorial or full-vectorial, but they are not sufficient for simulating nonuniform optical waveguides because it is inefficient in the discretisation of nonuniform mesh of waveguide cross-section and for curved boundaries, they present very crude approximation. There are some BPM algorithms with PML which keeps the form of Maxwell's equations that are based on finite element method (Obayya, 2000; Pekel and Mittra, 1995a and 1995b), can simulate complex and nonuniform structures but are formulated on the less accurate scalar wave equation and therefore cannot handle the 3-D optical waveguides with hybrid fields. The perfectly matched layer boundary condition which is incorporated into the full-vectorial FE-BPM formulations will be used in throughout this thesis.

The implementation of the PML in this work, can be demonstrated by the waveguide cross-section shown in Fig. 4.1, where *x* and *y* are the transverse directions, *z* is the longitudinal direction of propagation, regions Ω_1 and Ω_2 are the PML regions normally faced with x and y directions, respectively, regions Ω_3 corresponds to the four corners of the PML, Ω corresponds to the computational domain region, W is the width (or height) of the PML, and L_x and L_y are the width and height of the computational domain in the x and the y directions, respectively.

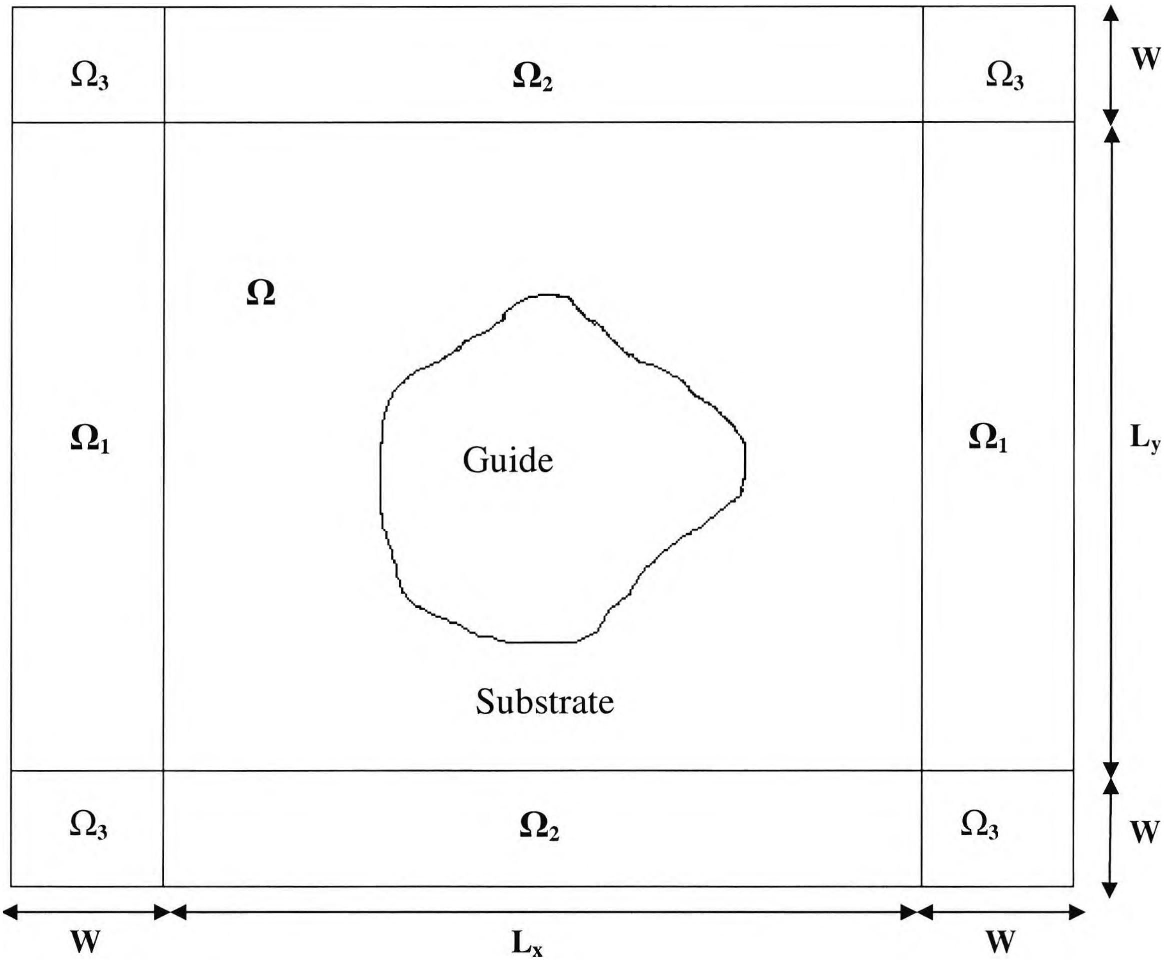

Fig. 4.1 PML sections with the optical waveguide cross-sections

The starting point of the of PML formulations, is the Maxwell's curl equations which can take the form

$$\nabla^1 \times H = j\omega\varepsilon_0 n^2 E \qquad 4.11$$

$$\nabla^1 \times E = -j\omega\mu_0 H \qquad 4.12$$

where $\boldsymbol{E}$ and $\boldsymbol{H}$ are the electric and magnetic field vectors, n^2 is the square of the refractive index, and ∇^l is the modified differential operator defined as

$$\nabla^1 = \hat{x}\alpha_x \frac{\partial}{\partial x} + \hat{y}\alpha_y \frac{\partial}{\partial y} + \hat{z}\frac{\partial}{\partial z} \tag{4.13}$$

where

$$\alpha_t(t = x, y) = \frac{1}{1 - j\dfrac{\sigma_e}{\omega\varepsilon_0 n^2}} = \frac{1}{1 - j\dfrac{\sigma_m}{\omega\mu_0}} \tag{4.14}$$

with σ_e and σ_m are the electric and magnetic conductivities of the PML, respectively. Relation (4.10) shows that the PML satisfies the impedance matching condition with an index n and wave impedance $\sqrt{\dfrac{\mu_0}{\varepsilon_0 n^2}}$.

The values of the parameters α_x and α_y are defined in the different regions as follows:

(1) Inside the computational domain, both α_x and α_y are set to unity.

(2) The regions in the transverse x-direction, $\alpha_x = \alpha_t$ and $\alpha_y = 1$.

(3) The regions in the transverse y-direction, $\alpha_x = 1$ and $\alpha_y = \alpha_t$.

(4) For regions in the four corners, both α_x and α_y are set to α_t.

In the PML regions, the electric conductivity is given by

$$\sigma_e(\rho) = \sigma_{\max}\left(\frac{\rho}{W}\right)^m \tag{4.15}$$

where ρ is the distance inside the PML, measured from the interface of the computational domain and the PML, $\sigma_{\max}$ is the maximum value of the electric conductivity, and m is the power of the conductivity profile and in this work, it will be taken as 2. For this conductivity profile, the theoretical reflection coefficient, R, at the interface between the PML and the computational domain is (Berenger, 1994),

$$R = \exp\left[-2\frac{\sigma_{\max}}{cn\varepsilon_0}\int_0^W\left(\frac{\rho}{W}\right)^2 d\rho\right] \qquad 4.16$$

where c is the velocity of light in free space. Performing the integration involved in (4.16), $\sigma_{\max}$ can be expressed as

$$\sigma_{\max} = \frac{3cn\varepsilon_0}{2d}\ell n\left(\frac{1}{R}\right) \qquad 4.17$$

Once the value of the theoretical coefficient is chosen, R (set to very small value), the maximum electric conductivity, $\sigma_{\max}$, is calculated using relation (4.17). Hence the electric conductivity profile $\sigma(\rho)$ and the PML parameters α_x and α_y will be determined for the different PML regions. With these arrangements of the PML in different regions, and nonphysical radiation wave will freely lave the computational domain whatever the angle and/or the strength it hits the boundary of the computational domain.

4.5 Vectorial Wave Equations

The starting point of deriving the vectorial wave equations are the Maxwell's curl equations (4.11) and (4.12). Taking the curl of equation (4.11) and using equation (4.12) gives

$$\nabla^1 \times (n^{-2}\nabla^1 \times H) - k_0^2 H = 0 \qquad 4.18$$

where k_0 is the free space wavenumber and is given by

$$k_0 = \omega\sqrt{\mu_0\varepsilon_0} = \frac{2\pi}{\lambda} \qquad 4.19$$

with λ is the free space wavelength.

Equation (4.18) is the full vectorial wave equation, i.e., it contains the three components of the magnetic field vector, ***H*****.** This wave equation can reduce to only the two transverse components, H_x and H_y, via the use of the zero divergence condition,

$$\alpha_x \frac{\partial H_x}{\partial x} + \alpha_y \frac{\partial H_y}{\partial y} + \frac{\partial H_z}{\partial z} = 0 \qquad 4.20$$

Substituting (4.20) into (4.18) results in the following two coupled wave equations

$$\frac{\partial}{\partial z}\left(n^{-2} \frac{\partial H_x}{\partial z} \right) + \alpha_y \frac{\partial}{\partial y}\left(n^{-2} \alpha_y \frac{\partial H_x}{\partial y} \right) + n^{-2} \alpha_x \frac{\partial}{\partial x}\left(\alpha_x \frac{\partial H_x}{\partial x} \right) + k_0^2 H_x +$$

$$+ n^{-2} \alpha_x \frac{\partial}{\partial x}\left(\alpha_y \frac{\partial H_y}{\partial y} \right) - \alpha_y \frac{\partial}{\partial y}\left(n^{-2} \alpha_x \frac{\partial H_y}{\partial x} \right) = 0 \qquad 4.21a$$

$$\frac{\partial}{\partial z}\left(n^{-2} \frac{\partial H_y}{\partial z} \right) + \alpha_x \frac{\partial}{\partial x}\left(n^{-2} \alpha_x \frac{\partial H_y}{\partial x} \right) + n^{-2} \alpha_y \frac{\partial}{\partial y}\left(\alpha_y \frac{\partial H_y}{\partial y} \right) + k_0^2 H_y +$$

$$+ n^{-2} \alpha_y \frac{\partial}{\partial y}\left(\alpha_x \frac{\partial H_x}{\partial x} \right) - \alpha_x \frac{\partial}{\partial x}\left(n^{-2} \alpha_y \frac{\partial H_x}{\partial y} \right) = 0 \qquad 4.21b$$

In deriving the wave equations (4.21) the assumption that the refractive index is slowly varying in the direction of propagation, $\left(\partial n^{-2} / \partial z \right) = 0$, has been made. Solving equations (4.21) is easier than eqn.(4.18), not only because it has a less number of unknown components, but also because the zero divergence condition is automatically satisfied through the derivation, and hence, there is no possibility for spurious solutions to propagate.

By assuming the wave travels along the +*z* direction, the fields can be separated as slowly-varying envelopes and a fast-oscillating phase term as

$$\begin{Bmatrix} H_x \\ H_y \end{Bmatrix} = \begin{Bmatrix} \psi_x \\ \psi_y \end{Bmatrix} \exp\,(-jn_0k_0z) \qquad 4.22$$

where n_0 is a reference index of refraction, and ψ_x and ψ_y are the slowly-varying envelopes of the H_x and H_y components, respectively. The reference index of the refraction, n_0, should be chosen such that the envelope varies very slowly in the +*z* direction. For this purpose, n_0 should be chosen very close for the effective index of the guided mode(s) of the concerned structure. For monomode waveguides, n_0 can be set equal to the effective index of the fundamental mode. But, for multimode waveguides the situation will be complicated as the effective indices of all guided modes have to be determined in order to set n_0 to the proper value. In this case, a better approximate is to set n_0 as the average of the guide and substrate refractive indices.

Substituting from eqn. (4.22) into eqns. (4.21) results in the following two coupled unidirectional wave equations

$$n^{-2}\frac{\partial^2\psi_x}{\partial z^2} - 2jn_0k_0n^{-2}\frac{\partial\psi_x}{\partial z} + \alpha_y\frac{\partial}{\partial y}\left(n^{-2}\alpha_y\frac{\partial\psi_x}{\partial y}\right) + n^{-2}\alpha_x\frac{\partial}{\partial x}\left(\alpha_x\frac{\partial\psi_x}{\partial x}\right) +$$

$$+ k_0^2(1-n^{-2}n_0^2)\psi_x + n^{-2}\alpha_x\frac{\partial}{\partial x}\left(\alpha_y\frac{\partial\psi_y}{\partial y}\right) - \alpha_y\frac{\partial}{\partial y}\left(n^{-2}\alpha_x\frac{\partial\psi_y}{\partial x}\right) = 0 \qquad 4.23a$$

$$n^{-2}\frac{\partial^2\psi_y}{\partial z^2} - 2jn_ok_on^{-2}\frac{\partial\psi_y}{\partial z} + \alpha_x\frac{\partial}{\partial x}\left(n^{-2}\alpha_x\frac{\partial\psi_y}{\partial x}\right) + n^{-2}\alpha_y\frac{\partial}{\partial y}\left(\alpha_y\frac{\partial\psi_y}{\partial y}\right) +$$

$$+k_0^2(1-n^{-2}n_0^2)\psi_y+n^{-2}\alpha_y\frac{\partial}{\partial y}\left(\alpha_x\frac{\partial\psi_x}{\partial x}\right)-\alpha_x\frac{\partial}{\partial x}\left(n^{-2}\alpha_y\frac{\partial\psi_x}{\partial y}\right)=0 \qquad 4.23b$$

Equations (4.19) will be solved for the slowly-varying envelope by the application of the finite element method in the following section.

4.6 Finite Elements Formulations For BPM

In this section, finite element algorithm is formulated for the BPM with the incorporation of the Pade wide-angle approximation, using the PML boundary conditions discussed in the section 4.4.3. Fig. 4.1 shows an arbitrary waveguide cross-section which is assumed discretised into a patchwork of first order triangular elements. Application of the standard Galerkin's procedure into equations (4.23), lead to

$$\int_e n^{-2}\frac{\partial^2\psi_x}{\partial z^2}N_i ds-\int_e 2jn_0k_0n^{-2}\frac{\partial\psi_x}{\partial z}N_i ds+\int_e\alpha_y^2\frac{\partial}{\partial y}\left(n^{-2}\frac{\partial\psi_x}{\partial y}\right)N_i ds+$$

$$+\int_e\alpha_x^2n^{-2}\frac{\partial^2\psi_x}{\partial x^2}N_i ds+\int_e k_0^2\left(1-n^{-2}n_0^2\right)\psi_x N_i ds+\int_e\alpha_x\alpha_y n^{-2}\frac{\partial^{-2}\psi_y}{\partial x\partial y}N_i ds-$$

$$-\int_e\alpha_x\alpha_y\frac{\partial}{\partial y}\left(n^{-2}\frac{\partial\psi_y}{\partial x}\right)N_i ds=0 \qquad 4.24a$$

$$\int_e n^{-2}\frac{\partial^2\psi_y}{dz^2}N_i ds-\int_e 2jn_0k_0n^{-2}\frac{\partial\psi_y}{\partial z}N_i ds+\int_e\alpha_x^2\frac{\partial}{\partial x}\left(n^{-2}\frac{\partial\psi_y}{\partial x}\right)N_i ds+$$

$$+\int_e\alpha_y^2n^{-2}\frac{\partial^2\psi_y}{\partial y^2}N_i ds+\int_e k_0^2\left(1-n^{-2}n_0^2\right)\psi_x N_i ds+\int_e\alpha_x\alpha_y n^{-2}\frac{\partial^2\psi_x}{\partial x\partial y}N_i ds-$$

$$-\int_e\alpha_x\alpha_y\frac{\partial}{\partial x}\left(n^{-2}\frac{\partial\psi_x}{\partial y}\right)N_i ds=0 \qquad 4.24b$$

where N_i are the shape functions with i=1,2,3,... over the first order triangular element, e, and $\int_e (.)\, ds$ stands for the integration over the element area. The properties of these first order shape functions, N_i, have been studied in details in the last chapter. In writing eqns. (4.24), it has been assumed that refractive index, n, and the PML parameters, α_x and α_y are fixed to constant values within each element. Hence, for the step index waveguides, the discontinuity of the refractive index and the associated interface boundary conditions will not be accounted for. But, using Green's theorem for integration by parts will result in line integrations, around each element, which can be utilized to satisfy the following interface boundary conditions

1) Continuity of E_z, and $E_t \propto n^{-2}\left(\frac{\partial \psi_y}{\partial x} - \frac{\partial \psi_x}{\partial y}\right)$

2) Discontinuity of $n^{-2}\frac{\partial \psi_x}{\partial x}$ and $n^{-2}\frac{\partial \psi_y}{\partial y}$ along the horizontal and vertical interfaces between two different media.

The application of Green's theorem for integration by parts to equations (4.24) and taking the above interface boundary conditions into consideration leads to

$$\int_e n^{-2}\frac{\partial^2 \psi_x}{\partial z^2}N_i ds - 2jn_0k_0\int_e n^{-2}\frac{\partial \psi_x}{\partial z}N_i ds - \int_e \alpha_y^2 n^{-2}\frac{\partial \psi_x}{\partial y}\frac{\partial N_i}{\partial y}ds - \int_e \alpha_x^2 n^{-2}\frac{\partial \psi_x}{\partial x}\frac{\partial N_i}{\partial x}ds +$$

$$\oint_{r_e} \alpha_x^2 n^{-2}\frac{\partial \psi_x}{\partial x}N_i n_x d\Gamma_e + \int_e k_0^2\left(1 - n^{-2}n_0^2\right)\psi_x N_i ds - \int_e \alpha_x\alpha_y n^{-2}\frac{\partial \psi_y}{\partial y}\frac{\partial N_i}{\partial x}ds +$$

$$\oint_{r_e} \alpha_x\alpha_y n^{-2}\frac{\partial \psi_y}{\partial y}N_i n_x d\Gamma_e + \int_e \alpha_x\alpha_y n^{-2}\frac{\partial \psi_y}{\partial x}\frac{\partial N_i}{\partial y}ds = 0 \qquad 4.25a$$

$$\int_e n^{-2}\frac{\partial^2 \psi_y}{\partial z}N_i ds - 2jn_0k_0\int_e n^{-2}\frac{\partial \psi_y}{\partial z}N_i ds - \int_e \alpha_x^2 N^{-2}\frac{\partial \psi_Y}{\partial x}\frac{\partial n_I}{\partial}ds - \int_e \alpha_y^2 n^{-2}\frac{\partial \psi_y}{\partial y}\frac{\partial N_i}{\partial y}ds +$$

$$\oint_{r_e} \alpha_y^2 n^{-2} \frac{\partial \psi_y}{\partial y} N_i n_y d\Gamma_e + \int_e k_0^2 \left(1 - n^{-2} n_0^2\right) \psi_y N_i da + \int_e \alpha_x \alpha_y n^{-2} \frac{\partial \psi_x}{\partial y} \frac{\partial N_i}{\partial x} ds +$$

$$\int_{r_e} \alpha_x \alpha_y n^{-2} \frac{\partial \psi_x}{\partial x} N_i n_y d\Gamma_e - \int_e \alpha_x \alpha_y n^{-2} \frac{\partial \psi_x}{\partial x} \frac{\partial N_i}{\partial y} ds = 0 \qquad 4.25b$$

where n_x and n_y are the direction cosines between the normal to the element boundary Γ_e and the x and y directions, respectively, and $\oint_{r_e} (.) d\Gamma_e$ denotes line integration around the element boundary, Γ_e. The line integrals involved in eqns (4.25), which are introduced to account for the interface boundary conditions, are so responsible for the polarization dependence and coupling. Hence, the inclusion of these integrals into the formulation is mandatory in order to get a true vectorial formulation. Over each element, e, and in terms of the shape functions, N_j, the transverse magnetic field envelopes can be expressed as

$$\psi_x^e(x, y, z) = \sum_{j=1}^{3} h_{xj}(z) N_j(x, y) \qquad 4.26a$$

$$\psi_y^e(x, y, z) = \sum_{j=1}^{3} h_{yj}(z) N_j(x, y) \qquad 4.26b$$

where $h_{xy}(z)$ and $h_{yj}(z)$ represent the element nodal values of the x- and y-components of the magnetic field, respectively, at any propagation distance. Subsituting from eqns. (4.26) into eqns. (4.25) and collecting the contributions from all elements results in

$$[\mathrm{M}] \frac{d^2\{h_t\}}{dz^2} - 2 j n_0 k_0 [\mathrm{M}] \frac{d\{h_t\}}{dz} + \left([\mathrm{K}] - n_0^2 k_0^2 [\mathrm{M}]\right)\{h_t\} = \{0\} \qquad 4.27$$

where $\{\mathbf{0}\}$ is a column vector with all zero entries, and

$$\{h_t\} = \begin{Bmatrix} h_x(z) \\ h_y(z) \end{Bmatrix} = \sum_e \begin{Bmatrix} h_{x1} \\ h_{x2} \\ h_{x3} \\ h_{y1} \\ h_{y2} \\ h_{y3} \end{Bmatrix} \qquad 4.28$$

with $h_x(z)$ and $h_y(z)$represent the nodal values of the *x*- and *y*- components of the magnetic field over the whole domain. The global matrices [**M**] and [**K**] can be expressed as a summation of the corresponding elements matrices as

$$[\mathrm{M}] = \sum_e [\mathrm{M}]_e = \sum_e \begin{bmatrix} [M_{xx}] & 0 \\ [0] & [M_{yy}] \end{bmatrix} \qquad 4.29$$

$$[\mathrm{K}] = \sum_e [\mathrm{K}]_e = \sum_e \begin{bmatrix} [K_{xx}] & [K_{xy}] \\ [K_{xy}] & [K_{yy}] \end{bmatrix} \qquad 4.30$$

where [0] is a 3x3 zero value matrix, and $\sum_e$ stands for the contributions of all elements matrices $[\mathrm{M}]_e$ and $[\mathrm{K}]_e$ into the global ones. The matrices $[\mathrm{M}_{xx}]$ and $[\mathrm{M}]_{yy}$ have the same form as

$$[\mathrm{M}_{xx}] = [\mathrm{M}_{yy}] = n^{-2} \begin{bmatrix} \int_e N_1^2 ds & \int_e N_1 N_2 ds & \int_e N_1 N_3 ds \\ \int_e N_2 N_1 ds & \int_e N_2^2 ds & \int_e N_2 N_3 ds \\ \int_e N_3 N_1 ds & \int_e N_3 N_2 ds & \int_e N_3^2 ds \end{bmatrix} \qquad 4.31$$

The matrices $[K_{xx}]$ and $[K_{yy}]$ can be arranged in the form

$$[K_{xx}] = [K_0] + [K_{xx}]_{r_e} \qquad 4.32$$

$$[K_{yy}] = [K_0] + [K_{yy}]_{r_e} \qquad 4.33$$

where

$$[K_0]=k_0^2\begin{bmatrix}\int_e N_1^2 ds & \int_e N_1N_2 ds & \int_e N_1N_3 ds\\ \int_e N_2N_1 ds & \int_e N_2^2 ds & \int_e N_2N_3 ds\\ \int_e N_3N_1 ds & \int_e N_3N_2 & \int_e N_3^2 ds\end{bmatrix}-n^{-2}\alpha_y^2\begin{bmatrix}\int_e N_{1y}^2 ds & \int_e N_{1y}N_{2y} ds & \int_3 N_{1y}N_{3y} ds\\ \int_e N_{2y}N_{1y} ds & \int_e N_{2y}^2 ds & \int_e N_{2y}N_{3y} ds\\ \int_e N_{3y}N_{1y} ds & \int_e N_{3y}N_{2y} ds & \int_e N_{3y}^2 ds\end{bmatrix}$$

$$-n^{-2}\alpha_x^2\begin{bmatrix}\int_e N_{1x}^2 ds & \int_e N_{1x}N_{2x} ds & \int_3 N_{1x}N_{3x} ds\\ \int_e N_{2x}N_{1x} ds & \int_e N_{2x}^2 ds & \int_e N_{2x}N_{3x} ds\\ \int_3 N_{3x}N_{1x} ds & \int_e N_{3x}N_{2x} ds & \int_e N_{3x}^2 ds\end{bmatrix} \qquad 4.34$$

where N_{ix} and N_{iy} denotes the x and y derivatives of the shape function N_i, respectively. The matrices $[K_{xx}]_{\Gamma_e}$ and $\lfloor K_{yy}\rfloor_{\Gamma_e}$ are related to the line integrals

$$[K_{xx}]_{\Gamma_e}=n^{-2}\alpha_x^2\begin{bmatrix}\oint_{\Gamma_e} N_1N_{1x}n_x d\Gamma_e & \oint_{\Gamma_e} N_1N_{2x}n_x d\Gamma_e & \oint_{\Gamma_e} N_1N_{3x}n_x d\Gamma_e\\ \oint_{\Gamma_e} N_2N_{1x}n_x d\Gamma_e & \oint_{\Gamma_e} N_2N_{2x}n_x d\Gamma_e & \oint_{\Gamma_e} N_2N_{3x}n_x d\Gamma_e\\ \oint_{\Gamma_e} N_3N_{1x}n_x d\Gamma_e & \oint_{\Gamma_e} N_3N_{2x}n_x d\Gamma_e & \oint_{\Gamma_e} N_3N_{3x}n_x d\Gamma_e\end{bmatrix} \qquad 4.35$$

$$\lfloor K_{yy}\rfloor_{\Gamma_e}=n^{-2}\alpha_x^2\begin{bmatrix}\oint_{\Gamma_e} N_1N_{1y}n_y d\Gamma_e & \oint_{\Gamma_e} N_1N_{2y}n_y d\Gamma_e & \oint_{\Gamma_e} N_1N_{3y}n_y d\Gamma_e\\ \oint_{\Gamma_e} N_2N_{1y}n_y d\Gamma_e & \oint_{\Gamma_e} N_2N_{2y}n_y d\Gamma_e & \oint_{\Gamma_e} N_2N_{3y}n_y d\Gamma_e\\ \oint_{\Gamma_e} N_3N_{1y}n_y d\Gamma_e & \oint_{\Gamma_e} N_3N_{2y}n_y d\Gamma_e & \oint_{\Gamma_e} N_3N_{3y}n_y d\Gamma_e\end{bmatrix} \qquad 4.36$$

The matrices $\lfloor K_{xy}\rfloor$ and $\lfloor K_{yx}\rfloor$ can also be expressed as

$$\lfloor K_{xy}\rfloor=[K_1]-[K_2]+\lfloor K_{xy}\rfloor\Gamma_e \qquad 4.37$$

$$\lfloor K_{yx} \rfloor = [K_2] - [K_1] + \lfloor K_{yx} \rfloor \Gamma_e \qquad 4.38$$

where

$$[K_1] = n^{-2}\alpha_x\alpha_y \begin{bmatrix} \int_e N_{1y}N_{1x}ds & \int_e N_{1y}N_{2x}ds & \int_e N_{1y}N_{3x}ds \\ \int_e N_{2y}N_{1x}ds & \int_e N_{2y}N_{2x}ds & \int_e N_{2y}N_{3x}ds \\ \int_e N_{3y}N_{1x}ds & \int_e N_{3y}N_{2x}ds & \int_e N_{3y}N_{3x}ds \end{bmatrix} \qquad 4.39$$

$$[K_2] = n^{-2}\alpha_x\alpha_y \begin{bmatrix} \int_e N_{1x}N_{1y}ds & \int_e N_{1x}N_{2y}ds & \int_e N_{1x}N_{3y}ds \\ \int_e N_{2x}N_{1y}ds & \int_e N_{2x}N_{2y}ds & \int_e N_{2x}N_{3y}ds \\ \int_e N_{3x}N_{1y}ds & \int_e N_{3x}N_{2y}ds & \int_e N_{3x}N_{3y}ds \end{bmatrix} \qquad 4.40$$

$$\left[K_{xy}\right]_{\Gamma_e} = n^{-2}\alpha_x\alpha_y \begin{bmatrix} \oint_{\Gamma_e} N_1N_{1y}n_x d\Gamma_e & \oint_{\Gamma_e} N_1N_{2y}n_x d\Gamma_e & \oint_{\Gamma_e} N_1N_{3y}n_x d\Gamma_e \\ \oint_{\Gamma_e} N_2N_{1y}n_x d\Gamma_e & \oint_{\Gamma_e} N_2N_{2y}n_x d\Gamma_e & \oint_{\Gamma_e} N_2N_{3y} d\Gamma_e \\ \oint_{\Gamma_e} N_3N_{1y}n_x d\Gamma_e & \oint_{\Gamma_e} N_3N_{2y}n_x d\Gamma_e & \oint_{\Gamma_e} N_3N_{3y}n_x d\Gamma_e \end{bmatrix} \qquad 4.41$$

$$\left[K_{yx}\right]_{\Gamma_e} = n^{-2}\alpha_x\alpha_y \begin{bmatrix} \oint_{\Gamma_e} N_1N_{1x}n_y d\Gamma_e & \oint_{\Gamma_e} N_1N_{2x}n_y d\Gamma_e & \oint_{\Gamma_e} N_1N_{3x}n_y d\Gamma_e \\ \oint_{\Gamma_e} N_2N_{1x}n_y d\Gamma_e & \oint_{\Gamma_e} N_2N_{2x}n_y d\Gamma_e & \oint_{\Gamma_e} N_2N_{3x}n_y d\Gamma_e \\ \oint_{\Gamma_e} N_3N_{1x}n_y d\Gamma_e & \oint_{\Gamma_e} N_3N_{2x}n_y d\Gamma_e & \oint_{\Gamma_e} N_3N_{3x}n_y d\Gamma_e \end{bmatrix} \qquad 4.42$$

The shape function integrals included in the calculation of the element matrices $[\mathrm{M}]_c$ and $[\mathrm{K}]_c$ can be evaluated using the following formulae

$$\int_e N_1^i N_2^j N_3^k ds = \frac{i!.j!.k!.2!}{(i+j+k+2)!} A_e \qquad 4.43$$

$$\int_e N_1^i N_2^j d\Gamma_e = \frac{i!.j!}{(i+j+1)!} l_{12} \qquad 4.44$$

where A_e is the element area and related (as studied in the last chapter) to the nodal coordinates of the element, and Γ_{12} and l_{12} are the part and length of the element boundary connecting the nodes 1 and 2, respectively. Similar expressions can also be written for integrations around other element boundaries.

From the above formulation of the element matrices, it can be noted that the element matrix $[\mathrm{K}]_e$ is responsible for the polarization dependence and coupling. The inclusion of the line integrals in the matrices $[\mathrm{K}_{xx}]$ and $[\mathrm{K}_{yy}]$ make them unequal, the hence, the polarization dependence is accounted for. Also, since the matrices $[\mathrm{K}_{xy}]$ and $[\mathrm{K}_{yx}]$ are not zeros, the coupling between the polarization states is taken into account. So, the above formulation is a true vectorial one albeit it considers only the two transverse components of the magnetic field. Another point of prime concern is that the resulting global matrices $[\mathrm{M}]$ and $[\mathrm{K}]$ are sparse, hence, only nonzero elements have to be stored, and also computationally-efficient matrix solver based on LU-decomposition can be used. This is a major advantage of the current vector formulation, where other vector formulations based on the transverse field components can lead to dense matrices. In some optical devices, the hybrid nature of the field is not so clear, so, the polarization coupling is very weak. In these cases, the matrices $[\mathrm{K}_{xy}]$ and $[\mathrm{K}_{yx}]$ can be neglected so that the formulation reduces to two decoupled wave equations for H_x and H_y. In this case, the formulation reduces to a semi-vectorial one. Moreover, for some weakly-guiding optical devices, even the polarization dependence may be neglected. Hence, the matrices $[\mathrm{K}_{xx}]$ and $[\mathrm{K}_{yy}]$ will be reduced to one matrix $[\mathrm{K}_{ll}]$ so that the formulation reduces to only one wave equation for H_x or H_y and the formulation reduces to a scalar one.

Equation (4.27) represents the exact non-paraxial vectorial wave equation to be solved in a step by step procedure in the z direction. The neglection of the z-second derivation term reduces to the approximate paraxial equation which is valid only for waves propagating very near to the axis of propagation, z. A better approximation to the situation can be obtained via the application of Pade approach (Hadley, 1992). Equation (4.27) can be re-written in the form

$$-2jn_ok_o[\mathrm{M}]\frac{d\{h_t\}}{dz_{i+1}} = -\frac{(\{\mathrm{K}\}-n_0^2k_0^2[\mathrm{M}])\{h_t\}}{1-\frac{1}{2jn_0k_0}\frac{d}{dz_i}} \qquad 4.45$$

with $\frac{d}{dz_0}=0$.

Utilising the first Pade approximation (Pade(1,0)) by putting *i*=0 in the recurrence Pade relation (4.45), the following equation results in

$$-2jn_0k_0\left[\overline{\mathrm{M}}\right]\frac{d\{h_t\}}{dz}+([\mathrm{K}]-n_0^2k_0^2[\mathrm{M}])\{h_t\}=\{0\} \qquad 4.46$$

where

$$\left[\overline{\mathrm{M}}\right]=[\mathrm{M}]+\frac{1}{4n_0^2k_0^2}([\mathrm{K}]-n_0^2k_0^2[\mathrm{M}]) \qquad 4.47$$

The paraxial equation is easily obtained from eqn.(4.46) by replacing the matrix $\left[\overline{\mathrm{M}}\right]$ by $[\mathrm{M}]$. Now, equation (4.46) can trace waves propagating off the propagation axis, *z*, more accurately than the paraxial equation, hence, it is called wide-angle equation. To solve eqn. (4.46) in a finite range of the *z*-domain, we divide it into sections each of a width Δz in which k = 1,2,3,... N where N is the total number of successive propagation steps. Over the k th section (shown in Fig. 4.2), the finite element method can also be used to approximate the field as (Zienkiewicz, 1977).

$$\{h_t(\zeta)\}=L_k(\zeta)\{h_t(\zeta_k)\}+L_{k=1}(\zeta)\{h_t(\zeta_{k+1})\} \qquad 4.48$$

where ζ is the local coordinate of the *k*th section, $\{h_t(\zeta_k)\}$ and $\{h_t(\zeta_{k+1})\}$ are the column vectors containing the field nodal values over the whole cross section at *k*th and (k+1)th propagation steps, respectively, and $L_k(\zeta)$ and $L_{k+1}(\zeta)$ are shape functions defined as

$$L_k(\zeta)=1-\zeta \tag{4.49}$$

$$L_{k+1}(\zeta)=\zeta \tag{4.50}$$

Substituting from eqns. (4.48), (4.49) and (4.50) into eqn. (4.46) and applying Galerkin's procedure, with weighting functions W_m, results in

$$[\mathrm{A}]_k\{h_t\}_{k+1}=[\mathrm{B}]_k\{h_t\}_k \tag{4.51}$$

where

$$[\mathrm{A}]_k=-2jn_0k_0[\mathrm{M}]_k+\theta\Delta z\left([\mathrm{K}]_k-n_0^2k_0^2[\mathrm{M}]_k\right) \tag{4.52}$$

$$[\mathrm{B}]_k=-2jn_0k_0[\mathrm{M}]_k+(\theta-1)\Delta z\left([\mathrm{K}]_k-n_0^2k_0^2[\mathrm{M}]_k\right) \tag{4.53}$$

with

$$\theta=\frac{\int_0^1 W_m\zeta d\zeta}{\int_0^1 W_m d\zeta} \tag{4.54}$$

where Δz is the propagation step size, θ is the scheme parameter, and the subscripts *k* and (*k*+1) denote the quantities related to the *k*th and (*k*+1)th propagation steps, respectively. It can be seen from Fig. 4.2a that the lines $\mathrm{L_k}$ and $\mathrm{L_{k+1}}$ show the region where the ζ is most suitable for numerical stability i.e. the point of intersection. Once the initial field is specified, equation (4.52) can be solved to get the field at the successive propagation steps.

The value of the scheme parameter, θ, depends on the choice of the weighting functions W_m as shown in Fig. 4.2. The scheme parameter, θ, decides the stability and the numerical losses of the propagation algorithm. At $\theta = 0$ as shown in Fig. 4.2b, W_m indicates a shift to the far left which gives poor numerical solution. For $\theta \geq 0.5$, the algorithm will be unconditionally stable (Zienkiewicz, 1977). For $\theta = 0.5$, as shown in Fig. 4.2c which corresponds to the finite difference Crank-Nicolson algorithm, the algorithm will be stable and conserving the propagating beam power as well. But, for Crank-Nicolson algorithm, some high frequency oscillations may appear in the field distribution. In other to overcome this problem, higher values of the scheme parameter, θ, can be used (up to $\theta = 1$ as shown in Fig. 4.2d where W_m indicates a shift to the far right), but at the expense of some nonphysical numerical losses. On the other hand, the use of the rigorous PML boundary conditions can eliminate these high frequency oscillations appearing with the field whenever Crank-Nicolson algorithm is used. Hence propagation algorithm proposed in this section is unconditionally stable ($\theta = 0.5$) and power conserving as well.

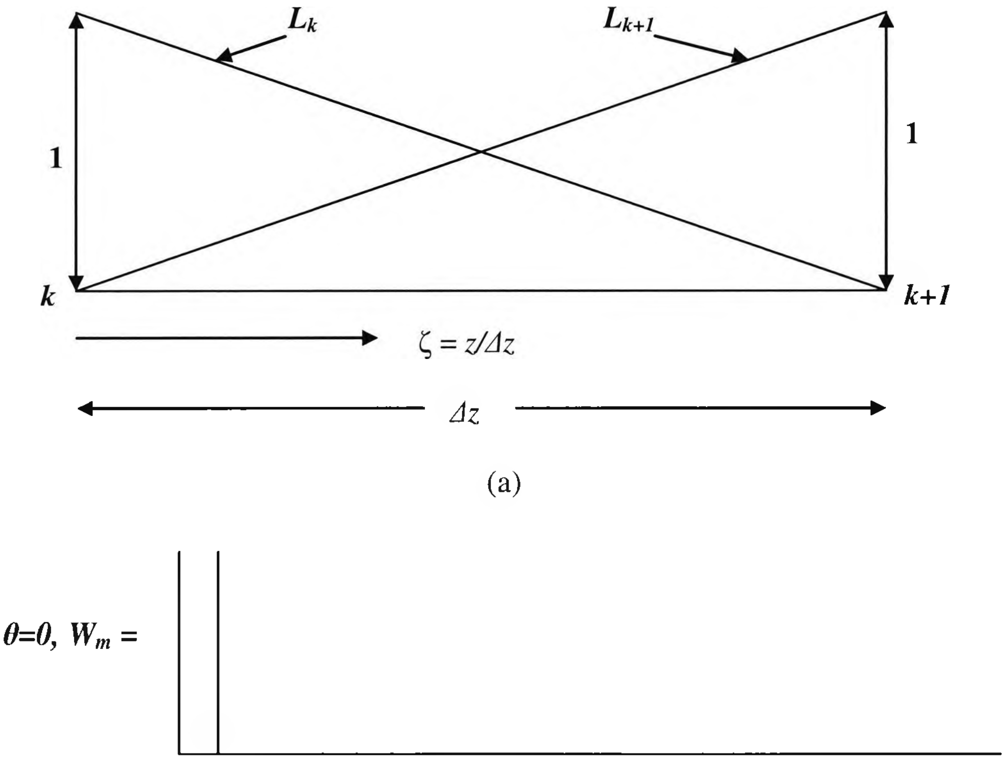

(a)

(b)

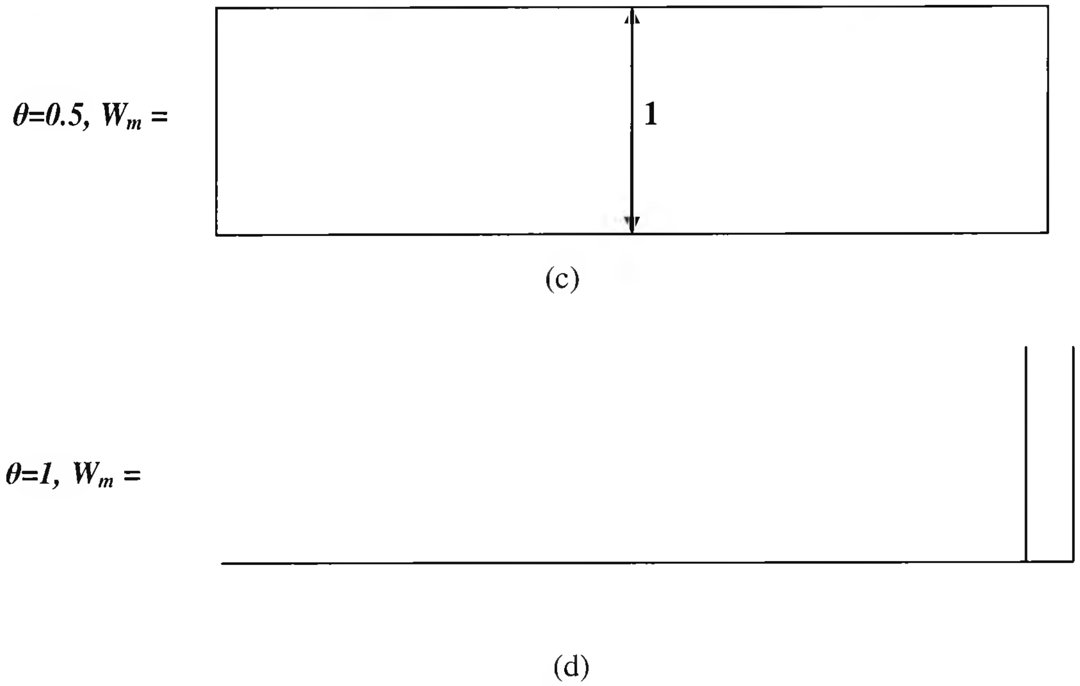

Fig. 4.2. Shape functions and different cases of weighting functions for discretisation along the longitudinal *z*-axis.

4.7 Wave Properties Formulations

In this section, the important parameters for characterising many photonic devices are formulated. The determinations of the propagating power, the spot-size, and power transfer efficiency are crucial for the characterization of the spot-size converters and tapers. The minimization of the propagation losses and subsequent optimisation of the power coupling efficiency are the essence of this study and worldwide research. The overlap integral (OI) is also incorporated into the BPM algorithm to calculate the coupling efficiency of the optical waveguide to a fibre for a single mode operation.

4.7.1 Propagating beam power

From Poynting's theorem, the power associated with a beam propagating in the +*z* direction is

$$\text{Power, } \mathrm{P}=\frac{1}{2}\mathrm{Re}\left(\int \mathbf{E}\times\mathbf{H}^{*}.\hat{z}\,d\Omega\right)=\frac{1}{2}\mathrm{Re}\left[\int\left(E_xH_y^{*}-E_yH_x^{*}\right)d\Omega\right] \qquad 4.55$$

Where Re stands for the real part, $\hat{z}$ is the unit vector in the z direction, and the integration is carried over the surface of the computational domain. The transverse electric field components can be expressed in terms of the corresponding magnetic field components as

$$E_x = \frac{n_0 k_0}{\omega \varepsilon_0} n^{-2} H_y \qquad 4.56$$

$$E_y = -\frac{n_0 k_0}{\omega \varepsilon_0} n^{-2} H_x \qquad 4.57$$

In deriving E_x and E_y expressions, the second order derivatives with respect to the transverse coordinates, x and y, have been neglected. Substituting from eqns. (4.56) and (4.57) into eqn. (4.55) results in

$$\mathbf{P} = \frac{n_0 Z_0}{2} \int n^{-2} \left(|H_x|^2 + |H_y|^2 \right) d\Omega \qquad 4.58$$

where Z_0 is the free space wave impedance (Z_0 = 120π ohms). Substituting from equations (4.22) and (4.26) results in

$$\mathbf{P} = \frac{n_0 Z_0}{2} \{\mathbf{h}_t\}^T [\mathbf{M}] \{\mathbf{h}_t\} \qquad 4.59$$

where $\{\mathbf{h}_t\}$ denotes the nodal values of the propagating field, T denotes complex conjugate transpose, and **[M]** is the global matrix defined in eqns. (4.29) and (4.31). From equation (4.58) integration of the H_v^2 over the surface of the computational domain can be expressed as

$$H_y^2(x, y) = \sum_{n=1}^{ne} \int H_y^2(x, y) \partial\Omega \qquad 4.60$$

and from finite element formulations in chapter 3, (4.60) can be expressed as

$$H_y^2(x,y) = \int \{H_y\}^T [N]^T [N]\{H_y\} \partial\Omega \tag*{4.61}$$

$$= \begin{Bmatrix} H_{y1} \\ H_{y2} \\ H_{y3} \end{Bmatrix}^T \begin{bmatrix} \Delta/6 & \Delta/12 & \Delta/12 \\ \Delta/12 & \Delta/6 & \Delta/12 \\ \Delta/12 & \Delta/12 & \Delta/6 \end{bmatrix} \begin{Bmatrix} H_{y1} \\ H_{y2} \\ H_{y3} \end{Bmatrix} \tag*{4.62}$$

$$= \{H_{y1} H_{y2} H_{y3}\} \begin{bmatrix} \Delta/6 & \Delta/12 & \Delta/12 \\ \Delta/12 & \Delta/6 & \Delta/12 \\ \Delta/12 & \Delta/12 & \Delta/6 \end{bmatrix} \begin{Bmatrix} H_{y1} \\ H_{y2} \\ H_{y3} \end{Bmatrix} \tag*{4.63}$$

$$= \{H_{y1} \quad H_{y2} \quad H_{y3}\} \begin{bmatrix} \Delta/6H_{y1} & \Delta/12H_{y2} & \Delta/12H_{y3} \\ \Delta/12H_{y1} & \Delta/6H_{y2} & \Delta/12H_{y3} \\ \Delta/12H_{y1} & \Delta/12H_{y2} & \Delta/6H_{y3} \end{bmatrix} \tag*{4.64}$$

$$= \begin{bmatrix} \Delta/6H_{y1}^{\ 2} & \Delta/12H_{y1}H_{y2} & \Delta/12H_{y1}H_{y3} \\ \Delta/12H_{y2}H_{y1} & \Delta/6H_{y2}^{\ 2} & \Delta/12H_{y2}H_{y3} \\ \Delta/12H_{y1}H_{y3} & \Delta/12H_{y2}H_{y3} & \Delta/6H_{y3}^{\ 2} \end{bmatrix} \tag*{4.65}$$

The implementation of the above matrix determines the propagating power in the waveguide device at each step in the longitudinal z-direction.

4.7.2 Spot-size Calculation

It is well known that a well-confined optical beam is required to optimize the performance of a wide range of photonic devices, such as semiconductor lasers, amplifiers, modulators or switches. When such a photonic integrated circuit (PIC) with a small and non-circular spot-size is directly butt-coupled to a single-mode fibre (SMF) with a large and circular spot-size, nearly 80-90% of the optical power can be lost due to a large mismatch between their spot-sizes. Majority of SSC designs reported recently do incorporate tapered structures, operating very close to the modal cut-off, to expand their spot-size. This will be discussed in details in Chapter 6 where some taper designs will be presented.

The spot-size (σ) of the fundamental quasi-TE modes have also been calculated by evaluating the corresponding Poynting vector, **ExH** as in the previous section 4.7.1.

$$\text{Power, } P = \frac{1}{2}\text{Re}\left(\int \mathbf{E} \times \mathbf{H}^{*}.\hat{z}\, d\Omega \right) = \frac{1}{2}\text{Re}\left[\int \left(E_x H_y^{*} - E_y H_x^{*} \right) d\Omega \right] \qquad 4.55$$

In this work the spot-size is defined as the area where field intensity falls to 1/eth of its maximum value (or its power intensity is 1/e^{2}).

4.7.3 Propagation Loss Calculation

Many losses are associated with optical waveguide devices when the optical beam is moving through the devices or from one device to another. These will be discussed in chapter 5 however, but it will be mentioned here briefly that the exponential attenuation coefficient is generally used to describe quantitatively the magnitude of the propagation loss, L, is given by,

$$L(dB) = 10\log_{10}\left(\frac{P_t}{P_0} \right) \qquad 4.72$$

where, P_0 is the power at the beginning of propagation and P_t is the propagating power at any point along the length of the waveguide.

4.7.4 Power Coupling Efficiency

This section deals with the ultimate test of any design in the field of engineering generally. In this work the waveguide designs are subjected to reliability and efficiency test in order to optimise the performance of these designs. In the simulation, it is assumed that the optical waveguide is butt coupled to a single mode fibre. In this approach, a Gaussian profile with an arbitrary beam waist (Ω_o) can be used as a fibre source which is coupled to the optical waveguide under test.

$$\text{The Gaussian field is given by } \Phi(x,y) = A\ \exp\text{-}\left[\frac{(x-x_0)^2 + (y-y_0)^2}{\Omega_0^{\ 2}} \right] \qquad 4.73$$

Where x_0 and y_0 are the coordinates of the Gaussian beam, Ω_0 is the Gaussian beam waist or radius, x and y are coordinates of the output field obtained from the waveguide. The incorporated overlap integral is used to determine the coupling efficiency. The overlap integral is given by (Damask, 2005)

$$OI = \frac{\int \Phi_1 \Phi_2 d\Omega}{\sqrt{\int \Phi_1^2 d\Omega \int \Phi_2^2 d\Omega}} \qquad 4.74$$

$$OI = \frac{P_{12}}{\sqrt{P_{11}}\sqrt{P_{22}}} \qquad 4.75$$

where, $P_{12} = \int \Phi_1 \Phi_2 d\Omega$ is the total propagating power,

$P_{11} = \int \Phi_1^2 d\Omega$ is the power due to the waveguide, and

$P_{22} = \int \Phi_2^2 d\Omega$ is the power due to the fibre (Gaussian beam).

4.8 Summary

In this section a powerful, and versatile vectorial BPM algorithm which is based on the finite element method have been presented. It is based on real vector of the six transverse magnetic field components which satisfies the appropriate interface boundary conditions and also automatically satisfies the zero divergence condition, which prevents the spurious solutions from affecting the propagation. This algorithm takes into account the effects of reflection and radiation waves during the propagation by using the rigorous PML boundary condition. Also taken into account is the realistic wide angle range approximation by using the Pade recurrence relation which can accurately determine the path of the waves propagating off the longitudinal z-axis. The global matrices generated are sparsed unlike other vector formulations which result in dense matrices, therefore, only nonzero entries are stored and efficient LU decomposition matrix solver is used. The vectorial BPM algorithm is extended to calculating some wave properties like propagating power, the spot size and the propagation loss. Also the overlap integral has been incorporated into the algorithm for the assessment of the coupling efficiency.

Chapter 5

Spot-size Converters

5.1 Introduction

In this section, the vectorial finite element method is used to design various types of monolithically integrated spot-size converters for efficient coupling of an active device to a standard optical fibre. Spot-size converters (SSC) with MMI and Twin-rib structures are investigated in this chapter. It is well known that a well confined optical beam is required to optimize the performance of a wide range of important photonic devices, such as semiconductor lasers, amplifiers, modulators or switches. When such a photonic integrated circuit (PIC) with a small and non-circular spot-size is directly butt-coupled to a single-mode fibre (SMF) with a larger and circular spot-size (as shown in Fig. 5.1), nearly 80-90% of the optical power can be lost due to a large mismatch between their spot-sizes. To overcome such a high loss, at present, when coupling a SMF to PIC, a microlens or lensed fibre is used to enhance the coupling efficiency: however, this approach also introduces the need for sub-micron alignment tolerances. This reduction of coupling loss, which is possible at the expense of the stringent alignment tolerance, results in a very large packaging cost. For a low-density subscriber network, such a large cost is inhibiting the rapid extension of (FTTH)

Waveguides are generally used for production of single mode operations to be used in optoelectronic integrated circuits (OEICs). But there have been cases where waveguides are needed to produce a wider multimoded waveguide which can be used in the design of some specific photonic devices. These waveguides are generally known as Multimoded interferometric (MMI) devices. They have got their own good qualities and usefulness such as:

1. They can be used as optical power splitters
2. They are more tolerant at the fabrication processes
3. They are polarization sensitive
4. They can be used as spot-size converters to improve coupling efficiency

Tapers are generally used either laterally or vertically to achieve the required spot-size for some photonic devices, but their fabrication often requires complicated techniques. Tapered waveguides are also known to cause performance degradation in many active devices from sudden reflections when sharply terminated. Therefore these disadvantages have led to the concept of using MMI as a SSC to expand the spot-size. Fig. 5.1 below shows the general principle of spot-size conversion. MMI-based design has been considered in this section to evaluate their properties to improve the coupling efficiency by using the finite element and the LSBR methods.

The spot-size converter waveguide structures described in this section are made from GaAlAs/GaAs semiconductor materials. This is a composition of III/V semiconductor system with a direct band gap. The binary, ternary and quaternary compositions GaAs or InP are transparent at $\lambda = 1.3$ or $1.55\ \mu m$, the wavelength important for optical communications and the study carried out in this section makes use of these wavelengths. Waveguides can be fabricated by epitaxially grown layers with different refractive indices. Horizontal guiding in accomplished group II or VI elements, so that electronic devices can also be produced.

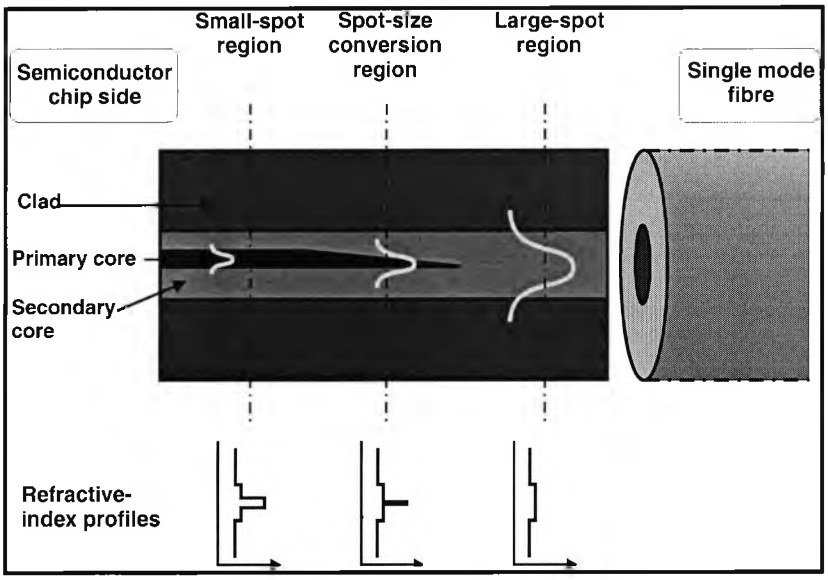

Figure 5.1: Spot-size conversion principle

Fig 5.1 illustrated the principle of spot-size conversion and power transfer from waveguide to a fibre. The spot-size is defined as the area where the power intensity falls to $1/e^2$ of its maximum value. The variation of the refractive index profiles is also shown in Fig. 5.1. As it can be observed the output of the semiconductor laser is sent to a strong guiding primary core with high refractive index. Due to the strong confinement and reduction of the width of primary core, the mode field is nearly limited to the width of this primary core, which is surrounded by a secondary core with lower refractive index. The primary core is tapered, i.e. its width is gradually decreased in the steps along the longitudinal direction of the waveguide. When the mode approaches the cut-off in the primary core, and the taper width is decreased further, the spot-size is pushed into the secondary core, as the primary core can no longer confine the growing mode and subsequently more power is transferred to the secondary core. When the primary core is tapered to a certain critical width, the mode is completely transferred to the large-spot region, where secondary core takes on the task of guiding. With proper designs this mode may match the mode field of a single mode fibre. The phenomenon of mode expansion near cut-off is employed in achieving the monolithically integrated spot-size converters in most cases. However there is still problem of field mismatch since both the size and shape of the beam need to be converted and stringent alignment tolerances is also needed by spot-size converters which causes increase in the packaging cost and make the production very unlikely. The idea of the micro machined alignment mirror was floated, in which the alignment of the fibre and waveguide is carried out with a movable micro-mirror. But the drawback in this case is that many additional fabrication steps will be required for SSCs and this will make mass production cumbersome. As a result the idea of producing efficient integrated SSCs has been a top priority to eminent optical scientists worldwide. This is because of the reduction in the cost of components, packaging and assembly which in turn leads to low cost components with compactness and reliability.

5.2 The Least Squares Boundary Residual Method

There has been a considerable interest in the analysis and design of integrated optical devices in which waveguide parameters vary along the axial direction. They play an important role in designing practical devices, such as, an isolated step discontinuity as in the simple butt-joining of two waveguides of different widths, or as finite cascades of discontinuities as in the bending of an optical waveguide in an integrated optical directional coupler circuit, the tapering of a channel waveguide for efficient coupling to an optical fibre, gratings on dielectric waveguides in certain components like bragg reflectors, or Y- junctions. Various methods for the analysis of the discontinuity problems in a dielectric waveguide have been developed by a number of authors (Clarricoats and Sharpe, 1972; Hockham and Sharpe, 1972; Mahmoud and Beal, 1975; Morishita *et al.*, 1979; Shigesawa and Tsuji, 1986). However, most of the theoretical analyses reported earlier have restricted limitations of practical application, since the radiated and reflected waves have been ignored and also used under the assumption of slight discontinuity.

The problem considered here is an abrupt discontinuity in the transverse plane, $z = 0$, between two arbitrarily shaped uniform waveguides. Each waveguide can have scalar or tensor permittivity that varies arbitrarily with the two transverse directions. The incoming wave incident upon the discontinuity plane is presumes of one mode. In this thesis, the discontinuities in dielectric waveguides are accurately analysed using the least squares boundary residual (LSBR) method (Rahman and Davies, 1988). Consequently, the LSBR method has been used along with the versatile vector finite element method (Rahman and Davies, 1984*a*) in order to calculate the power transfer from a waveguide section to another.

The least squares boundary residual method was introduced as an alternative to the point matching and Galerkin (Zienkiewicz, 1977; Desai, 1979; Silvester and Ferrari, 1990) methods, of solving problems numerically. The LSBR method satisfies the boundary conditions in the useful least-squares sense over the discontinuity interface. In contrast to point matching, the LSBR method is a rigorously convergent procedure, free from the phenomenon of relative convergence. The LSBR method has the flexibility of introducing an electric/magnetic weighting factor and, unlike the point matching, the errors being minimised are global rather than sampled just at discrete points. The method has been widely used to study discontinuity parameters in microwave and optical waveguides (Davies, 1973; Brooke and Kharadly, 1976; Matsumoto *et al.*, 1986; Cullen and Yeo, 1987; Fernandez and Davies, 1988). The LSBR method matches the continuity of the tangential electric and magnetic fields in the least squares sense considering many modes at the discontinuity plane to provide the generalised scattering matrix. In this study, it has been shown that the LSBR method is an accurate and versatile numerical tool to obtain the power transfer between coupled waveguides.

A brief explanation of the theory of the least squares boundary residual method is given in the next section, followed by a discussion of the use of FEM in the numerical analysis of the discontinuity problem.

5.2.1 LSBR Formulation

Consider the abrupt junction of two dielectric waveguides as illustrated in Fig. 5.2. It is assumed that the discontinuity junction is excited by an incident wave of one mode from side I. This incoming wave is partly reflected, partly transmitted, and radiated at the junction interface. Let E_t^{in} and H_t^{in} be the transverse components of the electric and magnetic fields of the incident wave, respectively. Some of the incident wave is reflected back into the side I. On the other hand, many modes will be generated at the discontinuity plane to satisfy the boundary conditions. These can be guided or radiated modes on both sides of the discontinuity. The total transverse electric and magnetic fields E_t^I and H_t^I in side I and E_t^{II} and H_t^{II} in side II at the discontinuity plane ($z = 0$), can be expressed in terms of the eigenmodes in side I and side II, respectively, as follows:

$$E_t^I = E_t^{in} + \sum_{i=1}^{\infty} a_i \, E_{ti}^I \qquad 5.1$$

$$H_t^I = H_t^{in} - \sum_{i=1}^{\infty} a_i \, H_{ti}^I \qquad 5.2$$

$$E_t^{II} = \sum_{i=1}^{\infty} b_i \, E_{ti}^{II} \qquad 5.3$$

$$H_t^{II} = \sum_{i=1}^{\infty} b_i \, H_{ti}^{II} \qquad 5.4$$

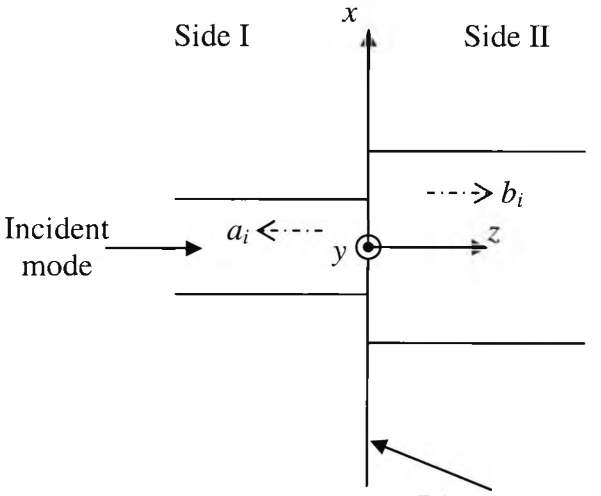

(a)

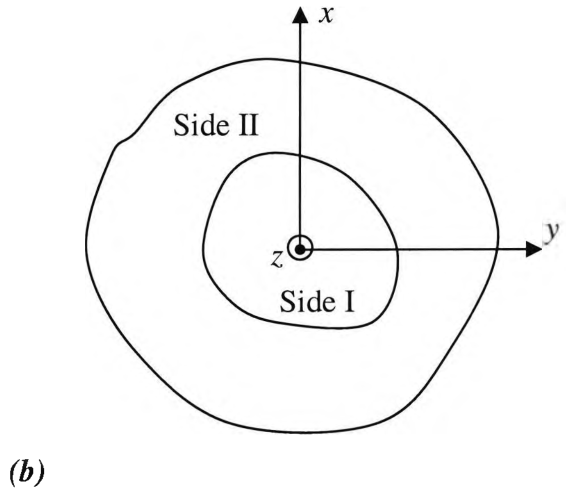

Fig. 5.2 Discontinuity junction of two dielectric waveguides *(a)* Vertical section of the discontinuity between side I and II. ***(b)*** Transverse cross section of the discontinuity at the junction of two sides.

The modes, which are incident at the discontinuity plane, may be propagating, radiating, or evanescent. Therefore E_{ti}^{I} and H_{ti}^{I} represent the transverse field components of the i^{th} mode reflected from the junction in side I and, a_i are the corresponding modal amplitudes of these reflected modes. Similarly, E_{ti}^{II} and H_{ti}^{II} are the transverse field components of the i^{th} mode transmitted in side II and, b_i are the modal amplitudes of those transmitted modes. These scattering coefficients, a_i and b_i have to be determined.

Considering the fields in either side of the discontinuity, the mean-squares error to the boundary condition in that plane can be defined as the functional:

$$J = \int \left|\mathbf{E}_t^{I} - \mathbf{E}_t^{II}\right|^2 + \delta . Z_0^{\,2} \left|\mathbf{H}_t^{I} - \mathbf{H}_t^{II}\right|^2 d\Omega \qquad 5.5$$

where δ is a convenient, positive and dimensionless weighting factor, and the integral is calculated over the discontinuity plane. Z_0 is the free-space wave impedance.

In the LSBR method, the aim is to look for a stationary solution to satisfy the continuity conditions of the tangential fields in a least square sense by minimising the functional (5.5). To obtain the approximate numerical solution to the problem, the infinite series expansions of (5.1) to (5.4) are truncated, including all relevant propagating modes plus as many radiating and/or evanescent modes as convenient. An evanescent wave is a nearfield standing wave exhibiting exponential decay with distance. Evanescent waves (means "tends to vanish") are always associated with matter, and are most intense within one-third wavelength from any acoustic, optical, or electromagnetic transducer. Optical evanescent waves are commonly found during total internal reflection. In optics, evanescent waves are formed when sinusoidal waves are (internally) reflected off an interface at an angle greater than the *critical angle* so that total internal reflection occurs. The physical explanation for their existence is that the electric and magnetic fields cannot be discontinuous at a boundary, as would be the case if there were no evanescent field. For an optical fiber or waveguide, a radiation mode or unbound mode is a mode which is not confined by the fiber core. Such a mode has fields that are transversely oscillatory everywhere external to the waveguide, and exists even at the limit of zero wavelength.

In this analysis, all the reflection, transmission and radiation fields are determined in such a way that $\boldsymbol{J}$ becomes a minimum. The electromagnetic fields thus obtained are the best approximate fields in the sense of least square error. The condition for eq. (5.5) being minimised is:

$$\frac{\partial \boldsymbol{J}}{\partial a_i} = 0\,, \qquad \frac{\partial \boldsymbol{J}}{\partial b_i} = 0 \qquad \text{for i} = 1.......\infty \qquad 5.6$$

which results in a set of linear equations:

$$\boldsymbol{C}\,\boldsymbol{x} = \boldsymbol{v} \qquad 5.7$$

The solution of this equation gives in $\{\boldsymbol{x}\}$, the required approximate modal coefficients of a_i and b_i. These constitute one column of the scattering matrix, corresponding to the chosen incident mode. $\boldsymbol{C}$ is a square matrix generated from the eigen vectors and $\boldsymbol{v}$ is an array due to the incident mode. The elements of $\boldsymbol{C}$ and $\boldsymbol{v}$ are given by:

$$C_{ij} = \langle E_{ti}, E_{tj} \rangle + \alpha . Z^2 \langle H_{ti}, H_{tj} \rangle \qquad 5.8a$$

$$v_i = \langle E_t^{in}, E_{ti} \rangle + \alpha . Z^2 \langle H_t^{in}, H_{ti} \rangle \qquad 5.8b$$

where $i, j = 1, \ldots\ldots N$, and N is the total number of modes in side I and II and the vectors E_t and H_t are made up of all the corresponding modal fields in both sides.

The inner products involved in the above expressions are defined as:

$$\langle x_1, x_2 \rangle = \int x_1 \cdot x_2^* \, ds \qquad 5.9$$

where x_1 and x_2 are two field vectors, x_2^* is the complex conjugate of x_2 and integration is carried out over the waveguide cross section.

The above gives a brief outline of the least squares boundary residual technique which will be applied in the next sections to analyse MMI waveguide problems concerning power transfer between waveguide and fibre.

5.2.2 Application of LSBR in Waveguide problems

The vector **H**-field finite element has become a powerful tool for the solution of microwave and optical waveguides as described in the previous chapter. One of the main advantages of **H**-field formulation is that the continuity of **H**-field components is automatically satisfied even with permittivity discontinuities. In this thesis, to analyse the characteristics of coupled waveguides, the rigorously convergent LSBR method is used conjunction with **H**-field FE program. The elimination of spurious solutions by using the penalty method, particularly improves the eigen vector quality, which is a very important fact for the analysis of discontinuity problems.

By employing the FE program, the nodal values of the complete **H**-field for each mode are obtained for both the waveguides (side I and side II). The **E**-field over each element are calculated using these nodal **H**-field values by using the Maxwell's equations. Modal eigenvalues and eigenvectors of all the modes in both sides of the discontinuity are used as the input data to the LSBR method. All these eigenvalues and eigenvectors are easily generated by employing the vector FEM program. The LSBR program reads all the input data and calculates the integral $\boldsymbol{J}$, and minimises the error criterion of eq. (5.5), with respect to each value of a_i and b_i for any given incidence, by solving a homogeneous linear equation (5.7). There is no need to generate the nodal **E**-fields as the nodal **H**-fields can be directly used to calculate the electric field part of the functional, $\boldsymbol{J}$. The solution of the eq. (5.7) gives the unknown vector $\{\boldsymbol{x}\}$ consisting of the reflected and transmitted coefficients of all the modes considered in the analysis. The singular value decomposition algorithm has been used to solve the linear equation (5.7). For numerical efficiency, the FE nodal points of side I are matched with the nodal points of side II across the transverse plane at the discontinuity.

The LSBR method can be applied to a wide range of discontinuity problems, involving abrupt changes at the transverse plane between arbitrary guiding structures of uniform cross section. These include vertical shifts, horizontal misalignments, sudden changes of width or height, change in guide dimensions or materials, or combinations of all these varieties. The method can also be used to guiding structures, such as optical fibres or channel waveguides with anisotropic or electro optic refractive indices. On the other hand, the LBSR method can be used to find the optimum matching of the two waveguides by controlling the geometries and material properties of the guides. In addition, by choosing the optimum guide parameters the radiation losses resulting from random fluctuations in waveguide geometry and refractive index can also be minimised. The resulting reflection matrix and the transmission matrix give a complete understanding of the discontinuity problem which facilitates better designs of optical and microwave devices.

5.2.3 Losses in optical waveguides

The source of losses in waveguide devices can be broadly classified as coupling loss and propagation loss. The coupling loss consists of;

(1) The Fresnel loss which is caused by back reflection at the interfaces between the waveguide and single mode fibre. This can easily be estimated by this relation, assuming normal incidence:

$$R_F = \left(\frac{n_1 - n_0}{n_1 + n_0} \right)^2 \qquad 5.10$$

where R_F is the fractional amount of incident light reflected back at each fibre end, n_0 is the refractive index of the medium between the fibres and n_1 is that of the fibre.

(2) The end alignment losses are the misalignment losses which are difficult to calculate because the power distribution across the fibres must be known.

The propagation loss is generally attributable to three different mechanisms: scattering, absorption and radiation.

(1) The scattering loss: in homogeneous media, there can be structural disorder in material's structure or composition. This is usually predominate in glass or dielectric waveguides

(2) Absorption loss is most important in semiconductors and other crystalline materials. It arises mostly from the presence of impurities especially in transition metals.

(3) Radiation losses become significant when waveguides are bent through a curve.

Photons can be either scattered, absorbed or radiated as the optical beam progresses through the waveguide, thus reducing the total power transmitted. To describe quantitatively the magnitude of the scattering loss, the exponential attenuation coefficient is generally used, and the intensity (power per unit area) at any point along the length of the waveguide is given by,

$$I(z) = I_0 e^{-\alpha z} \qquad 5.11$$

where I_0 is the initial intensity at $z = 0$ and α is the power attenuation coefficient.

Propagation loss is the loss taken into account throughout this thesis. For most coupling applications described in this thesis, the light is coupled in and out of one optical waveguide to another through a butt joint. The LSBR method analyses the waveguide junction efficiently in order to calculate the power transfer from the input guide to the other. When a guided TE or TM mode is incident on the discontinuity plane between two waveguides, some of the incident light energy is lost, called the insertion loss. The method can also be used to calculate this power loss suffered by the TE or TM mode, by utilising the scattering coefficients. If an incident mode of unit power is assumed then the insertion loss in decibels is given by:

$$L(dB) = 10log_{10}\left(\sum_{i=1}^{N} |b_i|^2\right) \qquad 5.12$$

where, b_i are the normalised transmission coefficients of the i^{th} mode and N is the total number of modes considered.

5.3 Multimode Interference (MMI) Waveguides

This section involves the concept, design and analysis of the principle of the multimode interference (MMI) waveguides. In the design of guided wave photonic devices, one of the most important numerical techniques is to obtain the modal solutions of the waveguide sections. For an MMI-based design, all the guided modes of the multimoded waveguide section should be obtained. There are many numerical approaches available, which may be used to find the modal solutions of optical waveguides, such as the effective index method (Hocker and Burn, 1977), the finite difference method (Stern, 1988), and beam propagation method (Feit and Fleck, 1980). The effective index method is simple but often inadequate and for a semiconductor optical waveguide with a large contrast ratio and two-dimensional modal confinement, where a more rigorous approach is necessary. The main advantage of the finite element method (FEM) over the finite difference method is its more accurate representation of the waveguide cross-section using triangles of irregular shapes and sizes. This particular advantage is more significant when waveguides have curved or slanted side walls, or have arbitrary shapes or index distributions. In the FEM approach, the vector **H**-field based formulation (Rahman and Davies, 1984*a*) has been established as one of the most accurate and efficient techniques, since unlike the alternative **E**-field formulation, all three components of the vector **H**-field are naturally continuous across the dielectric interfaces. This **H**-field based FEM is used in this work to obtain the modes and supermodes of the various types of SSC structures reported here.

It is also necessary to analyze the butt coupling between the SCC's and the SMF and also to obtain the scattering parameters inside the SSC section, such as a butt coupling of the modal solutions input/output waveguides and the MMI section. Often the overlap integral method is used to find the transmission coefficients and even a simpler impedance-based approach is used to find the reflection coefficients at the junction interfaces. However, it has been shown that the least squares boundary residual (LSBR) method (Rahman and Davies, 1988), is rigorously convergent, and can be used to obtain both the transmission and the reflection coefficients by considering all the guided and discretized radiation modes of the structures. This LSBR method has been used to find the power coupling efficiency between the SSC and the SMF and also the modal coefficients of the modes or higher order modes in the MMI sections.

5.4 Design of a MMI-based Spot-size converter

In this section a novel design approach using a multimode waveguide is presented (Ladele, *et al*, 2001). The principle of multimode interference (MMI) has been widely used in the design of optical power splitters (Rajarajan *et al.*, 1996), in which case it is important to design an MMI-section which produces the required number of images. In previous publications (Rajarajan *et al.*, 1996), it had been observed that at a particular location, the resulting image could be more suitable for a coupling to a SMF. Fig. 5.3 shows the schematic of an MMI-based SSC.

In this design, it is assumed that the height and width of the primary guide on the left-hand side are 0.5 and 1.0 μm, respectively. The core and substrate refractive indices are taken as 3.3989 and 3.1645 at the operating wavelength 1.55 μm. The height and width of the MMI-based SSC section are taken as 0.5 and 8.0 μm. The wider lateral dimension is selected to match the diameter of a typical SMF.

In this case, 10,000 first order triangular elements are used to represent the SSC cross-section. The dominant H_y field profile of the quasi-TE (H_{11}^{y}) mode in the PIC section is shown in Fig. 5.4. The dominant H_y field profile of the quasi-TE (H_{11}^{y}) mode of a typical SMF is also shown in Fig. 5.5, as a comparison. In this case, the core and cladding refractive indices of the fibre are taken as 1.50 and 1.49, respectively. If the PIC and the SMF are directly butt coupled the maximum transmission coefficient is 0.26, which represents only 7% optical power is coupled into the fibre.

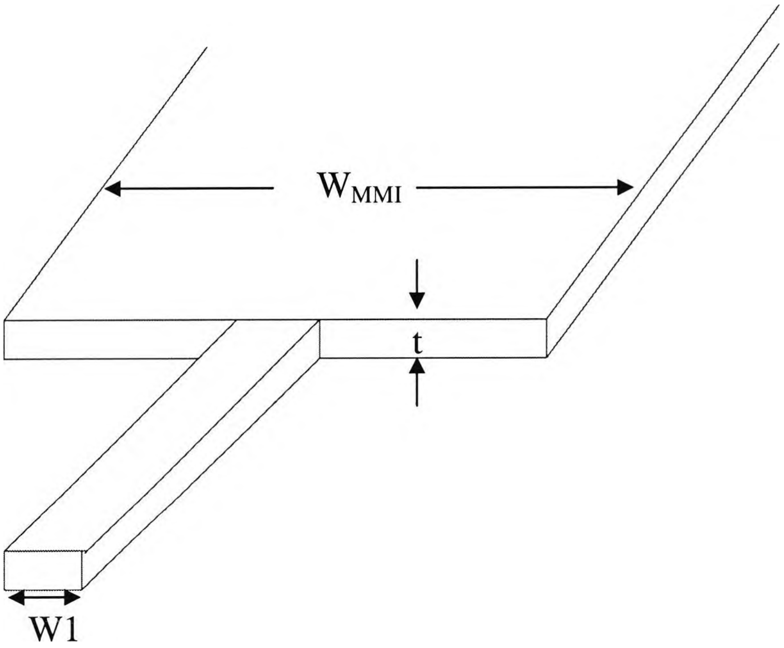

Fig. 5.3 Schematic of an MMI-based spot-size converter.

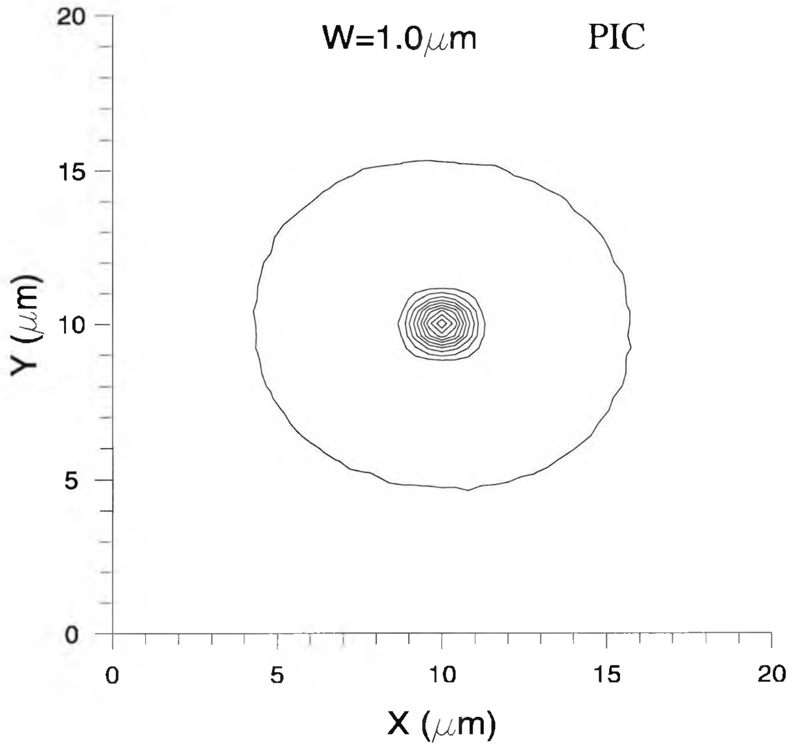

Fig.5.4 H_y field profile of the quasi-TE mode in the laser section.

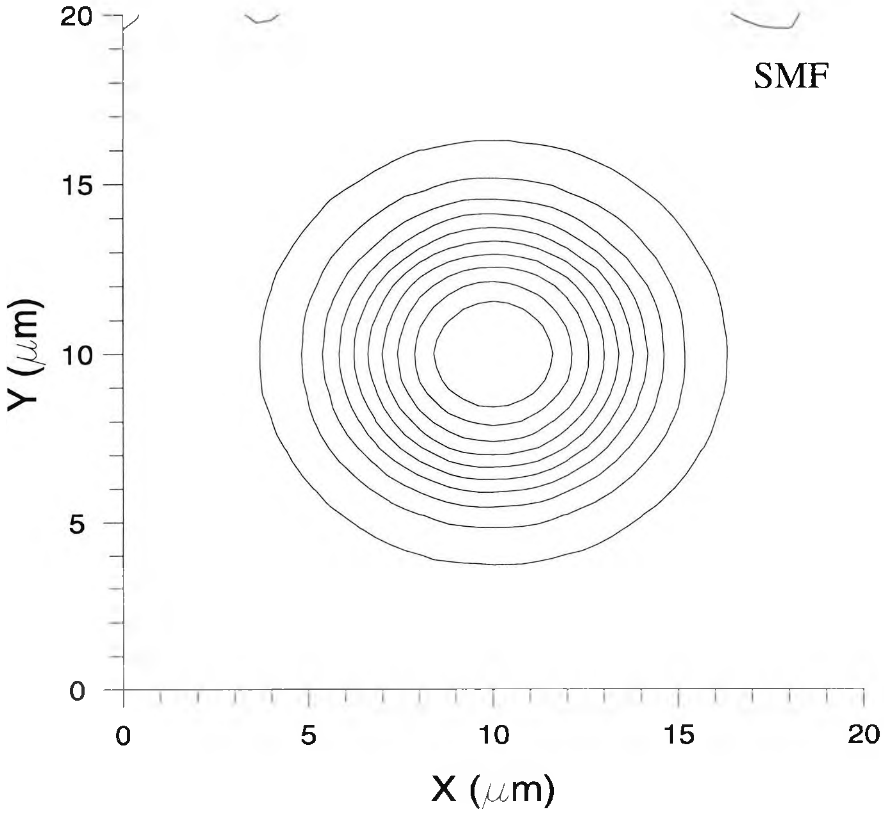

Fig. 5.5 H_y field profile of the fundamental quasi-TE mode in the fibre.

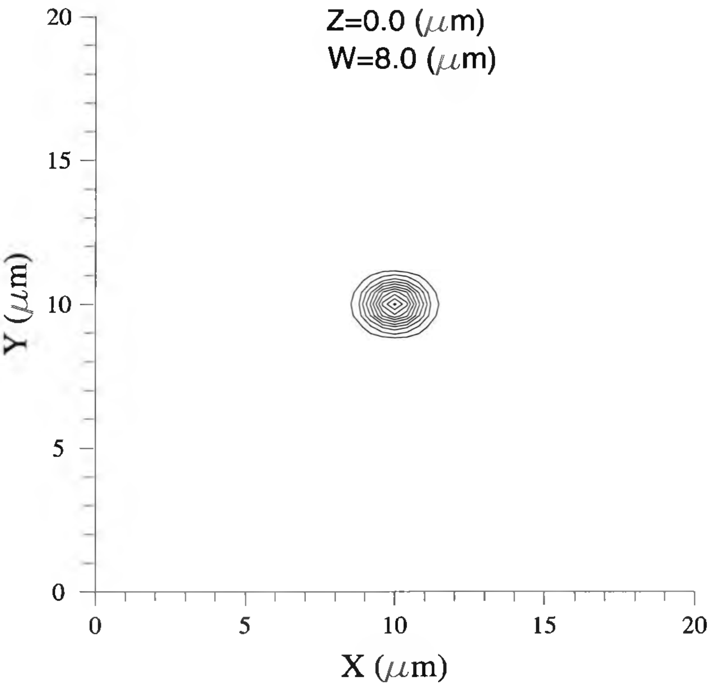

Fig. 5.6 Field profile at the start of the spot-size converter.

The FEM is used again to find the modal field profiles of the guided modes supported by the MMI waveguide. Subsequently, the LSBR method is used to find the coefficients of the modes in the MMI sections. From these modal coefficients and their modal field profiles, the overall field profile at the start of the MMI section is calculated, the result of which is shown in Fig. 5.6. This field profile is very similar to the field profile of the primary waveguide, as shown in Fig. 5.5, which illustrates that the continuity of the field components has been obeyed.

The optical field profiles along the MMI section would differ, as each mode in this section will propagate with its own propagation constants, causing relative phase shift between the modes. The composite field profiles were calculated and the LSBR method was employed to obtain the coupling efficiency to a SMF at each lateral position, as if the MMI section is terminated there. The variation of the optical power coupling efficiency with MMI length is shown in Fig. 5.7.

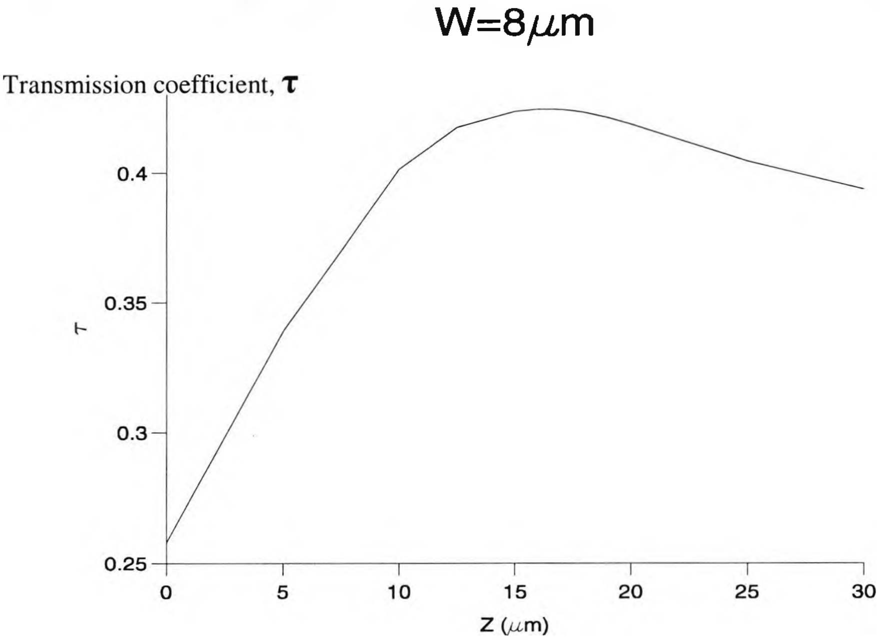

Fig. 5.7 Variation of optical power coupled to the SMF with the axial *distance, z.*

It can be observed from Fig. 5.7 that maximum coupling efficiency is obtained when the MMI length is only 16 μm. This demonstrates that a very compact SSC can be designed which can enhance the coupling efficiency from only 7% (τ=0.26) to a reasonably larger value of 18% (τ=0.42). The composite field profile at this position is shown in Fig. 5.8, which shows a significant enlargement of the overall field profile.

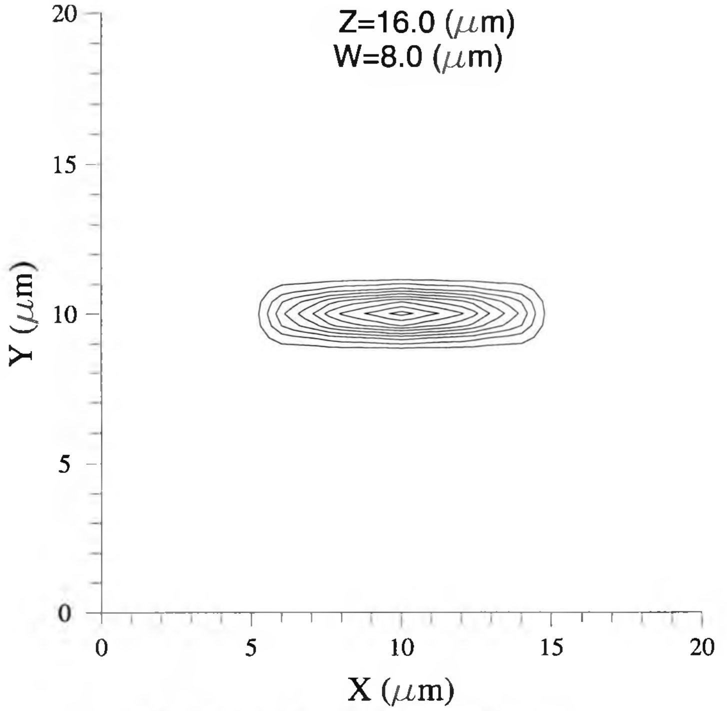

Fig. 5.8 Field profile at z = L= 16 um.

However, it can also be noted that MMI section allows the field to expand in the horizontal, but not in the vertical direction, which limits the maximum power coupling that can be achieved. To facilitate field expansion also in the vertical direction, two additional MMI sections are introduced at the upper and lower side of the original SSC structure. The schematic of this three-core MMI based SSC is shown in Fig. 5.9 (Ladele *et al.,* 2001). Initially it is assumed that two additional MMI guides have also the same thickness as the middle MMI guide, which was set at 0.5 μm. However, it was observed that the higher order modes were not extended appreciably into the two outer waveguides because the dimensions of the structure in which W >> t where W stands for width and t, thickness. The mode confinement is more in the lateral direction than vertical direction. To enhance the field coupling to the outer MMI guides, the thickness of these two guides was increased to 0.57 μm in each case. As a result, this complex structure supports as many as 30 guided modes. The dominant H_{11}^{y} filed profile for the H_{51}^{y} mode is shown in Fig. 5.10 which clearly shows 5 local maxima. The dominant H_{11}^{y} field profile for the H_{13}^{y} with three vertical maxima is shown in Fig. 5.11.

Subsequently, the LSBR method has been applied to calculate the modal coefficient of all the 15 guided modes of this structure and from these coefficients and their modal field profiles the evolutions of optical field is determined. The composite field profile at the start of the three-core MMI section is shown in Fig. 5.12. This field again resembles very closely to the modal field of the primary guide, as shown in Fig.5.4.

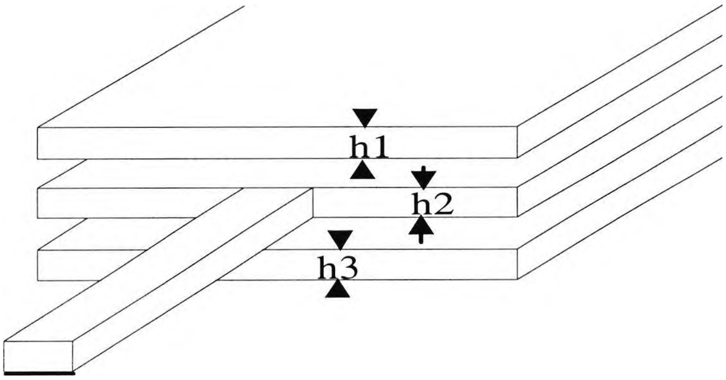

Fig. 5.9 Schematic of the three-core coupled MMI used as a spot-size converter.

The LSBR method is applied successively to obtain the power coupling efficiency to a SMF as the length of the SSC section is varied. The variation of the power coupling efficiency with the device length is shown in Fig. 5.13. It can be observed that the maximum power coupling efficiency can now reach 36% (τ=0.6), compared to the single-section MMI structure, as shown in Fig. 5.7. This represents 7.2 dB improvement over the direct PIC-SMF coupling.

The composite field profile at z= 17.5 μm is shown in Fig. 5.14, which has expanded more significantly in both the horizontal and the vertical directions. This demonstrates that a reasonably coupling efficiency can be achieved in a very short SSC using a MMI section, and it is believed that further improvement can be achieved by adjusting the SSC section parameters.

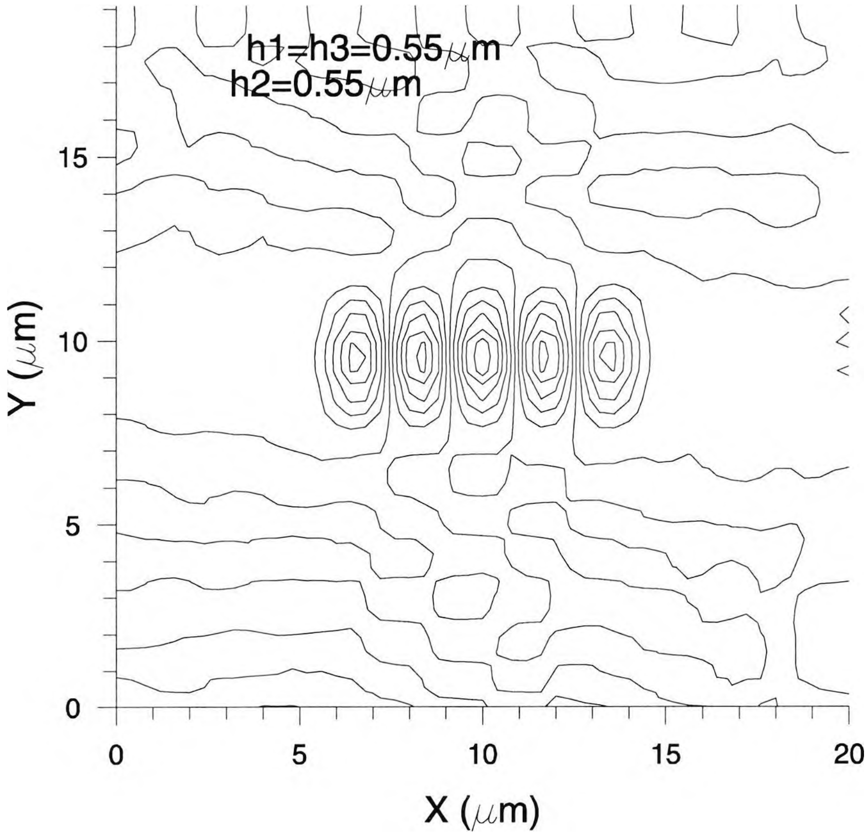

Fig. 5.10 H_y field profile of the H_{51}^{y} mode in the 3-core MMI section.

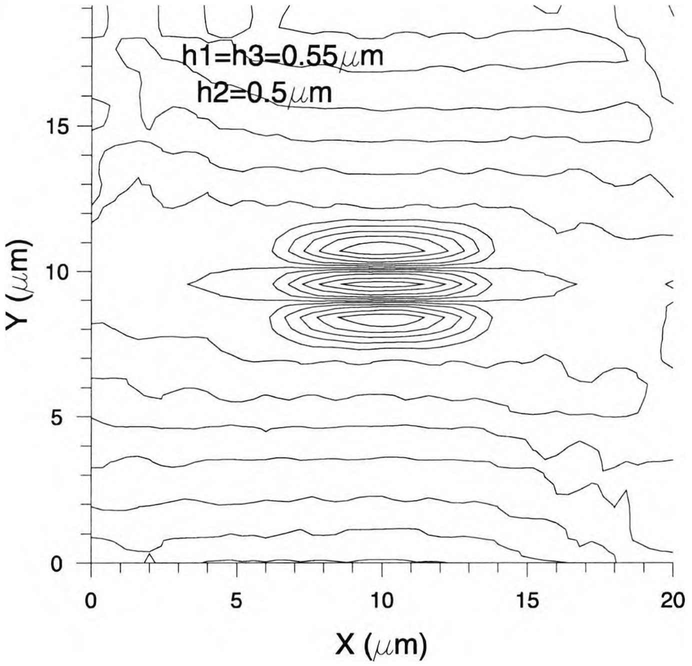

Fig. 5.11 H_y field profile of the H_{13}^{y} mode in the 3-core MMI section.

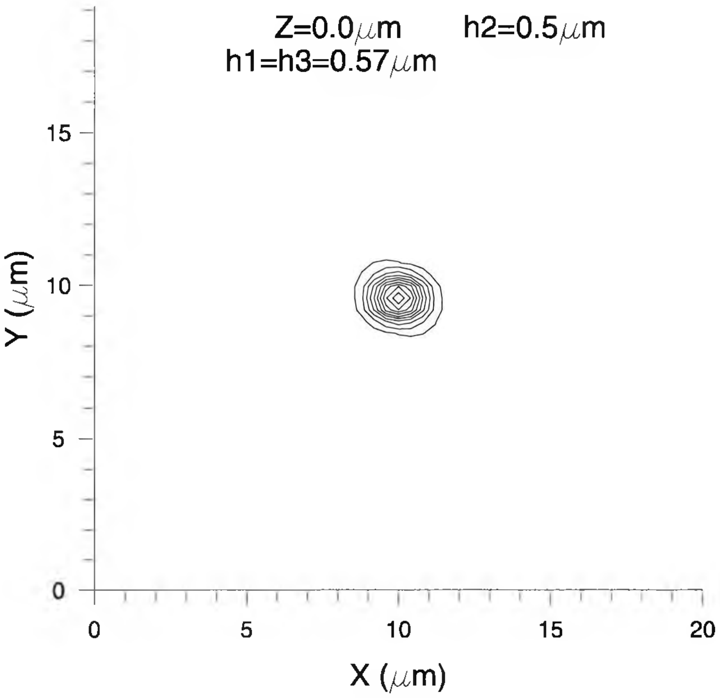

Fig. 5.12 H_y field profile at the start of the MMI-section.

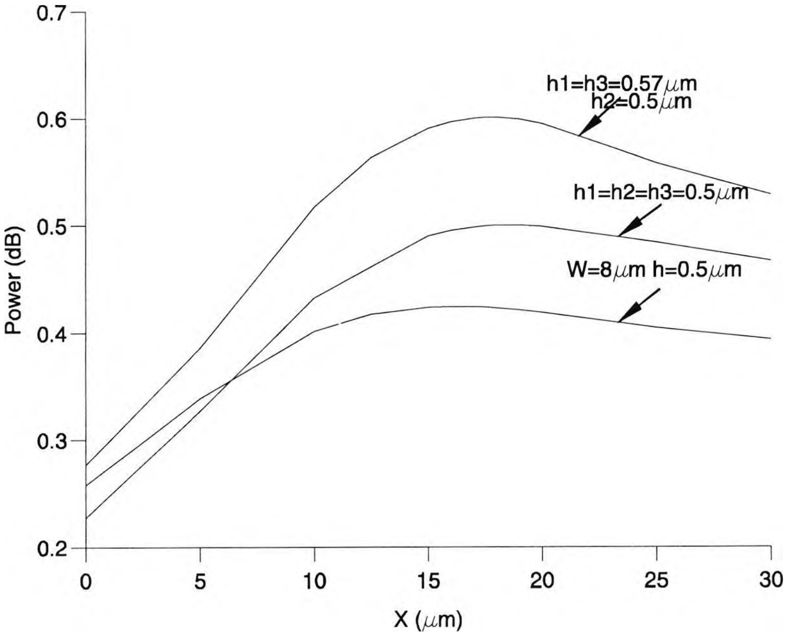

Fig. 5.13 Variation of the coupled power, Po, with the axial distance, z.

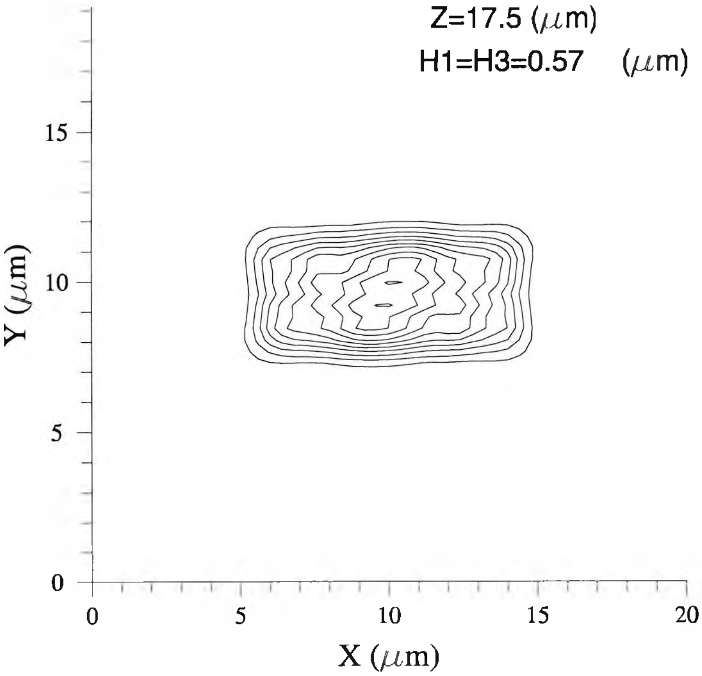

Fig. 5.14 H_y field profile at z = 17.5 um.

5.5 Design of a Twin rib waveguide Spot-size converter

Among the design of various types of monolithically integrated spot-size converters for efficient coupling to a standard optical fibre. There has been tremendous interest in improving the designs (IEEE J. Selected Topics in QE., 1997) of spot-size converter of which rib waveguides has been recognised as one of the best geometry for achieving effective coupling. In this work the idea of a twin rib waveguide will be implemented to further improve the coupling efficiency reported for the single rib waveguides (Sewell *et al.,* 1999). The versatile FEM is employed as the numerical technique tool to obtain the modal solutions of the waveguide cross-section using triangles of irregular shapes and sizes with arbitrary index distributions. In the FEM approach, the vector **H**-field based formulation is used because of its accurate and efficient techniques and all the three components are continuous across the dielectric interfaces. The choice of dimensions to be used in the design of the rib waveguide is of utmost importance as they need to be realistic and conform to the industry standards.

Fig. 5.15 shows the cross-section of a spot-size converter employing a twin rib waveguide (Rahman *et al.,* 2001). The twin rib waveguide structure being studied here had the following parameters: $W_2 = 10$ µm, $H_1 = 1$ µm, $H_2 = 5$ µm, $t = 5$ µm, $n_1 = 3.4092$, $n_1 = 3.3592$, $n_1 = 3.3088$, and the operating wavelength is 1.319 µm. At the beginning of the excitation, the upper rib waveguide (W_1) is wide enough, and most of the optical power is confined in the upper rib region. However, as this width is adiabatically reduced, below a certain width the upper guide cannot support a guided mode and the optical power is pushed downward and guided by the lower rib waveguide. The upper rib waveguide width, W_1, is varied to control the spot-size. The lower rib waveguide has a larger core area, comparable to that of a single mode fibre, but also has a lower core index, used to restrict the number of guided modes.

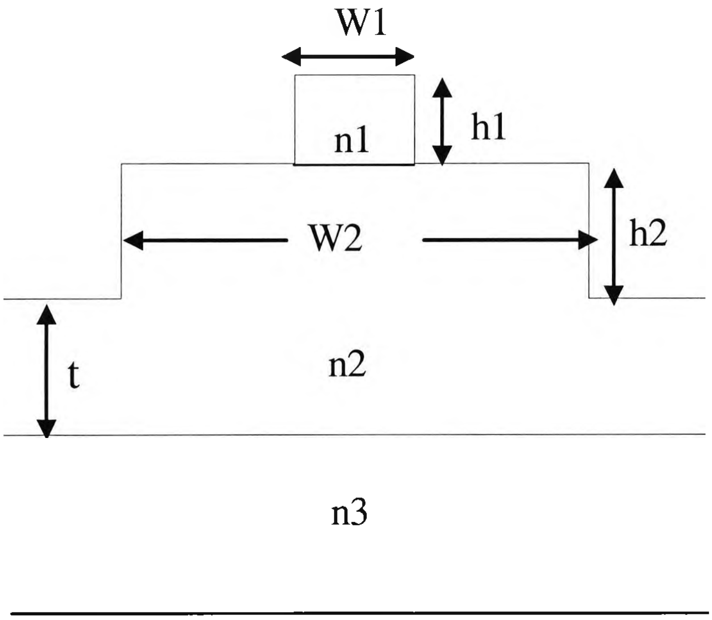

Fig.5.15 Cross-section of a spot-size converter employing a tapered upper rib waveguide.

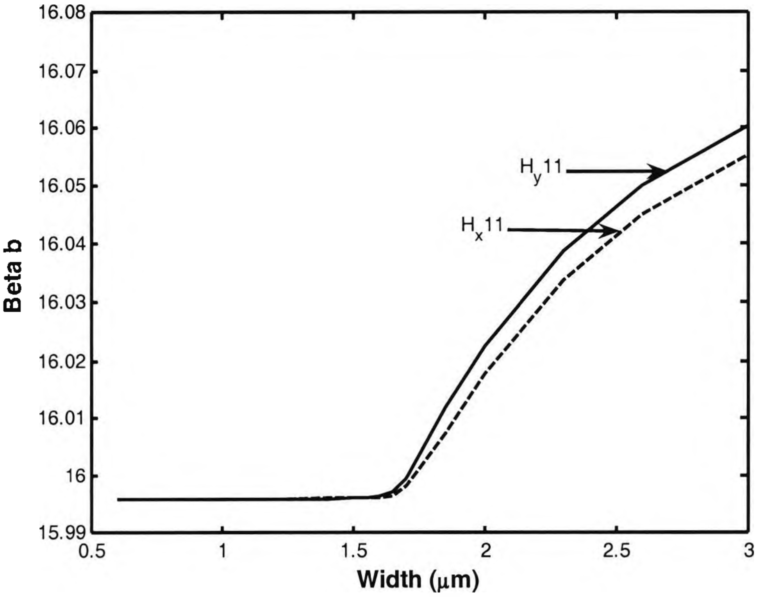

Fig. 5.16 Variation of the normalized propagation constant, b, with the upper rib width, W_1.

The vector **H**-field based FEM discussed in Chapter 3 is employed here to obtain the modal solutions. In this design, 20,000 first order irregular triangles have been used to represent half of the waveguide. Fig. 5.16 shows the variation of the normalized propagation constant, *b*, for the fundamental quasi-TE $\left(\mathrm{H}_{11}^{y}\right)$ and quasi-TM $\left(\mathrm{H}_{11}^{x}\right)$ modes with the upper rib width, W_1. Following general practice, the normalized parameter, *b* given as:

$$b = \frac{n_e^2 - n_3^2}{n_1^2 - n_3^2} \qquad 5.12$$

is presented here, which is a more sensitive parameter than the propagation constant, β, or the effective indices, $n_e = (\beta/k_o)$, where k_o is the wavenumber. It can be observed for both the modes as the upper waveguide, W_1 reduces the normalized propagation constant, *b*, and asymptotically reaches its cutoff value. However, it can be observed that for the all values of the rib width, normalized propagation constant values for the H_{11}^{y} mode are higher than that of the H_{11}^{x} mode. The results for the H_{11}^{y} mode agree well with that of previously published work (Sewell *et al.*, 1999).

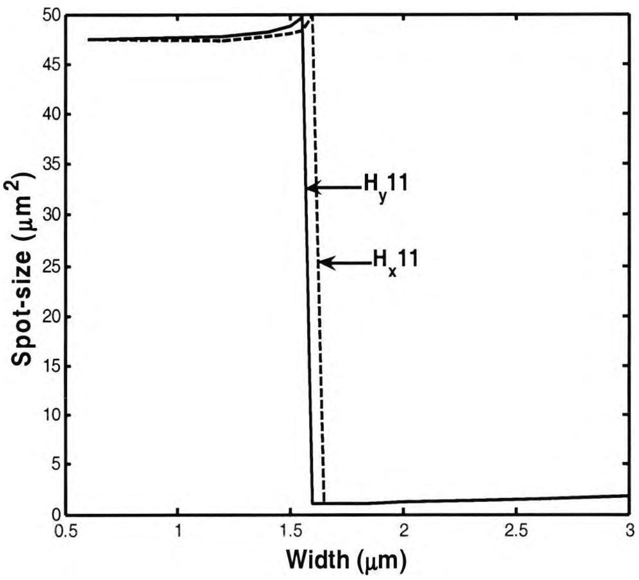

Fig. 5.17 Variation of the spot-size with the upper rib width, W_1.

The resulting spot-size (σ) of the fundamental quasi-TE and TM modes have also been calculated by evaluating the corresponding Poynting vector, **ExH**. In this work the spot-size is defined as the area where field intensity falls to 1/eth of its maximum value (or its power intensity is 1/e^2). The variation of the spot-size with the upper rib width, W_1, is shown in Fig. 5.17. It can be observed that the spot-size increases abruptly when W_1, is reduced from 1.6 μm to 1.55 μm for the quasi-TE mode spot-size increases from 1.0 μm^2 to 51 μm^2. Similar changes for the quasi-TM mode takes place when rib width is reduced from 1.65 to 1.60 μm. Although, Fig. 5.16 shows only a smaller change of the *b* value in the corresponding region, however, it can be clearly observed from this figure that quasi-TM mode approaches its cutoff slightly before that of the quasi-TE mode.

The total power fraction in each of the waveguide regions has also been calculated. The variations of the power fraction in the upper rib P_2, the lower rib P_3, and the substrate regions P_5 are shown in Fig. 5.18. It can be noted that as the upper rib width is reduced, power P_2 carried by the upper rib area is also reduced. It can be further noted that as rib width is reduced, the power fraction P_3 in the lower waveguide core is significantly increased.

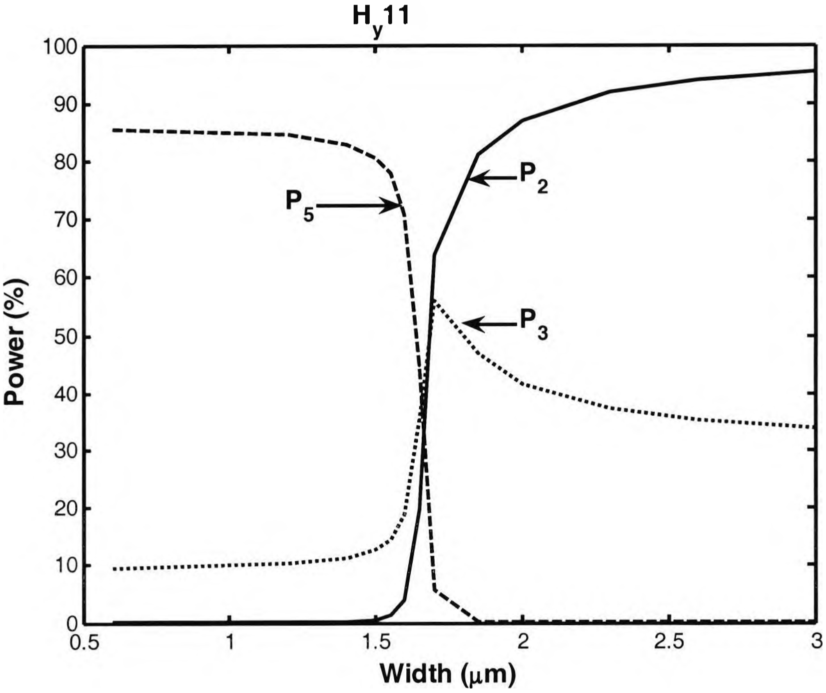

Fig. 5.18 Variation of the power fractions with the upper rib width, W_1.

For the quasi-TM modes, the H_x field is the dominant component of the fully hybrid optical modes, the contour for the H_x field for the fundamental quasi-TM mode $\left(H_{11}^{x}\right)$ mode is shown in Fig. 5.19, when $W_1 = 1.85$ μm. This figure clearly shows the optical field is mostly confined in the upper rib region.

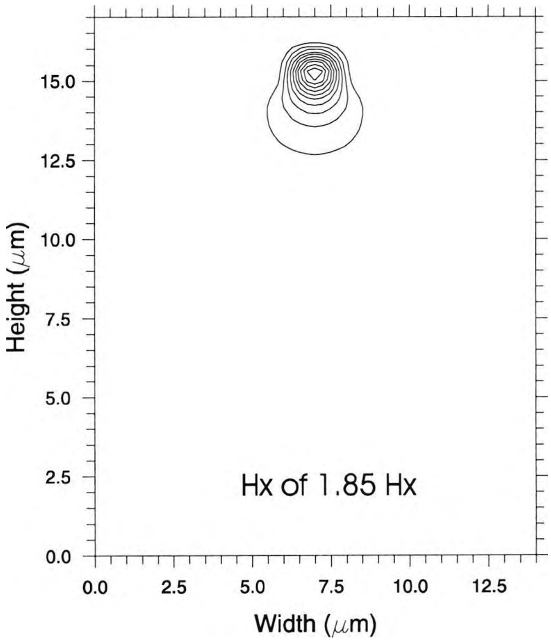

Fig. 5.19 H_x field contour for the fundamental quasi TM mode when W_1= 1.85 μm.

The field contour for the dominant H_x component is shown in Fig. 5.20 for the structure in which the upper rib width is 1.65 μm. It can be observed that in this case, that confinement of the optical power is shared between the upper rib and the lower waveguide region. The optical power is

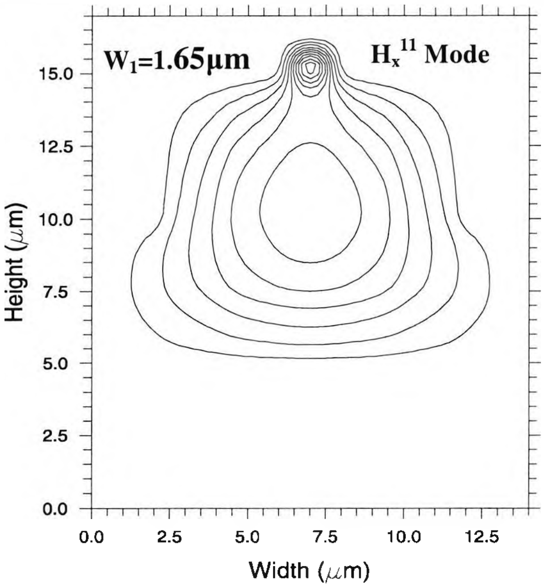

Fig. 5.20 H_x field contour for the fundamental quasi-TM mode when W_1 = 1.65 μm.

Fig. 5.21 shows the structure when the upper rib width is further reduced to 1.60 μm and it can be seen that most of the optical power is confined in the lower waveguide core region. It can be noted that an abrupt change of the overall field profile occurred when the upper rib waveguide width is changed only slightly from 1.65 μm, as shown in Fig. 5.20, to 1.60 μm, as is shown in Fig. 5.21.

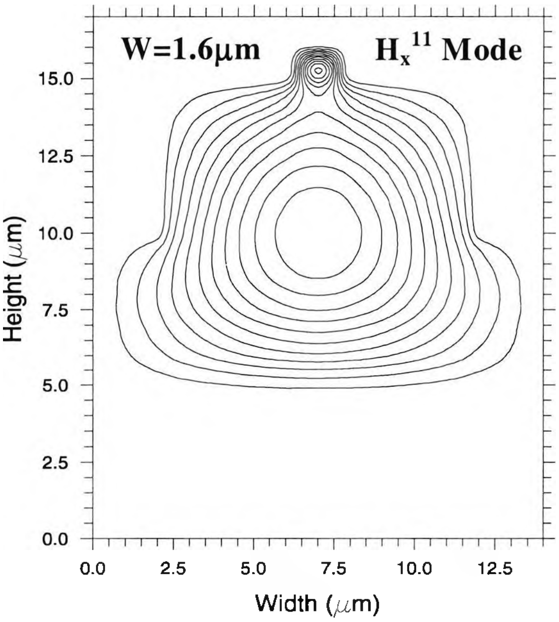

Fig. 5.21 H_x field contour for the fundamental quasi-TM mode when W_1 = 1.60 μm.

It can be seen that for a lower rib waveguide width the field expands considerably and if the PIC is now butt-coupled to a SMF, the coupling efficiency would be considerably higher although in this case, we did not calculate the coupling efficiency as this would be calculated in Chapter 6 where a tapered SSC is designed. However, it can also be noted that a field profile is not completely symmetrical, which would restrict any further improvement in the coupling efficiency. The lower waveguide cross-section may be adjusted to improve the symmetry of the field profile: however, using such a non-circular lower waveguide core, it would rather be difficult to obtain a circular spot-size.

5.6 Summary

The principle of spot-size conversion of the beam evolution in a waveguide and the need to have integrated spot-size converters has been presented in this chapter. The numerical analysis of the waveguide discontinuity problems is also addressed by using least squares boundary residual method. In this method, an abrupt discontinuity in the transverse plane, $z = 0$, between two arbitrarily shaped uniform waveguides is considered. A functional has to be minimised by obtaining a stationary solution which satisfies the continuity conditions of the tangential fields in a least square sense. The versatile vectorial FEM together with LSBR method is applied to the novel design of the multimode mode waveguide as a spot-size converter to improve the coupling efficiency to a single mode fibre from 18% to 36%. The phenomenon of spot-size conversion is also demonstrated in the design of a twin rib SSC to improve the coupling efficiency to a SMF. In this section, the VFEM has been used as a stand-alone in this work to examine the prospect of achieving bigger spot-size for efficient coupling. The spot-size conversion occurred when the upper rib waveguide is 1.6 μm with the quasi-TE mode spot-size increases from 1.0 μm^2 to 51 μm^2. However both SSC designs may need further improvement to achieve a more circular spot-size in future.

Chapter 6

Tapers

6.1 Introduction

In this chapter, an optimized design of a Tapered Spot-size Converter (SSC) using the versatile Finite Element Method (FEM) and Beam Propagation Method (BPM) is presented. The numerical precision and efficiency of the BPM is demonstrated by comparisons with the **H**-field Vector Finite Element Method (VFEM) used alone in Chapter 5 to design SSC. In particular, the focus is on varying different SSC structural parameters to optimize the design issues such as the SSC length, radiation losses, and the coupling efficiency.

A well-confined optical beam is required to optimize the performance of a wide range of photonic devices, such as semiconductor lasers, amplifiers, modulators or switches. It is well known that for such a photonic integrated circuit (PIC) with a small and non-circular spot-size, if directly butt-coupled to a single-mode fibre (SMF) with a large and circular spot-size, nearly 80-90% of the optical power can be lost due to a large mismatch between their spot-sizes. In the past, to overcome such a high loss, when coupling a SMF to PIC, a micro lens (Liau *et al.,* 1995) or lensed fibre (Yamada *et al.,* 1980; Edwards *et al.,* 1993) has been used to enhance the coupling efficiency. However, there is still problem of field mismatch since both the size and shape of the beam needs to be converted and stringent alignment tolerances are also required for the photonic devices, which causes an increase in the packaging cost and makes the production more difficult, as was mentioned in the last chapter. For a low-density subscriber network, such a large cost would inhibit the rapid extension of fibre-to-the-home (FTTH).

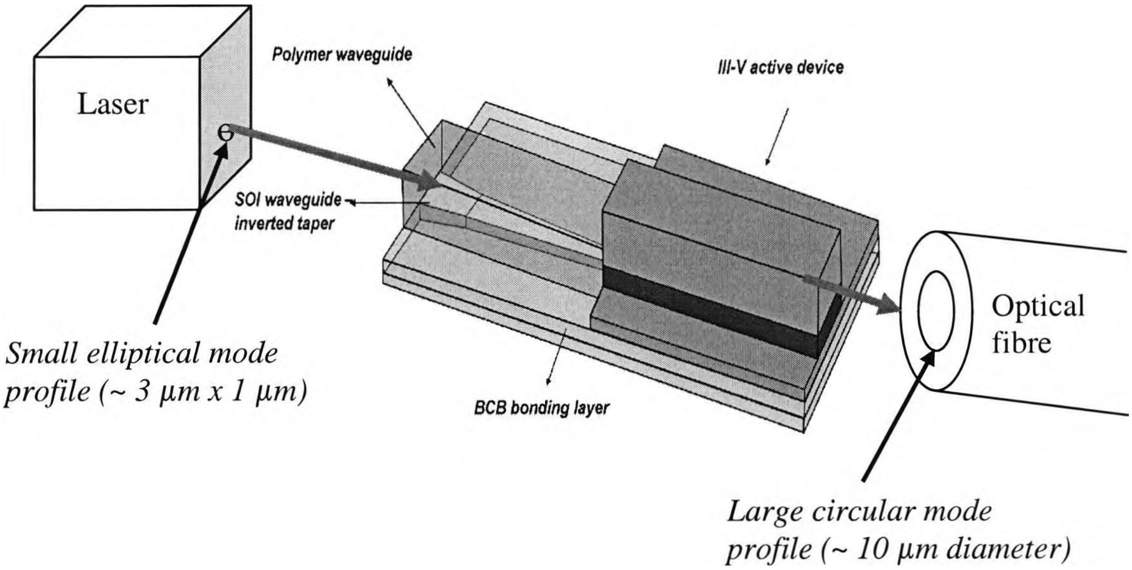

Fig 6.1 Laser to fibre coupling using tapered waveguide.

In this section, a combination of both VFEM and FVBPM are employed to investigate the propagation of a well-confined beam travelling along the longitudinal z-direction of the taper. A taper is a waveguide in which the width of its primary core is gradually decreased in steps along the longitudinal direction of the waveguide. In carrying out the optimisation, a lateral taper design which has minimum loss and maximum coupling efficiency will be presented. Fig. 6.1 shows the optical arrangement by which a tapered waveguide can be used to enhance the coupling between devices such as laser and a single mode optical fibre. The arrangement of the laser, tapered waveguide, and optical fibre, as can be seen from Fig. 6.1, shows that alignment tolerances will be a very important issue when the optical devices are butt-joint coupled for maximum power transfer to occur.

6.2 Types of Tapers

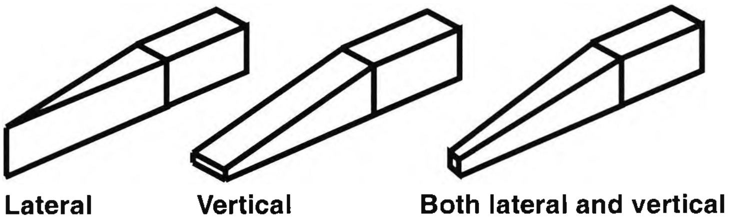

Fig. 6.2 Different types of tapers waveguides

The majority of SSC designs reported recently do incorporate tapered structures, operating very close to the modal cut-off, to expand their spot-size. These designs have been shown to yield an improved coupling efficiency and at the same time show more relaxed alignment tolerances. Various types of tapers such as lateral tapers (Kasaya *et al.,* 1993; Mersali *et al.,* 1995) which are easy to fabricate, vertical tapers (Tohmori et al, 1993; Brenner *et al.,* 1992), more difficult to fabricate, or combinations of both lateral and vertical tapers (Fan and Hooker, 1999) all require the use of more complicated fabrication techniques.

Fig. 6.2 shows the three types of taper waveguides normally used for the controlled reduction of the width which leads to spot-size expansion. In the lateral taper only the width of the primary core is reduced and to minimise loss, the width reduction must be adiabatic. An adiabatic taper is one in which all of the energy remains constant in the initially excited mode throughout the propagation, and the taper is said to be loss-less. It is well known that if a taper is made long enough and has a less steep gradual taper slope, the taper can have loss-less adiabatic propagation (Wu *et al.*, 1997). In the vertical taper only the thickness of the primary core is reduced while in the combined taper, both the width and thickness of the primary core undergoes reduction simultaneously. The investigations carried out throughout this thesis focused on the lateral tapers since they are relatively easy to fabricate. The fact that they do not require any additional growth steps apart from those initially makes them the favourite choice of most optical design engineers. The initial growth is then followed by photolithography and finally the dry or wet etching takes place as discussed in the next chapter. For vertical tapers, additional growth steps are normally required during fabrication which cannot be carried out using standard processing techniques.

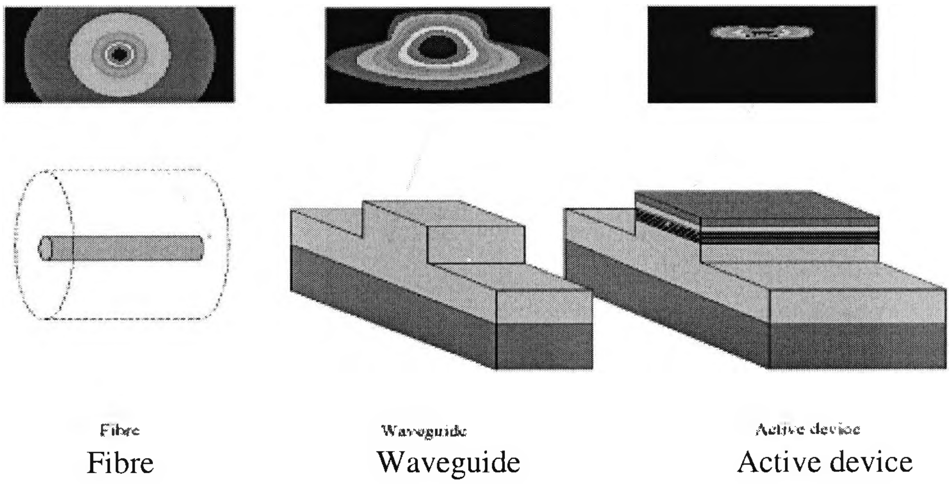

Fig. 6.3 Waveguides used for spot-size conversion

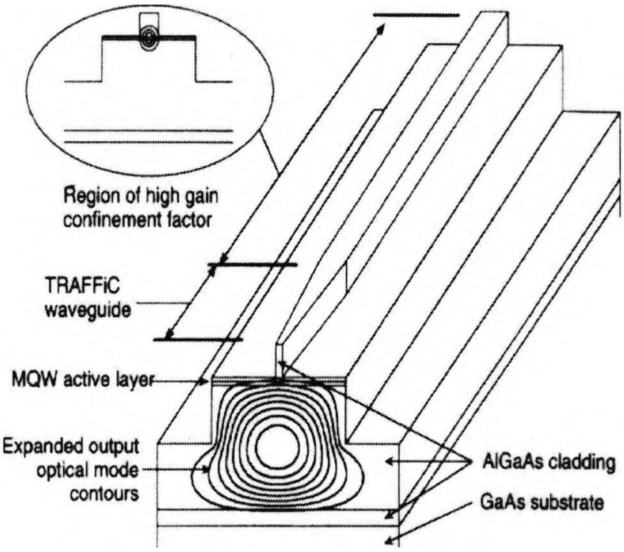

Fig. 6.4 Tapered twin rib structure with contours of optical mode at the input and output (Vawter *et al.*, 1997)

Among the lateral tapers available, the rib waveguide design shown in the middle of Fig. 6.3 is the most popular and well studied taper structure. When the width of the upper rib, the primary core is reduced to the extent that the optical mode reaches the modal cut-off in the region, the power is transferred to the lower rib, the secondary core. The evolution of the mode transformation goes from the strongly confining upper rib to the weakly confining lower rib. Fig. 6.4 shows the twin rib structure and the contours of the expanded optical mode transmission which is the output (Vawter *et al.*, 1997). The optical mode at the region of strong confinement which is the input is shown in the inset of Fig. 6.4.

6.3 Modal Cut-off for Spot-size profiles

This section is devoted to the determination of the cut-off region for various material configurations. In this work, the modal cut-off region for spot-size profiles is defined as the width at which the effective index, n_{eff}, of the quasi-TE mode field becomes less than the refractive index of the core material. For example if the effective index n_{eff} is less than the refractive index of the cladding materials, n_3 i.e. $n_{eff} < n_3$, the taper width at which it occurs is known as cut-off region of the width. In the first example, the dependence of the cut-off region on the discretisation structure of the waveguide. The waveguide under consideration is identical to the one shown in the inset of Fig. 6.5. The taper structure is descretised in first order irregular mesh with number of nodes $n_p = 121 \times 121 = 14{,}641$ and the number of elements used is $n_e = 28{,}800$ to represent half of the waveguide and similar mesh is used for all the designs in this section. It should be mentioned that most of the modal solutions depend on mesh divisions. When sufficient mesh divisions are used, the result converges. As a result it is important that tests are carried out on stability/convergence criteria in order to ensure very good results near the modal cut-off regions. The waveguide has the following material parameters; refractive index n_1 = 3.48 for silicon, n_2 = 3.0 for polyethyleneoxide, n_3 = 2.98 polymethylphenyl siloxane (more examples of materials with the refractive index used in this work are discussed in Chapter 7). The simulation was carried out in two phases; (1) for full-structure of the waveguide; (2) for a half-structure of the waveguide. The height H for the primary core is H = 0.5 μm and H_2 =

3.0 μm, as secondary core. This means that the initial expansion of the beam takes place from the primary core to the secondary core and later into the cladding or substrate which both are of the same material in this work and therefore n_3.

As a result, the modal cut-off will occur under two conditions

1. if $n_3 < n_{eff} < n_2$
2. if $n_{eff} < n_3 < n_2$

The structure under consideration is shown in the inset of Fig. 6.5 where silicon has refractive index n_1 = 3.48, doped polymer has refractive index n_2 which is taken as either 3.0 or 1.47 and refractive index n_3 = 2.98 or 1.45. The work in this section is only concerned with the main or primary core modal cut-off which takes place when the effective index n_{eff} is less than the doped polymer index which is taken as either n_2 = 3.0 or 1.47.

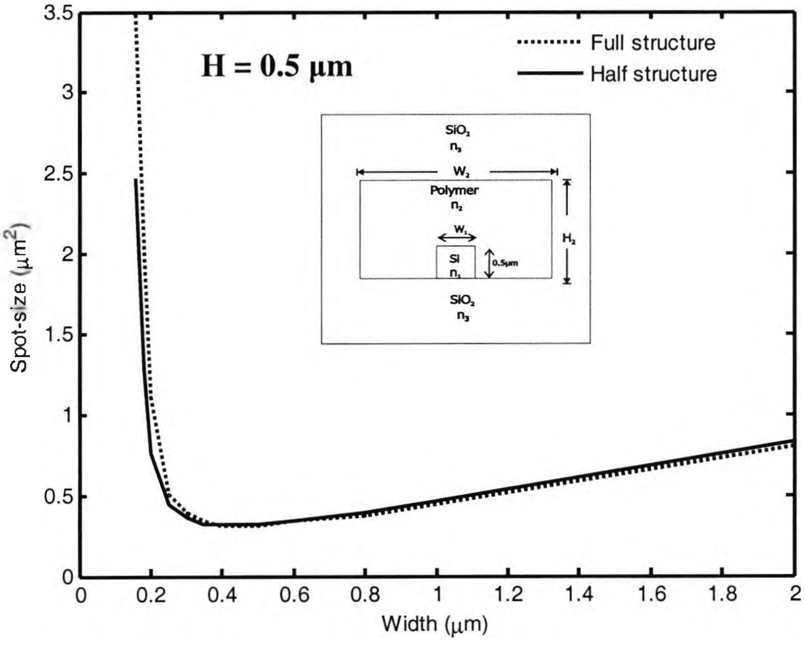

Fig. 6.5 Variation of spot-size profile along the width of the waveguide to determine the width for the modal cut-off region for the structure with indices 3.48/3.0/2.98.

Fig. 6.5 shows the variation of spot-size profile along the width of the waveguide to determine the width for the modal cut-off region. The material indices used are 3.48/3.0/2.98. At the beginning the buried waveguide width W_1 is wide enough and most of the optical power is confined in the primary core region. However as the width is adiabatically reduced, below a certain width the buried guide cannot support the guided mode and the optical power is pushed into the polymer/ doped polymer region for the mode-giving to continue. The primary core width W_1 is varied to control the spot-size. Since the buried waveguide has a higher core index of 3.48, the fundamental mode is confined in this area when its width is sufficiently large. The polymer waveguide has a larger core area comparable to that of a single mode fibre but also has a lower core index used to restrict the number of the guided modes. As the width W_1 is reduced, the value of n_{eff} and the spot-size (σ) are also reduced until the reduction reaches a threshold known as spot-size minimum ($\sigma_{\min}$) and subsequent reduction brings a change in σ and it starts to expand as the width W_1 reduction continues. The value of n_{eff} also exhibits further reduction as the width is reduced. Initially the graph is linear until it reaches close proximity to $\sigma_{\min}$ where it shows an exponential relationship. Further reduction shows an increase in the value σ and the graph return to its linear state until the calculated value of the n_{eff} index is lower than the polymer index and the width W_1 where the last guided mode occurs is known as modal cut-off region width.

It can be seen that for the full structure (FS) the value of $\sigma_{\min}$ is 0.3097 μm^2 at W_1 =0.45 μm while that for the half structure (HS) is 0.3196 μm^2 at W_1 = 0.38 μm. For the FS, the cut-off region occurs when the width reduced to 0.25 μm with the spot-size area of 0.5068 μm^2 while that for the HS is 0.25 μm with the spot-size area of 0.4471 μm^2. This shows that the there is no significant improvement in spot-size predictions by using the HS for the simulations although the HS result is slightly better. For half structure simulations it is advantageous to use symmetry for modal solutions as it gives results with higher accuracy (within a given level of computer resources) than is achieved for the full-structure, especially in this case where 28,800 triangular elements are used.

In the next study, the effect of the height H of the primary core is simulated using the half structure of the waveguide. The waveguide has the following parameters; refractive index n_1 = 3.48 for silicon, n_2 = 3.0 for polyethyleneoxide, n_3 = 1.45 for silica. The results for the three values of H = 1.0 μm, 0.5 μm and 0.3 μm are presented in Fig. 6.6. For H = 1.0 μm, the spot-size min (σ_{min}) is 0.4647 μm^2 at W_1 = 0.35 μm and the cut-off width W = 0.11 μm with the spot-size of 1.294 μm^2. For H = 0.5 μm, the σ_{min} is 0.31957 μm^2 at W = 0.38 μm and the cut-off width W = 0.22 μm with the spot-size of 0.5678 μm^2. For H = 0.3 μm, σ_{min} is 0.3530 μm^2 at W_1 = 0.6 μm while the cut-off width W = 0.41 μm with spot-size of 0.4611 μm^2. The design with H = 0.3 μm has the highest cut-off width, while that with H = 1.0 μm has the lowest. Therefore the probability of achieving a single mode output field with H = 0.3 is highest since number of modes it can produce is greatly restricted while that with H = 1.0 will give a highly multimoded design.

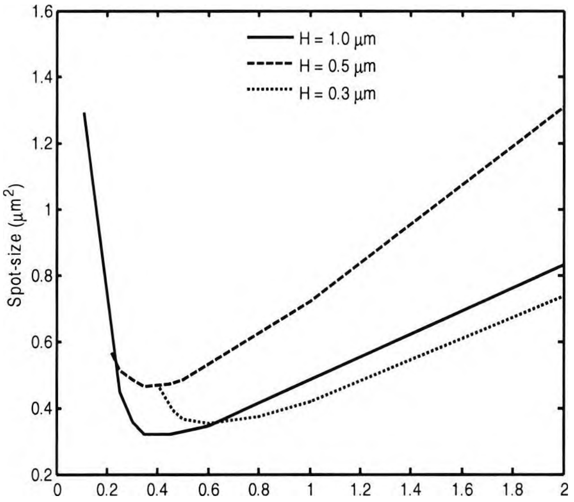

Fig. 6.6 Variation of spot-size profile along the width of the waveguide to determine the modal cut-off region for the structure with indices 3.48/3.0/1.45.

Fig. 6.7 shows the variation of spot-size profile for the typical arrangement for a silicon-on-insulator waveguide which is identical to the one shown in the inset of Fig. 6.5 and has the following parameters; refractive index n_1 = 3.48, n_2 = 1.47, n_3 = 1.45. The height H for the primary core is H = 0.5 μm.

The full structure is simulated in this case and it can be seen that the value of σ_{min} is 0.0988 μm^2 at width W_1 = 0.34 μm and the cut-off width is 0.16 μm with a spot-size area of 0.8041 μm^2. From the value of the spot-size area for the cut-off width, 0.34

μm and the height of the primary core, it will be difficult to predict that the emerging spot-size will be single moded.

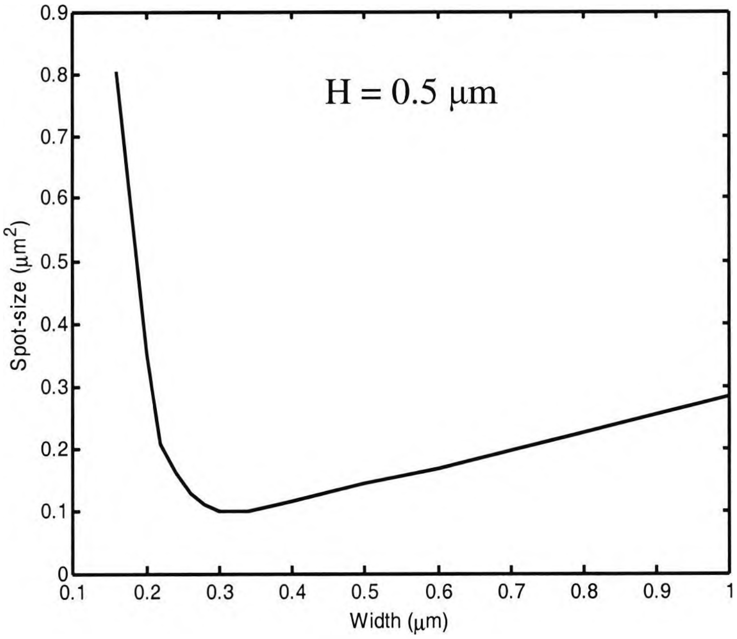

Fig. 6.7 Spot-size profile for the silicon-on-insulator with 3.48/1.47/1.45 in which the modal cut-off is 0.34 μm and the spot-size area is 0.1 μm^2.

The next study involves a comparison between two designs that have a marked difference in the material indices composition already shown in Figs. 6.5 and 6.7 for H = 0.5 μm. Fig. 6.8 shows the comparison between the two designs. The first case is where 3.48/1.47/1.45 in which the σ_{min} is 0.0988 μm^2 at width W_l = 0.34 μm and the cut-off width is 0.16 μm with the spot-size area of 0.80413 μm^2. The second case is for 3.48/3.0/2.98 in which the σ_{min} is 0.3097 μm^2 at W_l =0.45 μm and the cut-off width is 0.25 μm with the spot-size area of 0.5068 μm^2. The larger the value of the cut-off width, the better can the number of modes that can be restricted and thus there is an improved possibility of achieving a single moded output beam for coupling to a single mode fibre.

It is important to observe how small changes in material properties of a photonic device can have a major effect on its operation. It further shows the dependence of waveguide device operations on geometric dimensions of its structure. The study carried out in this section gives valuable information to the experimental optical scientist on parameters that can assist in the compact fabrication of spot-size converters with more systematic design approach, avoiding the simple and inaccurate trial and error method.

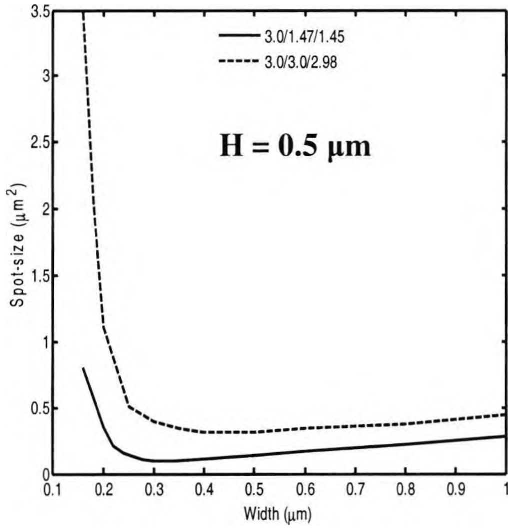

Fig. 6.8 Comparison of the spot-size profiles for the silicon-on-insulator with 3.48/1.47/1.45 and 3.48/3.0/2.98 materials.

6.4 Design of a Twin Rib Lateral Taper

6.4.1 Computational Techniques

In this work, the most important numerical techniques have been used to obtain modal solutions of the uniform waveguide sections. In other to understand the expansion of the mode shape in the tapered section, it is useful to obtain the modal field profile at each segment of the tapered structure. The main advantage of the finite element method (FEM) over other numerical methods is that its vector solution is more accurate and its use of the infinite element more useful as the mode expands near cut-off. All these attributes make the FEM the preferred choice for this work. The Finite element method, as stated in Chapter 3, is more accurate in its representation of the waveguide cross-section using triangles of irregular shapes and sizes. This particular advantage is more significant when the waveguides have curved or slanted side walls, or have arbitrary shapes or index distributions. In the FEM approach, the vector **H**-

field based formulation (Rahman and Davies, 1984*a*) has been established as one of the most accurate and efficient techniques, since unlike the alternative **E**-field formulation, all three components of the vector **H**-field are naturally continuous across the dielectric interfaces. This vector **H**-field based VFEM is used in this work to obtain the modes of the various types of SSC structures reported here. Also used in this work is the full-vector beam propagation method (FVBPM) (Obayya *et al.*, 2000), which is field evolutionary in its approach and computationally more costly than the FEM or FDM based modal solution approaches, but an essential approach for a guidedwave structure with a continuously changing waveguide cross-section. The BPM is widely used for the analysis of light propagation in longitudinally varying waveguides. In this case, the FEM-based BPM (Obayya *et al.*, 2000), is computationally more efficient than the FDM or FFT-based BPM. To show the validity and usefulness of this approach, numerical results are shown for Gaussian-beam excitation of straight and tapered rib waveguide and guided-mode propagation in a rib waveguide, and are compared with the other VFEM results.

It is also necessary to analyze the butt coupling between the SSCs and the SMF and also to obtain the coupling parameters inside the SSC section. In this work the overlap integral has been used to find the power coupling efficiency between the SSC and the SMF.

6.4.2 Design Parameters and Spot-size evolution

A SSC structure, composed of twin rib waveguides shown in Fig. 6.9 is similar to that discussed in the last chapter and is the same as shown in Fig. 6.4. Sewell *et al.*, (1999) reported a design similar to this structure; however, to produce a more symmetrical spot-size in this design, it is assumed that the lower rib is etched completely until the lower cladding is reached. The particular structure being studied (see Fig. 6.9) here has the following parameters: $W_2 = 10$ μm, $H_1 = 1$ μm, $H_2 = 4$ μm, $t = 4$ μm, $n_1 = 3.4092$, $n_2 = 3.3592$, $n_3 = 3.3552$, $n_4 = 3.3292$, and the operating wavelength is 1.319 μm (Rahman *et al.*, 2002).

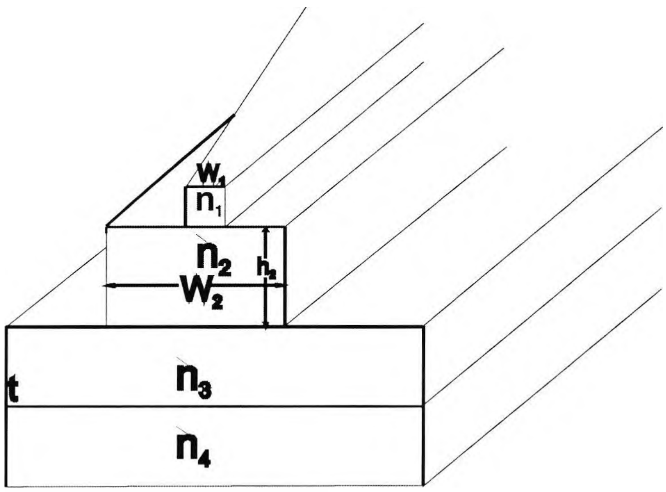

Fig. 6.9 Schematic diagram of a twin rib waveguide spot-size converter structure.

The upper rib waveguide width, W_1 is varied to control the spot-size. When the upper rib waveguide width (W_1) is sufficiently wide, most of the optical power is confined to the upper rib region. However, as this width is gradually reduced, below a certain width the upper guide cannot support a guided mode and the optical power is pushed downward and guided by the lower rib waveguide. The upper rib waveguide has a larger core index and hence the fundamental mode is confined in this area when its width is sufficiently large. The lower waveguide has a larger core area, comparable to that of a single mode fibre, and there is a substrate with a lower core index, used to restrict the number of guided modes.

The **H**-field based FEM is employed here to obtain the modal solutions. In this example, 11,312 first order irregular triangles have been used to represent half of the waveguide. Fig 6.9 shows the resulting spot-size (σ) of the fundamental quasi-TE H_{11}^{y} and TM H_{11}^{x} modes have also been calculated by evaluating the corresponding Poynting vector, **ExH**. In this work the spot-size is defined as the area where field intensity falls to 1/eth of its maximum value (or its power intensity is $1/e^2$).

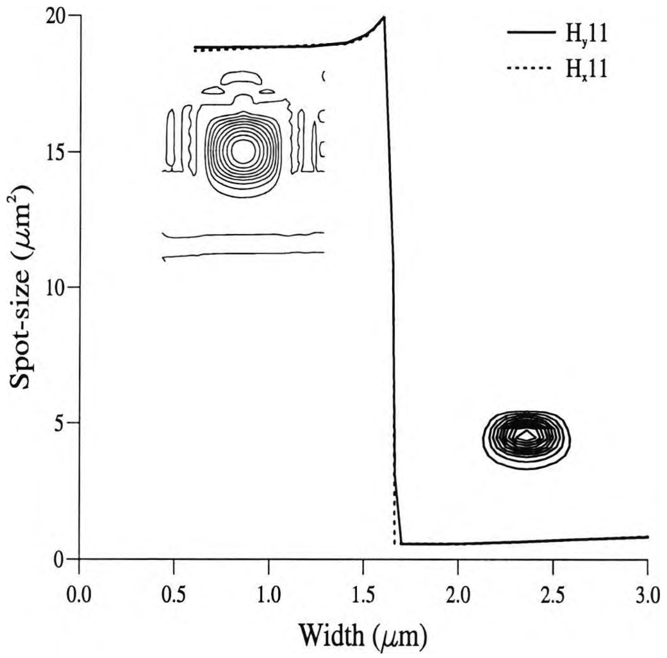

Fig. 6.10 Variation of the spot-size with the width of the taper for the H_x11 and H_y11. Please note that the insets are not drawn on the same scale.

The variation of the spot-sizes with the upper rib width, W_1, is shown and it can be observed that spot-size increases abruptly when W_1 is reduced. This sudden change happens when W_1 is reduced from 1.65 μm to 1.6 μm for the quasi-TE mode spot-size increases from 0.6 μm^2 to about 20 μm^2. The insets show the modal field profile at $W_1 = 3$ μm before expansion and $W_1 = 1.2$ μm after expansion has occurred.

In this work, the BPM has been used to study the evolution of spot-size transformation along the tapered optical structure. To test the stability of the BPM developed, initially the evolution of the modes in a uniform optical structure is carried out. In the BPM, either a mode profile (obtained by any modal solution approach, such as the FEM) or a Gaussian profile with arbitrary beam waist (Ω_o) can be used as the initial field. Fig. 6.10 shows the variation of normalized propagating power, P_t, with the propagating distance, Z, of the waveguide for various incident beam waist Ω_o, of the Gaussian input.

The Gaussian field used here as the input excitation is given by

$$\Phi(x,y) = A \exp-\left[\frac{(x-x_0)^2+(y-y_0)^2}{\Omega_0^{\,2}}\right] \qquad 6.1$$

The parameters x_0 and y_0 are the coordinates of the Gaussian beam, Ω_0 is the Gaussian beam waist or radius, x and y are coordinates of the output field obtained from the waveguide. The x_0 can be determined by dividing into two the sum of divisions in the x –direction e.g. there are 8 divisions, x1, x2, x3, x4, x5, x6, x7 and x8. Then as a result

$$x_0 = (x1 + x2 + x3 + x4 + x5 + x6 + x7 + x8)/2 \qquad 6.2$$

and

$$y_0 = (y1 + y2 + y3 + y4 + y5 + y6 + (y7/2) \qquad 6.3$$

With reference to Fig. 6.9, there are 9 divisions in the y –direction for y1, y2, y3, y4, y5, y6, y7, y8 and y9. In equation 6.3, y_0 is defined in relation to the centre of the Gaussian beam in the vertical direction which falls in the middle of the 7th division; therefore the 7th division has to be divided into two to give the y_0 coordinate.

Fig. 6.11 shows the variation of the spot-size with propagating distance for uniform Gaussian radii 0.5 µm, 1.0 µm, 1.5 µm, 3.0 µm and an input modal solution. The top horizontal line is for the case when the modal solution of upper waveguide for W_1 = 3.0 µm, is used as the input, which shows that little or no power loss occurs through radiation modes. The negligible power loss arises because the fundamental mode from the modal solution matches very well with that of the BPM solution and no higher order mode is generated; hence no appreciable power loss occurs from the mode coupling. On the other hand, when a Gaussian-shaped beam is used, it excites higher order modes besides the fundamental mode and these higher order modes would radiate out. Power carried by the excited higher order modes depends on the mismatch between the mode guided by the structure and its initial excitation used by the BPM simulations. It can be seen from this figure that input Gaussian radius Ω_o = 1.0 µm is the optimum for this case. For the Gaussian input Ω_o = 1.0 μm is the optimum beam, when 90% normalized optical power couples, but for either when Ω_o < 1.0 μm or Ω_o > 1.0 μm overall loss is increased. It can be seen from this figure that when Ω_o = 0.5 μm, the power is about 58% and for Ω_o = 1.5 μm, the power is about 78%.

It can also be seen that in all cases, the propagating power stabilizes in the region of 600 μm and above for all the curves as Ω_o is reduced from 3.0 μm to 1.0 μm because the radiation modes responsible for the field mismatch at the beginning of the propagation radiate out quickly.

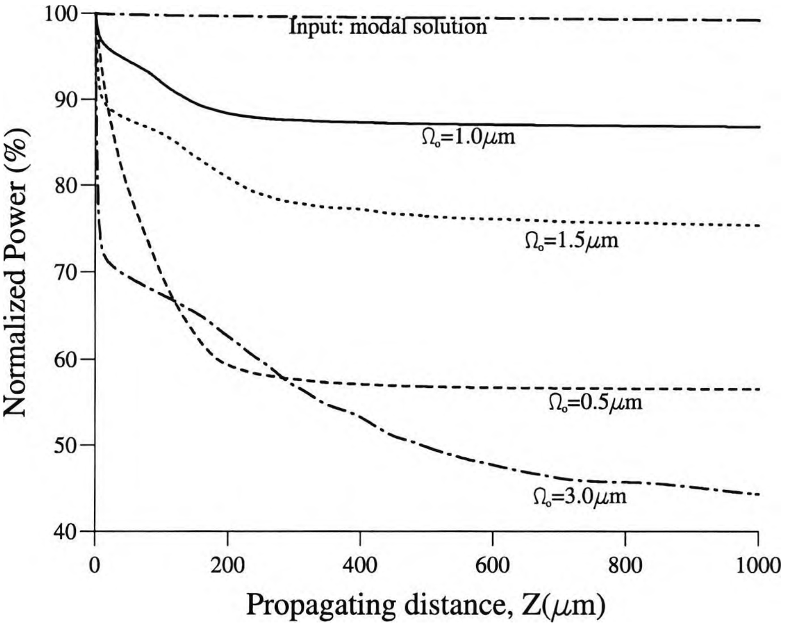

Fig. 6.11 Variation of normalized power along the propagating distance for various Gaussian radii.

Fig. 6.12 shows variation of the spot size of the evolving beam with the propagating distance, Z, for two different Gaussian radii Ω_o = 1.0 μm and 3.0 μm as input beams into the uniform guide with W_I = 3.0 μm. The result shows that the final spot-sizes with Ω_o = 1.0 μm and 3.0 μm are almost identical, because the Gaussian beam launched has eventually settled to the guided modes of the uniform structure. However, the Gaussian beam also excites higher order modes, which causes mode beating and the resulting oscillation in its spot-size is clearly observed. As higher order modes radiate out, the spot-size (σ) stabilizes when Z > 450 μm to about σ = 0.9 μm^2 which further demonstrates the accuracy and stability of the BPM, even when arbitrary Gaussian input fields were used. The oscillating peak deviates more from stablity σ for $\Omega_0 = 3.0$ μm (see (A) in Fig. 6.12). The visible twin peak (see (B) in Fig. 6.12) indicates mode beating between the fundamental and two higher order modes, but as 3rd mode radiates out more quickly than the 2nd mode, the Gaussian beam settles as propagation proceeds.

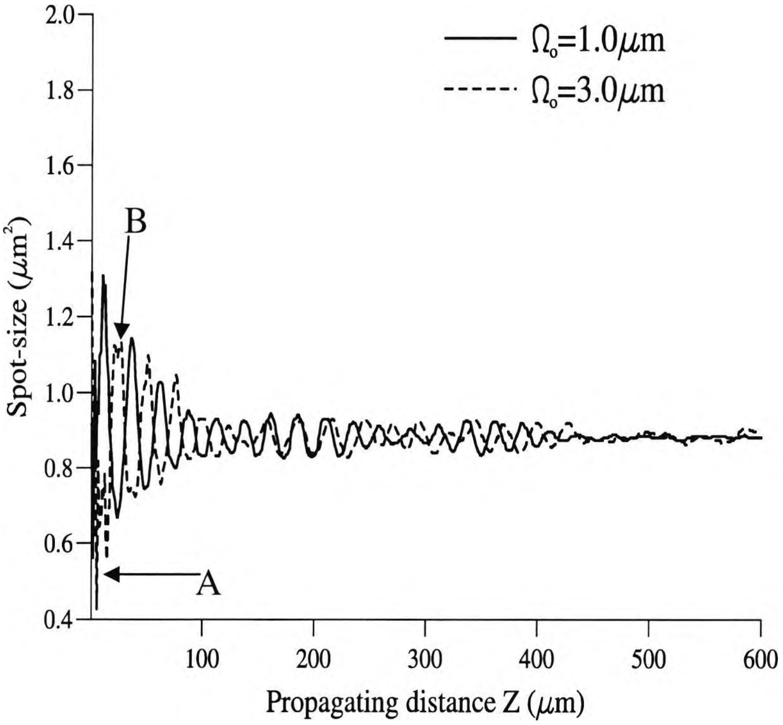

Fig. 6.12 Variation of the spot-size with propagating distance for uniform Gaussian radii 1.0 and 3.0 μm.

6.4.3 Comparison of FEM and BPM SSCs

The resulting output field profile for a BPM Gaussian output for $W_1 = 3.0$ μm when $\Omega_0 = 3.0$ μm is shown in Fig. 6.13. It can be observed that it is almost identical to the modal solution for $W_1 = 3.0$ μm as shown as an inset in Fig. 6.10, which indicates a close agreement between the predictions of the BPM and FEM.

Comparison between the BPM and FEM for calculating the spot-size for different widths of the uniform waveguides was carried out by using BPM. The results obtained for the BPM were then compared with those of the FEM, as shown in Fig 6.14. The Gaussian-beam excitation was used with Ω_o = 3.0 μm for a propagating distance Z = 1000 μm. The location of the expansion for the BPM is W_1 = 1.5 μm. When the modal solution simulation is carried out for a width reduction from W_1 = 3.0 μm, the location of the expansion for the FEM is W_1 = 1.7 μm.

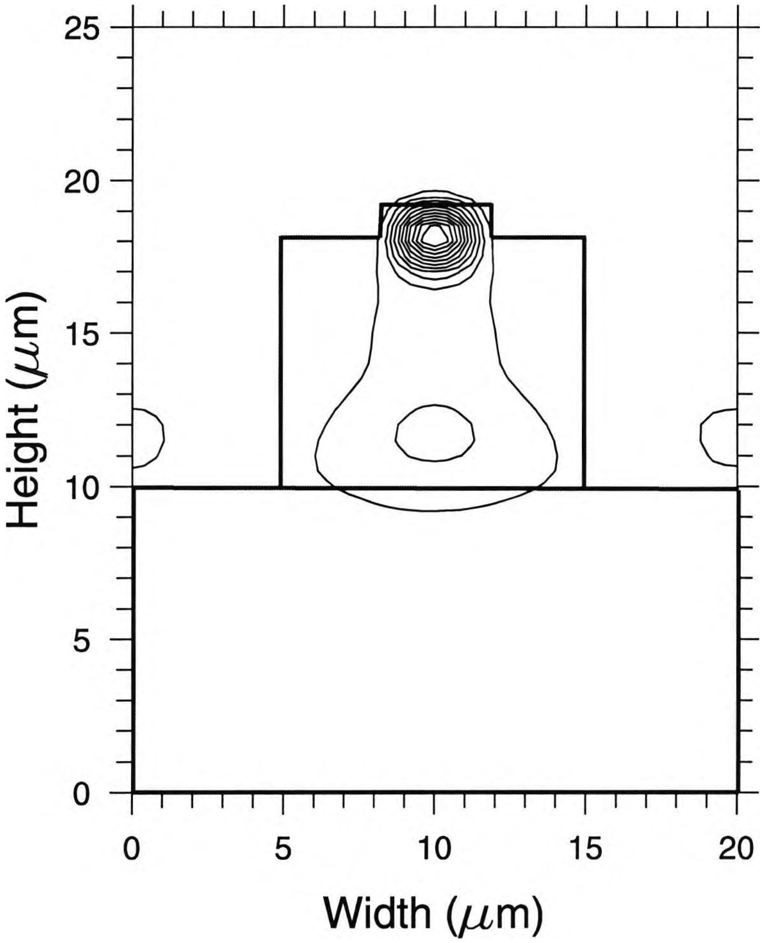

Fig. 6.13 The output field profile for a BPM Gaussian output for W_1 = 3.0 μm

The reason for this difference in the expansion point can be attributed to the use of the PML layer which cut out the interference of the unwanted radiations with the evolution of the spot-size transformation and this reduces the size of the primary core which leads to earlier expansion in BPM. For this comparison to be effective, the same parameters are used for both FEM and BPM simulations, such as uniform guide, material indices and same mesh. There is no PML layer in the FEM formulations. It can be seen that there is very close agreement between the two results.

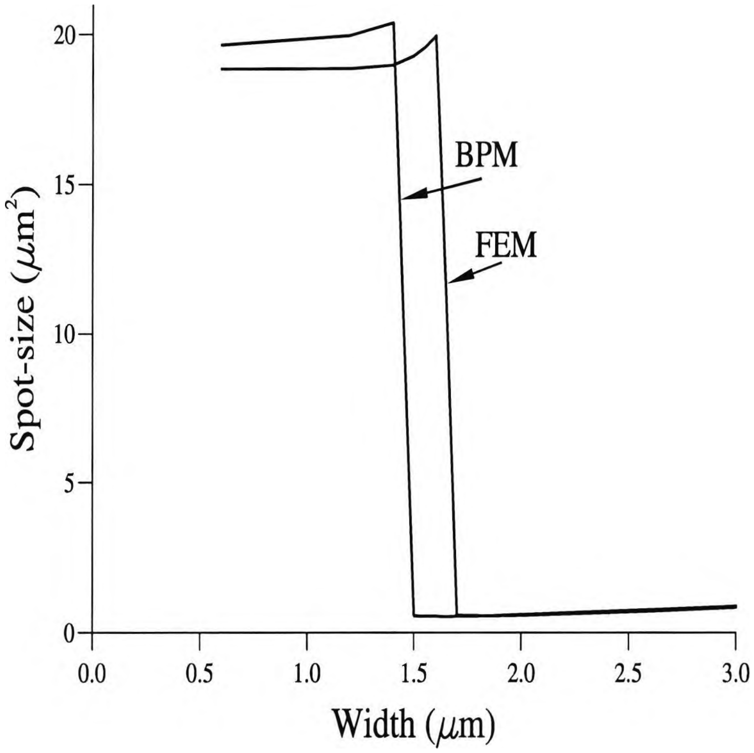

Fig. 6.14 Comparison between the BPM and FEM for calculating spot-size for different width of uniform waveguides

6.4.4 Observed Mode Beating Analysis

Subsequently the BPM was used for calculating the spot-size for an actual tapered rib waveguide. The variation of the spot-size with the propagating distance, Z = 4000 μm where the initial width, W_i = 2 μm and the final width, W_f = 0.3 μm is shown in Fig 6.15. The result shows the initial spot-size expansion at Z = 1300 μm: however peaks occur at periodic intervals for the spot-size. The periodicity observed in the spot-size result is due to the ***mode-beating*** phenomenon. The spot-size oscillation occurs between 66.5 μm^2 and 27.7 μm^2 from Z = 1300 μm to 4000 μm.

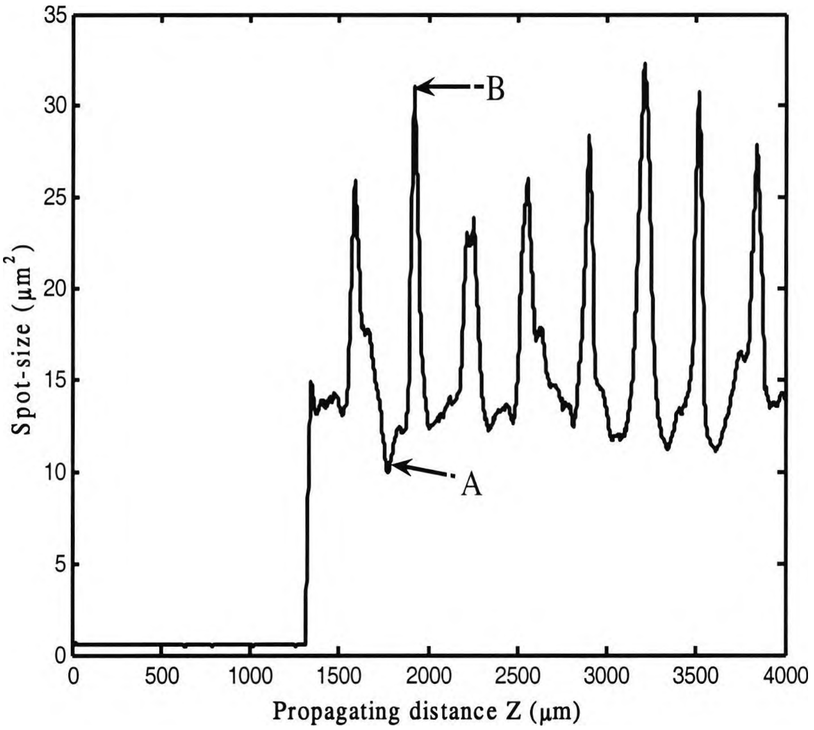

Fig. 6.15 Variation of the spot-size for the lateral taper rib waveguide exhibiting mode beating phenomenon

To identify the mode beating, beam profiles are plotted in selected positions. Fig. 6.16a shows the field profile at Z = 1775 μm where σ showed a minimum value and it can be seen that the corresponding field has not expanded and it is small compared to the field profile shown in Fig. 6.16b, where σ shows a peak at Z = 1923 μm in which the field profile is large and has expanded well into the lower rib and slab regions. The σ points are shown in Fig. 6.15 as **A** and **B** respectively. The two field profiles shown are possible combinations of two or more higher order modes. These fields occurred as a result of the ***mode-beating*** phenomenon, which is due to the combination of two or more higher order modes. The oscillations produced by the mode-beating have an adverse effect on the spot-size imaging of the waveguide under consideration and this also makes the system unstable.

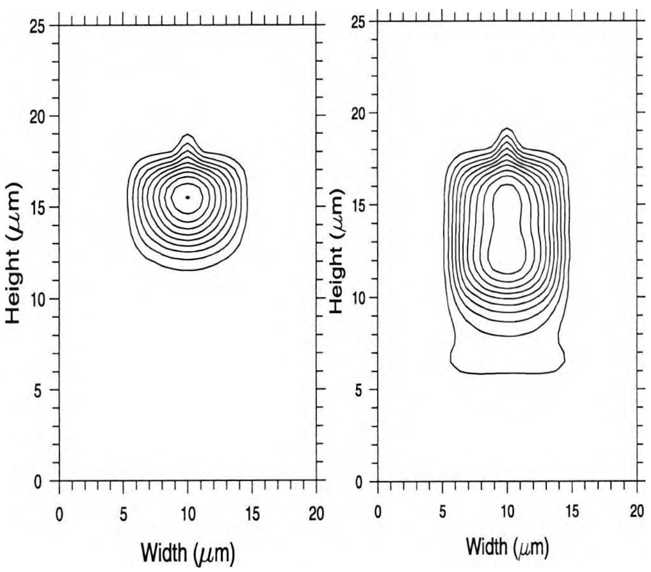

Fig. 6.16 The field profiles at propagating distance (a) Z = 1775 μm and (b) Z = 1923 μm

It can be seen that for a lower rib waveguide width the field expands considerably and if the PIC is now butt-coupled to a SMF, the coupling efficiency will be considerably higher. The power coupling efficiency for the taper SSC was then calculated by incorporating the Overlap Integral method (OI).

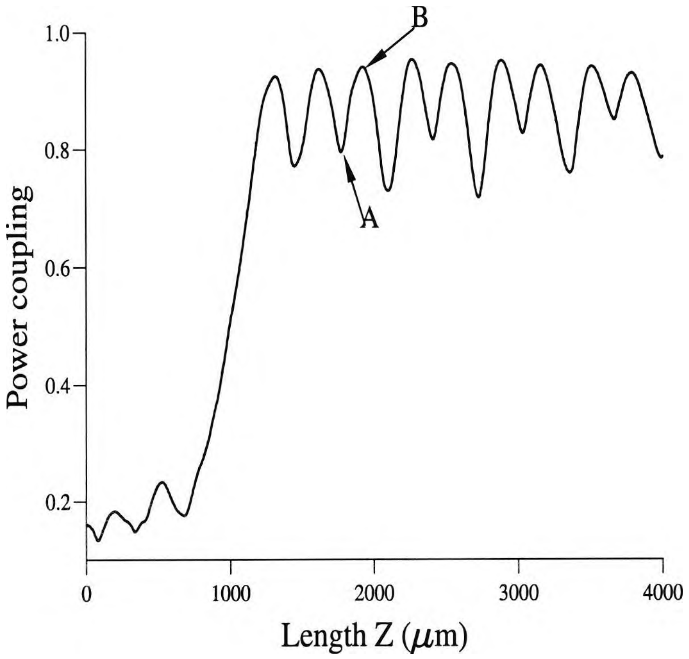

Fig. 6.17 Variation of Power coupling efficiency along the propagating length with the mode-beating oscillations

6.4.5 Optimisation for the Lateral Taper

The analysis described above is for a taper with a length L = 4000 μm, W_i = 2.0 μm and W_f = 0.3 μm. It can be observed from Fig. 6.15 and Fig. 6.17 that it would be more desirable to have a taper design with a shorter length. However, the very narrow final taper width, W_f = 0.3 μm used causes excessive mode beating, so using a slightly wider final taper width but of short length is investigated in light of the need for the rapid extension of fibre-to-the-home (FTTH) in to be achieved with this design. As a result some simulations with wider taper widths were carried out for W_f = 1.2, 1.3, 1.4, 1.5 μm while W_i = 2.0 μm is fixed for a distance L = 1200 μm. The resulting Fig. 6.18 shows the power coupling against length for various widths. It can be seen that all the curves peak, except for W_f = 1.5 μm where the spot-sizes have not completed their full expansion within the length L = 1200 μm.

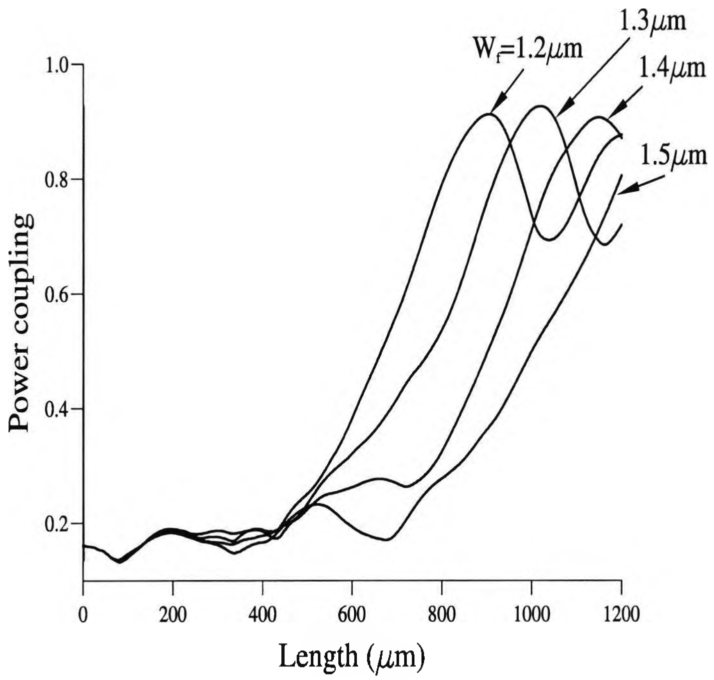

Fig. 6.18 Variation of the Power coupling along the propagation length for various taper widths

Similarly, the variation of the spot-size against various widths for L = 1200 μm is shown in Fig. 6.14. The curves showed some similarity to those in Fig. 6.9 but it is more pronounced in the case of W_f = 1.2 μm but less so for W_f = 1.4 μm.

The results obtained in Figs. 6.18 and 6.19 are a pointer to the need for more work to determine the optimum width, W_{opt} and optimum length, L_{opt}, to be able to obtain the optimum taper design that would be suitable for a fibre-to-the-home package. Fig. 6.20 shows a curve of W_{opt} versus L_{opt} for simulations carried out for lengths between L = 100 μm and 1200 μm. W_{opt} and L_{opt} are defined as the points where the maximum coupling efficiency occurred for various lengths. It can be observed that the longer the value of L_{opt}, the wider is W_{opt}. As L becomes longer, the values of W_{opt} converge. The longer value of L allows the local width, W to better 'settle' the beam, but the shorter L allows for less opportunity for this to occur so a smaller value of W is needed to expand the spot-size.

The device losses at the optimum length are shown in Fig. 6.21. The losses are quite stable at L_{opt} = 200 μm and above and are in the range –0.1 and –0.2 which is remarkable as an acceptable value range in this type of taper design, in which losses are at the bare minimum.

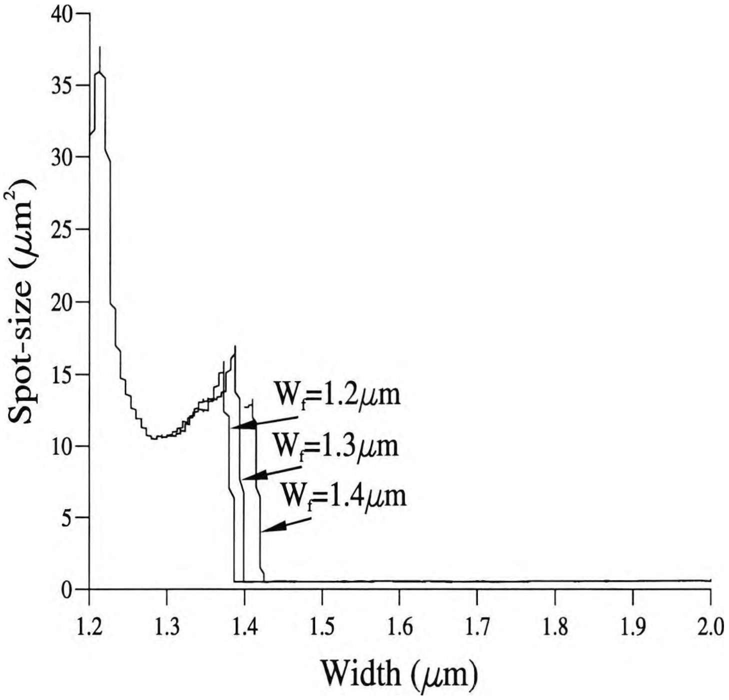

Fig. 6.19 Variation of the Spot-size with the Width of the taper for various final widths W_f

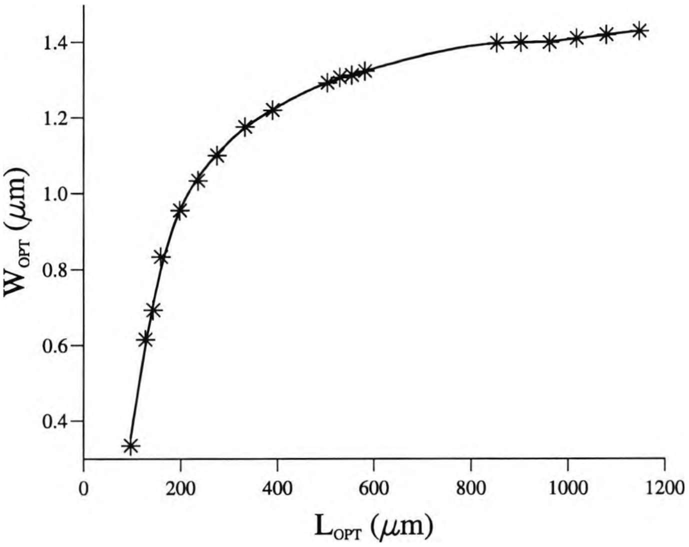

Fig. 6.20 Variation of the optimum taper Widths W_{OPT} against the optimum taper length L_{OPT}

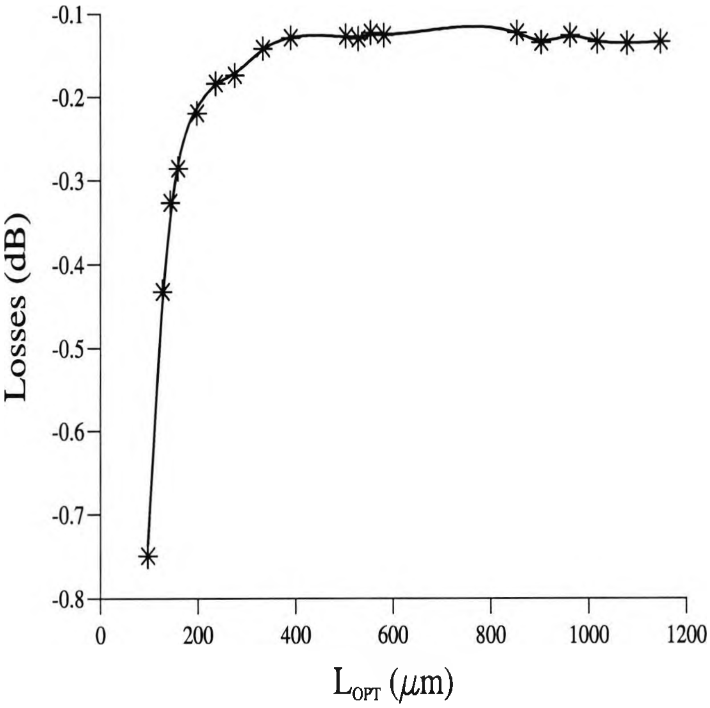

Fig. 6.21 Variation of taper Losses against the optimum taper length L_{OPT}

6.5 Summary

The work presented in this Chapter has illustrated various design options for spot-size converters using the BPM incorporating the overlap integral approach, designed to improve the coupling between a PIC and a SMF. Determination of the cut-off regions for various materials and the geometry of the waveguides and their corresponding spot-size profiles were presented initially. A compact lateral taper SSC design has been produced, which has minimum length, minimum radiation losses, and maximum coupling efficiency of 90%. It has been compared with other conventional SSC designs using the VFEM, and the accuracy of the BPM with the overlap integral has been shown to be excellent. The mode-beating can be experienced when designing taper structures but, as has been shown, this can be avoided by the correct choice of length and width parameters.

Chapter 7

Silicon-On-Insulator Optoelectronics

7.1 Introduction

For optical communications, the primary aim of making Silicon photonics attractive and interesting is the ability to combine optics and electronics on the same substrate. The emerging optoelectronic integrated circuits (OEICs) will perform better than optical or electronics circuits operating independently. In other words, a strong motivation to study silicon-on-insulator (SOI) structures has risen from the desire to monolithically integrate SOI based optical components and control electronics. In recent years, there has been a significant interest in development of optical devices using SOI waveguides. Two main reasons are (1) material and the processing are relatively low cost. (2) The high index contrast between silicon and silica makes it possible for high density integration and this gives rise to size reduction of integrated optical structures. The vertical optical confinement of the buried oxide, offer the ability to integrate optical devices at very high density. Furthermore the silicon-on-insulator is becoming a very promising alternative to doped-glass waveguides for integrated optoelectronics devices because of the availability of the inexpensive SOI substrates, the maturity of silicon processing techniques, and the potential for integration with microelectronic devices.

The fabrication process of silicon wires limits its application in optical communication such as high cost electron-beam lithography, high optical loss of the wires and high coupling loss with other devices like fibres or laser. The high index contrast of SOI wafer offers us the possibility to reduce the sizes of optical devices; but the great obstacle is the designing of the geometry configuration to realise it, which still makes the large cross-section single mode condition preferable.

Another important attribute of the SOI waveguides is their weak polarization dependence. A TE-TM polarisation shift has been reported (Trinh *et al.*, 1997) for a rib waveguide of a phased array grating. The polarisation sensitivity in OEICs occurs basically from two major sources: (1) intrinsic material birefringence and the stress in the waveguiding layer and (2) the cross-sectional geometry of the waveguide. SOI waveguides do not have intrinsic stress unlike their silica (glass) counterparts (Jalali *et al.*, 1998). Therefore the main source of polarisation dependence in SOI waveguides is due to the asymmetry of the device geometry. The TE-TM shift dependence was nearly eliminated with a deep waveguide etching. Care should be taken as a very deep etching can result in multimode waveguiding and concomitant distortion of the spectrum (Jalali *et al.*, 1998).

In networking, due to heavy traffic in passing information from one place to another, there is a need for cost effective, fast and high-capacity optical communications systems to assist in manipulation of large data across various networks in the world in form of data downloads on the internet for example. It is therefore of interest to consumers that optical device manufacturers should pay much attention to optical production device and packaging cycle known as FTTH. It is necessary to be able to couple light from one device to another and make the device as small as possible, and have complex packaging with low tolerances. The heterogeneous nature of the OEICs does not help the mass production which can bring reduction in the cost of these devices.

The main advantage of using silica-based for photonic waveguides is the good optical confinement quality, cheap price and availability with well known characteristics. The silica waveguide fabrication usually starts by deposition of a silicon dioxide layer a few microns thick or alternatively by direct oxidation of the silicon at high temperature. The silica layer is able to (1) provide low index region for allowing optical confinement of light and (2) prevent the formation of highly absorbing silicon substrate. Silica is able to reduce or prevent formation of silicon by consuming silicon in a chemical reaction with oxidants to form silicon oxide in an oxidation process. This is why it is called a buffer layer. A buffer layer is a term that typically refers to a layer sandwiched between two layers of materials to accommodate difference in their physical or chemical properties. The waveguide core is formed by chemical vapour deposition (CVD) method or the flame hydrolysis deposition (FHD) method (Kawachi, 1990) of high index materials such as oxynitride, polymers or silicon. Polymer materials are very special and are able to show some very useful physical properties for example electrooptic, piezoelectric and non-linear effects. Polymer has got thermal coefficient which is ten times more than the corresponding coefficients for silica. Polymer layers are easily formed by deposition of the molten polymeric material and their easy processing offer great flexibility when choosing a substrate such as glasses, silicon dioxide (silica), silicon, indium phosphide, and gallium arsenide. The main advantage of polymer-based integrated optical devices is their high promising ability for use in the field of chemical and biological sensors since the organic groups in the polymeric compounds can react against a specific medium. Some high speed and low voltage switches and modulators have been manufactured using their large electrooptic coefficient properties, for the telecommunication market, offering high performance at low cost.

Silicon wire waveguides based on SOI structure has a lot of potential for high-density integration of OEICs. Fabrication technology and substrate for silicon semiconductors is popular and easy to achieve and will be useful for mass productions. A very good device of submicron silicon devices for OEICs will go a long way to help solve the problem of FTTH.

7.2 Applications of SOI Waveguides

Since 1960s silicon research has steadily advance with the production of solar cells, photodiodes, light emitters from a p-n junction, field-effect modulators, silicon photodetectors and mid-infrared photoelastic modulators etc. In the 1970s there were developments of charge-coupled-device (CCD) images, optical-absorption modulators, high-loss optical waveguides, Schottky-barrier infrared detectors, visible light waveguides, silicon-on-sapphire etc. In the 1980s there are developments of infrared-guided photonics, silicon-on-silicon waveguides with doped epilayers, the first set of SiGe/Si photodetectors were made and these led to more research and other developments of silicon-on-insulator, silicon-on-silicon, and SiGe/Si waveguides. Since 1990s to date research has progressed into silicon-based waveguides and guided photodetectors, laser diodes, optical amplifier and efficient LEDs (Soref, 1993).

There has been steady progress in the development of photonic devices in Group IV materials such as silicon, germanium, carbon and tin. The Group IV photonic components can be classified into the following categories: Low-loss optical waveguides; In Photodetectors, SOI waveguides are ideal for integration with active devices. Using etch and regrowth, an integrated device based on GeSi-SOI Photodetector butt coupled to a passive SOI waveguide has been demonstrated (Jalali *et al.*, 1994; 1998). Light emitters; Long-wave infrared detectors; Optical micro-modulator based on thermooptic effect (Cocorullo *et al.*, 1995); Photoelastic; Acoustooptic; Electromechanical; Micromechanical; SOI-based ring resonators are suitable for polarization independence filters, optical switches, electrooptic modulators, and optical sensors (Xu *et al.*, 2006). The study of ultra-small silicon wire waveguides as a low-loss optical waveguides, offer a large potential for high-density OEICs. There are so many applications of silicon which include fibre-optic transmitters and receivers, wireless transceivers, optical controllers for phased-array microwave antenna, information display panels, printing elements for xerograph, spatial light modulators for optical signal processing, etc. There has been use of SOI strip waveguide to realise compact waveguide arrays, tight bends, waveguide mirrors, short MMI couplers (Aalto *et al.*, 2003); directional couplers on SOI (Trinh *et al.*, 1995; Powell, 2002; Cao *et al.*, 2005*a* and 2005*b*). Passive submicron structures such as ultra-low-loss strip waveguides (Lee *et al.*, 2001), efficient couplers (Barrios *et al.*, 2003a), microring resonators (Little *et al.*, 1998), and nanocavities (Foresi *et al.*, 1997) on SOI have been demonstrated. Active waveguide devices such as electrooptic modulators (Barrios *et al.*, 2003a; 2003b) and optical switches (Zhao *et al.*, 1997) have been fabricated on micrometer-size silicon-on-insulator waveguides. Bragg grating filters based on silicon-on-insulator (Murphy *et al.*, 2001). Asymmetric Mach-Zehnder interferometers (Zhao *et al.*, 1995) wavelength filters have been reported. Wet chemical etching of the SiO_2 has been used to realise movable SOI waveguides with potential applications in switching and sensors (Eng *et al.*, 1995). Also asymmetrically coupled SOI and polymer waveguides have been used to demonstrate wavelength selective photodetection has been reported (Pezeshki, 1996). Compact optical resonators built on SOI waveguides have been reported (Kiyat *et al.*, 2005).

7.3 Fabrication Technologies

Complementary metal-oxide-semiconductor (CMOS) technology is the most useful because it offers great potential for mass production of SOI devices (Bogaerts *et al.*, 2005; Roelkens *et al.*, 2005*b*). Other techniques of growth for SOI structures consist of the following:-

1. Separation by implantation of oxygen (SIMOX) technology (Guerra, 1990; Rickman *et al.*, 1994) uses implantation of oxygen at high concentration ($\sim 10^{18}$ cm^{-3}) followed by a high temperature anneal to form a buried SiO_2 layer in a silicon wafer. A strong dependence of the mode loss on interface roughness and mode confinement has been reported experimentally (Rickman *et al.*, 1994).

2. The bond-and-etchback SOI (BESOI) (Meszera *et al.*, 1998) is a process in which a silicon wafer is first oxidised using wet or dry oxidation techniques followed by hydrophilic bonding to a bare silicon wafer, and a subsequent heat treatment. The first

wafer is then thinned and polished by mechanical and chemical processes to the desired thickness.

3. Separation by implantation of nitride (SIMNI), zone melting of an amorphous Si film to recrystalline that layer (ZMR) (Fen *et al.*, 1981).

4. Two-step dry etch process with a relaxed mask alignment tolerance and no need for epitaxy (Aalto *et al.*, 2006). This is simple to fabricate and it is insensitive to small misalignments between the masks. Also reflections and mode mismatch losses can be minimised with antireflection coatings and the input and output waveguide cross-sections can be optimised.

5. The smart-cut process (Bruel, 1995) is one of the latest SOI technology. In this process, a silicon wafer is oxidised followed by implantation of hydrogen at doses in the range of 10^{16}-10^{17} cm^{-3} followed by hydrophilic bonding to a bare wafer and subsequent heat treatment. The heat treatment causes the implanted wafer to split into two parts leaving a thin layer of SiO_2 and Si bonded to the second wafer. The heat treatment also causes the roughness of the wafer surfaces due to microcavities formation. The rough surfaces are then polished. The main advantage of this method is that the SiO_2 layer can be as thick as in the BESOI, but the silicon over-layer has better uniformity and can be thicker due to the larger implantation range of hydrogen compared to that of oxygen. There is economic advantage in that the second wafer can be reused.

6. Silicon-on-saphire (SOS). Silicon devices are known to have problems which are basic to dependent circuit components due to junction capacitances (Sze, 1985). They cannot take advantage of their semi-insulating substrates to minimize these capacitances. One of the ways of avoiding this problem is to grow silicon devices on an insulating substrate. This gives rise to silicon-on-sapphire (SOS) in which silicon is grown epitaxially on a substrate called sapphire. Recent advances in optoelectronics explore and use the process of silicon-on-insulator (SOI) instead, where sapphire has been replaced with insulator.

7. Solid source Molecular Beam Epitaxy (MBE) has been used to grow layers SiGe-Si on top of an SOI waveguide. The waveguide was made using reactive ion etching (RIE) of Si and SiGe layers.

8. Chemical Vapour Deposition (CVD) reactor epitaxy i.e. growing layers on substrates of Si and Ge.

Some SOI waveguides have been fabricated using wet silicon etching process (Fischer *et al.*, 1996). Production of OEICs using wet etching is difficulty due to the modest critical dimension control. Fabrications using dry etching gives the required anisotropic etch profile and is therefore preferred in practical applications (Solehmainen *et al.*, 2005). The dry etch technology with low pressure chemical vapour deposition (LPCVD) have been optimised with the elimination of reflection losses at the interface between the SOI waveguide and an optical fibre. The tantalum pentoxide Ta_2O_5 antireflections coatings (ARCs) were deposited on waveguide-end facets with atomic layer deposition (ALD). The Ta_2O_5 was used because it is transparent at the $\lambda = 1.55$ μm and it's refractive index is very suitable for the Si/SiO_2 interface.

There are many technologies for fabricating silicon optoelectronic materials like molecular beam epitaxy (MBE), chemical vapour decomposition (CVD) reactor epitaxy and silicon-on-insulator (SOI) is now widely used in optics. It is very important to efficiently couple waveguides to single mode fibres (SMF) especially when the ultra-small wire WG is made up of silicon-on-insulator (SOI) device. It is well known that the development of silicon components which are compatible to the standard silicon technology will be very useful in order to take advantage of the day-to-day productions of the OEICs.

7.4 Design Concept

It has been reported in some previous works that the standard complementary metal-oxide-semiconductor (CMOS) technology can be used for mass production of SOI devices (Bogaerts *et al.*, 2005; Roelkens *et al.*, 2005*b*) but this alone will not solve the problem of integrated optical components unless there is the capability to provide them with low-loss interfaces on mass production scale to an optical fibre. To overcome the problems of mode mismatch and loss mechanism due to the bending radius (i.e. radiation into the substrate) when coupling light from an SOI waveguide into an optical fibre, several approaches have been proposed in the literature to tackle this problem. Grating couplers are one of the best devices because they do not need cleaved facets. However they intrinsically suffer from a compromise between efficiency and optical bandwidth, therefore cannot be used in some applications (Taillert *et al.*, 2002). As a result, we are making use of an approach presented in the literature to use a spot-size converter to transform the SOI waveguide mode to a polymer waveguide mode which matches a lensed fibre mode (Shoji *et al.*, 2002). The optical bandwidth is very large, more than 100nm, and efficiencies are high (Roelkens *et al.*, 2005*b*).

In our work, material loss has been neglected and the mode mismatch between the SOI and polymer waveguide interface is also assumed negligible. Numerical simulation is performed for transverse-electric (TE) polarised light. The geometry and the high index contrast nature of the SOI waveguide make it polarisation-dependent.

Polymer optical waveguide devices play a key role in several rapidly developing areas of broadband communications, such as optical networking, metropolitan/access communications, and computing systems due to their easier processibility and integration over inorganic counterparts. The combined advantages also makes them an ideal integration platform where foreign material systems such as YIG (yttrium iron garnet) and lithium niobate, and semiconductor devices such as lasers, detectors, amplifiers, and logic circuits can be inserted into an etched groove in a planar lightwave circuit to enable full amplifier modules or optical add/drop multiplexers on a single substrate (Ma *et al.*, 2002). Moreover, the combination of flexibility and toughness in optical polymers makes it suitable for vertical integration to realize 3D and even all-polymer integrated optics. As a result of the above attributes, the polymer optical waveguide is being used in this thesis as a connecting device (such as optical interconnects) because of its low-loss and low reflectivity to develop the SOI waveguide. It is critical to ensure that digital and optical signals transferred between components suffer minimal loss of vital information. A simple structure design for this work is an adiabatic inverse taper that is easier to fabricate has been applied as a mode size converter between the silicon core and the silica-based waveguide. The inverse taper was located inside a W_2 x H_2 μm polymer waveguide which has a higher refractive index than the silica-based waveguide. In this case the cross-section 0.5 x 0.5 μm of the silicon core has been used to achieve a single-mode condition (Shoji *et al.*, 2002) as these dimensions, after some simulations, give satisfactory result considering difficulties in fabrication technologies.

There are two methods of realising the single-mode SOI waveguide; (a) The narrow silicon wire (Yamada *et al.*, 2005; Dumon *et al.*, 2004), and (b) Large cross-section rib waveguide (Schmidtchen *et al.*, 11991; Soref *et al.*, 1991). The sub-micron size silicon wire can provide compact system but often it is associated with high propagation and coupling loss with either fibre or laser devices. Recently low waveguide propagation losses were obtained for SOI high index contrast nanophotonic waveguide structure (Dumon *et al.*, 2004; Lee *et al.*, 2001). This work focused on butt-joint coupling between optoelectronic devices and passive nanophotonic tapered polymer waveguides (Roelkens *et al.*, 2005*a*). In butt-joint coupling, the device layers can be grown first, then the substrate is partially covered by a dielectric mask leaving only the taper region unmasked. Then selective re-growth can be carried out to form the taper. The main advantage of the butt-joint is its flexibility to separately design the device layers and the taper layers (Moerman *et al.*, 1997).

An adiabatic taper is a one in which all of the energy remains constant in the initially excited mode through out the propagation, and the taper is said to be loss-less. The lateral taper used here is fairly long. Numerical simulations were considered for various taper lengths from 1000 – 2500 μm, the taper of 2000 μm length gives satisfactory result in order to have a very low loss adiabatic propagation and a good TE mode output. It is well known that if a taper is made long enough and has a less steep gradual taper slope, the taper can have loss-less adiabatic propagation (Agrawal, 1992; Lee *et al.*, 1993; Sakai and Marcatili, 1991; Weder, 1998). The fibre mode was simulated using the normal Gaussian approximation of the mode (Fan *et al.*, 1997).

The modern practical waveguide fabrication techniques cannot overcome the precise control of taper's shape and index profile which the completely adiabatic structures will need. In other words, a loss-less, strictly adiabatic taper cannot be fabricated. We therefore focus on a design that is aimed at getting (1) an improved coupling efficiency, (2) low coupling loss and (3) avoiding higher order modes. There are several different methods that can be used to analyze taper structures such as intrinsic mode calculations (Marcatili, 1985; Arnold *et al.*, 1985), the step transition method (Lu, 1991; Kim *et al.*, 1993; Mitomi *et al.*, 1994), the coupled mode calculations (Marcuse, 1980; Song and Tomlinson, 1992; Yumin *et al*, 1994), and beam propagation methods (Milton and Burns, 1977; Vassallo, 1994; Haxha *et al.*, 2006). From these methods of analyzing taper structures, it is generally believed that an infinite length taper would be strictly adiabatic. It has been shown that taper lengths which are several order of hundreds of microns can achieve low loss (Soref, 1993; Haxha *et al.*, 2006).

7.5 Computational Techniques

The design considerations will not be complete without the mention of the numerical methods used for the calculations of the device parameters. The computational techniques are similar to those used in previous published works (Haxha *et al.*, 2006; Rahman *et al.*, 2003; 2005). The **H**-field Vector Finite Element Method (VFEM) (Rahman and Davies, 1984*b*) and Full-Vectorial Beam Propagation Method (FVBPM) (Obayya *et al.*, 2000) has been employed in order to achieve an optimum coupling efficiency to a standard SMF and the single mode behaviour of silicon wire waveguide must be obtained. This is where the **H**-field full-vectorial finite element method (FVFEM) has advantage over other numerical techniques and has been established as one of the most rigorous full-vectorial approaches for the characterization of the wide range of optical waveguides (Rahman *et al.*, 2005; Rahman and Davies, 1984*c*). The waveguide cross-section is represented by a large number of triangles, which can be of irregular shapes and different sizes. The **H**-field formulation being full-vectorial is used in this study, which is particularly useful for the high refractive index contrast of the SOI materials.

The **H**-field Vector Finite Element Method (VFEM) and Full Vectorial Beam Propagation Method (FVBPM) has been employed in order to achieve an optimum coupling efficiency to a standard SMF and the single mode behaviour of silicon wire waveguide must be obtained. Over the past two decades, several techniques have been employed to analyze optical waveguide structures. There are many numerical approaches available that may be used to account for the modal solution of the optical waveguides. These include the effective index method (Hocker and Burn, 1977), the finite difference method (Stern, 1988), to mention few. Unfortunately many of these techniques would not be able to accurately handle waveguides operating near their cut-off conditions. This is where the **H**-field full vectorial finite element method (FVFEM) (Rahman and Davies, 1984*c*) has advantage over other numerical techniques and has been established as one of the most rigorous full vectorial approaches for the characterization of the wide range of optical waveguides (Rahman and Davies, 1984*a*; Rahman *et al.*, 2005; Obayya *et al.*, 2003). The waveguide cross-section is represented by a large number of triangles, which can be of irregular shapes and different sizes. The full vectorial **H**-field formulation is used in this study, which enables each element to have different properties. This technique has been used to obtain modal solutions of linear, non-linear, diffused, anisotropic, passive, and active waveguides, including the SSCs (Rahman *et al.*, 2003; Wongcharoen *et al.*, 2001).

The versatile full vectorial finite-element based beam propagation method (FVBPM) (Obayya *et al.*, 2000) has been employed to study the optical-mode evolution and transformation of the spot-size along the tapered waveguide. The three-dimensional algorithm incorporates a non-paraxial wide-angle approach and the perfectly matched layer (PML) boundary conditions (Berenger, 1994; Huang *et al.*, 1996) around the computational window are considered. Finally, the overlap integral method (Kobayashi *et al.*, 1997; Haxha *et al.*, 2006) is incorporated into the FVBPM to account for the coupling efficiency between the SSCs and the SMF.

7.6 Results and Discussions

The **H**-field VFEM has been used to obtain modal solution for a simple SOI structure shown in schematic diagram in Fig. 7.1. The geometry of the SOI waveguide is a primary core region, square shaped silicon wire core 0.5 x 0.5 μm, and refractive index n = 3.48 buried under a high-index square shaped polymer secondary core W_2 x H_2 μm. In this arrangement, refractive index for Silicon = n_1 Polymer = n_2 and Silica = n_3. The high-index polymer core is covered by the silica SiO_2 over-cladding. The whole arrangement is fabricated on top of a substrate which is the low-index silica under-cladding and has also silica as over-cladding. The taper had to be fairly long if adiabatic mode of spot-size conversion is to be used. In this work, the design is optimised at a wavelength of 1.55 μm. The cross-section of the silicon wire is 0.25 μm^2 which is suitable for a single mode condition. The normal diameter of a SMF is usually about 6 – 10 μm and this large difference leads to a large coupling loss between the waveguides and the electronic circuits. A spot-size converter (SSC) design is considered that consists of a silicon taper and a connecting device with low-loss, low reflectivity, low refractive-index contrast waveguide made of polymer to enable the functionality of the Si wire waveguide in the OEICs technology. In this study we report the design of a Si wire SSC taper and its characteristics. In this study we report the design of a SSC taper in silicon wire and its characteristics.

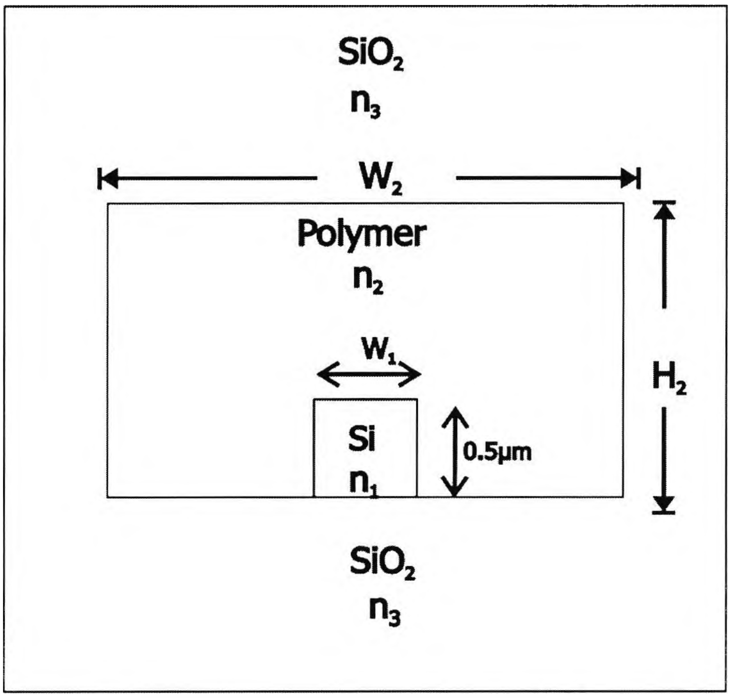

Fig. 7.1 Schematic diagram of the Silicon-on-insulator (SOI).

The modal solution obtained from the FVFEM is used as an input field to the FVBPM code to study the application of polymer as a connecting device between the silicon and the silica due to their high refractive index difference and coupling to the SMF in the SOI arrangement. The mode is more tightly confined by the lower cladding where the index step is greater i.e. Δn_{12} is between 0.48 – 2.01, and is less tightly confined above the guiding region where the index difference is lower i.e. Δn_{23} is between 0.02 – 1.55. The propagating length of the taper is chosen equal to $L = 2000\ \mu$m because of the adiabacity of the conversion i.e. the need to minimise loss as much as possible. The propagating power, spot-size, propagation loss and coupling efficiency were determined when the structure was tapered laterally from initial width W_i, to a final W_f . The Si wire was butt coupled to a SMF and the overlap integral was used to calculate the coupling efficiency.

Refractive Index of Polymers

The refractive index of typical organic polymers is usually between 1.3 and 1.7 depending on the wavelength of the materials (Branrup and Immergut, 1989). The refractive index of polymers can be enhanced by the addition of colloidal particles with high refractive index (Weibel, *et al.*, 1991). Example of such colloidal particle is Lead sulphide (PbS) that exhibits a refractive index on the order of 4 in a wide range of wavelengths (Palik, 1985). The combination of lead sulphide and polyethyleneoxide exhibit refractive index of up to 2.9 at 632.8 nm and up to 3.0 – 3.4 in the whole range of 1000 – 2500 nm (Zimmermann, *et al.*, 1993). Polymer materials with controlled layer thickness and refractive index can be fabricated by adding a hydrogen sulphide solution to a solution containing the polymer and lead ions. Other examples of materials with refractive index 3.0 are Polycarbonate, Polymethylmethacrylate (Dow Corning, 2005) and synthetic polymers. Examples of materials with refractive index 2.98 are Polymethylphenyl siloxane (Dow Corning, 2005), polyethyleneoxide, and synthetic polymers. Polymerized cements, Synthetic fused silica, (Optica Acta, 1967), Polypropylene (Mitchell, 2004), are typical examples of materials with refractive index 1.47. Examples of the type of materials that can give the refractive indices used in this study are summarised in Table 1 below.

Refractive Index	Materials
3.48	Silicon.
3.0	Polyethyleneoxide; Polymethylmethacrylate; Polycarbonate; Synthetic polymers.
2.98	Polymetylphenyl siloxane; Synthetic polymers.
1.47	Synthetic fused silica; Polypropylene; Polymerized cements.
1.45	Silica.

Table 7.1. Table of refractive index and optically associated materials.

The results and discussions are divided into the following sections;

(1) The Silicon SOI taper arrangement when $n_1 = 3.48$, $n_2 = 3.0$, $n_3 = 1.45$, and the Synthetic polymer cross-section is 3x3 μm.

(2) The Silicon SOI taper arrangement when $n_1 = 3.48$, $n_2 = 1.47$, $n_3 = 1.45$, and the Synthetic fused silica cross-section is 3x3 μm.

(3) The Silicon SOI taper arrangement when $n_1 = 3.48$, $n_2 = 3.0$, $n_3 = 2.98$, and the Synthetic polymer cross-section is 3x3 μm.

(4) The Silicon SOI taper arrangement when $n_1 = 3.48$, $n_2 = 3.0$, $n_3 = 1.45$, and the Synthetic polymer cross-section is 6x6 μm.

(5) The Silicon SOI taper arrangement when $n_1 = 3.48$, $n_2 = 1.47$, $n_3 = 1.45$, and the Synthetic fused silica cross-section is 6x6 μm.

(6) The Silicon SOI taper arrangement when $n_1 = 3.48$, $n_2 = 3.0$, $n_3 = 2.98$, and the Synthetic polymer cross-section is 6x6 μm.

Case 1, When $n_1 = 3.48$, $n_2 = 3.0$, $n_3 = 1.45$. The Synthetic polymer cross-section is 3x3 μm.

In the first example, Case 1, the index difference is high at $\Delta n_{12} = 0.48$ between silicon and polymer. The index difference is also very high at $\Delta n_{23} = 1.55$ between polymer and silica, and this study investigates the effects the index difference has on the SOI characteristics. Figs. 7.2 and 7.3 shows the output of the full-vectorial **H**-field of the finite element method which also serves as the input for the full-vectorial beam propagation methods and output TE mode field profiles for the laterally tapered SSC before and after the mode conversion respectively. Initially the fundamental TE mode was confined in the core width $W_i = 0.5$ μm. As the core width is reduced to the final width $W_f = 0.1$ μm, the optical-field mode had undergone some transformation from the inner core and has expanded into the secondary guide with width $W_2 = H_2 = 3.0$μm of the polymer core with refractive index $n_2 = 3.0$. It should be noted that the propagating length, L = 2000 μm and wavelength, λ = 1.55 μm is the same for all the cases considered in this work. Initially the Gaussian radius, $\Omega_o = 2.5$ μm is used for the calculation of the overlap integral when butt coupled to a fibre. The waveguide exhibited low modal loss 0.74 dB (shown in Fig. 5), however, existence of the local maxima in the field profile clearly demonstrates existence of higher order modes.

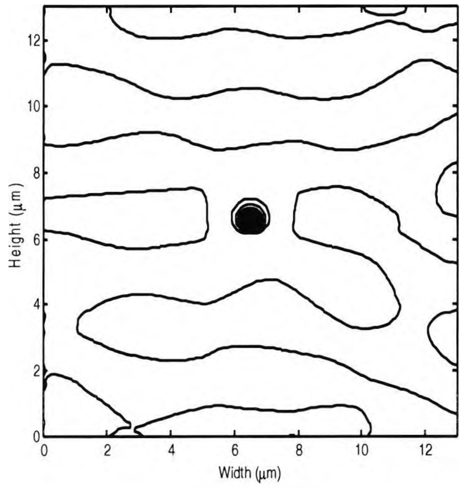

Fig 7.2. The TE mode field profile from FVFEM at the start of the laterally tapered SSC.

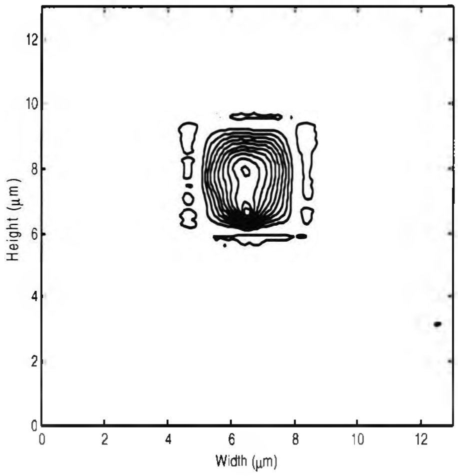

Fig. 7.3. Case 1. The output TE field profile from the FVBPM at the end of the laterally tapered SSC.

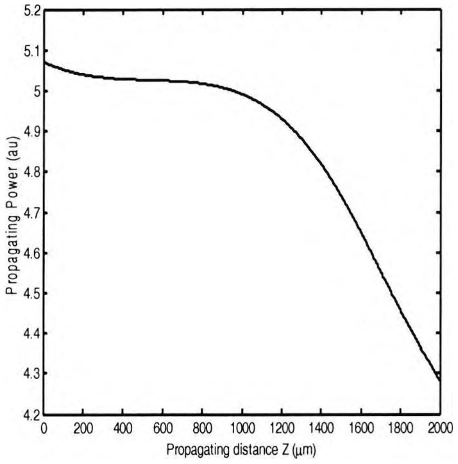

Fig. 7.4. Case 1. Variation of the Power along the length of the device.

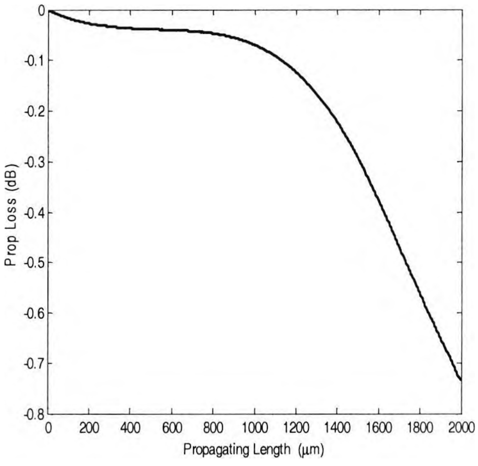

Fig. 7.5. Case 1. Variation of the Propagation loss along the length of the device.

Fig. 7.4 shows the power of the propagating optical beam in this device. It was able to retain its power between 5.07 and 4.28 au., for about a length of 1300 μm of the 2000 μm total length. This is a desirable attribute for all OEICs. Fig. 7.5 shows the variation of propagation loss along the length of the device. This shows a very low propagation loss which is steady until the propagation reaches the half of the device and finally reaches 0.74 dB which is an acceptable value. To understand the beam transformation, Fig. 7.6 shows the expansion of the spot-size along the length of the taper. The spot-size area is defined in this work as the area where the field intensity is greater than 1/e of its maximum strength (i.e. the power intensity is $1/e^2$). It can be seen that the spot-size increases from 0.3 to 4.8 μm^2 along the taper. The coupling efficiency can reach a high value of 79% (shown in Fig. 7.7) but this can be further improved. However, due to the large difference in the refractive index between the polymer and the silica cladding, the polymer secondary waveguide is multimoded. The sidewall roughness can affects the optical beam as it expands into the 3x3 μm polymer where higher modes are also supported. The spot-size expansion is not very large, and the spot-size oscillations phenomenon, generally known as mode-beating, is visible in Fig. 7.3, and is not desirable. Mode beating also modulates the spot-size which is clearly visible in Fig. 7.6. Further investigation is needed to avoid these oscillations during the TE optical-mode transformation and improve the spot-size expansion. This design can be improved by reducing the overcladding index from 3.0 to 1.47 in the next simulation.

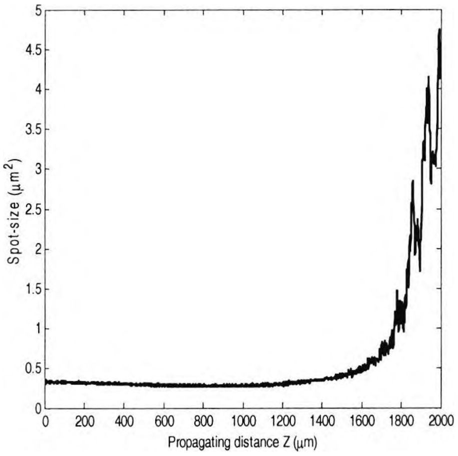

Fig. 7.6. Case 1. Mode conversion of the laterally tapered spot-size converter along the length of the waveguide.

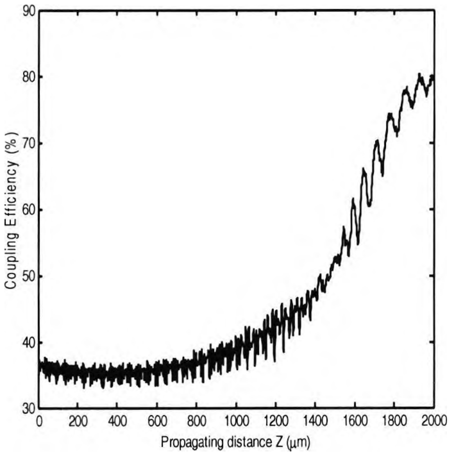

Fig. 7.7. Case 1. The coupling efficiency of the TE mode of the waveguide coupled to the single mode fibre.

Case 2, When n_1 = 3.48, n_2 = 1.47, n_3 = 1.45. The Synthetic Fused Silica cross-section is 3x3 μm.

In order to improve the previous design, a low-index secondary core is considered as Case 2, with $n_1 = 3.48$, $n_2 = 1.47$, $n_3 = 1.45$ (Materials are shown in Table 1). In this case, the index difference extremely high at $\Delta n_{12} = 2.01$ between silicon and the secondary guide core, but index difference $\Delta n_{23} = 0.02$ is not as high between polymer and silica, described in Case 1. In this arrangement similar structural dimension, $W_1 = W_i = 0.5$ μm, and $H_i = 0.5$ μm and $W_2 = H_2 = 3.0$μm are taken.

Fig. 7.8 shows a forced expansion to low quality output (i.e. sagged output field lines). This may be due to the large index difference, $\Delta n_{12} = 2.01$ of the tapered primary core, which may affect the quality of the image of the SSC produced when compared to the output obtained as shown in Fig. 7.3 for Case 1. Fig. 7.9 shows the variation of the power along the length of the device. There is a reduction of about

40% in the value of the power compared to the design in Case 1. Fig. 10 shows the variation of the propagation loss along the length of the taper which has relatively high value of 10.81 dB, which is not suitable. The explanation of this is not far fetched because the secondary guide is single moded as Δn_{23} is small and Δn_{12} is higher which increases the lattice mismatch and the roughness at the walls, so the power loss along the tapered structure is also higher. This also explain why the taper's width is reduced from $W_i = 0.5\ \mu m$ to $W_f = 0.007\mu m$ for the mode to undergo conversion to spot-size but full conversion could not be reached. The spot-size expanded to 8.44 μm^2 the SOI arrangement greatly improves the spot-size evolution and transformation along the longitudinal direction of the waveguide which can be seen in Fig. 7.11. Unlike the first example, the spot-size oscillations are suppressed in this design. Fig. 7.12 shows that the design exhibits good coupling efficiency of 98%. The main advantage of this device is that a single mode operation can be expected because the taper's width for mode cut-off region in this case is shorter than the previous case since the polymeric index is now lower. Therefore support for higher order modes is minimum for this design.

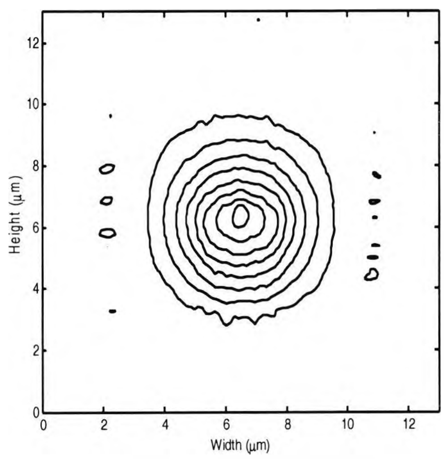

Fig. 7.8. Case 2 The output TE mode field profile from the FVBPM at the end of the mode conversion in the laterally tapered SSC.

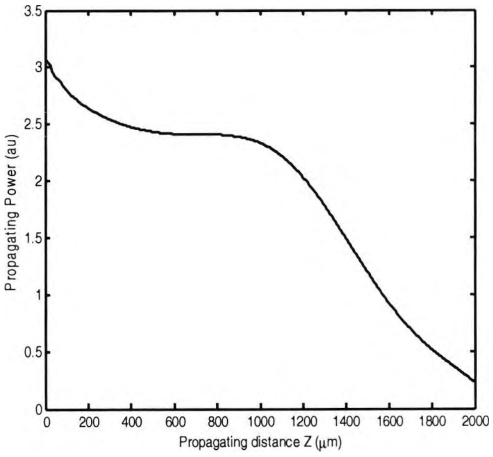

Fig. 7.9. Case 2. Variation of the Power along the length of the taper.

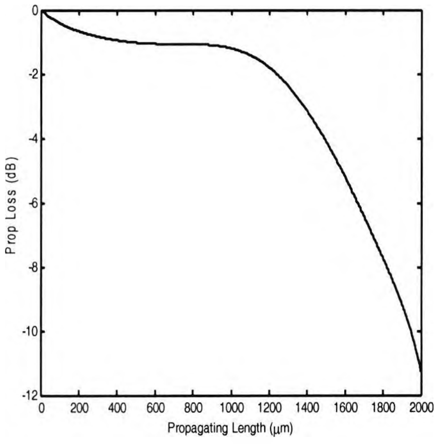

Fig. 7.10. Case 2. Variation of the Propagation loss along the Length of the device.

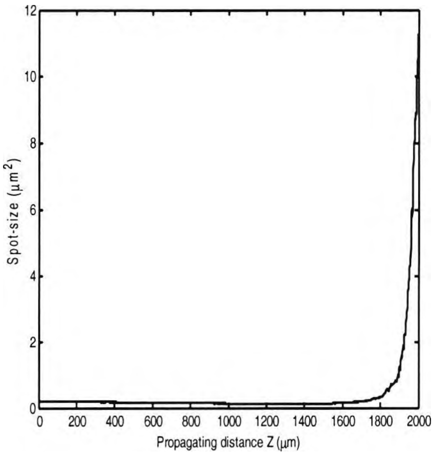

Fig. 7.11. Case 2 shows the variation of the laterally tapered spot-size along the length of the waveguide.

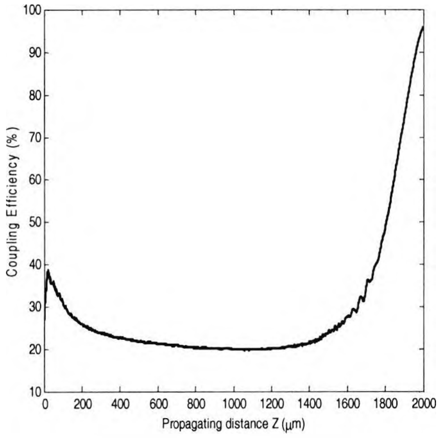

Fig. 7.12. Case 2. Variation of the Coupling efficiency to the Length of the device.

Case 3, When $n_1 = 3.48$, $n_2 = 3.0$, $n_3 = 2.98$. The Synthetic polymer cross-section is 3x3 μm.

It is required to improve this design which may be possible, by adjusting the doping of both the synthetic polymeric index values to 3.0 and 2.98 respectively by assuming heavy doping of the materials (Materials are shown in Table 1). In the next example, Case 3, a moderate index difference of $\Delta n_{12} = 0.48$, between silicon and polymer and a low index difference of Δn_{23} = 0.02 between polymer and doped polymer is considered. As in previous cases, $W_1 = W_i = 0.5$ μm, and $H_i = 0.5$ μm and $W_2 = H_2 = 3.0\mu$m. The silicon wire waveguide was tapered from $W_i = 0.5$ to $W_f = 0.02$ μm and taper's width for mode cut-off is wider (about 3.4 μm) and low Δn_{12} and Δn_{23} for this SOI device. Fig. 7.13 shows the output TE mode field profile from the beam propagation method for this arrangement. Fig. 7.14 shows the propagating power is high compare to previous models which is 5.4 au. Variation of the spot-size mode conversion along the propagating distance of the device is shown in Fig. 7.16. Fig. 7.15 shows the variation of the propagation loss along the length of the taper and this has been reduced to 2.04 dB, which could be satisfactory for this SOI device. In this case, it can be seen from Fig. 7.16 that spot-size expansion starts to take place at about z = 1500 μm and full expansion occurs close to the end of the propagation at z = 2000 μm where the value of the spot-size is 9.78 μm^2 which makes it better than the Case 2 design. It can also be seen from the diagram that there is complete absence of the mode-beating phenomenon in this model. The model exhibits coupling efficiency of 97% between the Si waveguide and the SMF for a Gaussian radius of 2.5 μm and this can be seen clearly in Fig. 7.17.

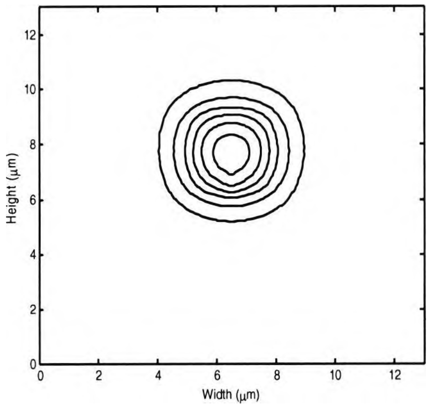

Fig. 7.13. Case 3. The output TE mode field profile from the FVBPM at the end of the mode conversion in the laterally tapered SSC.

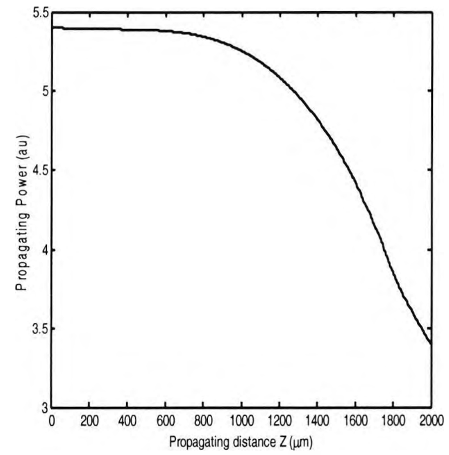

Fig. 7.14. Case 3. Variation of the Propagating Power against the length of the taper.

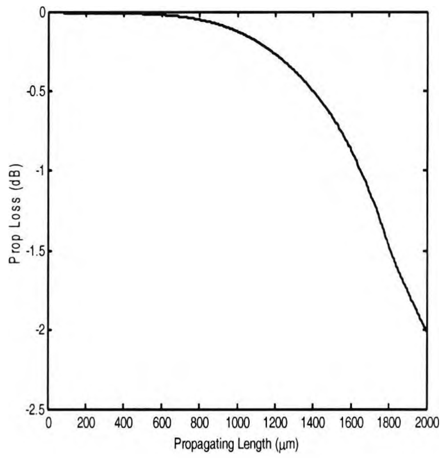

Fig. 7.15. Case3. Variation of the Propagation loss to the Length of the device.

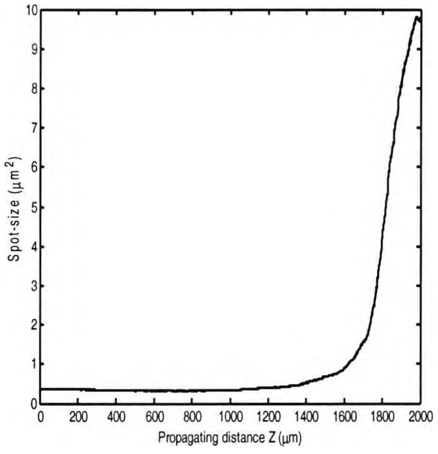

Fig. 7.16. Case 3. Mode conversion of the laterally tapered spot-size along the length of the waveguide.

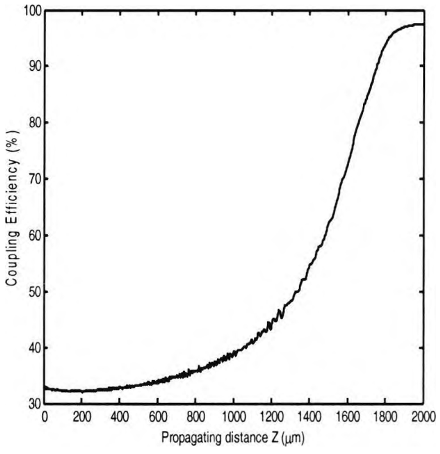

Fig. 7.17. Case3. The coupling efficiency of the TE mode of the waveguide coupled to the single mode fibre.

The third case, with the final tapering width of 0.02 μm gives a high propagating power, low loss, good quality output TE mode field profile, good and very smooth spot-size expansion with no oscillations observed and a very high butt coupling efficiency to a single mode fibre. These are excellent characteristics, which makes the model better than the previously reported work. This particular model is in good agreement with the work of Fan and Hooker (1999) on polymer tapers. However, since the secondary guide is only 3μm x 3μm, the mode expansion is also limited. This particular design could be suitable for coupling to fibre with smaller dimension, such as EDFA.

The next 3 models have similar SOI characteristics as the first three but the secondary core has been replaced by a large polymer cross-section of 6x6 μm which doubles the dimension, but 4 times the polymer cross-section area of Cases 1 – 3. This is expected to expand the spot-size further to improve the good characteristics of the previous designs.

Case 4, When $n_1 = 3.48$, $n_2 = 3.0$, $n_3 = 1.45$. The Synthetic polymer cross-section is 6x6 μm.

In this Case 4, the index difference is high at $\Delta n_{12} = 0.48$ between silicon and polymer. The index difference is also extremely high at $\Delta n_{23} = 1.55$ between polymer and silica as in Case 1. Therefore Case 4 is simply an extension of Case 1 in polymer section. The output TE mode (shown in Fig. 7.18) in this case is larger than the output TE mode in Fig. 7.2, Case 1 and this is expected because the polymer cross-section is larger. The tapering is done from 0.5 to 0.14μm and a single mode operation can be expected with this final width. The quality of the mode field lines is consistent with the $\Delta n_{12} = 0.48$ for the SOI waveguide in previous models but shows a little bit of mode-beating, which is visible in Fig. 7.18. Fig. 7.20 shows an extremely low propagation loss of 0.52 dB better than that of Case 1. However Fig. 7.19 shows reduction in the propagation power of 2.58 au. This is about half of the observed value of power in Case 1. It seems the lager polymer section has an inverse effect on the propagating power in this case to the large $\Delta n_{23} = 1.55$ in the SOI – waveguide and this also manifests in the formation of the output TE mode profile in Fig. 7.18. Fig. 7.21 shows an improvement in the spot-size curve to the one observed in Fig 6, Case1. In this case the oscillations observed for the mode-beating in Fig. 7.6, Case 1 has reduced drastically with an increase from 4.3 to 17.78 μm^2 courtesy of the large polymer section. It should be noted that the mode conversion in this case although improve over that of Case 1, is almost complete but not fully completed.

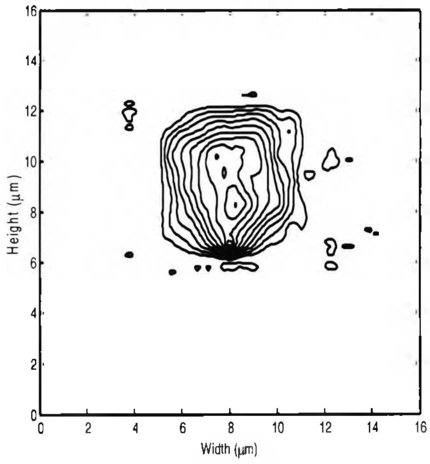

Fig. 7.18. Case 4. The output TE mode field profile from the FVBPM at the end of the mode conversion in the laterally tapered SSC. $W_f = 0.14\ \mu m$.

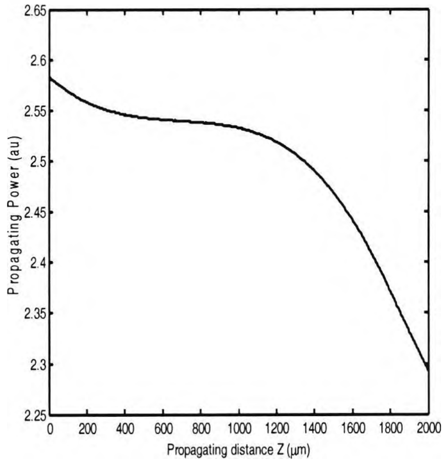

Fig. 7.19. Case 4. Variation of the Propagating Power against the length of the taper.

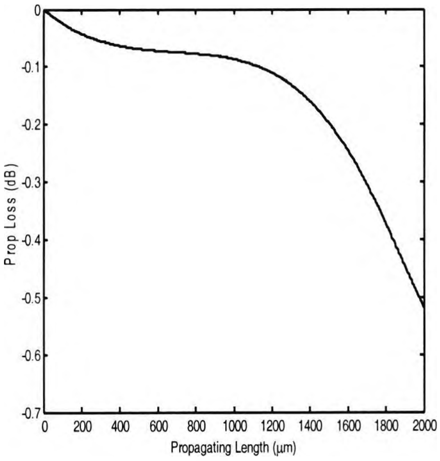

Fig. 7.20. Case 4. . Variation of the Propagation loss to the Length of the device

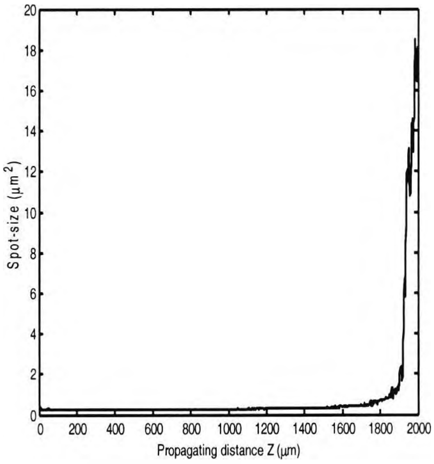

Fig. 7.21. Case 4. Spot-size expansion of the lateral taper. $W_f = 0.14\ \mu m$.

The variation of the coupling efficiency of the SOI waveguide to the single mode fibre along the propagating length is shown in Fig. 7.22. The overlap integral gives the final efficiency to be 97% which shows a very good butt coupling between the two OEIC devices and this is better than the efficiency seen in Fig. 7.7, Case 1 where the efficiency curve is marred by oscillations as a result of mode-beating. It can be concluded that the increase in the polymer cross-sectional area has marked improvement on this SOI model.

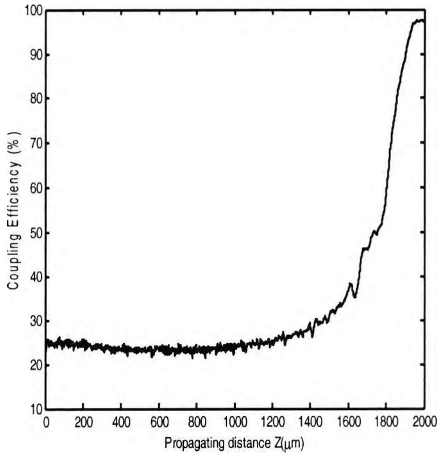

Fig. 7.22. Case 4. Coupling efficiency of the taper waveguide butt coupled to a SMF.

Case 5, When n_1 = 3.48, n_2 = 1.47, n_3 = 1.45. The Synthetic fused silica cross-section is 6x6 μm.

In this Case 5, the index difference is extremely high at $\Delta n_{12} = 2.01$ between silicon and polymer. But the index difference $\Delta n_{23} = 0.02$ remain the same between polymer and silica. Case 5 is also an extension of Case 2 in which the polymer section is doubled to 6 x 6 μm. This is to expand the spot-size further to improve the good characteristics of the previous designs.

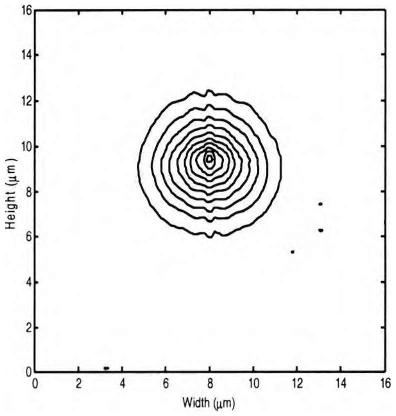

Fig. 7.23. Case5. The output TE mode field profile from the FVBPM at the end of the mode conversion in the laterally tapered SSC. $W_f = 0.007$ μm.

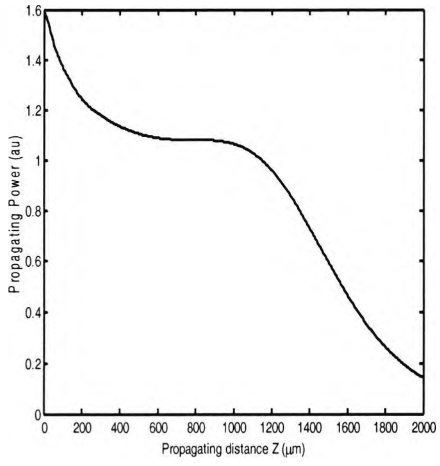

Fig. 7.24. Case5. Variation of the Propagating Power against the length of the taper.

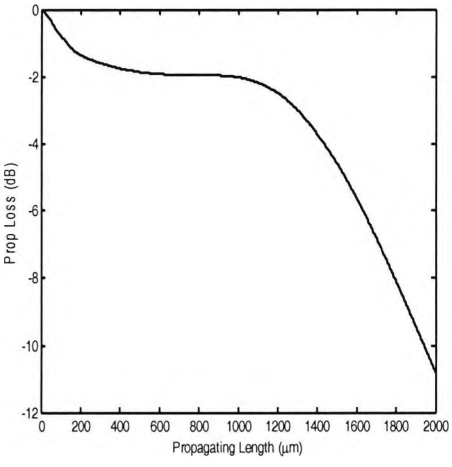

Fig. 7.25. Case5. Variation of the Propagation loss to the Length of the device

Fig. 7.23 shows the output TE mode field profile for a final width of 0.007 μm. The size of the output field did not increase with the increase in polymer section as expected (instead slight decrease) although the field lines are consistent with the $\Delta n_{12} = 2.01$ for Fig. 7.8, Case 2. The failure to expand fully into the polymer core can be seen as saturation of the mode transformation such that even at $W_f = 0.007$ μm no further increase can be obtained. Therefore the increase in polymer core has no effects on the output field. Fig. 7.24 shows the variation of the propagating power along the direction of propagation. The power in this case is 1.6 au and this is about half of the power seen in Case 2 which is consistent with the observed reduction between Cases 1 and 4. Again this can be explained as the lager polymer section has an adverse effect on the propagating power to the large $\Delta n_{12} = 2.01$ in the SOI – waveguide and this also manifests in the formation of the output TE mode profile in Fig. 7.23. Fig. 7.25 shows variation of the propagation loss along the direction of propagation. The propagation loss is 10.48 dB which is relatively high and the same as seen in Case 2. Fig. 7.26 shows that the spot-size field profile has not expanded fully into the polymer core. Although the taper's width is reduced from $W_i = 0.5$ μm to $W_f = 0.007\mu$m for the mode to undergo conversion but due to the extraordinary Δn_{12} of the SOI waveguide, full conversion could not be reached. Since the output field profile in this case is slightly less than the output field in Case 2, consequently the expanded spot-size is also slightly less than the spot-size in Case 2. This further proves that the increase in polymer core has little or no effects on this SOI model. Fig. 7.27 shows the variation of the coupling efficiency along the direction of propagation. The coupling efficiency is 98.9% in this case which is very remarkable for this design. It can be concluded that the increase in the polymer core has little or no effects on the characteristics of this SOI model except for the slight improvement in the coupling efficiency.

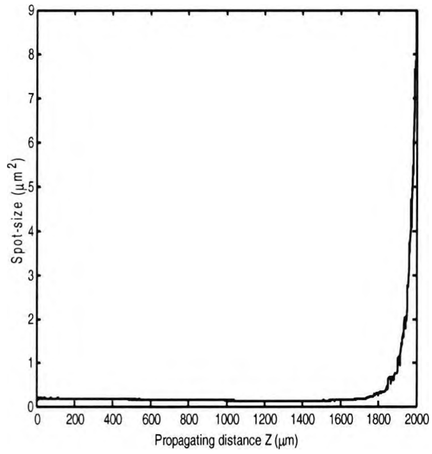

Fig. 7.26. Case 5. Spot-size expansion of the lateral taper. $W_f = 0.007$ μm.

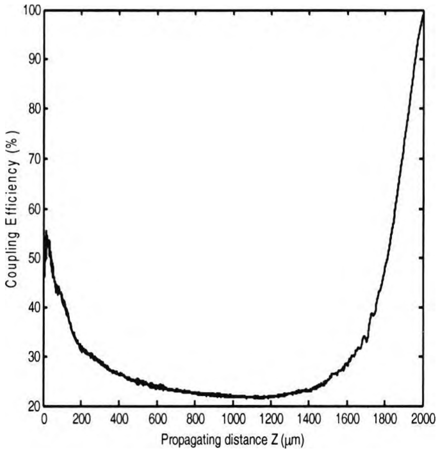

Fig. 7.27. Case 5. Coupling efficiency of the taper waveguide butt coupled to a SMF.

Case 6, When $n_1 = 3.48$, $n_2 = 3.0$, $n_3 = 2.98$. The Synthetic polymer cross-section is 6x6 μm.

The next simulation, Case 6, is carried out with secondary core 6μm x 6μm to expand the spot-size further to improve the good characteristics of the previous design in Case 3. In this case, the index difference remains moderate at $\Delta n_{12} = 0.48$ between silicon and polymer and a low value at $\Delta n_{23} = 0.02$ remain the same between polymer and doped polymer. This is an extension of previous design in which only the polymer section is doubled to 6 x 6 μm, but $W_1 = W_i = 0.5$ μm, and $H_i = 0.5$ μm. In this case, the output TE mode field profile of the Si waveguide is tapered from $W_i = 0.5$ to $W_f = 0.02$ μm. It can be seen in Fig. 7.28, that the output mode field is fully expanded and fills the secondary polymer core. The mode field size is twice the output mode field in Case 3. Fig. 7.29 shows the variation of the power along the z-direction where the power is 5.66 au which is slightly better than the power seen in Case 3. Fig. 7.30 shows that the value of the low propagation loss to be 1.39 dB for the SOI waveguide which is considered good such device. Fig. 7.31 shows the variation of the spot-size along the z-direction where expansion start to occur at about z = 1700 μm to a value of 28.94 μm^2. However, this spot-size curve has two peaks and a trough, which forms a kind of oscillation when the spot-size has fully expanded into the secondary polymer core. The first peak occurs at z = 1842 μm identified as 'A' and the trough occurs at z = 1911 μm identified as 'B'. Since the observed oscillations occur in the polymer secondary core, it can be anticipated that the expanded polymer cross-section is now able to support multimode operation hence given rise to mode-beating right inside the polymer secondary core. The coupling efficiency is 99%, the maximum recorded for all the designs is shown in Fig. 7.32. It can be concluded that the increase in the polymer cross-section improves the mode-field of the SOI waveguide generally. However, increase in the waveguide cross-section by keeping the same index contrast, Δn_{23}, allowed the higher order mode to be generated and guided.

Further analysis is carried out to investigate the mode field profile inside the polymer core and the fields at point 'A' and 'B'. The mode field profile at position 'A' identified in Fig. 7.31, is shown in Fig. 7.33. This mode-field clearly shows two peaks whereas the field at point 'B', shown in Fig. 7.34 looks much reduced in the vertical direction. Further analysis is made to investigate the mode field profile inside the polymer core and the fields at point A and B are shown in Figs. 7.33 and 7.34 respectively. It can be seen that the mode field at point A is bigger that at point B. Point A mode-field looks like two modes combined in one whereas the point B mode-field looks like half of a mode. Figs. 7.35 and 7.36 give the field lines for the two points A and B respectively where the mode-fields are maximum in the x-direction. Fig. 7.37 shows the absolute resultant effect of subtracting the field-lines at point 'B' from 'A' magnitude is very small and it shows no effect of mode-beating in the region.

Similarly Figs. 7.38 and 7.39 give the field lines for the two points A and B respectively where the mode-fields are field variation along the y-direction. Further analysis is carried out to determine the field profile along the vertical direction for the two points 'A' and 'B'. Fig. 7.40 shows the absolute resultant effect of subtracting the field-lines at point B from A and the second peak shows the presence of a second mode which proves the effect of mode-beating in the region in the tapered SSC. No existence of higher order mode was observed in the lateral direction.

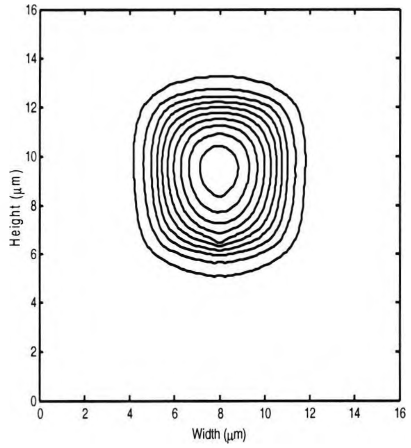

Fig. 7.28. Case 6. The output TE mode field profile from the FVBPM at the end of the mode conversion in the laterally tapered SSC. $W_f = 0.02\ \mu m$.

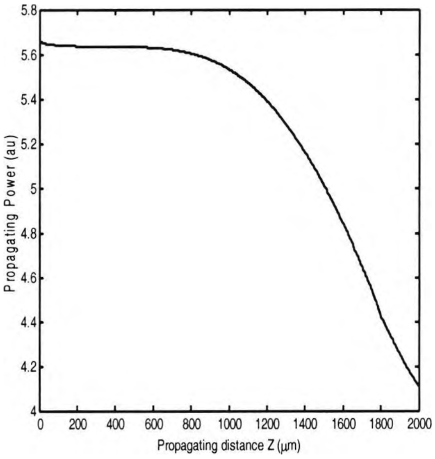

Fig. 7.29. Case 6. Variation of the Propagating Power against the length of the taper.

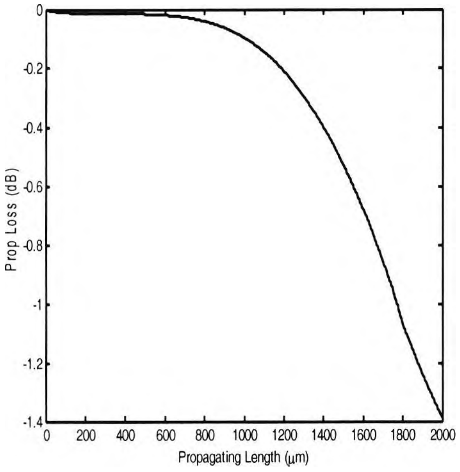

Fig. 7.30. Case 6. Variation of the propagation loss to the Length of the device.

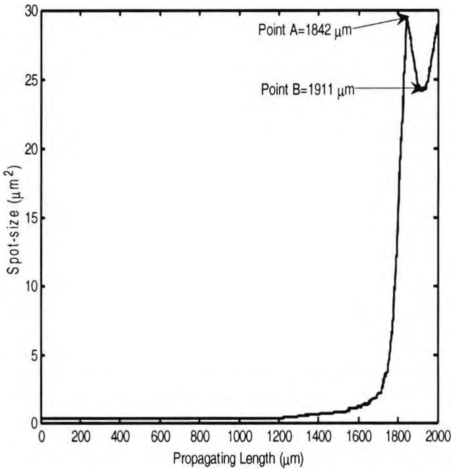

Fig. 7.31. Case 6. Spot-size expansion of the lateral taper. $W_f = 0.02\ \mu m$.

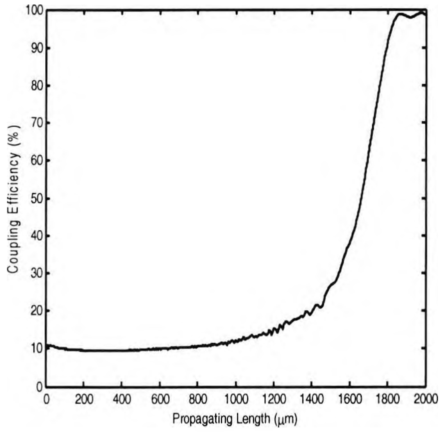

Fig. 7.32. Case 6. The coupling efficiency of the TE mode of the waveguide coupled to the single mode fibre.

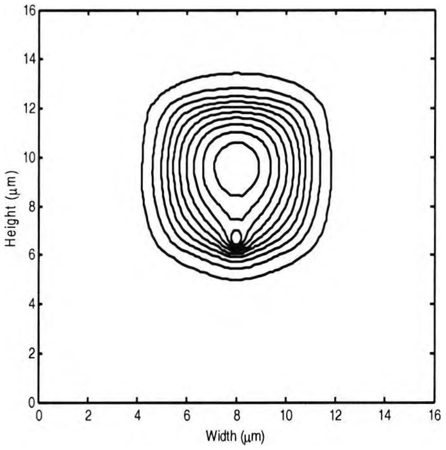

Fig. 7.33. Case 6. TE mode profile at point A = 1842 μm in fig 31 for the spot-size expansion of the tapered SSC.

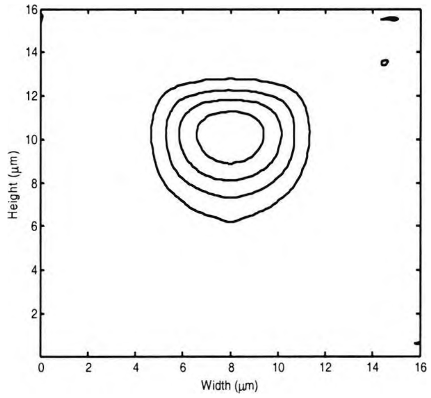

Fig. 7.34. Case 6. TE mode profile at point B = 1949 μm in fig 31 for the spot-size expansion of the tapered SSC.

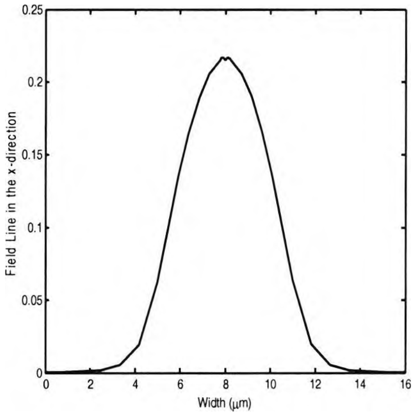

Fig. 7.35. The field line in the x-direction for point A = 1848 μm where the spot-size first peak occurred.

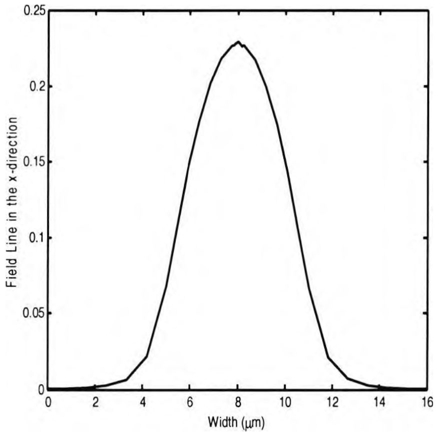

Fig. 7.36. Case 6. The field variation along the x-direction at point B = 1949 μm, where the spot-size first trough occurred.

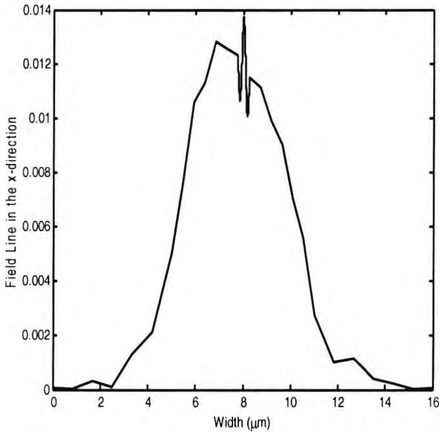

Fig. 7.37. Case 6. Field difference in the x-direction between point A and point B of Fig. 31 for the spot-size expansion.

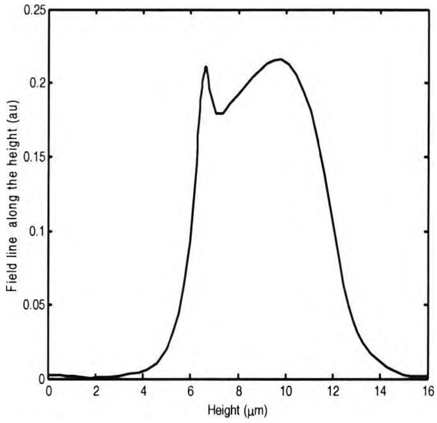

Fig. 7.38. Case 6. The field variation along the y-direction at point A = 1848 μm, where the spot-size first peak occurred.

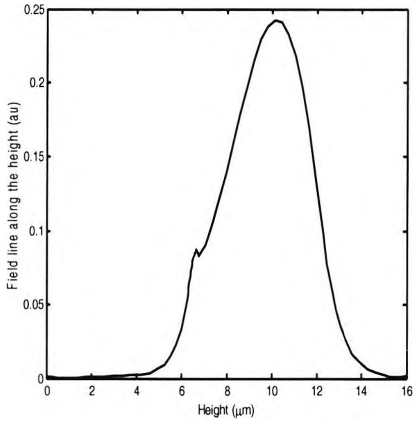

Fig. 7.39. Case 6. The field variation along the y-direction at point B = 1949 μm, where the spot-size first trough occurred.

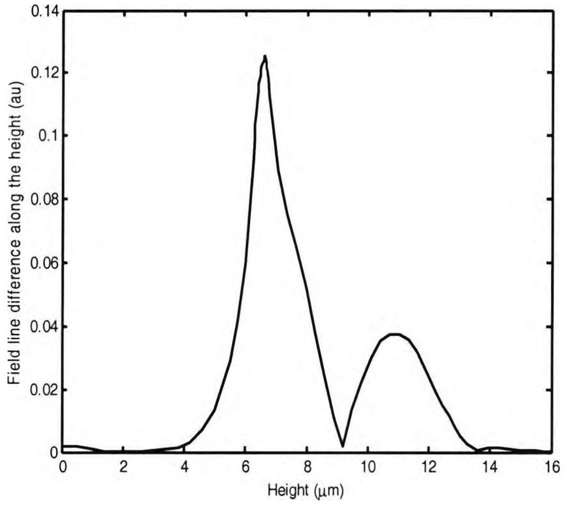

Fig. 7.40. Case 6. . Field difference along the y-direction between the points A and B of Fig. 31.

Further simulations were carried out to show that the observed mode beating can be reduced or eliminated by either reducing the polymer cross-section to 6x5 μm or by reducing the high-index difference, Δn_{23} to 0.015 or 0.01. The first suggestion is more preferable to the second because from fabrication point of view, it is far easier to reduce polymer cross-section from 6x6 μm to 6x5 μm because of the vertical confinement than reduce the index difference from 0.02 to 0.015 or 0.01.

Improved case 6x5, When n_1 = 3.48, n_2 = 3.0, n_3 = 2.98. The Synthetic polymer cross-section is 6x5 μm.

Finally, the SSC structure considered here is symmetrical along the x-axis, but not along the y-axis. In this case, Case 6x5, the index difference remains moderate at Δn_{12} = 0.48 between silicon and polymer and low at Δn_{23} = 0.02 remain the same between polymer and doped polymer but the polymeric cross-section is now 6.0 μm x 5.0 μm. The vertical confinement is asymmetrical and slightly stronger than that in the horizontal direction. Hence, in order to reduce the dimension of the secondary guide, only its height is reduced. Therefore, the height of polymer section is reduced by 1 μm in order to stem down the multimoded effect produced by the excitation of the propagating field in the vertical direction. All other parameters such as material index and dimensions remain the same as in the previous design, Case 6.

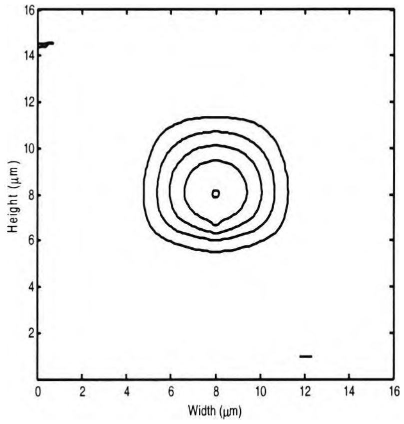

Fig. 7.41. Case 6x5. The output TE field profile from the FVBPM at the end of the laterally tapered SSC, with $W_f = 0.02$ μm.

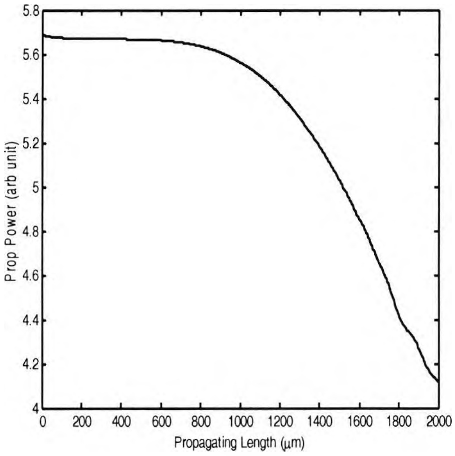

Fig. 7.42. Case 6x5. Variation of the Propagating Power against the length of the taper.

Fig. 7.41 shows the output TE mode field for Case 6x5. There is slight reduction in the output TE mode field profile for the same parameters for Case 6x5 than in the Case 6 which is expected. The propagating power in Fig. 7.42 shows very slight improvement for Case 6x5 than in Case 6. The propagation loss remains almost the same as shown on Fig. 7.43 for the two cases under consideration as the difference in the propagation loss is negligible. The field mode reduction has very slight effect on the propagating power and loss which is a good attribute of this design. Variation of the coupling efficiency along the propagation distance is shown in Fig. 7.44. There is slight improvement with regards to the coupling efficiency for Case 6x5 than in Case 6. It can be observed that the butt coupling efficiency of the waveguide to a 2.5 μm single mode fibre (SMF) is excellent, almost 100%. This is the highest observed for all the designs considered in this work. The variation of the spot-size along the propagation distance is shown in Fig. 7.45 similar to the spot-size on Fig. 7.31 for Case 6 but there is a reduction observed in the size from 29 μm^2 to 25 μm^2. Also observed is the significant reduction in the amplitude of the mode beating oscillation compared to that of Case 6. Figs. 46 – 60 show detail analysis of the high and low points of the plots which will be discussed later.

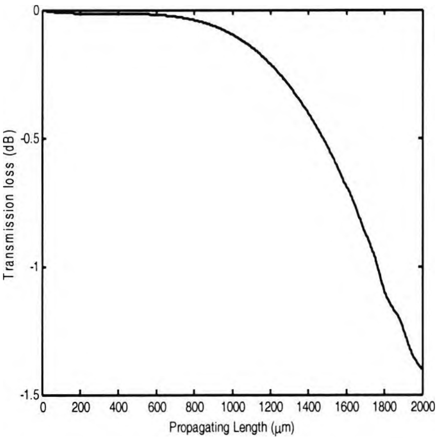

Fig. 7.43. Case 6x5. Variation of the propagation loss to the Length of the device.

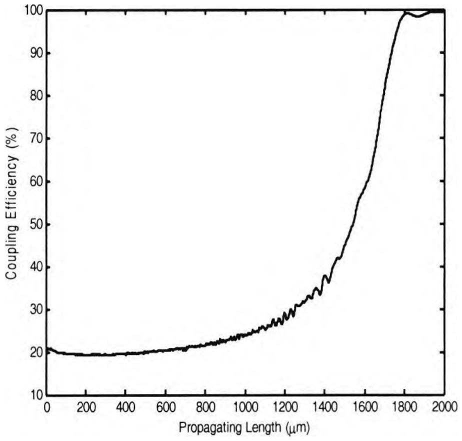

Fig. 7.44. Case 6x5. The coupling efficiency of the TE mode of the waveguide coupled to the single mode fibre.

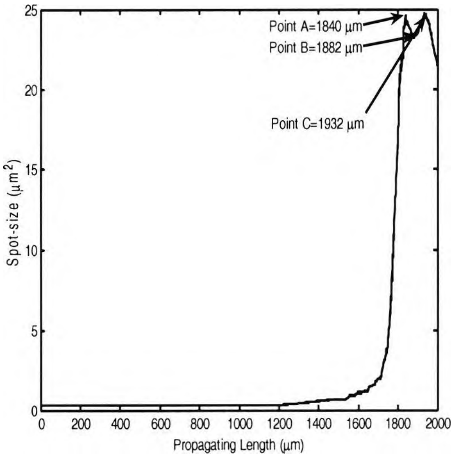

Fig. 7.45. Case 6x5. Spot-size expansion of the lateral taper. $W_f = 0.02\ \mu m$.

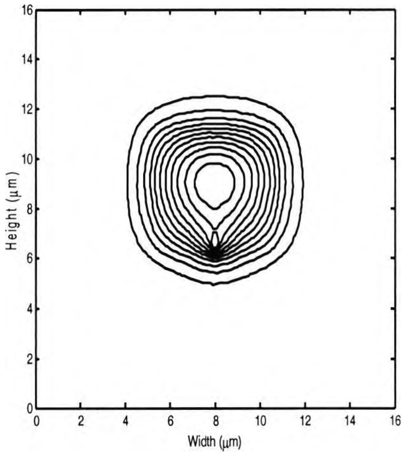

Fig. 7.46. Case 6x5. TE mode profile at point A = 1840 μm in fig 45 for the spot-size expansion of the tapered SSC.

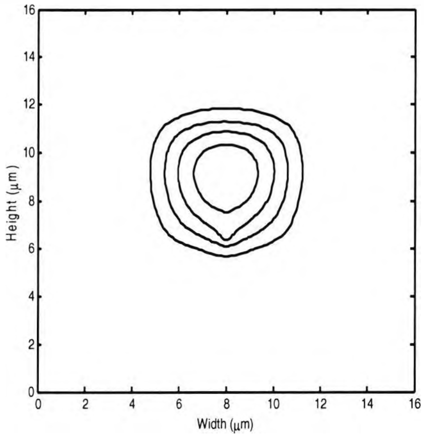

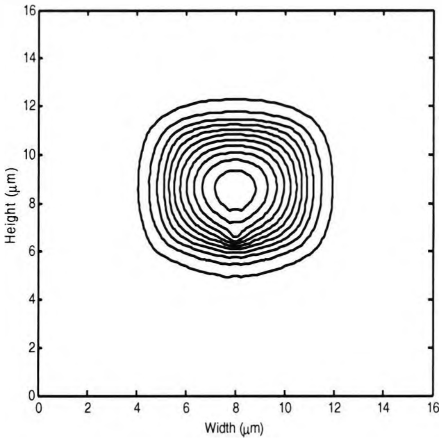

Fig. 7.47. Case 6x5. TE field profile at point B = 1882 μm (in Fig. 45) for the tapered SSC.

Fig. 7.48. Case 6x5. TE profile at point C = 1932 μm (in fig 45) for the tapered SSC.

The TE field profile at the three points 'A', 'B' and 'C' (shown in Fig. 7.45) are shown on Figs. 7.46, 7.47 and 7.48 respectively. Points 'A' and 'C' are the highs and 'B' is the low. The Figs. 7.46 and 7.48 show the high field profiles which are not symmetrical, but a little bit distorted, while the Fig. 7.47 shows a low field profile which is also a little bit distorted. As discussed before, an oscillation has been seen when the spot-size has fully expanded into the secondary polymer core which supports multimode propagations hence given rise to mode-beating right inside the polymer core. The first peak occurs at a point 'A' = 1840 μm and the trough occurs at a point 'B' = 1882 μm and the second peak at a point 'C' = 1932 μm, further analysis is made to investigate the field profile inside the polymer core and the fields at point 'A', 'B' and 'C'. It can be seen that the field at point 'A' is much bigger that at point 'B'. Point 'A' field looks like two modes combined in one whereas the point 'B' mode-field looks a lot smaller than that at point 'A'. The field at point 'C' is very similar to the field at 'A'. Fig. 7.49 shows the variation of the field along y-direction at the end of the propagation. It can be seen that the mode beating has been greatly reduced to the bearest minimum.

Taking the two points 'A' and 'B' (in Fig. 7.45) and finding H_y TE field variation along the field in the vertical y-direction (H_y versus 'y'), are shown in Figs. 7.50 and 7.51 respectively. It can be seen from Fig. 7.52 that the resultant effect of subtracting the field lines at point ‘B’ from ‘A’ gives a curve with two peaks. The big peak is the fundamental mode while the small peak shows the presence of the second mode which indicate mode-beating in the vertical y-direction. Again this result is consistent with the earlier result obtained with the polymer 6x6 μm. As observed in Case 6, the absolute resultant effect of subtracting the field-profile at point ‘B’ from ‘A’ in the x-direction shows no sign of mode beating. The Figures are similar to the ones shown in Figs. 7.35 - 7.37, and are therefore not repeated in this section.

The analysis moves a step further to compare the two sets of results obtained for the 6x5 μm and 6x6 μm waveguides. The first comparison is shown on Fig. 7.53 where the two curves of spot-size for 6x5 μm and 6x6 μm are plotted together. It is clearly evident that there is significant reduction in the mode-beating oscillations curve seen in 6x5 μm compared to that of 6x6 μm. Smaller variation of σ_{max}, σ_{min} means that amplitude of 2nd mode was smaller. For comparison, spot-size variation for Case 6 is also shown by a solid line. The spot-size is also similar to the spot-size in Fig. 7.31 but there is a reduction observed in the size from 29 μm^2 to 25 μm^2 because the waveguide dimension has also been reduced. It is also observed that the significant reduction in the amplitude of the mode beating oscillation compared to that of Case 6. Fig. 7.53 shows the first comparison of the Case 6 and the corrective Case 6x5, which shows that there is significant reduction in the mode-beating oscillations curve. There is oscillation between the 23.2 and 24.6 μm^2 for Case 6x5 waveguide whereas it is between 24.2 and 29.5 μm^2 for Case 6 design. The amplitude of oscillation for Case 6x5 is calculated to be 0.7 μm^2 and that for Case 6 is 2.7 μm^2, which shows marked difference in the reduction of the mode-beating and proves amplitude of 2nd mode is much smaller..

The second comparison is shown on Fig. 7.54 in which the variation of the field profile along the vertical lines for the two cases, Case 6 and the improved Case 6x5, are plotted together. It can be seen that the spread along the y-direction is smaller for Case 6x5 since the height has been reduced. The two peaks for Case 6 measure 0.126 and 0.038 and those for the improved Case 6x5 measure only 0.044 and 0.012, which demonstrates a significant reduction in their amplitude. This again shows that for the reduction in the height of the SOI waveguide can be seen as a balance or trade-off to the value of spot-size needed for the design to reduce or eliminate the mode-beating completely.

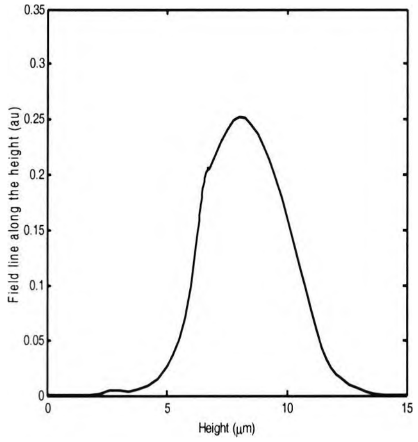

Fig. 7.49. Case 6x5. Variation of the field line along the y-direction for the output TE mode at the end of propagation i.e. z = 2000 μm.

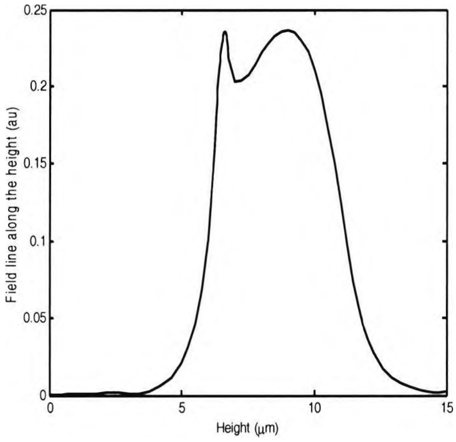

Fig. 7.50. Case 6x5. The spot-size (y) in the y-direction for point A = 1840 μm where the spot-size first peak occurred.

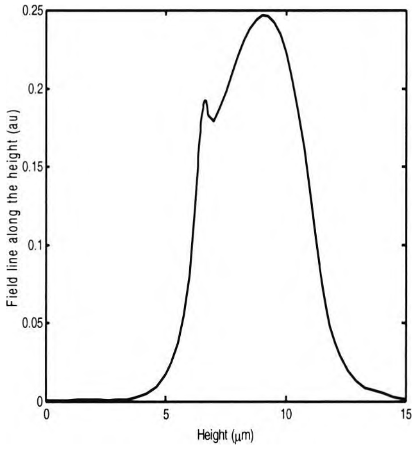

Fig. 7.51. Case 6x5. The field line in the y-direction for point B = 1882 μm where the spot-size first trough occurred.

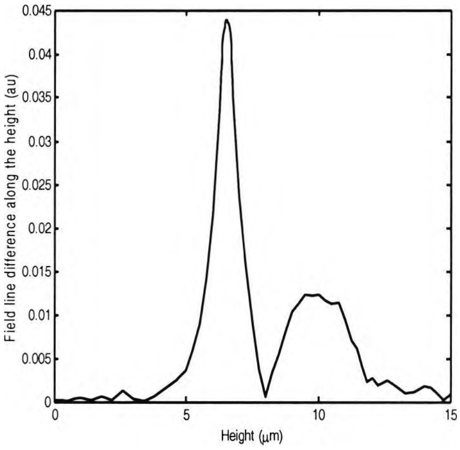

Fig. 7.52. Case 6x5. The field line difference along the y-direction between point A and point B of Fig. 44 for the spot-size expansion.

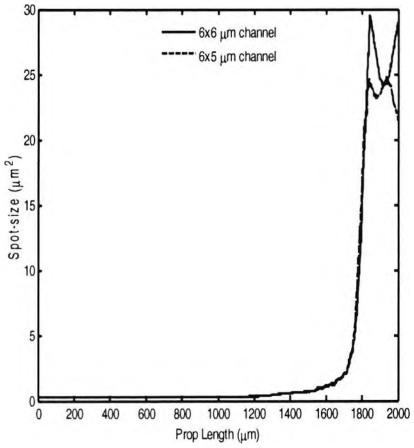

Fig. 7.53. Comparison of spot-size figs for two cases 6 and 6x5 to show reduction in the oscillations between the two cases.

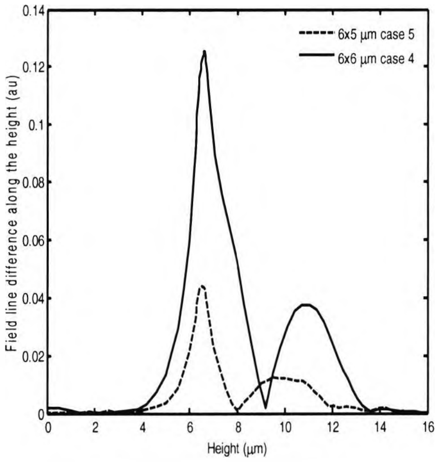

Fig. 7.54. Comparison of figs 40 and 56 for the field line difference along the vertical direction.

7.7 Tapered SOI waveguide and Chip – Fibre Coupling

Further works were carried out to investigate the butt coupling efficiency of these SOI waveguide designs with single mode fibres (SMF) with different spot-size in order to determine the optimum coupling efficiency Ω_o. This would enable us to know the kind of coupling efficiency to expect when sub-micron waveguide structures are being coupled to various waveguides with radial spot-size between 0.5 to 5.0 μm. Simulations were carried out for the Case 3, for example, in which each SMF radius, obtained from Gaussian algorithm were butt-coupled in turn to the submicron waveguide structures. The results obtained are shown on Fig. 7.55, which shows the comparison between the coupling efficiency curves for the Case 3, with 3μm x 3μm secondary core and the improved Case 6x5, with 6μm x 5μm secondary core waveguides. The Ω_o for Case 3 for 0.5 μm is 54%, for 1.0 μm, it is 62%, and as Ω_o increases it gets to Ω_{opt} = 98% at 2.0 μm when Ω_o starts to decrease. The optimum coupling fibre radius for the 3x3 waveguide is for Ω_o = 2.0 μm and the efficiency range is from 52% to 82% for Ω_o values from 0.5 to 5.0 μm respectively. Whereas in the Case 6x5, 0.5 μm is 38%, for 1.0 μm, it is 44%, and as Ω_o increases it gets to Ω_{opt}

= 99% at 2.5 μm when Ω_o starts to decrease. The optimum beam radius is Ω_{opt} = 2.5 μm and the efficiency spectrum from 38% to 88% for 0.5 to 5.0 μm respectively. It can be seen that the Case 6x5 waveguide has a wider efficiency spectrum than Case 3 waveguide. This can be explained from the point of view that the connecting polymer layer of Case 6x5 waveguide has a larger spot-size area which matched the Gaussian radius, Ω_{opt} = 2.5 μm better than that of when Case 3 waveguide is matched to Ω_{opt} = 2.0 μm. These curves give us good idea of the range of coupling efficiency to expect when coupling SOI waveguides to various SMF radii.

Further investigation was done to obtain the curve of coupling efficiency against the propagation length for various coupling fibres with Gaussian radii, Ω_o = 1.0, 2.0, 2.5, 5.0 μm of case 5 waveguide. It can be seen from Fig. 7.56 that the curve of Gaussian radius Ω_o = 2.5 μm gives the optimum coupling efficiency which is 99.3%. On the other hand, it shows the maximum efficiency for a smaller Ω_o = 2.0 μm is 96.8%, Ω_o = 1.0 μm has maximum at 67.1%. As the Ω_o increases to 5.0 μm, the maximum efficiency is 86.5%, which is also lower than that of 2.5 μm which agrees well with Fig. 7.55, shows maximum efficiency can be obtained when Ω_o = 2.5 μm. This study also shows that the design is considerably robust with axial distance tolerances. This study will go a long way to let optoelectronic designers know what to expect when dealing with such waveguides.

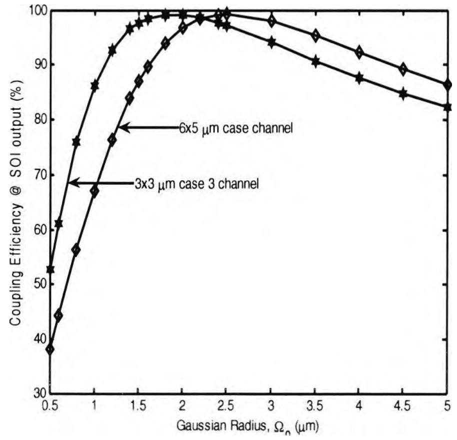

Fig. 7.55. Comparison between the coupling efficiency curves for the 3x3 channel and 6x5 channel waveguides for various Gaussian radii.

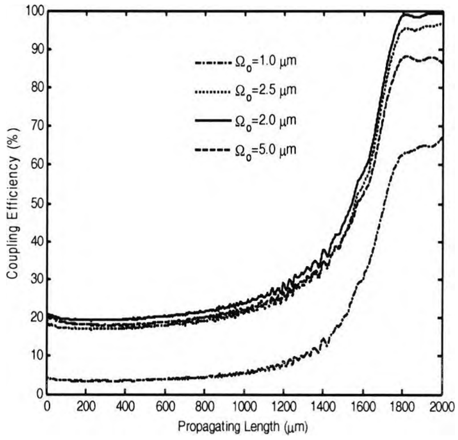

Fig. 7.56. The coupling efficiency against the propagation length for various Gaussian radii, Ω_o = 1.0, 2.0, 2.5, 5.0 μm of 6x5 channel waveguide.

Table 7.2: Data for SOI waveguide properties

MODELS $n_1/n_2/n_3$ W_2 x H_2 (μm)	FINAL WIDTH (μm)	PROP POWER (au)	PROP LOSS (dB)	SPOT SIZE (μm^2)	COUPLING EFFICIENCY (%)
3.48/3.0/1.45 **3 x 3**	0.1	5.07	-0.74	4.30	79.5
3.48/1.47/1.45 **3 x 3**	0.007	3.08	-10.81	8.44	97.7
3.48/3.0/2.98 **3 x 3**	0.02	5.40	-2.04	9.78	97.2
3.48/3.0/1.45 **6 x 6**	0.14	2.58	-0.52	17.78	97.5
3.48/1.47/1.45 **6 x 6**	0.007	1.59	-10.48	8.86	99.0
3.48/3.0/2.98 **6 x 6**	0.02	5.66	-1.39	28.94	99.0
3.48/3.0/2.98 **6 x 5**	0.02	5.69	-1.40	21.46	99.3

7.8 Summary

In this work, we have analyzed and optimised the design parameters of a spot-size converter in silicon-on-insulator waveguides (SOI). The designs have been symmetric laterally tapered and asymmetric vertically and we have demonstrated light is more tightly confined in the SOI waveguides than in many other layered semiconductor guides. In Case 1, SSC had a low-loss which is good, but the coupling efficiency was also low. The transmission power is good, but a poor spot-size conversion which is marred by mode-beatings. For Case 2, the loss value was high which is not desirable, but the coupling efficiency was higher. The transmission power is low but the spot-size is good with little or no mode-beatings. Case 3, shows an excellent design optimisation with low-loss, good coupling efficiency, good power, and fully expanded spot-size with no mode-beating oscillations. This is in good agreement with previously published experimental works of Fan and Hooker, 1999; Roelkens, *et al.*, 2005; and Shoji *et al.*, 2002. Of all the three cases considered initially in which the polymer channels are 3 x 3 μm, Case 3 have been found to transmit low-order modes and filter out higher order modes.

Case 4 suggests the lowest transmission loss of 0.52 dB, supported by a mode conversion which is mode-beating free. Although the coupling efficiency is high, the model suffers a higher power loss. As an extension to Case 1, the polymer cross-sectional area has marked improvement on this SOI model. Case 5 is similar to Case 2 in that it has a high loss value. Low power, spot-size conversion improvement from 4.3 to 8.86 μm^2 with very low oscillations. As an extension to Case 2, the polymer channel has little or no effect on the characteristics of this SOI model except for the slight improvement in the coupling efficiency. There are improvements in all the observed characteristics of Case 3 model when polymer channel is extended in Case 6. However the extension is large enough to support higher order modes in which some mode-beating oscillations were observed. Further efforts were made to correct this phenomenon and this gives rise to case 6x5 μm design. This model is similar to the Case 6 model in its power and loss characteristics. It has higher coupling efficiency but the mode-beating oscillations have been drastically reduced. With this result, it can be concluded that a further reduction in the height of the polymer channel of the SOI will eliminate completely the observed mode-beating. A trade-off has to be made between the vertical height of the polymer connecting channel and the level of spot-size mode conversion required. The combination of SOI rib waveguides loss, modal characteristics, fibre optical compatibility, and the ability to modulate the refractive index of these waveguides efficiently in the MHz range makes SOI technology a potential candidate for high-accuracy interferometric sensor applications (Rickman *et al.*, 1994).

Rigorous and accurate numerical simulations has been used to examine and design SOI polymer waveguide tapers which can perform beam transformation for improved coupling between output waveguiding structures with different mode shapes and sizes. In other words the monolithically integrated SOI waveguide can be used to couple light between arbitrary optoelectronics devices like modulators, directional couplers, amplifiers, switches etc. with different mode sizes. The hallmark of this work is the presentation of very simple design geometries and materials that are easy to fabricate with the popular and versatile CMOS technology on the basis of mass production of SOI devices to achieve the effective FTTH package.

Chapter 8

General Conclusions

8.1 General Conclusions

Modelling and Optimisation of compact spot-size converters in Photonics Integrated circuits (PICs) has been the primary objective of the work carried out in this thesis. In this work, numerical simulations based on the versatile and accurate vector finite element method (VFEM) has been the foundation which other numerical methods namely, full-vector beam propagation method and least squares boundary residual method have been developed and used in the design, optimization and characterisation of various types of 3-dimensional compact spot-size converters. Geometrical and material parameters used in modelling the SSCs are similar to the ones used in fabricating the real photonic devices and their charaterisations on operational parameters such as propagation power, propagation loss, spot-size, maximum coupling efficiency and minimum length of the device have been calculated. A novel design for multimode interference (MMI) spot-size converter was designed. Twin rib spot size and silicon-on-insulator (SOI) spot-size converters are also designed and optimised. In this thesis, the emphasis has been placed on developing the finite element-based techniques for further use in the modelling and analysis of these practical spot-size converters and more advances of photonics integrated circuits can be achieved.

The consistency and validity of the numerical simulation techniques developed in this thesis has been demonstrated and the objectives set out in the first chapter have been competed successfully with detailed analysis of the results obtained. The results obtained in this thesis have been compared with other previously published experimental results and are in close agreement which confirms the validation of the techniques developed.

In summary, the aims and objectives set out in Section 1.5 were achieved as follows:

(1) To investigate different fabrication technologies and suitable materials in the production of optical waveguides especially the CMOS process which is employed for mass production of silicon integrated circuits.

This is illustrated in Section 2.2 – 2.4, where it is stated that most of the design materials reported in this thesis can be fabricated by using the epitaxial or deposition techniques. The following materials; silica, GaAs, InP substrates fall under the group which undergoes photolithographic processes and ething techniques after deposition because their lateral dimensions are just few microns. These materials are commonly used in practical situations and their material indices are used throughout this thesis. The epitaxial growth techniques are the popular deposition methods for materials like GaAs and InP, while complimentary metal- oxide semiconductor (CMOS) is emphasised as the most important technology for the fabrication of microelectronic circuits especially silicon integrated circuits. The technology for Twin-well CMOS process and its usefulness is described.

(2) To investigate different approaches to the solution of optical waveguide problems and to provide a basis for the effective employment of the finite element method.

This is illustrated in Section 2.5, where the computational techniques in which various analytical and numerical methods are described briefly. The advantages of numerical method over analytical method is emphasised and the justification for the use of Finite element method is highlighted as the main tool to be used throughout this thesis.

(3) To develop and implement the rigorous, accurate and efficient finite element method based on vector **H**-field variational formulation for the analysis of optical waveguides with arbitrary cross sectional shapes.

The whole of Chapter 3 is devoted to the vector finite element method which is presented in detail as one of the most powerful numerical methods that has become very popular among research scientists because it offers a high degree of versatility and accuracy. Among the other formulations reported so far, the vector **H**-field formulation has been used especially because of its boundary conditions attributes since it is naturally continuous across dielectric interfaces and this is presented in Section 3.6.2. The associated natural boundary conditions are that of an electric wall and this is easier to implement in most practical waveguide cases. The **H**-field formulation normally starts with the triangular discretisation of the system or region of interest. The variational principle, shape functions and vector formulation were explained in details. The non-physical or spurious solutions were eliminated by implementing the $\nabla \cdot \mathbf{H}=0$ condition and additional penalty term in the variational formulation. This formulation has stand a test of time in problems involving complex and arbitrary cross-section, index profile, and so on, determining the model field profiles and the propagation characteristics of the guidewave practical photonic integrated devices.

(4) To implement the least squares boundary residual (LSBR) in conjunction with the accurate modal solutions obtained from the finite element method in order to develop accurate coupling properties of multimode interference (MMI) coupler waveguides.

This is illustrated in Section 5.2 – 5.4 where the principle of spot-size conversion of the beam evolution in a waveguide and the need to have integrated spot-size converters has been presented. The robustness and usefulness of least squares boundary residual method (LSBR) is also presented. The versatile vectorial FEM together with the LSBR method is applied to the novel design of the multimode interference (MMI) waveguide as a spot-size converter to improve the coupling efficiency to a single mode fiber from 18% to 36%. This is a novel idea and more can still be done to improve the coupling efficiency recorded in this work due to time constraint.

(5) To apply full-vectorial finite elements techniques developed and implemented in (3) in the study of designing a spot-size to solve mode-matching problems in optoelectronics.

This is illustrated in Section 5.5. The phenomenon of spot-size conversion in 2-D is also demonstrated in the design of a twin rib spot-size converter to improve the coupling efficiency to a SMF. In this section, the VFEM has been used as a stand-alone in this work to examine the prospect of achieving bigger spot-size for efficient coupling. The spot-size conversion occurred when the upper rib waveguide is 1.6 μm and the quasi-TE mode spot-size increases from 1.0 μm^2 to 51 μm^2. This is a remarkable spot-size expansion which shows the versatility of the VFEM as a very good design tool in optoelectronics.

(6) To develop and implement an efficient and robust beam propagation method which combines the finite element discretisation in the transverse domain with the stable z-stepping Crank-Nicholson scheme in the longitudinal direction.

This is achieved in Chapter 4 which reports on the study of the propagation of guided waves in the longitudinally z-variant structures. While the powerful vector **H**-field finite element has been described as having the capability to design and characterise variety of photonic integrated devices in their stationery 2-D stated or an invariant situation in the longitudinal direction. But vector **H**-field finite element formulation is not capable of simulating the propagation and interaction of light with media in the longitudinally non-uniform devices such as bends, junctions and tapers. The solution to this problem gives rise to versatile, robust and efficient finite element-based Beam Propagation Method (BPM). The VFEM is always employed to provide the modal solutions quasi TE or TM mode field profiles. It is based on real vector of the six transverse magnetic field components which satisfies the appropriate interface boundary conditions and also automatically satisfies the zero divergence condition, which prevents the spurious solutions from affecting the propagation. This algorithm takes into account the effects of reflection and radiation waves during the propagation by using the rigorous PML boundary condition. Also taken into account is the realistic wide angle range approximation by using the Pade recurrence relation which can accurately determine the path of the waves propagating off the longitudinal z-axis. The global matrices generated are sparsed unlike other vector formulations which result in dense matrices, therefore, only nonzero entries are stored and efficient LU decomposition matrix solver is used. The vectorial BPM algorithm is extended to calculating some wave properties like propagating power, the spot size and the propagation loss. Also the overlap integral has been incorporated into the algorithm for the assessment of the coupling efficiency.

(7) To apply the developed and implemented beam propagation method in the design and optimisation of a novel semiconductor based (AlGaAs-GaAs) spot-size converters by using full vectorial numerical methods implemented in (3) to the characterisation of GaAs and vector **H**-field variational formulation tapers.

This is illustrated in Section 6.4. The quest to have compact spot-size converters in 3-D now moves to the situation whereby the propagation and interaction of light in the longitudinal z-variant structures such as tapers need to be examined. In Chapter 6, the VFEM is used in conjunction with the FVBPM to optimize design of tapered Spot-size Converter (SSC) in the longitudinal z-direction. The work presented here illustrates various design options for spot-size converters using the BPM incorporating the overlap integral, to improve the coupling between a PIC and a SMF. A compact lateral twin-rib taper SSC design has been produced, which has minimum length, minimum radiation losses, and maximum coupling efficiency of 90%. It has been compared with other conventional SSC design using VFEM, and the accuracy of the BPM with the overlap integral has been shown to be excellent. The mode-beating can be experienced when designing taper structures but can be avoided by correct choice of length and width parameters.

(8) To apply the full vectorial numerical techniques implemented in (3) and (6) in the study of designing and characterising various optical waveguides involved in silicon-on-insulator (SOI) spot-size converter issues in optoelectronics.

This is fully illustrated in the whole of Chapter 7 where the principles and operations of silicon-on-insulator (SOI) are presented. There has been significant interest in development of optical devices using SOI waveguides because the material and the processing are relatively low cost and also the high index contrast between silicon and silica makes it possible for high density integration and this gives rise to size reduction of integrated optical structures. The properties, applications and fabrications of SOI waveguides were discussed and simple but realistic seven models are presented in this work with emphasis on the Δn characterisations. The computational techniques involve the use of VFEM and FVBPM to carryout these designs.

The highest coupling efficiency achieved is 99.25% and low-loss of 0.52dB is recorded. Painstaking and accurate numerical simulations has been used to examine and design SOI polymer waveguide tapers which can perform mode transformation for improved coupling between waveguiding structures with different mode shapes and sizes. In other words the monolithically integrated SOI waveguide can be used to couple light between arbitrary optoelectronics devices like modulators, fibres, directional couplers, amplifiers, switches etc. with different mode sizes. The hallmark of this work is the presentation of very simple design geometries and materials that are easy to fabricate with the popular and versatile complimentary metal-oxide-semiconductor (CMOS) technology on the basis of mass production of SOI devices to achieve the effective ‘fibre-to-the-home’ (FTTH) package.

8.2 Suggestions For Future Work

Design, analysis and optimisation of compact spot-size converters have been carried out in this thesis. It has been shown that a photonic integrated circuit (PIC) with a small and non-circular spot-size (typically of about 1 μm) can be directly butt-coupled to a single-mode fiber (SMF) with a larger and circular spot-size (typically of about 10 μm). However, most SSC designs reported so far do not have exactly circular spot-size shape that will match the type of circular spot-size normally seen in a single-mode fiber. More works still need to be done for further improvement to achieve a more circular spot-size in future. Such an achievement will mark another milestone in the work of optical research workers as adiabatic tapers will be easier to fabricate.

The combinations of the VFEM and FVBPM have been employed to calculate some parameters like the spot-size, propagation losses, propagating power and the overlap integral has been incorporated to calculate the coupling efficiency of guidedwave devices. Another important consideration for future work would be the incorporation of the least squares boundary residual method into the beam propagation method to calculate propagating parameters like the power transfer from a waveguide section to another, to obtain both the transmission and the reflection coefficients, which overlap integral cannot handle excellently. The development of such a numerical model will provide researchers with a powerful tool for the study and analysis of various waveguides.

References

- Alferov Zh.I., Andreev V.M., Portnoi E.L. and Trukkan M.K., "AlAs-GaAs heterojunction injection lasers with a low-room temperature threshold," *Soviet Physics Semiconductors* 3: 1107-1110. 1970.
- Aalto, T., Himala, S., Yliniemi, Y., Kapulainen, S., and Leppihalme, M. "Fabrication and characterization of waveguide structures on SOI," in Proc. SPIE, vol. 4944, pp. 183-194, 2003.
- Aalto, T., Solehmainen, K., Harjanne, M., Kapulainen, M., and Heimala, P. "Low-Loss Converters between Optical Silicon Waveguides of different Sizes and Types," IEEE Photon. Technol. Lett., vol. 18, no. 5, pp. 709-712, Mar. 2006.
- Agrawal, G. *Fiber-Optic Communication Systems.* New York: Wiley, 1992.
- Ahmed, S. and Daly, P., "Waveguide solutions by the finite element method," *Radio and Electronic Engineer,* vol. 38, pp. 217-223, 1969.
- Anderson B. D., "Optical and Electro-optic information Processing" MIT Press, Cambridge, 1965.
- Anwar, N S., Obayya, S. S. A, Haxha S, Themistos C, Rahman B. M. A, and Grattan K. T. V., "The Effect of Fabrication Parameters on a Ridge Mach-Zender Interferometric (MZI) Modulator," *Journal of Lightwave Technology,* LT-20 (5): 826-833, 2002.
- Aoki, M., Komori, M., Suzuki, M., Sato, H., Takahashi, M., Ohsoshi, T., Uomi, K. and Tsuji, S., "Wide-temperature-range operation of 1.3 μm beam expander-integrated laser diodes grown by in-plane thickness control MOVPE using a silicon shadow mask", IEEE Photon. Technol. Lett., vol. 8, no. 4, pp. 479-481, 1996.
- Aoki, M., Komori, M., Sato, H, Tsuchiya, T., Taike, A., Takahashi, M., Uomi, K. and Tsuji, S., "Reliable wide-temperature-range operation of 1.3 μm beam-expander integrated laser diode for passively aligned optical modules", IEEE J. of Selected Topics in Quantum Electron., vol. 3, no. 6, pp. 1405-1412, 1997.

- Arnold, J., Belghoraf, A., and Dendane, A., "Intrinsic mode theory of tapered optical waveguides," Inst. Elec. Eng. Proc., vol. 132, pt. J, no. 6, Dec. 1985.
- Balland, G., Paski, R. M., and Baker, R. A., "TAT-12/13 integration development tests – interim results," in *Proc. International Conf. Optical Fibre Submarine Telecom.*, Paper 3.6, March 1993.
- Barrios, C.A., Almeida, V.R.., Panepucci, R.,and Lipson, M. "Electro optic Modulation of silicon-on-insulator sub micrometer-size waveguide devices," *J. Lightwave Technol.,* vol. 21, no. 10, pp. 2332-2339, Oct. 2003a.
- Barrios, C. A., Almeida, V. R., and Lipson, M. "Low-power-consumption short-length and high-modulation-depth silicon electro-optic modulator," *J. Lightwave Technol.,* vol. 21, no. 4, pp. 1089-1098, 2003b.
- Bathe K. J., and Wilson, E. L., "Numerical methods in finite element analysis" *New Jersey: Prentice Hall*, 1976.
- Berenger, J.P. "A Perfectly matched layer for the absorption of electromagnetic waves, '' *J. Comput. Phys.,* vol. 114, no 2,, pp. 185-200, 1994.
- Bogaerts, W., Baets, R., Dumon, P., Wiaux, V., Beckx, Taillaert, S. D., B. Luyssaert, Van Campenhout, J., Bienstman, P., and Van Thourhout, D. "Nanophotonic waveguides in silicon-on-insulator fabricated with CMOS technology," *J. Lightwave Technol.,* vol. 23, no. 1, pp. 401-412, Jan. 2005.
- Bossavit, A., and Mayergoyz, I., "Edge-elements for scattering problems," *IEEE Trans. Magnetics*, vol. 25, no. 4, pp. 2816-2821, July 1989.
- Bossi, D. E., Goodhue, W. D., Finn, M. C., Rauschenbach, K., Bales, J. W. and Rediker, R. H., "Reduced-confinement antennas for GaAlAs integrated optical waveguides", *Appl. Phys. Lett.,* vol. 56, no 5, pp. 420-422, 1990.
- Bossi, D. E., Goodhue, W. D., Johnson, L. M. and Rediker, R. H., "Reduced-confinement GaAlAs tapered waveguide antennas for enhanced far-field beam directionality," *IEEE J. Quantum Electron.,* vol. 27, pp. 687-695, 1991.
- Brandrup, J. and Immergut, E. H., "Polymer handbook." *Edited John Wiley & Sons, New York,* 1989.
- Brenner, T., Hunziker, W., Smit, M., Bachmann, M., Guekos, G., and Melchoir, H., "Vertical InP/InGaAsP tapers for low-loss optical fiber-waveguide coupling, *Electron. Lett.,* vol. 28, no. 22, pp. 2040-2041, 1992.

- Brenner, T., and Melchior, H., "Integrated optical mode-shape adapters in InGaAs/InP for efficient firber-to-waveguide coupling", *IEEE Photon. Technol. Lett.,* vol. 5, pp. 1053-1056, 1993.
- Brooke, G. H. and Kharadly, M. M. Z., "Step discontinuities on dielectric waveguides," *Electron. Lett.,* vol. 12, no. 18, pp. 473-475, 1976.
- Bruel, M. "A new silicon-on-insulator material technology," *Electron. Lett*, vol. 31, no. 14, pp. 1201-1202, 1995.
- Burke, S. V., "Spectral index method applied to coupled rib waveguides," *Electron. Lett.*, vol. 25, no. 9, pp. 605-606, 1989.
- Burke, S. V., "Spectral index method applied to two nonidentical closely separated rib waveguides," *IEE Proc. Pt. J*, vol. 137, no. 5, pp. 289-292, 1990.
- Burke, S. V., "Planar waveguide analysis by the spectral index method: II. Multiple layers, optical gain and loss," *Opt. Quantum Electron.*, vol. 26, no. 2, pp. 63-77, 1994.
- Cao, G. B., Gao, F., Jiang, J. and Zhang, F., "Directional couplers realized on silicon-on-insulator," *IEEE Photon. Technol. Lett.,* vol. 17, no. 8, pp. 1671-1673, Aug. 2005a.
- Cao, G. B., Dai, L.J.; Wang, Y.J.; Jiang, J.; Yang, H.; Zhang, F., "Compact integrated star coupler on silicon-on-insulator" *IEEE Photon. Technol. Lett.,* vol 17, no. 12, pp. 2616-2618, Dec 2005b.
- Chiang, K. S., "Analysis of optical fibres by the effective-index method," *Appl. Opt.,* vol. 25, no. 3, pp. 348-354, 1986*a*.
- Chiang, K. S., "Dual effective index method for the analysis of rectangular dielectric waveguides," *Appl. Opt.*, vol. 25, no. 13, pp. 2169-2174, 1986*b*.
- Chiang, K. S., "Review of numerical and approximate methods for the modal analysis of general optical dielectric waveguides," *Opt. Quantum Electron.*, vol. 26, no. 3, pp. S113-S134, 1994.
- Chiang, K. S., Lo, K. M., and Kwok, K. S., "Effective-index method with built-in perturbation correction for integrated optical waveguides," *J. Lightwave Technol.*, vol.14, no. 2, pp. 223-228, 1996.

- Clarricoats, P. J. B. and Sharpe, A. B., “Modal matching applied to a discontinuity in a planar surface waveguide,” *Electron. Lett.,* vol. 8, no. 2, pp. 28-29, 1972.
- Cocorullo, G., and Iodice, M., Rendina, I., and Sarro, P.M. “Silicon thermo-optical micro-modulator with 700 kHz -3 dB bandwidth,” *IEEE Photon. Technol. Lett.,* vol. 7, pp. 363-365, 1995.
- Colas, E., Shahar, A. and Tomlinson, W. J., “Diffusion-enhanced epitaxial growth of thickness-modulated low-loss rib waveguides on patterned GaAs substrates,” *Appl. Phys. Lett.,* vol. 56, no 10, pp. 955-957, 1990.
- Courant, R. L., “Variational method for the solution of problems of equilibrium and vibration,” *Bulletin of the American Mathematical Society,* vol 49, pp. 1-23, 1943.
- Csendes, Z. J. and Silvester, P., “Numerical solution of dielectric loaded waveguides: I – Finite-element analysis,” *IEEE Trans. Microwave Theory Tech.*, vol. MTT-18, no. 12, pp. 1124-1131, 1970.
- Cullen, A. L., Ozkan, O., and Jackson, L. A., “Point-matching technique for rectangular-cross-section dielectric rod,” *Electron. Lett.*, vol. 7, no. 17, pp. 497-499, 1971.
- Cullen, A. L. and Yeo, S. P., “Using the least-squares boundary residual method to model the summetrical five-port waveguide junction,” *IEE Proc. Pt. H*, vol. 134, no. 2, pp. 116-124, 1987.
- Dagli, N. and Fonstad, C. G., “Microwave equivalent circuit representation of rectangular dielectric waveguides,” *Appl. Phys. Lett.*, vol. 49, no. 6, pp. 308-310, 1986.
- Dai, D., He, J., and He, S. “Elimination of multimode effects in a silicon-on-insulator etched diffraction grating demultiplexer with bi-level taper structure,” *IEEE J. Select. Topics Quantum Electron.,* vol. 11, no. 2, pp. 439-443, Mar 2005.
- Dake, F. J., “Dake Annotated Reference Bible, Kings James version”, *Dake Publishing*, 2006.

- Daly P., "Finite element approach to propagation in elliptical and parabolic waveguides", *International Journal of Numerical Methods 20* (4): 681-688. 1984.
- Damask, J. N., "Polarisation optics in telecommunications" Springer, 2005.
- Davies, J. B., "Review of methods for numerical solution of the hollow-waveguide problem," *Proc. IEE*, vol. 119, no. 1, pp. 33-37, 1972.
- Davies, J. B., "A least-squares boundary residual method for the numerical solution of scattering problems," *IEEE Trans. Microwave Theory Tech.*, vol. MTT-21, no. 2, pp. 99-104, 1973.
- Davies, J. B., "The finite element method, in Numerical techniques for microwave and millimeter-wave passive structures," Edited by T. Itoh, *New York: Wiley,* pp. 33-132, 1989.
- Davies, J. B., "Finite element analysis of waveguides and cavities – a review," *IEEE Trans. Magnetics*, vol. 29, no. 2, pp. 1578-1583, 1993.
- Desai, C. S., *Elementary finite element method*, Prentice-Hall Inc., New Jersey, 1979.
- Dow Corning, "Highly transparent silicone materials," *Photonic Solutions,* Dow Corning Corporation, 2005.
- Dumke, W. P., "Interband transitions and maser action," *Phys. Rev.,* vol. 127, pp. 1559-1563, 1962.
- Dumon, P., Bogaerts, W., Wiaux, V., Wouters, Beckx, J. S., Camperhout, J. V., Taillaert, D., Luyssaert, B., Bienstman, P., Thourhout, D. V., and Baets, R., "Low-loss SOI photonic wires and ring resonators fabricated with deep UV lithography," *IEEE Photon. Technol. Lett.*, vol. 16, no. 5, pp. 1328 – 1330, May 2004.
- Dutton, H. J. R., "Understanding optical communications", *Redbooks, IBM, First Edition,* 1998.
- Edwards, C., Presby, H., and Dragone, C., "Ideal microlenses for laser to fiber coupling," *J. Lightwave Technol.,* vol. 11, pp. 252-257, Feb. 1993.
- El Yumin, S., Komori, K., Arai, S., and Bendelli, G. "Taper-shape dependence of tapered-waveguide travelling wave semiconductor laser amplifier (TTW-SLA)," *IEICE Trans. Electron.,* vol. E77-C, no. 4, pp. 642-632, Apr. 1994.

- Eng, T. T. H., Sin, S. S. Y., Kan, S. C., and Wong, G. K. L. "Surface-micro machined movable SOI optical waveguides," *Sensors & Actuator Tech.*, vol. 1, pp. 348-350, 1995.
- English, W. J. and Young, F. J., "An E vector variational formulation of the Maxwell equations for cylindrical waveguide problems," *IEEE Trans. Microwave Theory Tech.*, vol. MTT-19, no. 1, pp. 40-46, 1971.
- Fan, R. S., Goodwill, D. J., Hooker, R. B., Lee, Y. C., McComas, B. K., Mickelson, A. R., and Morozova, N. D., "Polymer tapered waveguides and flip-chip solder bonding as compatible technologies for efficient OEIC coupling," in *Proc. ECTC '97*, pp. 788-796, 1997.
- Fan, R. S., and Hooker, R. B., "Tapered polymer single-mode waveguides for mode transformation," *J. Lightwave Technol.,* vol. 17, no. 3, pp. 466-474, 1999.
- Feit, M. D. and Fleck, J. A. "Light propagation in graded-index optical fibres," *Appl. Opt.*, vol 17, no.24, 3990-3998, 1978.
- Feit, M. D. and Fleck, J. A, "computation of mode properties in optical fibres wave guides by a property beam method," *Appl. Opt.*, vol.19, no. 7, pp.1154-1164, 1980.
- Fen, J. C.C., Geis, M. W., and Tsaur, B. Y. "Lateral epitaxy by seeded solidification for growth of single-crystal Si film on insulator," *Appl., Phys., Lett.*, vol. 38, no. 5, pp. 365-367, Mar. 1981.
- Fernandez, F. A. and Davies, J. B., "Least-squares boundary residuals solution of microstrip step discontinuities," *Electron. Lett.,* vol. 24, no. 10, pp. 640-641, 1988.
- Fischer, U., Zinke, T., J. Kroop, J. R., Arndt, F., and Petermann, K. "0.1 dB/cm waveguide losses in single-mode SOI rib waveguides," *IEEE Photon. Technol. Lett.,* vol. 8, no. 5, pp. 647-648, May 1996.
- Foresi, J. S., Villeneuve, P. R., Ferrera, J., Theon, E. R., Stein Meyer, G., Fan, S.,Joannopoulos, J. D., Kimerling, L.C., Smith, H. I., and Ipren, E. P. "Photonic-band gap micro cavities in optical waveguides," *Nature, vol.* 390, pp143, 1997.
- Goell, J. E., "A circular-harmonic computer analysis of rectangular dielectric waveguides," *Bell Syst. Tech. J.*, vol. 48, pp. 2133-2160, 1969.

- Gordon, J. P. and Mollenauer, L. F., "Effects of fiber nonlinearities and amplifier spacing on ultra-long distance transmission," *J. Lightwave Technol.*, vol. 9, no. 2, pp. 170-173, 1991.
- Guerra, M. A., "The status of SIMOX technology," *Solid State Technol.*, vol. 33, no. 11, pp. 75-78, 1990.
- Hadley, G.R., "Transparent boundary condition for beam propagation methods,'' *Opt. Lett.*, vol. 16, no. 9, pp. 624-626, 1991.
- Hadley, G.R. 'Wide angle beam propagation using Pade approximation operators, '' *Opt. Lett.*, vol. 17, no. 20, pp.1426-1428, 1992.
- Hall R.N., Fenner G.E, Kingsley J.D., Soltys T.J. and Carison R.O. (1962). Coherent light emission from GaAs junctions. *Physical Review Letters 9* (9): 366-368.
- Haxha, S., Ladele, E.O., AbdelMalek and Rahman, B. M. A. "Optimization of compact lateral, vertical, and combined tapered spot-size converters by use of the beam propagation method," *Applied Optics*, vol. 45, no. 2, pp. 288-296, Jan. 2006.
- Hayashi I., Panish M.B., Foy P.W. and Sumski S. (1970). Junction lasers which operate continuously at room temperature. *Applied Physics Letters* 17 (3): 109-111.
- Hayata, K., Koshiba, M., Eguchi, M., and Suzuki, M., "Novel finite-element formulation without any spurious solutions for dielectric waveguides," *Electron. Lett.*, vol. 22, no. 6, pp. 295-296, 1986.
- Hirayama, K. and Koshiba, M., "Analysis of discontinuities in an open dielectric slab waveguide by combination of finite and boundary elements," *IEEE Trans. Microwave Theory Tech.*, vol. MTT-37, no. 4, pp. 761-767, 1989.
- Hocker, G. B., and Burn, W. K., "Mode dispersion in diffused channel waveguides by the effective index profiles," *Appl. Opt.*, vol. 16, no. 1, 113-118, 1977.
- Hockham, G. A. and Sharpe, A. B., "Dielectric – waveguide discontinuities," *Electron. Lett.,* vol. 8, no. 9, pp. 230-231, 1972.
- http://www.orc.soton.ac.uk/oc.html

- http://www.freepatentsonline.com/4332706.html "Internal reflection suppressing coating material for optical glass: Polymerized cements," *Optica Acta,* vol. 14, pp. 401-435, 1967.
- Huang, W. P., Xu, C. L., Lui, W., and Yokoyama, K. "The perfectly matched layer (PML) boundary condition for the beam propagation method," *IEEE Photon. Technol. Lett.,* vol. 8, no. 5, pp. 649-651, May 1996.
- Hunsperger R.G. (1984). Integrated Optics: Theory and Technology. 2nd ed. (Berlin: Springer-Verlag).
- IEEE J. Selected Topics in Quantum Electronics, special issue, vol. 3, Dec., 1997.
- Jacobs, B., Zengerle, R., Faltin, K. and Weiershausen, W., "Vertically tapered spot-size transformers fabricated by a simple masking technique", *Electron. Lett.* vol. 31, no. 10, pp. 794-795, 1994.
- Jalali, B., Yegnanarayanan, S., Yoon, T., Yoshimoto, T., I. Rendina, T.I., and F. Coppinger, "Advances in Silicon-on-insulator optoelectronics," *IEEE J. Select. Topics Quantum Electron.*, vol. 4, no. 6, pp. 938-947. 1998.
- Jalali, B., Naval. F.,Levi, J, "Si-based receivers for optical data links," *J. Lightwave Technol.,* vol. 12, no. 1, pp. 930-935, 1994.
- Kagami, S. and Fukai, I., "Application of boundary-element method to electromagnetic field problems," *IEEE Trans. Microwave Theory Tech.*, vol. MTT-32, no. 4, pp. 455-461, 1984.
- Kao K.C. and Hockham G.A. "Dielectric-fibre surface waveguides for optical frequencies," *Proceedings IEE* 113: 1151-1158, 1966.
- Kapany N.S. "Fibre Optics: Principles and applications" (New York: Academic Press), 1967.
- Kasaya, K., Mitomi, O., Naganuma, M., Kondo, Y., and Noguchi, Y., "A simple laterally tapered waveguide for low-loss coupling to single-mode fibers," *IEEE Photon. Technol. Lett.,* vol. 5, pp. 345-347, Mar. 1993.
- Kasukawa, A., Nishikata, K., Yamanaka, N., Arakawa, S., Iwai, N., Mukaihara, T. and Matsuda, T., "Structural dependence of 1.3 μm narrow-beam lasers fabricated by selective MOCVD growth", *IEEE J. of Selected Topics in Quantum Electron.,* vol. 3, no. 6, pp. 1413-1419, 1997.

- Kawachi, M., "Silica waveguides on silicon and their application to integrated-optic components", *Optical and Quantum Electronics*, 22, pp. 391-416, 1990.
- Kendall, P. C., McIlroy, P. W. A., and Stern, M. S., "Spectral index method for rib waveguide analysis," *Electron. Lett.*, vol. 25, no. 2, pp. 107-108, 1989.
- Kim, H., Sinha, S., and Ramaswamy, R. "An MQW_SQW tapered waveguide transition," *IEEE Photon. Technol. Lett.,*, vol. 5, pp. 1049-1052, Sept. 1993.
- Kiyat, I., Aydinli, A., and Dagli, N. "Polarisation characteristics of compact SOI rib waveguide racetrack resonators," *IEEE Photon. Technol. Lett.,*, vol. 17, no. 10, pp. 2098-2101, Oct. 2005.
- Knox, R. M. and Toulios, P. P., "Integrated circuits for the millimeter through optical frequency range," in *Proceedings, Symposium on Submillimeter Waves.* Brooklyn: Polytechnic Press, pp. 497-516, 1970.
- Kobayashi, H., Yamamoto, T., Ekawa, M., Watanabe, T., Ishi-kawa, T., Fuji, T., Soda, H., Ogita and Kobayashi, M. "Narrow-beam divergence 1-3 μm multiple-quantum-well laser diodes with monolithically integrated tapered thickness waveguides," *IEEE J. Select. Topics Quantum Electron.* vol. 3, pp. 1384-1391, Nov. 1997.
- Koch, T. L., Koren, U., Eisenstein, G., Young, M. G., Oron, M., Giles, M. C. R., and B. I. Miller, B. I., "Tapered waveguide InGaAs/InGaAsP multiple-quantum-well lasers", *IEEE Photon. Technol. Lett.,*, vol. 2, no. 2, pp. 88-90, 1990.
- Kogelnik, H., *Theory of optical waveguides in: Guided-wave optoelectronics*, Ed. By T. Tamir, Heidelberg, Springer-Verlag, 1990.
- Koshiba M. (1992). Optical waveguide analysis. (Tokyo: McGraw-Hill).
- Koshiba, M. and Suzuki, M., "Vectorial wave analysis of optical waveguides with rectangular cross-section using equivalent network approach," *Electron. Lett.*, vol. 21, no. 22, pp. 1026-1028, 1985.
- Koshiba, M. and Suzuki, M., "Boundary-element analysis of dielectric slab waveguide discontinuities," *Appl. Opt.*, vol. 25, no. 6, pp. 828-829, 1986*a*.
- Koshiba, M., and Suzuki, M., "Vectorial wave analysis of dielectric waveguides for optical integrated circuits using equivalent network approach," *J. Lightwave Technol.*, vol. 4, no. 6, pp. 656-664, 1986*b*.

- Koshiba, M., Hayata, K., and Suzuki, M., "Improved finite-element formulation in terms of the magnetic-field vector for dielectric waveguides," *IEEE Trans. Microwave Theory Tech.*, vol. MTT-33, no. 3, pp. 227-233, 1985*b*.
- Koshiba, M., Hayata, K., and Suzuki, M., "Approximate scalar finite-element analysis of anisotropic optical waveguides," *Electron. Lett.*, vol. 18, no. 10, pp. 411-413, 1982.
- Koshiba, M., Hayata, K., and Suzuki, M., "Vectorial finite-element method without spurious solutions for dielectric waveguide problems," *Electron. Lett.*, vol. 20, no. 10, pp. 409-410, 1984.
- Koshiba, M., and Inoue, K., "Simple and efficient finite-element analysis of microwave and optical waveguides," *IEEE Trans. Microwave Theory Tech.*, vol. MTT-40, no. 2, pp. 371-377, 1992.
- Kumar A., Thyangarajan K. and Ghatak A.K., "Analysis of rectangular-core waveguides: An accurate perturbation approach", *Optics Letters*, 8 (1) 63-65, 1983.
- Ladele, E. O., Rahman BMA, Wongcharoen T., Obayya, S. S. A. and Grattan, K. T. V., "Design optimization of monolithically integrated semiconductor spot-size converters for efficient laser-fiber coupling" *International symposium on electron devices for microwave and optoelectronic applications*, pp 301-306, Nov., 2001.
- Lagasse, P.E., and Baets, R. "Application of propagating beam methods to electromagnetic and acoustic wave propagation problems: a review'' *Radio Science,* vol.22, no.7pp.1225-1233, 1986.
- Lee, K. K., Lim, D. R., Luan, H. C., Agarwal, A., Foresi, J., and Kimberling, L.C. "Effect of size and roughness on light transmission in Si/SiO$_2$ waveguide: Experiment and model," *Appl. Phys. Lett.*, vol. 77, (11), 2000.
- Lee, K. K., Lim, D. R., and Kimerling, L. C. "Fabrication of ultra low-loss Si/SiO$_2$ waveguides by roughness reduction," *Opt. Lett.*, vol. 26, no. 23, pp. 1888, 2001.
- Lee, C., Wu, M., Sheu, L., Fan, P., and Hsu, J. "Design and analysis of completely adiabatic tapered waveguides by conformal mapping" *J. Lightwave Technol.,* vol. 15, pp. 403-410, Feb. 1993

- Li, B., Li, G., Lui, E., Jiang, Z., Qie, J., and Wang, X., “Monolithic integration of a SiGe/Si modulator and multiple quantum well photodetector for 1.55 μm operation”, *Applied Physics Letters*, vol. 73(24), pp. 3504-3505, 1998.
- Liau, Z. L., Walpole, J. J., Livas, J., Kintzer, E., Mull, D., Misaaggia, L., and DiNatale, W., “Fabrication of two-sided anamorphic microlenses and direct Coupling of tapered high power diode laser to single-mode filter,” *IEEE Photo. Technol. Lett.,* vol. 7, pp. 1315- 1317, Nov. 1995.
- Lifante, Ginés., “Integrated Photonics Fundamentals”, *John Wiley*, 2003.
- Lin, C., Kobrinski, H., Frenkel, A., and Brackett, C. A., “Wavelength-tunable 16 optical channel transmission experiment at 2 Gbit/s and 600 Mbit/s for broadband subscriber distribution,” *Electron. Lett.*, vol. 24, no. 19, pp. 1215-1216, 1988.
- Little, B. E., Foresi, J. S., Stein Meyer, G., Theon, E. R., Chu, S. T., .Haus, H. A., Ipren, E. P., Kimerling, L. C., and Greene, W. “Ultra-compact Si-SiO$_2$ micro ring resonator optical channel dropping filters,” *IEEE Photon. Technol. Lett.,* vol. 10, no. 4, pp. 549-551, 1998.
- Livescu, G., “Optical Technology,” *New Jersey: Holmdel*, 2002.
- Lousteau, J., Furniss, D., Seddon, A. B., Benson, T. M., Vukovic, A., and Sewell, P. “The single-mode condition for silicon-on-insulator optical rib waveguides with large cross section,” *J. Lightwave Technol.,* vol. 22, no. 8, pp. 1923-1930, Aug. 2004.
- Lu, I., “Intrinsic modes in wedge-shaped taper above an anisotropic substrate,” *IEEE J. Quantum Electron.*, vol. 27, pp. 2373-2377, Nov. 1991.
- Lu, R., Liao, Y. and Wang, W., “Design of symmetric Y-branch with a substrate Prism and two tapered output waveguides on LiNbO$_3$,” *IEEE Photo. Technol. Lett.,* vol. 10, no. 9, pp. 1274-1276, Sept. 1998.
- Ma, H., Jen, A. K. Y. and Dalton, L. R., “Polymer-based optical waveguides: Materials, processing and devices,” *Advanced Materials,* vol. 14, no. 19, pp. 1339-1365, 2002.
- Mabaya, N., Lagasse, P. E., and Vandenbulcke, P., “Finite element analysis of optical waveguides,” *IEEE Trans. Microwave Theory Tech.*, vol. MTT-29, no. 6, pp. 600-605, 1981.

- Mahmoud, S. F., and Beal, J. C., “Scattering of surface waves at a dielectric discontinuity on a planar waveguide,” *IEEE Trans. Microwave Theory Tech.*, vol. MTT-23, no. 2, pp. 193-198, 1975.
- Maiman, T. H., “Stimulated optical radiation in ruby,” *Nature*, vol. 187, pp. 493-494, 1960.
- Marcatili, E. A. J., “Dielectric rectangular waveguide and directional coupler for integrated optics,” *Bell Syst. Tech. J.*, vol. 48, pp. 2071-2102, 1969.
- Marcatili, E. “Dielectric tapers with curved axes and no loss,” *IEEE Photon. Technol. Lett.,* vol. QE-21, pp. 307-314, Apr. 1985.
- Marcuse, D. “Radiation losses of step-tapered channel waveguides” *Appl. Opt.*, vol. 19, no. 21, pp. 3676-3681, Nov. 1980.
- März, R., “Integrated Optics: Design and Modelling” *Artech House*, 1995.
- Matera F., Curti F., Tosi-Beleffi G., Franco P., Schiffini A., Corsini R., Paoletti A., Alberti F., Gloanec M., Bauknecht R., Gaspar M., Leclerc E., Boula-Picard R., Michel N., Vidmar M., Monteiro P., Violas M., Pinto A., Suche H., Sohler W., Galtarossa A., Pizzinat A., de Angelis C., Gringoli F., Burr E., Seeds A.J., Lattanzi L., Guglielmucci M., Cascelli S., Martelli F., D'Ottavi A. and Contestabile G., “Experiments on 40 Gb/s Transmission with Wavelength Conversion: Results from the IST ATLAS Project,” *Fiber And Integrated Optics*, vol. 21, no. 5, pp. 371-389 September 2002.
- Matsumoto, T. and Kano, H., “Endlessly rotatable fractional-wave devices for single-mode-fibre optics,” *Electron. Lett.,* vol. 22, no. 2, pp. 78-79, 1986.
- Mears, R. J., Reekie, L., Jauncey, L., and Payne, D. N., “High-gain, rare-earth-doped fibre amplifier at 1.54 µm,” in *Proc. Conf. Optical Fibre Communication (OFC),* Paper W12, 1987.
- Mersali, B., Bruckner, H., Feuillade, M., Sainson, S., Ougazzaden, and Carenco, A., *J. Lightwave technol.,* vol. 13, pp. 1865-1871, Sept. 1995.
- Meszera, W. P., Goetz, G., Caviglia, A., and McKinerick, J. B., “Bonding of silicon wafers for silicon-on-insulator,” *J. Appl., Phys.*, vol. 64, no. 10, pp. 4943-4950, 1988.
- Miller, S. E., “Integrated optics: An introduction,” *Bell Syst. Tech. J.*, vol. 48, no. 7, pp. 2059-2069, 1969.

- Milton A., and Burns, W. "Mode coupling in optical waveguide horns," *IEEE J. Quantum Electron.,* vol. QE-13, no. 10, pp. 828-834, Oct. 1977.
- Mitomi, O., Kasaya, K., and Miyazawa, H. "Design of a single-mode tapered waveguide for low-loss chip-to-fiber coupling," *IEEE J. Quantum Electron.*, vol. 30, pp. 1787-1793, Aug 1994.
- Mitchell, B. S., "An introduction to Materials, Engineering and Science for Chemical and Materials Engineers," *John Wiley & Sons,* 2004.
- Moerman, I., D'Hondt, M., Vanderbauwhede, W., Coudenys, G., Haes, J., De Dobbelaere, P., Baets, R., Van Daele, P. and Demeester, P., "Monolithic integration of a spot-size transformer with a planar buried heterostructure InGaAsP/InP laser using the shadow masked growth technique", *IEEE Photon. Technol. Lett.*, vol. 6, no. 8, pp. 888-890, 1994.
- Moerman, I., Vanderbauwhede, W., D'Hondt, M., Van Daele, P., Demeester, P., "InGaAsP/InP strained MQW laser with integrated mode size converter using the shadow masked growth technique", *IPRM '95,* FBI.3, pp. 717-720, 1995.
- Moerman, I., Van Daele, P. P. and Demeester, P. M., "A review of fabrication technologies for the monolithic integration of tapers with III-V semiconductors devices," *IEEE J. Select. Topics Quantum Electron.* vol. 3, no. 6, pp. 1308-1320, Dec. 1997.
- Mollenauer, L. F., Lichtman, E., Neubelt, M. J., and Harvey, G. T., "Demonstration using sliding-frequency guiding filters, of error-free soliton transmission over more than 20 Mm at 10 Gbit/s single channel, and over more than 13 Mm at 20 Gbit/s in a two-channel WDM," *Electron. Lett.*, vol. 29, no. 10, pp. 910-911, 1993.
- Montanari E., Selleri S., Vincetti L. and Zoboli M., "Finite-element full-vectorial propagation analysis for three-dimensional z-varying optical waveguides", *Journal of Lightwave Technology*, vol. 16, no. 4, pp. 703-714, 1998.
- Möri, L., Weinert, C. M., Reier, F., Stoll, L., and Nolting, H. P., "Uncladded InGaAsP/InP rib waveguides with integrated thickness tapers for efficient fiber-butt coupling", *Electron., Lett.*, vol. 32, no. 1, pp. 36-37, 1996.

- Morishita, K. and Kumagai, N., “Unified approach to the derivation of variational expression for electromagnetic fields,” *IEEE Trans. Microwave Theory Tech.*, vol. MTT-25, no. 1, pp. 34-40, 1977.
- Morishita, K., Inagaki, S., and Kumagai, N., “Analysis of discontinuities in dielectric waveguides by means of the least squares boundary residual method,” *IEEE Trans. Microwave Theory Tech.*, vol. MTT-27, no. 4, pp. 310-315, 1979.
- Murphy, T. E., Hasting, J. T., and Smith, H. I.” Fabrication and characterization of narrow-band Bragg-reflector filters in silicon-on-insulator ridge waveguides,” *J. Lightwave Technol.,* vol., no. , pp. 1938-1942, 2001.
- Nakazawa, M., Suzuki, K., Yamada, E., Kubota, H., Kimura, Y., and Takaya, M., “Experimental demonstration of soliton data transmission over unlimited distances with soliton control in time and frequency domains,” *Electron. Lett.*, vol. 29, no. 9, pp. 729-730, 1993.
- Nathan M. J., Dumke W. P., Burns G., Dill F. H. Jr. and Lasher G. (1962). Stimulated emission of radiation from GaAs p-n junctions. *Applied Physics letters,* 1 (3): 62-64.
- Naval, L., Jalali, B., Gomelsky, L., and Lui, J. M., “Optimization of Si1-*x*Ge*x*/Si Waveguide Photo detectors Operating at λ=1.3 μm,” *J. Lightwave Technol.,* vol. 14(5), pp. 787-797, 1996.
- Ng, F. L., “Tabulation of methods for the numerical solution of the hollow waveguide problem,” *IEEE Trans. Microwave Theory Tech.*, vol. 22, no. 3, pp. 322-329, 1974.
- Obayya, S. S. A., Haxha, S., Rahman, B. M. A., Thermistors, C., and Grattan, K. T. V. “Optimisation of the optical properties of deeply etched semiconductor electro-optic modulators,” *J. Lightwave Technol.,* vol. 21, pp. 1813-1819, 2003.
- Obayya, S. S. A., Rahman, B. M. A., and El-Mikati, H. “New full vectorial numerical efficient propagation algorithm based on the finite element method,” *J. Lightwave Technol.,* vol. 18, pp. 409-415, 2000.
- Okuno, M., Sugita, A., Jinguji, K., and Kawachi, M. “Birefringence control of silica waveguides on Si and its application to a polarization-beam splitter/switch,” *J. Lightwave Technol.,* vol. 12, no. 4, pp. 625-633, Apr. 1994.

- Palik, E. D., Ed. "Handbook of Optical Constants of Solids." *Orlando, FL: Academic,* 1985.
- Park, S. R. and Beom-hoan, O., "Novel design concept of waveguide mode adapter for low-loss mode conversion," *IEEE Photo. Technol. Lett.,* vol. 13, no. 7, pp. 675-677, July 2001.
- Pearson, M. R. T., Bezinger, A., Delage, A., Fraser, J. W., Janz, S., Jessop, P. E., and Xu, D. X. "Arrayed waveguide grating demultiplexers in silicon-on-insulator," *Proc. SPIE*, vol. 3593, pp. 11-18, 2000.
- Pekel, U., and Mittra, R. "An application of the perfectly matched layer (PML) concept to the finite element method frequency domain analysis of scattering problems," *IEEE Microwave and Guided Wave Lett.,* vol. 5, no. 8, pp. 258-260, 1995*a*.
- Pekel, U., and Mittra, R., "A finite element method frequency domain application of the perfectly matched layer (PML) concept," *Microwave and Opt. Technol. Lett.,* vol 9, no. 3, pp.117-122, 1995*b*.
- Peng S.T. and Oliner A.A., "Guidance and leakage properties of a class of open dielectric waveguides: Part I-Mathematical formulations", *IEEE Transactions on Microwave Theory Techniques* MTT-29 (9): 843-855, 1981.
- Pezeshki, B., Agahi, F., Kash, J. A., Welser, J. J., and others, "Wavelength-selective waveguide photo detectors in silicon-on-insulator," *Appl. Phys. Lett.*, vol. 68, no. 6, pp. 741-743, Feb. 5, 1996.
- Pola, J. R. P., Biehlig, W., and Lederer, F., "A generalization of the spectral index method toward multiple rib waveguides," *J. Lightwave Technol.*, vol. 14, no. 3, pp. 454-461, 1996.
- Powell, O. "Single-mode condition for silicon rib waveguides," *J. Lightwave Technol.,* vol. 20, no. 10, pp. 1851-1856, Oct. 2002.
- Qiao, L. and Wang, J., "A modified ray-optic method for arbitrary dielectric waveguides," *IEEE J. Quantum Elect.*, vol. 28, no. 12, pp. 2721-2727, 1992.
- Quist T.M., Rediker R.H., Keyes R.J., Krag W.E., Lax B., McWhorter A.L. and Zeigler H.J., "Semiconductor maser of GaAs", *Applied Physics letters* 1 (4): 91-92, 1962.

- Rahman, B. M. A., and Davies, J. B. "Finite element solution of integrated Optical waveguides," *J. Lightwave Technol.,* vol. 2, pp. 682-688, 1984*a*.
- Rahman, B. M. A. and Davies, J. B., "Finite-element analysis of optical and microwave waveguide problems," *IEEE Trans. Microwave Theory Tech.*, vol. MTT-32, no. 1, pp. 20-28, 1984*b*.
- Rahman, B. M. A. and Davies, J. B., "Penalty function improvement of waveguide solution by finite elements," *IEEE Trans. Microwave Theory Tech.*, vol. MTT-32, no. 8, pp. 922-928, 1984*c*.
- Rahman, B. M. A. and Davies, J. B., "Analysis of optical waveguide discontinuities," *J. Lightwave Technol.*, vol. 6, no. 1, pp. 52-57, 1988.
- Rahman B. M. A, Ladele E. O, Wongcharoen T. and Grattan, K.T. V., "Spot size converters for efficient laser-fiber coupling" *Conference on active and passive optical components for WDM communications,* pp 281-291, Aug., 2001.
- Rahman B. M. A, Wongchaoen T, Ladele E. O, and Grattan, K. T. V., "Design of tapered, uniform, and compact monolithically integrated semiconductor spot-size converters for efficient laser-fiber coupling" *5th International conference on Applications of photonic technology* (ICAPT 2002), pp 727-734, Jun., 2002.
- Rahman, B. M. A., Boonthittanont, W., Obayya, S. S., Wongcharoen, T., Ladele, E. O., and Grattan, K. T. V. "Rigorous beam propagation analysis of tapered spot-size converters in the deep-etched semiconductor waveguides," *J. Lightwave Technol.,* vol. 21, pp. 3392-3398, Apr. 2003.
- Rahman, B. M. A., Wongcharoen, T., Thermistors, C., Abdallah, R., Kabir, A. K. M. S., Ladele, E. O., Somasiri, N., Alam, M. S., Rajarajan M.,and Grattan, K. T. V. "Finite element characterisation of photonic devices for optical communications," *IEE Proc. Circuits Devices Syst.*, vol. 152, no. 5, pp 532-538, 2005.
- Rajarajan, M., Rahman, B. M. A., Wongcharoen, T. and Grattan, K. T. V., "Accurate analysis of MMI devices with two-dimensional confinement," *J. Lightwave Technol.*, vol. 14, pp. 2078-2084, 1996.
- Reddy J.N., "An Introduction to the Finite Element Method", *Singapore: McGraw-Hill, Inc.*, 1993.

- Regis S. Fan. and Brian Hooker. R., "Tapered polymer single-mode waveguides for mode transformation" *J. Lightwave Technol.*, vol. 17, no. 3, pp. 466 – 474, Mar 1999.
- Rein, H. M., Hauenschild, J., Moller, M., McFarland, W., Pettengill, D., and Doernberg, J., "30 Gbit/s multiplexer and demultiplexer ICs in silicon bipolar technology," *Electron. Lett.* vol. 28, no. 1, pp. 97-99, 1992.
- Richard, J. S., Soref, R. A., and Petermann, K., "Large Single-Mode Rib Waveguides in GeSi-Si and Si-on-SiO2", *IEEE Journal of Quantum Electronics*, vol. 27, pp. 1971-1974, 1991.
- Rickman, A. G., Reed, G. T., and Namavar, F. "Silicon-on-insulator optical rib waveguide loss and mode characteristics," *J. Lightwave Technol.,* vol. 12, no. 10, pp. 1771-1776, Oct. 1994.
- Roelkens, G., Van Thourhout, D., and Baets, R. "Coupling schemes for heterogeneous integration of III – IV membrane devices and SOI waveguides" *J. Lightwave Technol.,* vol. 23, no. 11, pp. 3827-3831, Nov. 2005a.
- Roelkens, G., Dumon, P., Bogaerts, W., Van Thourhout, D., and Baets, R., "Efficient silicon-on-insulator fiber coupler fabricated using 248-nm-deep UV Lithography," *IEEE Photon. Technol. Lett.,* vol. 17, no. 12, pp. 2613-2615, Dec. 2005b.
- Runge, P. K., "Impact of fibre optics on undersea communication," in *Proc. Conf. Optical Fibre Communication (OFC)*, Invited paper ThH2, 1992.
- Saad, M. S., "Review of numerical methods for the analysis of arbitrarily-shaped microwave and optical dielectric waveguides," *IEEE Trans. Microwave Theory Tech.*, vol. 33, no. 10, pp. 894-899, 1985.
- Sakai, J., and Marcatili, E. "Lossless dielectric tapers with three-dimensional geometry," *J. Lightwave Technol.,* vol. 9, pp. 386-393, Mar. 1991.
- Saleh, B. E. A. and Teich, M. C., "Fundamentals of Photonics" *John Wiley & Sons, New York,* 1991.
- Schmidtchen, J., Splett, A., Schuppert, B., and Petermann, K. "Low loss single mode optical waveguides with large cross-section in silicon-on-insulator," *Electron. Lett*, vol. 27, pp. 1486-1488, Aug. 1, 1991.

- Schüppert, B., Schmidtchen, J., Splett, A., Fischer, U., Zinke, T., Moosburger, R., and Petermann, K., "Integrated Optics in Silicon and SiGe-Heterostructures", *J. Lightwave Technol.*, vol. 14(10), pp.2311-2323, 1996.
- Sewell, P., Benson, T. M., and Kendall, P. C., "Rib waveguide spot-size transformers: Modal properties," *J. Lightwave Technol.,* vol. 17, no. 5, pp. 848-856, May 1999.
- Shahar, A., Tomlingson, W. J., Yi-Yan, A., Seto, M. and Deri, R. J., "Dynamic etch mask technique for fabricating tapered semiconductor optical waveguides and other structures," *Appl. Phys. Lett.,* 56 (12), pp. 1098-1100, 1990.
- Shigesawa, H. and Tsuji, M., "Mode Propagation through a Step Discontinuity in Dielectric Planar Waveguide," *IEEE Transactions on Microwave Theory and Techniques,* vol. 34, no. 2, pp. 205-212, Feb. 1986.
- Shoji, T., Tsuchizawa, T., Watanabe, T., Yamada, K., and Morita, H. "Low loss mode size converter from 0.3 μm square Si wire waveguides to single mode fibres," *IEEE Photon. Technol. Lett.*, vol. 38, no. 25, pp. 1669-1670, Dec. 2002.
- Silvester, P., "Finite element solution of homogeneous waveguide problems," *Alta Frequenza,* vol. 38, pp. 313-317, 1969.
- Silvester, P. P. and Ferrari, R. L., "Finite Elements For Electrical Engineers," 2nd Edition, *Cambridge University Press,* Cambridge, 1990.
- Solehmainen, K., Aalto, T., Dekker, J., Kapulainen, M., Harjanne, M., Kukli, K., Heimala, P., Kolari, K., and Leskela, M. "Dry-etched silicon-on-insulator waveguides with low propagation and fiber-coupling losses," *J. Lightwave Technol.,* vol. 23, no. 11, pp. 3875-3880, Nov. 2005.
- Song G., and Tomlinson, W. "Fourier analysis and synthesis of adiabatic tapers in integrated optics," *J. Opt. Soc. Amer. A*, vol. 9, no. 8, pp. 1289-1300, Aug. 1992.
- Soref, .R.A. "Silicon-based Optoelectronics," *Proceedings of the IEEE*, vol. 81, no. 12, pp. 1680-1706, Dec. 1993.
- Soref, R., Schmidtchen, J., and Petermann, K. "Large single-mode rib waveguides in GeSi-Si and Si-on-SiO_2," *J. Quantum Electron.*, vol. 27, pp. 1971-1974, Aug. 1991.

- Srivastava, R., Kao, C. K., and Ramaswamy, R. V., "WKB analysis of planar surface waveguides with truncated index profiles," *J. Lightwave Technol.*, vol. 5, no. 11, pp. 1605-1609, 1987.
- Stern, M. S., "Semivectorial polarized finite difference method for optical waveguides with arbitrary index profiles," *Proc. IEE Optoelectron.*, 135, 56-63, 1988.
- Stern, M. S., Kendall, P. C., and McIlroy, P. W. A., "Analysis of the spectral index method for vector modes of rib waveguides," *IEE Proc. Pt. J*, vol. 137, no. 1, pp. 21-26, 1990.
- Svedin, J. A. M., "A numerically efficient finite element formulation for the general waveguide problem without spurious modes," *IEEE Trans. Microwave Theory Tech.*, vol. MTT-37, no. 11, pp. 1708-1715, 1989.
- Syms, R. R. A., "Optical guided waves and devices", *McGrawhill, Berkshire*, 1992.
- Sze, S. M., "Semiconductor devices, physics and technology" *John Wiley & Sons, New Jersey,* 1985.
- Taillert, D., Bogaerts, W., Bienstman, W., Krauss, T. F., Van Daele, P., Moerman, I., Verstuyft, S., Mesel, S. K. DE., and R. Baets, "An out-of-plane grating coupler for efficient butt-coupling between compact planar waveguides and single-mode fibers," *J. Quantum Electron.*, vol. 38, no. 7, pp. 949-955, July 2002.
- Tamir T., "Integrated Optics" 2nd Edition. *New York: Springler-Verlag*, 1979.
- Tamir T., "Guided wave optoelectronics" 2nd Edition. *Berlin: Springer-Verlag*, 1990.
- Tien, P. K., "Light waves in thin films and integrated optics," *Appl. Opt.,* vol. 10, no. 11, pp. 2395-2413, 1971.
- Toba, H., Oda, K., Nakanishi, K., Shibata, N., Nosu, K., Takato, N., and Fukuda, M., "100-channel optical FDM transmission/distribution at 622 Mb/s over 50 km," in *Proc. Conf. Optical Fibre Communication (OFC),* Paper PD1-1, 1990.
- Tohmori, Y., Suzaki, Y., Fukano, H., Okamoto, M., Sakai, Y., Mitomi, O., Matsumoto, S., Yamamoto, M., Fukuda, M., Wada, M., Itaya, Y., and Sugie, T.,

"Spot-size converted 1.3μm laser with butt-jointed selectively grown vertically tapered waveguide," *Electron. Lett.,* vol. 31, no. 13, pp. 1069-1070, 1993.

- Trinh, P.D., Yegnanarayanan, S., Coppinger, S.F. and Jalali, B. "Silicon-on-insulator (SOI) phased-array wavelength multi-demultiplexer with extremely low-polarisation sensitivity," *IEEE Photon. Technol. Lett.*, vol. 9, pp. 940-942, July 1997.
- Trinh, P.D., Yegnanarayanan, S., and Jalali, B. "Integrated optical directional couplers in silicon-on-insulator," *Electron. Lett*, vol. 31, no. 24, pp. 2097-2098, Nov. 1995.
- Tsuji, Y., Koshiba, M. and Shiraishi, T., "Finite Element Beam Propagation Method for three-dimensional optical waveguide structures," *J. Lightwave Technol.,* vol.15, no. 9, pp. 1728-1734, Sept. 1997.
- Turner, M.J., Clough, R.W., Martin, H.C. and Topp, L.C., "Stiffness and Deflection Analysis of Complex Structures". *Journal of the Aeronautical Sciences* **23**, pp. 805–824 1956.
- Van de Velde, K., Thienpont, H., and Van Green, R., "Extending the effective index method for arbitrarily shaped inhomogeneous optical waveguides," *J. Lightwave Technol.,* vol.6, no. 6, pp. 1153-1159, 1988.
- Van Der Tol, J. J. G. M. and Baken, N. H. G., "Correction to effective index method for rectangular dielectric waveguides," *Electron. Lett.*, vol. 24, no. 4, pp. 207-208, 1988.
- Vassallo, C., "Analysis of tapered mode transformers for semiconductor optical amplifiers," *Optic. Quantum Electron.*, vol. 26, pp. S235-S248, 1994.
- Vassalo, C., "1993-1995 optical mode solvers," *Opt. Quantum Electron.*, vol. 29, no. 2, pp. 95-114, 1997.
- Vassallo, C, and Collino, F., "Highly efficient absorbing boundary conditions for the beam propagation method," *J. Lightwave Technol.,* vol 14, no.6, pp. 1570-1577, 1996.
- Vassallo, C, and Van der keur, J.M. "Highly efficient transparent boundary conditions for the finite difference beam propagation method at order four," *J. Lightwave technol.*, vol. 15, no.10, pp. 1958-1965, 1997.

- Vawter, G. A., Sullivan, C. T., Wendt, J. R., Smith, R. E., Hou, H. Q. and Klem, J. F., "Tapered rib adiabatic following fibre couplers in etched GaAs materials for monolithic spot-size transformation," *IEEE J. Select. Topics Quantum Electron.* vol. 3, no. 6, pp. 1361-1371, Dec. 1997.
- Vivien, L., Laval, S., Dumont, B., Lardenois, S., Koster, A., and Cassan, E., "Polarization-independent single-mode rib waveguides on silicon-on-insulator for telecommunication wavelengths," *Opt. Comm.,* vol. 210, pp. 43-49, 2002.
- Weder, R. "Dielectric three-dimensional electromagnetic tapers with no loss," *IEEE J. Quantum Electron.*, vol. 24, pp.775-779, May 1988.
- Weibel, M., Caseri, W., Suter, U. W., Kiess, H. and Wehrli, E., "Preparation of polymer nanocomposites with ultrahigh refractive index," *Polymers for Advanced Technologies,* vol. 2, no. 2, pp. 75-80, 1991.
- Wilson, J., and Hawkes, J. F. B., "Optoelectronics –An Introduction", 2nd Edition. *Prentice Hall*, 1989.
- Wongcharoen, T., Rahman, B. M. A., Rajarajan, M., and Gratan, K. T. V. "Spot-size conversion using uniform waveguide sections for efficient laser-fiber coupling," *J. Lightwave Technol.,* vol. 19, pp. 708-716, 2001.
- Wu, M., Fan, P., and C. Lee, C. "Completely adiabatic s-shaped bent tapers in optical waveguides" *IEEE Photon. Technol. Lett.*, vol. 9, PP. 212-214, Feb. 1997.
- Wu, R.B. and Chen C.H., "A scalar variational conformal mapping technique for weakly guiding dielectric waveguides", *IEEE Journal of Quantum Electronics*, 22 (5): 603-609, 1986.
- Xu, C. L., Huang, W. P., and Chaudhuri, S. K., "Efficient and accurate vector mode calculations by beam propagation method, '' *J. Lightwave Technol.,* vol.9, pp. 1209-1215, 1993.
- Xu, D., Janz, S., and Cheben, P. "Design of Polarization-Insensitive Ring Resonators in Silicon-on-Insulators using MMI Couplers and Cladding Stress Engineering." *IEEE Photon. Technol. Lett.*, vol. 18, no. 2, pp. 343-346, Jan. 2006.
- Xu, D., Cheben, P., Dalacu, D., Delage, A., Janz, S., Lamontagne, B., Picard, M., and Ye, W. N. "Eliminating the birefringence in silicon-on-insulator ridge

waveguides using the cladding stress," *Opt. Lett.*, vol. 29, no. 20, pp. 2384-2386, 2004.

- Yamada, H., Chu, T., Ishida, S., and Arakawa, Y., "Optical directional coupler based on Si-wire waveguides." *IEEE Photon. Technol. Lett.*, vol. 17, no. 3, pp. 585-587, Mar. 2005.
- Yamamda, J., Murakami, Y., Sakai, J., and Kimura, T., "Characteristics of a hemispherical microlens for coupling between a semiconductor laser and single mode fiber," *IEEE J. Quantum Electronics,* vol. QE-16, pp. 1067-1072, Oct. 1980.
- Yamazaki, H., Kudo, K., Sasaki, T., Sasaki, J., Furushima, Y., Sakata, Y., Itoh, M. and Yamaguchi, M., "1.3 μm spot-size converter integrated laser diodes fabricated by narrow-stripe selective MOVPE", *IEEE J. of Selected Topics in Quantum Electron.*, vol. 3, no. 6, pp. 1392-1397, 1997.
- Yariv, A., "Introduction to Optical Electronics" 2nd Edition. *Holt, Rinehart and Winston,* 1976.
- Ye, W. N., Xu, D. X., Janz, S., Cheben, P., Picard, M. J., Lamontagne, B., and Tarr, N. G., "Birefringence Control Using Stress Engineering in Silicon-on-Insulator Waveguides," *J. Lightwave Technol.,* vol. 23, no. 3, pp. 1308-1318, Mar. 2005.
- Yeh, C., Ha, K., Dong, S. B., and Brown, W. P., "Single-mode optical waveguides," *Appl. Opt.*, vol. 18, no. 10, pp. 1490-1504, 1979.
- Yevick, D., and Bardyszewski, W., "Correspondence of variation finite-difference (relaxation) and imaginary-distance propagation methods for modal analysis, "*Opt. Lett,* vol. 17, no5, pp. 329-330, 1992.
- Yoshimoto, N., Kawano, K., Takeuchi, H., Kondo, S., and Noguchi, Y., "Spot-size converters using InP/InAlAs multi-quantum-well waveguides for low-loss single mode fiber coupling", *Electron. Lett.* vol. 28, no. 17, pp. 1610-1611, 1992.
- Zhao, C. Z., Chen, A. H., Liu, E. K., and Li, G. Z. "Silicon-on-insulator asymmetric optical switch based on total internal reflection," *IEEE Photon. Technol. Lett.,* vol. 9, no. 8, pp. 1113, 1997.

- Zhao, C. Z., Li, G. Z., Liu, E. K., Gao, Y., and others, "Silicon-on-insulator Mach-Zehnder waveguide interferometers operating at 1.3 μm," *Appl. Phys. Lett.*, vol. 67, no. 17, pp. 2448-2449, Oct. 23, 1995.
- Zienkiewicz, O. C., "The finite element method" *McGraw Hill*, 1977.
- Zimmermann, H., "Integrated Silicon Optoelectronics" *Springer*, 2000.
- Zimmermann, L., Weibel, M., Caseri, W. and Suter, U. W., "High refractive index films of polymer nanocomposites," *J. Material Research,* vol. 8, no. 7, pp. 1742-1748, July 1993.

Appendix

List of Publications by the Author

(1) Rahman BMA, **Ladele, E. O.**, Wongcharoen T, "spot size converters for efficient laser-fiber coupling" Conference on active and passive optical components for WDM communications, pp 281-291, Aug., 2001.

(2) **Ladele, E. O.**, Rahman BMA, Wongcharoen T, et al. "Design optimization of monolithically integrated semiconductor spot-size converters for efficient laser-fiber coupling" International symposium on electron devices for microwave and optoelectronic applications, pp 301-306, Nov., 2001.

(3) Rahman BMA, Wongchaoen T, **Ladele, E. O.**, et al "Design of tapered, uniform, and compact monolithically integrated semiconductor spot-size converters for efficient laser-fiber coupling" 5th International conference on Applications of photonic technology (ICAPT 2002), pp 727-734, Jun., 2002.

(4) Rahman BMA, Wongchaoen T, **Ladele, E. O.**, et al "Designs of compact monolithically integrated semiconductor spot-size converters for efficient laser-fiber coupling" 19TH Congress of the internationally- commission-for-optics, pp 499-500, Aug., 2002.

(5) Rahman BMA, Wongchaoen T, Boonthittanont W, **Ladele, E. O.**, "Designs of compact monolithically integrated tapered spot-size converters for efficient

laser-fiber coupling" 10th IEEE International symposium on electron devices for microwave and optoelectronic applications, EDMO 2002, pp 289-293, Nov., 2002.

(6) Rahman, B. M A., Boonthittanont, W., Obayya, S. S., Wongcharoen, T., **Ladele, E. O.**, and Grattan, K. T. V. "Rigorous beam propagation analysis of tapered spot-size converters in the deep-etched semiconductor waveguides," J. Lightwave Technol., vol. 21, pp. 3392-3398, Apr. 2003.

(7) Rahman BMA, Wongchaoen T, **Ladele, E. O.**, "Designs of compact monolithically integrated semiconductor spot-size converters for efficient laser-fiber coupling" Conference on active and passive optical components for WDM communications 111, pp 665-675, Sep., 2003.

(8) Rahman BMA, Wongchaoen T, **Ladele, E. O.**, et al. "Characterization of monolithically integrated spot-size converters for efficient laser-fiber coupling" Conference optics and photonic integrated circuits, pp 105-113, Apr., 2004.

(9) Rahman, B. M. A., Wongcharoen, T., Thermistors, C., Abdallah, R., Kabir, A. K. M. S., **Ladele, E. O.**, Somasiri, N., Alam, M. S., Rajarajan M.,and Grattan, K. T. V. "Finite element characterisation of photonic devices for optical communications," IEE Proc. Circuits Devices Syst. Vol. 152, no. 5, pp 532-538, 2005.

(10) Haxha, S., **Ladele, E.O.**, AbdelMalek and Rahman, B. M. A. "Optimization of compact lateral, vertical, and combined tapered spot-size converters by use of the beam propagation method," Applied Optics, vol. 45, no. 2, pp. 288-296, Jan. 2006.